THE UNIVERSITY OF CHICAGO

EXCITED-STATE STRUCTURES AND DYNAMICS OF LIGHT HARVESTING COMPLEXES IN PHOTOSYNTHETIC BACTERIA: HOW NOVEL SPECTROSCOPY UNVEILS DESIGN PRINCIPLES IN PHOTOSYNTHESIS

A DISSERTATION SUBMITTED TO
THE FACULTY OF THE DIVISION OF THE PHYSICAL SCIENCES
IN CANDIDACY FOR THE DEGREE OF
DOCTOR OF PHILOSOPHY

DEPARTMENT OF CHEMISTRY

BY
PO-CHIEH TING

CHICAGO, ILLINOIS
AUGUST 2021

Copyright © 2021 by Po-Chieh Ting

All Rights Reserved

To my dear wife Stella, who has walked through this journey with me all along.

"I have seen something else under the sun:

The race is not to the swift
or the battle to the strong,
nor does food come to the wise
or wealth to the brilliant
or favor to the learned;
but time and chance happen to them all."

- King Solomon, in *Ecclesiastes 9:11 (NIV)*

TABLE OF CONTENTS

LIST OF FIGURES

LIST OF TABLES

ACKNOWLEDGMENTS

A doctoral dissertation is a culmination of multi-year original research projects and a proof of the student's ability to conduct independent research. It is also a demonstration of developed skills that an aspiring scientist possess, such as critical thinking, self-driven curiosity, teamwork, communications, and mentorship. I was graciously granted matriculation to pursue a doctoral degree in chemistry at The University of Chicago after finishing my college and mandatory military training in Taiwan. Throughout my years in graduate school, I have been haunted by the imposter syndrome, pondering now and then whether the matriculation was just an unintentional mistake from the department. I sometimes view other peers' success as an invalidated proof of my failure in the program. The truth is, few people can expect the best and worst that can happen, and be able to step into graduate school fully prepared. Graduate school is a unique place to prepare ourselves for our future as independent thinkers and investigators of this world. I feel so fortunate to have spent my years surrounded by brilliant minds and warm souls here in Chicago, and now I can proudly call Chicago my "home away from home."

Choosing a dissertation advisor is often talked about as the most important decision any graduate student has to make in their doctoral studies, and I have been strongly convinced by this credo. I thank my dissertation advisor, Professor Greg Engel, for his mentorship during my graduate school. I thank Greg for guiding me to shape my own research projects, encouraging me to pivot toward alternative projects during my wall-hitting periods, and mostly a complete support on my professional and personal decisions. I also want to give thanks to my two other dissertation committee members, Professor Steven Sibener and Professor Bozhi Tian. I thank them for sitting on my committee and navigating me through the finish line of this long journey of graduate school.

Scientific research is an ongoing collaborative process, and none of the work presented in this Dissertation would have been complete had there not been a close partnership and

mentorship in the Engel group. In no particular order, I would like to pay tribute to several members and alumni from our group. I thank Dr. Ved Singh for his mentorship early on in my graduate school, getting me involved in one of the pioneer projects in the group on chiral 2D spectroscopy. I thank Dr. Pete Dahlberg for his incredible passion and encouraging mentorship in our projects on light-harvesting and energy transfer network in the purple bacteria, and also just being a good man. I thank Dr. Sara Massey for her all-time upbeat attitude toward science and a leading voice in shaping the science and culture in our group, and our wonderful collaboration on the 2D anisotropy on LH2 membranes. I thank Jake Higgins for his joyful company and demonstration of unrelenting persistence toward research in the Condon lab. I thank Sid Sohoni, Sami Abdulhadi, Nick Cleland and James Hayman for their diligence and expertise in biological sample preparations and assistance in acquiring spectroscopic data for the cyanobacteria project. I thank Dr. Sara Sohail for her incredible sense of science and meticulous analysis on multiple discussions. I thank Dr. John Otto for his selfless sharing of knowledge on instrumental operations and career advice. I thank Dr. Nick Williams for his valuable views on my projects, expertise in laser operation and promoting social connections through summer inter-divisional softball league games. I thank Dr. Marco Allodi for valuable conversations on various projects and life experience. I thank Dr. Ryan Wood for his sharing the expertise in machine operation, data acquisition and materials science. I thank Sarah Zinn for her cheerful heart and unquestionable skills in interior design. I thank Dr. Polina Navotnaya for her valuable discussions and camaraderie of our office life. I thank Lawson Lloyd for his demonstration of incredible diligence and scientific rigor as a younger student. I thank Dr. Richard Mazuski for his kind soul and accurate remarks on having a mature mindset at times. I thank Elizabeth Bain for showing me her fearless attitude and now promising outlook toward a challenging project I once tried unsuccessfully. I thank all the rest of current Engel group members, including Caitlin Bellora, Hugh Cairney, Anna Dardia, Indranil Ghosh, Dr. Will Hollingsworth, Ainsley Iwanicki,

Karen Ji, Coco Li, Sarah Martin, Rudy Mendez Reina, Chidera Ndife, and Qijie Shen, for they all remind me of the virtue of staying enthusiastic over what I do. The whole Engel group has evolved quite a lot during my time, and is now still evolving into a different group of cohorts; I am grateful for spending a third of my life for so many years with you, and thank you all for making this experience as uniquely memorable as it can be.

The collaborative aspect of scientific research goes beyond one group and one country. I would like to extend my gratitude toward our collaborators at University of Sheffield in the United Kingdom. I thank Professor C. Neil Hunter and his group, specifically Dr. Elizabeth Martin, Dr. Andrew Hitchhock, and Dr. Craig MacGregor-Chatwin for their inputs on cell cultures and generosity in providing the *Rhodobacter sphaeroides*, *Synechocystis* PCC 6803, and *Synechococcus elongatus* cell samples. This Dissertation can not be done without their support and collaboration.

I also want to give my shout-outs to numerous unsung heroes that promote a smooth and friendly research environment during my time at The University of Chicago. I thank Dr. Justin Jureller of Materials Research Science and Engineer Center (MRSEC) for providing training sessions on UV-Vis spectrophotometer, spectrofluorometer and confocal Raman microscope. I thank Dr. Elena Solomaha of BioPhysics Core Facility for training on circular dichroism spectrometer. I thank former and current secretaries responsible for the Engel group, Brenda Thomas and Pegg Anderson of The James Franck Institute, for their unbeatable friendliness and countless phone calls to leftover food after departmental seminars. I thank Melinda Moore and Dr. Vera Dragisich from Department of Chemistry for all the administrative assistance in the Program. I thank former and current facilities managers, John Phillips and Bentley Wall of Facilities Services, for keeping the environment at East Wing of GCIS building stable for otherwise impossible spectroscopic experiments conducted in this Dissertation. I thank former and current machine shop supervisors, Helmut Krebs and Luigi Mazzenga, for training and guidance on machining parts for building the spectrometer. I thank former staff

at Office of Research Safety, Dr. James Wright and the late Kimberly Mormann, for their meticulous instructions on lab safety during my time as the Lab Safety Contact.

The academic part of the graduate school experience is unique and difficult for everyone who has gone through or in the midst of it, yet I was blessed and fortunate to have great peers, friends and fellowship who walked alongside my journey and shared the joy and burdens together. I thank Dr. Yi-Yun Timothy Tsao for being my best man, sending me cheering messages from time to time, and a true witness to my adult life throughout our twelve-year friendship. I thank Dr. Chi-Jui Feng for being my only frequent company from Taiwan and sharing countless dinner adventures in Chicago and heart-to-heart conversations with me. I thank Dr. Johnny Alfaro for being one of my first friends in Chicago, a caring soul to everyone around him, and a safe driver when none of us had had cars yet during our first year. I thank Dr. Percival Yang-Ting Chen for being a stern yet sincere friend who dares to speak the truth, and being that one step ahead of me that I have been looking up to since our high school years. I thank Dr. Peter Chih-Cheng Yeh for always hitting me up for meals whenever he was in town. I thank Dr. Timothy C. Wang for being a encouraging friend and taking me out for a couple grocery trips when I first arrived. I thank Pastor Kensen Lam, Noah Chung, and all the fellowship I have had at Park Community Church Bridgeport over the past five years, for they show me what it's like to be in one big family.

Being a first-generation college graduate and a soon-to-be doctor of philosophy, I owe too much to my family in Taiwan, who have raised me up and provided me with resources I needed. Even though you may not really know why I have been in "school" for all my life so far, I am forever grateful for your trust in my decision to pursue higher education and scholarly training. I thank my late father, who I was blessed to have spent my first twenty one years of life with, for being a quiet supporter of me, and showing me his way of love. Dad, I wish I could celebrate this monumental step, as well as many more life events with you, and watch all the Stephen Chow movies together once again. I thank my mother, my

older brother Alex and sister-in-law Nina and my lovely nieces Bella, Vita, Hannah, and Raina, for you all have brought me joy, comfort and a sense of relief during my breaks in Taiwan. I thank my Grandma for showing her tenacity as a strong pillar to the family, and always preparing a hearty chicken soup during a chilly winter day. Grandma, may you get well soon and continue to live well. I thank my aunt, who I truly consider a second mother, for having kindly taken me and my father under her roof fifteen years ago, and for dedicating her retirement life to taking care of Grandma. I thank all the rest of the extended family for their support throughout these years.

I thank my family-in-law for welcoming me into a new family almost five years ago. I thank my better half, Stella, for having tremendous patience and empathy toward my pursuit of this degree, and for being the loudest cheerleader even when the rest of the world turns silent. Thank you for showing me a true covenant looks like, and thank you for being especially understanding over the last six months in spite of carrying a new life. And to my dear lovely daughter: I'm not sure if you'll ever read this, but if you do, remember that at the time of writing this paragraph, I can't wait to welcome you into this world. I love you both.

If I were to ask every Ph.D holder before me how they had felt during their graduate school studies, I would expect to hear comments on feeling a sense of fulfillment as well as feeling on the edge of burnout at one point. This is exactly how I have been feeling for all the years that led me to this moment. I have thrived and also failed; I have felt energized and also discouraged. I thank God for His faithfulness in me and lessons He taught me throughout these years. I thank Him for showing me the virtues of humility, self-acceptance, and perseverance. Lastly, I want to thank my old self for not giving up even when the urge of leaving had been lurking in the back of my mind.

My counselor had said to me, "The best dissertation is a finished dissertation." As I wrap up this long chapter of my life, I want to say to all of you who have crossed my paths: Thank you for being part of this journey.

ABSTRACT

Natural photosynthesis is the process of converting solar light into chemical energy through a series of photophysical and biochemical processes. Photosynthesis in Nature is an ancient yet still vibrant process that fascinates scientists by its delicacy in both its necessary structural components and intricately coordinated biochemical processes. Light harvesting processes, which occurs in the first tens of femtoseconds (10^{-15} s) to tens of picoseconds (10^{-12} s) upon light absorption, involve capturing energy from solar light and, through a series of photophysical events, transferring to the reaction centers where photochemical reactions take place. Throughout almost three-quarters of Earth's history, Nature has evolved a set of design principles for optimizing photosynthetic light harvesting efficiency among different species dwelling in extremely different habitats. To this date, Nature still leaves us with a lot of questions on detail mechanisms and biological purposes of these design principles. In this dissertation, we seek to answer the questions regarding the design principles of excited state structures and dynamics of natural light-harvesting complexes inside photosynthetic organisms with a novel ultrafast spectroscopy. In particular, we seek to achieve this goal by studying two different light harvesting systems in two organisms, LH1 complex from purple bacterium *Rhodobacter sphaeroides* and phycobilisomes from cyanobacterium *Synechococcus elongatus* PCC 7942, with ultrafast two-dimensional electronic spectroscopy (2DES). We present some of the first results of 2DES in both LH1-only chromatophores and isolated phycobilisomes, highlighting their hidden excited state features and vibronic structures. We also seek to discuss their implications on designing efficient light harvesting machinery.

CHAPTER 1

INTRODUCTION

1.1 Overview

The 21^{st} century has witnessed extreme natural phenomena more frequently than any others in human history: strong hurricanes sweeping through ocean coasts and islands; wildfire raging in dry lands and forests; descents of the polar vortex from the Arctic freezing the majority of North America in winter; heat waves scorching the Eurasia in summer. Scientists have attributed a lot of these unusually frequent events to the acceleration of global warming due to human activities. Ever since Industrial Revolution started in the 18^{th} century with the first steam engine, our reliance of fossil fuels as the main sources of has grown drastically. Unceasing burning of coal and petroleum as a means of propelling our society has pushing the atmospheric carbon dioxide (CO_2) level to "the point of no return." Furthermore, heavy reliance on coal and crude oil exposes humanity to a potential energy drought due to the outpacing population growth with respect to the formation of fossil fuels. It is thus imperative that all possible solutions to climate change and sustainable energy be rapidly pursued without reservation.

Two major targets of combating climate change in the realm of physical and biological sciences are the reduction on the CO_2 concentration in the atmosphere and increasing the percentage of utilization on alternative energy. Regarding the atmospheric CO_2 reduction, there are research ideas and progress on sequestration of CO_2 either by physical means (such as molecular traps and mineral traps), or by biochemical processes such as carboxylation. As far as alternative energy sources are concerned, many such as wind power, geothermal energy, tidal power are already put to use. To paint the picture in an even more optimistic way, efforts on "catching two birds in one stone" are already underway.

One way to simultaneously consider both targets is to look for inspiration from the

Nature, which has already developed its own mechanisms through billion years of evolutionary progress-namely, photosynthesis. Photosynthesis is a biological process of utilizing sunlight and, through a series of chemical events, converting solar energy into chemical energy required to sustain life, often in the forms of adenosine triphosphate (ATP) and/or saccharides [1]. In plants and many other organisms, photosynthesis involves light-dependent reactions and carbon fixation. Researches on artificial photosynthesis are blooming over the past decades, seeking to mimic the mechanisms in which the Nature uses the solar energy. ...

Solar energy is considered to be one of the most promising alternative energy sources in the future. One argument supporting this idea is that given its natural abundance, there are a few orders of magnitude more energy per day the Earth receives from the Sun then is captured and put to use in human activities. Finding ways to better convert the solar energy into usable and storable forms of energy can ideally transform our lifestyles in a more sustainable fashion. It is thus very enticing to conduct researches aiming at understanding the fundamental principles of natural light harvesting, which is also the philosophical motivation of all the works presented in this Dissertation.

This Dissertation will be organized in the following structure: Chapter 1 will provide a scientific review on the photosynthetic light harvesting process, with purple bacteria and cyanobacteria as two examples. Chapter 2 will review the theoretical backgrounds on the time-dependent quantum mechanics and their applications to spectroscopy. Chapter 3 will introduce the concepts and experimental setups of the main spectroscopic tools utilized in this Dissertation, specifically the two-dimensional electronic spectroscopy (2DES) and its variant. Chapter 4 and 5 will present the original research works of 2DES on membranes of the core antenna complex LH1 from purple bacterium *Rhodobacter sphaeroides*, including the ultrafast relaxation processes and coherences observed from higher-lying excited states. Chapter 6 will discuss some preliminary work of 2DES on isolated phycobilisome supercomplex from cyanobacterium *Synechococcus elongatus* PCC 7942. Chapter 7 will present some future

challenges and directions on studying light harvesting processes of photosynthesis. And finally, Chapter 8 will seek to bring this Dissertation to an end and provide a holistic conclusion.

1.2 Photosynthetic Light Harvesting: A Short Review

The earliest evidence of living organisms on Earth can be dated back as early as around 3.5 billion years ago, according to some geological studies on stromatolites, layered sedimentary fossils formed by microorganisms [2, 3, 4, 5, 6, 7, 8]. A recent research has also dated the early evolution of photosynthetic organism of Archean origin back around 3.4 billion years ago [9, 10]. This marked a evolutionary significance in that the energy from the Sun had started to be harvested through new pathways other than thermal radiation. From then on, the biology of photosynthesis had been continuing to evolve for more robust and efficient harnessing processes of solar energy.

The process of photosynthesis in the Nature involves several photochemical and biochemical steps, ranging widely both in their time scales [1]. Photosynthesis is initiated upon absorption of sunlight by organisms, promoting their molecular systems onto the electronic excited states. This excitation energy on the excited states is then directed to the reaction center (RC), where the energy is converted into chemical energy in the form of charge-separated states; these energy transfer and charge separation events typically occur within the first nanosecond upon sunlight absorption. Followed by the charge separation is a series of electron and proton transfer events taking place within one second, leading to a more stable storage of chemical energy for later uses such as ATP synthesis and/or carbon metabolism, which occur on time scales of a few minutes to hours. With the advent of modern laser technologies, scientists are able to probe sub-nanosecond photochemical events with better temporal resolution, closing in every day on the knowledge gaps of light harvesting processes in photosynthesis [11, 12].

Generally speaking, light harvesting in photosynthetic organisms occurs in a set of

pigment-protein complexes called antenna complexes with a notable exception of chlorosomes found in green sulfur bacteria, which lack protein matrices surrounding their photosynthetic pigments. Sizes of these antenna complexes can amount to nearly a few hundred kilo-Daltons (kDa), depending on the particular species. Inside the antenna complexes are pigment molecules, which are small organic molecules often carrying the structural moiety of conjugated π-systems (tetrapyrroles, tetraterpenoids and others.) Chemically speaking, these conjugated system have more delocalized highest-occupied molecular orbitals (HOMOs) and lowest-unoccupied molecular orbitals (LUMOs) and smaller energy gaps between HOMOs and LUMOs than their non-conjugated counterparts. These facts result in the ability of pigment molecules to absorb more visible to near-infrared light, giving rise to apparent colors of many photoautotrophic organism such as plants, algae, and photosynthetic bacteria. Common pigment molecules found in photosynthetic organisms include chlorophylls, bacteriochlorophylls, carotenoids and bilins.

Pigment molecules of the antenna complexes are, with few exceptions, embedded inside the protein quaternary structures. Usually bound to lipid bilayer membranes, the protein of an antenna complex serve as a scaffold holding pigment molecules in closer proximity. There are numerous advantages having such arrangement between pigments and their protein scaffold. For one, absorption cross section is increased by aligning more electric transition dipoles in an orderly fashion, thereby boosting the overall photon uptakes and the subsequently generated chemical energy. For another, the protein scaffold arranges pigments to facilitate energy transfer to the RC by forming a pigment aggregate, resulting in largely delocalized electronic excited states and creating channels through which the energy flows. Yet another function for the existence of a protein scaffold around the pigments is to take up some excess energy during the often downhill energy transfer processes, meaning that the energy of light absorbed initially is higher than that received at the end of the energy transfer chain close to the RC. In addition, the protein scaffold provides an additional layer for pigment molecules

against undesired photochemical damages and preserves their effectiveness of the overall light harvesting function.

In describing the spectroscopic properties of natural light harvesting systems, it is useful to think of the energy absorbed by the antenna complexes as being stored and transferred within a molecular aggregate in the form of a molecular exciton, or a bound electron-hole pair [13]. A Frenkel molecular exciton model has been extensively applied to explain the experimental observations [14, 15]:

$$H = \sum_{n} \epsilon_{nn} |n\rangle \langle n| + \sum_{m,n} J_{mn}(|m\rangle \langle n| + |n\rangle \langle m|) \tag{1.1}$$

In this model, the system Hamiltonian of a molecular aggregate H consists of both the site energy ϵ_{nn} of each pigment molecule, defined as the resonant energy required to promote an electronic transition from the HOMO to the LUMO, and the interaction energy between different molecules, J_{mn}, defined as dipole-dipole interactions between two electronic transition dipoles. Allowing such Coulombic interactions between a pair of transition dipoles provides an alternative basis set in which the total wavefunction can be written. The Hamiltonian in Equation 1.1 is expressed in the site basis, where each value of n represents a particular electronic transition on the n^{th} molecule of the aggregate. An alternative basis set can be determined by solving the time-independent Schrödinger equation of the Frenkel exciton Hamiltonian, yielding the resulting eigenbasis:

$$|\Psi_k\rangle = \sum_{n} a_{kn} |n\rangle \tag{1.2}$$

where $\{a_{kn}\}$ is the coefficients of the eigenvector $|\Psi_k\rangle$ of the Frenkel exciton Hamiltonian. The total wavefunction of a molecular aggregate can now be expressed in the exciton basis, $\{|\Psi_k\rangle\}$; put it another way, the molecular aggregate can be cast into a one-exciton manifold of N exciton states, where N is the total number of electronic transitions considered in the

Frenkel exciton model, which often equals to the number of pigment molecules. The most distinct feature of a Frenkel exciton model of a molecular aggregate is its ability to predict the energy levels and extents of delocalization of excitation energy on the electronic excited states. A Frenkel exciton model is able to describe the energy transfer phenomenon among the light harvesting complexes inside photosynthetic organisms.

The energy transfer process between individual antenna complex is often categorized as a Förster process [16, 17] due to the fact that the distance between separate pigment aggregates is over several angstroms to a few nanometers. A Förster energy transfer process is a resonant process where the energy donor unit passes its excitation energy to the acceptor unit without any nonradiative energy loss. The theoretical rate of energy transfer, $k_{FRET,m\to n}$, in a Förster process can be expressed as follows [18]:

$$K_{FRET,m\to n} = \frac{|J_{mn}|^2}{2\pi} \int_{-\infty}^{\infty} d\omega \widetilde{F_m}(\omega)\widetilde{A_n}(\omega) \tag{1.3}$$

where F_m and A_n are the fluorescence lineshape of the donor and absorption lineshape of the acceptor, respectively. (A more detailed description on lineshapes will be discussed in Chapter 2.) In Förster theory, the distance between the donor and the acceptor are assumed to be far enough such that the Coulombic interaction between their transition dipoles is weak enough to be treated perturbatively. The initial excitation on the donor is thought to be localized on the molecular site until the energy transfer "hops" from the donor to the acceptor, hence the term "hopping mechanism" sometimes seen in the literature when discussing the Förster energy transfer mechanism. The Förster transfer rate depends on three main factors: the relative orientation of electronic transition dipoles between the donor and the acceptor, the distance between the donor and the acceptor, and the spectral overlap between the donor fluorescence and the acceptor absorption. An extension of Förster theory has been proposed to account for the multichromophoric nature of a light harvesting antenna, in a sense that both donor and the acceptor units in the antenna consist of more than one

pigment molecules; this extension of the theory is referred to as multichromophoric Forster energy transfer (MC-FRET) [19, 20]. Regarding the accuracy of Förster theory on explaining the observed energy transfer, the typical rate of an inter-antenna energy transfer process ranges between $(5\text{ ps})^{-1}$ and $(100\text{ ps})^{-1}$, well within the predictions from Förster theory.

Intra-antenna energy transfer processes in some light harvesting complexes, however, can take place in a sub-picosecond regime, beyond the limit posed by Forster theory. This is due to the fact that with the distance between the donor and the acceptor being under just a few angstroms, the Coulombic interaction between two transition dipoles becomes nontrivially large such that Förster theory, which treats the dipole-dipole interaction only perturbatively, breaks down. In this strong interaction regime, the molecular orbitals on the donor and the acceptor are no longer isolated from one another; instead, a mixing of the HOMOs and LUMOs on both the donor and the acceptor creates a new basis set of orbitals that have various degrees of spatial overlap between the donor and the acceptor. When the donor takes up the excitation energy, that energy is no longer localized solely on the donor unit; rather, it is now shared, or delocalized, among the donor-acceptor system. Energy transfer between the donor and the acceptor under this scenario can be pictured as a process of redistributing energy. This concept of delocalization is linked to the Frenkel exciton model mentioned above in a way that each excitonic state is a superposition of localized excitation on each molecule in the aggregate. By introducing weak electronic-phonon interactions between the donor-acceptor unit and the local vibrations of the environment, Alfred G. Redfield derived a theoretical expression for the rate of energy transfer under strong Coulombic regime [18, 21, 22]:

$$K_{Redfield,k\to k'} = \sum_n |a^*_{kn} a_{k'n}|^2 \widetilde{C_n}(\omega_{kk'}) \tag{1.4}$$

where $C_n(\omega_{kk'})$ is the spectral density of the phonon modes at the n^{th} pigment as a function of the energy gap between the k^{th} and the k'^{-th} exciton states. Redfield theory emphasizes

the role of local vibrations on assisting the energy transfer process between two exciton states through system-bath interactions. In the Redfield limit of quantum dynamics, chromophore-bath interactions govern both pure dephasing processes of excitonic states as well as population transfer events between two excitonic states whose wavefunctions have non-zero spatial overlap; the term "coherent energy transfer" is coined to describe the delocalization of excitation energy through such overlapping wavefunctions.

While both Förster and Redfield theories are adequately deployed to approximate the observed rates of energy transfer processes in many light harvesting complexes, they fail to explain the case where the Coulombic interactions between transition dipoles and the system-bath interactions are on a similar magnitude. Advanced theoretical models are developed to provide a better picture of the actual energy transfer dynamics inside the light harvesting apparatus. Such models, which are beyond the scope of this Dissertation, include modified Redfield theory (MRT) [18] for the intermediate coupling regime, coherent modified Redfield theory (CMRT) [23, 24] for coherence transfer processes, and hierarchical equations of motion (HEOM) [25] for numerically exact solutions to the quantum Liouville equation.

The actual molecular architecture of the light harvesting machinery differs greatly from species to species, reflecting the evolutionary needs for each species to survive in their respective natural habitats. Within the scope of this Dissertation, two particular light harvesting antennae are in the research focus: the LH1 complex from purple bacteria, and the phycobilisomes from cyanobacteria. In the following sections, some fundamentals of these organisms pertaining to their light harvesting will be reviewed. A recent review has also highlighted research works on photosynthetic bacteria over the past decades, and is recommended here to readers for further references [26].

1.3 Light Harvesting in Purple Bacteria

Purple bacteria are anaerobic photosynthetic prokaryotes that can convert solar energy into chemical energy through the process of anoxygenic photosynthesis, meaning that they carry out photosynthesis only under oxygen-free conditions [27]. Purple bacteria are autotrophic and can survive with CO_2 as their only carbon source; purple bacteria are often found in abundance in ponds, lakes and other water bodies. The pigment molecules inside purple bacteria are bacteriochlorophylls and some carotenoids, such as sphaeroidene and lycopene, altogether giving rise to the apparent purplish-red color of the suspended cell cultures, hence the name of the organisms. The synthesis of these pigments in purple bacteria is suppressed by molecular oxygen, thus making them anoxygenic photoautotrophs. Pigments of purple bacteria are situated within intracytoplasmic membranes, forming membrane vesicles or other types of enclosures that separate the hydrophobic pigment-protein ensemble from the water environment inside the cell.

The light harvesting architecture of purple bacteria consists of three major compartments: the peripheral complex, the core complex, and the reaction center (RC). Peripheral complexes, referred to as LH2 complexes in the literature, are responsible for the initial light absorption. The LH2 complex absorbs near-infrared part of the solar spectrum, and has its largest absorption cross section at 800 and 850 nanometers (nm). A light absorption event promotes the LH2 complex into its electronic excited state, and this excitation energy is then transferred amongst neighboring LH2 complexes on the intracytoplasmic membrane until it reaches the core complex, namely the LH1 complex; this energy transfer process is completed within a few picoseconds [28].

Core LH1 complexes, contrast to the LH2 complexes, absorb light at longer wavelengths with peak absorption at around 875 nm to 880 nm for species containing bacteriochlorophyll a (BChl-a) as its major pigments; though some purple bacteria species containing bacteriochlorophyll b (BChl-b) in its LH1 complex has been characterized to absorb lights around

1,010 nm, according to a very recent study [29]. In wild-type purple bacteria, LH1 complex encloses the RC, giving rise to the name LH1-RC (or RC-LH1) complex. The basic apoprotein constituting an LH1 complex is the $\alpha\beta$ subunit, which has two major α-helices, each holding one bacteriochlorophyll molecule; in addition, one carotenoid molecule is non-covalently bound to one subunit. The overall subunit can be expressed in a shorthand notation of $\alpha\beta$-$BChl_2Car$. A typical LH1 complex consists of 15 to 28 $\alpha\beta$-$BChl_2Car$ subunits, depending on the particular species [30]. Structural variation of LH1 complexes among different species of purple bacteria is quite large as well, thanks to recent advances in structural characterization techniques such as X-ray crystallography and cryogenic electron microscopy (cryo-EM) [30]; the overall physical shape of an LH1 complex formed by $\alpha\beta$-$BChl_2Car$ subunits can be either a closed elliptical ring, an open elliptical ring or an S-shaped ribbon. In addition, LH1 complexes in different species have extra or missing protein subunits allowing quinone/quinol exchanges that facilitate charge separation and electron transfer: in *Rhodobacter sphaeroides* [31], quinone molecules pass through the gap formed by the PufX protein; in *Blastochloris viridis* [32], quinone molecules are channeled through the gap created by the absence of one polypeptide chain out of a total of 17 subunits on its LH1 complex; in *Thermochromatium tepidum* [33], quinone molecules complete the electron transfer on the α-helices of its LH1 complex. The main function of the LH1 complex is to serve as the energy sink, concentrating the excitation energy from the peripheral LH2 complexes and funneling the energy into the enclosed RC. It is worth noting that in some purple bacteria, *Rhodobacter sphaeroides* for example, an uphill energy transfer takes place from the LH1 complex to the RC.

1.4 Light Harvesting in Cyanobacteria

Cyanobacteria, also known as blue-green algae, are a group of prokaryotes capable of performing photosynthesis; they can be widely found in aquatic habitats. Cyanobacteria are early archaeological evidences that demonstrate the origin of oxygenic photosynthesis

on Earth; they are important for the enrichment of atmospheric oxygen level, boosting the evolution of algae and green plants during early history of Earth [34, 35]. Photosynthesis inside cyanobacteria occurs on the thylakoids, which are intracellular membrane vesicles harboring both the light harvesting apparatus and electron transport components that are necessary for light-dependent reactions during photosynthesis [36].

Light harvesting machinery in cyanobacteria is composed of three major protein supercomplexes: phycobilisomes (PBS), photosystem I (PSI, plastocyanin-ferredoxin oxidoreductase), and photosystem II (PSII, water-plastoquinone oxidoreductase) [37]. PSII and PSI supercomplexes are significantly larger in size than the light harvesting complexes in purple bacteria: a PSI trimer from *Synechococcus elongatus*, for example, has 12 protein subunits and 127 cofactors, with the overall diameter and height reaching 210 Åand 90 Å, respectively [38, 39]; a PSII homodimer from *Thermosynechococcus elongatus* has 20 protein subunits and 77 cofactors, with the overall dimensions of 110 Å(width) $\times$ 205 Å(length) $\times$ 105 Å(height) [40, 41]. Both PSII and PSI are embedded in thylakoids and parts of the electron transport chain; PSII absorbs light at 680 nm, whereas PSI absorbs light at 700 nm. In both PSII and PSI, the main chromophores are chlorophyll a (Chl a) and b (Chl b); their absorption spectra have peaks at red and blue edge of the photosynthetically active radiation (PAR). Both PSII and PSI funnel their energy from the antenna Chl molecules to the reaction center Chl, P680 and P700, respectively, where charge separation processes at P680 and P700 work in tandem as a part of the famous "Z-scheme" [1] of the light-dependent reaction, resulting in water splitting and proton gradient across the thylakoids, the latter prompting ATP synthesis. PBS, on the other hand, are not embedded within thylakoids but are anchored to PSII, or in rarer cases to PSI, through the membrane-docking domain of the core-membrane linker protein, ApcE (L_{CM}). Spectroscopically, PBS fill in the "green gap" of the absorption neatly with phycobiliproteins (PBP) that covalently bind phycobilins, a group of tetrapyrroles that absorbs between 450 nm and 650 nm, as their chromophores.

A PBS supercomplex is a huge assembly of light-harvesting PBP plus colorless linker proteins, with overall dimensions reaching as large as 80 nm $\times$50 nm $\times$ 12 nm due to its lack of any constraint imposed by the membrane thickness of thylakoids [42, 43]. PBS supercomplexes also constitute most of the protein content with a cyanobacterial cell. A PBS supercomplex are divided into two domains: the rod domain and the core domain. The core domain is surrounded by the rod domain, with rod-core linker proteins (L_{RC}) connecting the two. The rod domain consists of 6 to 8 cylinders, while the core domain consists of 2 to 5 cylinders, both exact numbers depending on the particular cyanobacterial species. Each cylinder is assembled through rod linkers (L_R) or core linkers (L_C), and consists of a stack of 2 to 4 hexameric PBP discs. A hexameric disk of PBPs is formed by self-assembly of two trimers, each of which is a self-assembly of three PBP monomers [43]. There are a few common PBPs existing in cyanobacteria: allophycocyanin (APC) in the core domain; phycocyanin (PC), phycoerythrin (PE), and phycoerythrocyanin (PEC) in the rod domain. The existence and number of particular types of PBPs also depend on the species. Combining all these structural information, it is not surprising to see how wide the variety of PBS in cyanobacteria can be.

Spectroscopically, PE absorbs at the shortest wavelength among all PBPs, around 545-560 nm; PEC at a slightly loner wavelength around 575 nm; PC at around 620 nm, and APC at around 650 nm. The light harvesting in cyanobacteria occurs through the absorption of green light by the PEC/PE/PC in the rod domain, inter-disk excitation energy transfer processes within the rod domain toward the rod-core interface, inter-domain energy transfer processes from the rod to the core domain, intra-domain energy transfer processes within the core domain, and finally core-to-photosystem energy transfer processes.

1.5 Concluding Remarks

In this Chapter, important aspects of photosynthetic light harvesting are covered, and specific examples on purple bacteria and cyanobacteria are given to lay the ground for the original research works to be presented in this Dissertation. In the next Chapter, focus will be switched to learning the basic principles behind the spectroscopic experiments conducted in the works for this Dissertation.

REFERENCES

[1] Robert E. Blankenship. *Molecular mechanisms of photosynthesis*. Wiley/Blackwell, Chichester, West Sussex, UK, 2nd edition, 2014.

[2] M. R. Walter, R. Buick, and J. S. R. Dunlop. Stromatolites 3,400-3,500 Myr old from the North Pole area, Western Australia. *Nature*, 284(5755):443–445, 1980.

[3] David I. Groves, John S. R. Dunlop, and Roger Buick. An Early Habitat of Life. *Sci Am*, 245(4):64–73, 1981.

[4] M. Van Kranendonk. Volcanic degassing, hydrothermal circulation and the flourishing of early life on Earth: A review of the evidence from c. 3490-3240 Ma rocks of the Pilbara Supergroup, Pilbara Craton, Western Australia. *Earth-Science Reviews*, 74(3-4):197–240, 2006.

[5] J. William Schopf, Anatoliy B. Kudryavtsev, Andrew D. Czaja, and Abhishek B. Tripathi. Evidence of Archean life: Stromatolites and microfossils. *Precambrian Research*, 158 (3-4):141–155, 2007.

[6] M. Van Kranendonk, P. Philippot, K. Lepot, S. Bodorkos, and F. Pirajno. Geological setting of Earth's oldest fossils in the ca. 3.5Ga Dresser Formation, Pilbara Craton, Western Australia. *Precambrian Research*, 167(1-2):93–124, 2008.

[7] Martin J. Van Kranendonk. Morphology as an Indictor of Biogenicity for 3.5-3.2 Ga Fossil Stromatolites from the Pilbara Craton, Western Australia. In *Advances in Stromatolite Geobiology*, volume 131, pages 537–554. Springer Berlin Heidelberg, Berlin, Heidelberg, 2011. Series Title: Lecture Notes in Earth Sciences.

[8] Raphael J. Baumgartner, Martin J. Van Kranendonk, David Wacey, Marco L. Fiorentini, Martin Saunders, Stefano Caruso, Anais Pages, Martin Homann, and Paul Guagliardo.

Nano-porous pyrite and organic matter in 3.5-billion-year-old stromatolites record primordial life. *Geology*, 47(11):1039–1043, 2019.

[9] Tanai Cardona. Early Archean origin of heterodimeric Photosystem I. *Heliyon*, 4(3): e00548, 2018.

[10] Tanai Cardona, Patricia Sánchez-Baracaldo, A. William Rutherford, and Anthony W. Larkum. Early Archean origin of Photosystem II. *Geobiology*, 17(2):127–150, 2019.

[11] Thomas Renger, Volkhard May, and Oliver Kühn. Ultrafast excitation energy transfer dynamics in photosynthetic pigment-protein complexes. *Physics Reports*, 343(3):137–254, 2001.

[12] Tihana Mirkovic, Evgeny E. Ostroumov, Jessica M. Anna, Rienk van Grondelle, Govindjee, and Gregory D. Scholes. Light Absorption and Energy Transfer in the Antenna Complexes of Photosynthetic Organisms. *Chemical Reviews*, 117(2):249–293, 2017.

[13] Herbert van Amerongen, Leonas Valkunas, and Rienk van Grondelle. *Photosynthetic Excitons*. World Scientific, Singapore, 2000.

[14] Wei Min Zhang, Torsten Meier, Vladimir Chernyak, and Shaul Mukamel. Simulation of three–pulse–echo and fluorescence depolarization in photosynthetic aggregates. *Philosophical Transactions of the Royal Society of London. Series A: Mathematical, Physical and Engineering Sciences*, 356(1736):405–419, 1998.

[15] Wei Min Zhang, Vladimir Chernyak, and Shaul Mukamel. Multidimensional femtosecond correlation spectroscopies of electronic and vibrational excitons. *The Journal of Chemical Physics*, 110(11):5011–5028, 1999.

[16] Th. Förster. Zwischenmolekulare Energiewanderung und Fluoreszenz. *Annalen der Physik*, 437(1-2):55–75, 1948.

[17] Th. Förster. 10th Spiers Memorial Lecture. Transfer mechanisms of electronic excitation. *Discussions of the Faraday Society*, 27:7–17, 1959.

[18] Mino Yang and Graham R. Fleming. Influence of phonons on exciton transfer dynamics: comparison of the Redfield, Förster, and modified Redfield equations. *Chemical Physics*, 282(1):163–180, 2002.

[19] Hitoshi Sumi. Theory on Rates of Excitation-Energy Transfer between Molecular Aggregates through Distributed Transition Dipoles with Application to the Antenna System in Bacterial Photosynthesis. *The Journal of Physical Chemistry B*, 103(1): 252–260, 1999.

[20] Seogjoo Jang, Marshall D. Newton, and Robert J. Silbey. Multichromophoric Förster Resonance Energy Transfer. *Physical Review Letters*, 92(21):218301, 2004.

[21] A. G. Redfield. On the theory of relaxation processes. *IBM Journal of Research and Development*, 1(1):19–31, 1957.

[22] A. G. Redfield. The Theory of Relaxation Processes. In *Advances in Magnetic and Optical Resonance*, volume 1, pages 1–32. Elsevier, 1965.

[23] Yu-Hsien Hwang-Fu, Wei Chen, and Yuan-Chung Cheng. A coherent modified Redfield theory for excitation energy transfer in molecular aggregates. *Chemical Physics*, 447: 46–53, 2015.

[24] Yu Chang and Yuan-Chung Cheng. On the accuracy of coherent modified Redfield theory in simulating excitation energy transfer dynamics. *The Journal of Chemical Physics*, 142(3):034109, 2015.

[25] Akihito Ishizaki and Graham R. Fleming. Unified treatment of quantum coherent and incoherent hopping dynamics in electronic energy transfer: Reduced hierarchy equation approach. *The Journal of Chemical Physics*, 130(23):234111, 2009.

[26] Rafael G. Saer and Robert E. Blankenship. Light harvesting in phototrophic bacteria: structure and function. *Biochemical Journal*, 474(13):2107–2131, 2017.

[27] C. Neil Hunter and Fevzi Daldal, editors. *The purple phototrophic bacteria*. Number 28 in Advances in photosynthesis and respiration. Springer, Dordrecht, 2009.

[28] Richard J. Cogdell, Andrew Gall, and Jürgen Köhler. The architecture and function of the light-harvesting apparatus of purple bacteria: from single molecules to *in vivo* membranes. *Quarterly Reviews of Biophysics*, 39(3):227–324, 2006.

[29] Y. Kimura, T. Yamashita, R. Seto, M. Imanishi, M. Honda, S. Nakagawa, Y. Saga, S. Takenaka, L.-J. Yu, M. T. Madigan, and Z.-Y. Wang-Otomo. Circular dichroism and resonance Raman spectroscopies of bacteriochlorophyll b-containing LH1-RC complexes. *Photosynthesis Research*, 2021.

[30] Alastair T. Gardiner, Tu C. Nguyen-Phan, and Richard J. Cogdell. A comparative look at structural variation among RC–LH1 'Core' complexes present in anoxygenic phototrophic bacteria. *Photosynthesis Research*, 145(2), 2020.

[31] Pu Qian, Miroslav Z. Papiz, Philip J. Jackson, Amanda A. Brindley, Irene W. Ng, John D. Olsen, Mark J. Dickman, Per A. Bullough, and C. Neil Hunter. Three-Dimensional Structure of the *Rhodobacter sphaeroides* RC-LH1-PufX Complex: Dimerization and Quinone Channels Promoted by PufX. *Biochemistry*, 52(43):7575–7585, 2013.

[32] Pu Qian, C. Alistair Siebert, Peiyi Wang, Daniel P. Canniffe, and C. Neil Hunter. Cryo-EM structure of the Blastochloris viridis LH1-RC complex at 2.9 å. *Nature*, 556 (7700):203–208, 2018.

[33] Long-Jiang Yu, Michihiro Suga, Zheng-Yu Wang-Otomo, and Jian-Ren Shen. Novel features of LH1-RC from *Thermochromatium tepidum* revealed from its atomic resolution structure. *The FEBS Journal*, 285(23):4359–4366, 2018.

[34] Bettina E. Schirrmeister, Muriel Gugger, and Philip C. J. Donoghue. Cyanobacteria and the Great Oxidation Event: evidence from genes and fossils. *Palaeontology*, 58(5): 769–785, 2015.

[35] Bettina E. Schirrmeister, Patricia Sanchez-Baracaldo, and David Wacey. Cyanobacterial evolution during the Precambrian. *International Journal of Astrobiology*, 15(3):187–204, 2016.

[36] Conrad W. Mullineaux. Co-existence of photosynthetic and respiratory activities in cyanobacterial thylakoid membranes. *Biochimica et Biophysica Acta (BBA) - Bioenergetics*, 1837(4):503–511, 2014.

[37] Roberta Croce and Herbert van Amerongen. Natural strategies for photosynthetic light harvesting. *Nature Chemical Biology*, 10(7):492–501, 2014.

[38] Patrick Jordan, Petra Fromme, Horst Tobias Witt, Olaf Klukas, Wolfram Saenger, and Norbert Krauß. Three-dimensional structure of cyanobacterial photosystem I at 2.5 å resolution. *Nature*, 411(6840):909–917, 2001.

[39] Petra Fromme, Patrick Jordan, and Norbert Krauß. Structure of photosystem I. *Biochimica et Biophysica Acta (BBA) - Bioenergetics*, 1507(1-3):5–31, 2001.

[40] K. N. Ferreira. Architecture of the Photosynthetic Oxygen-Evolving Center. *Science*, 303(5665):1831–1838, March 2004.

[41] Bernhard Loll, Jan Kern, Wolfram Saenger, Athina Zouni, and Jacek Biesiadka. Towards complete cofactor arrangement in the 3.0 å resolution structure of photosystem II. *Nature*, 438(7070):1040–1044, 2005.

[42] William Samsonoff and Robert MacColl. Biliproteins and phycobilisomes from cyanobacteria and red algae at the extremes of habitat. *Archives of Microbiology*, 176(6):400–405, 2001.

[43] Dvir Harris, Shira Bar-Zvi, Avital Lahav, Itay Goldshmid, and Noam Adir. The Structural Basis for the Extraordinary Energy-Transfer Capabilities of the Phycobilisome. In J. Robin Harris and Egbert J. Boekema, editors, *Membrane Protein Complexes: Structure and Function*, volume 87, pages 57–82. Springer Singapore, Singapore, 2018.

CHAPTER 2

THEORY OF QUANTUM DYNAMICS AND THIRD–ORDER SPECTROSCOPY

Studies on light harvesting processes inside photosynthetic bacteria involve understanding on both the structure and the excited-state characteristics of light harvesting complexes. To that end, some advanced time-resolved spectroscopic techniques are heavily relied upon within the scope of this Dissertation. In this Chapter, some fundamental theoretical descriptions on quantum dynamics and third-order spectroscopy pertaining to the experimental techniques used in this Dissertation will be reviewed. Most of the concepts are derived from the textbook by Mukamel [1].

2.1 Brief Summary on Quantum Dynamics

2.1.1 Time-Evolution Operator

Quantum dynamics concerns any time evolution aspect of quantum systems and establishes the theoretical foundation of spectroscopy experiments. In particular, quantum dynamics seek to apply the basics of quantum mechanics to propagate a given quantum system in time, in order to retrieve information on how probability densities of quantum states and expectation values of observables of interest changes with time. In quantum mechanics, a pure time-evolving quantum system S with time is fully described by its total wavefunction, $|\Psi(t)\rangle$ (in the bra-ket notation), which satisfies time-dependent Schrödinger equation.

$$\boldsymbol{H}_{total}\,|\Psi(t)\rangle = -i\hbar\frac{d}{dt}\,|\Psi(t)\rangle \tag{2.1}$$

where $\boldsymbol{H}_{total}(t)$ is the total Hamiltonian of the system. One can solve the time-dependent Schrödinger equation by first diagonalizing the total Hamiltonian to obtain the eigenvalues

(called the eigenenergies), E_n, and their corresponding eigenvectors (called stationary states), ϕ_n, followed by propagation of the total wavefunction at initial time point, t_0, with time:

$$|\Psi(t)\rangle = \boldsymbol{U}(t, t_0)\,|\Psi(t)_0\rangle \tag{2.2}$$

where $\boldsymbol{U}(t, t_0)$ is the time-evolution operator that takes system S from initial time, t_0, to a later time, t. (Notice that by definition, $\boldsymbol{U}(t_0, t_0) = 1$, and $\boldsymbol{U}(t_2, t_0) = \boldsymbol{U}(t_2, t_1)\boldsymbol{U}(t_1, t_0)$). Depending on the nature of the total Hamiltonian, one can express $\boldsymbol{U}(t, t_0)$ in appropriate forms. If the total Hamiltonian is independent of time (free of time–varying external field, for example), or if the total Hamiltonian at two different time points are commute (i.e. $[\boldsymbol{H}_{total}(t_1), \boldsymbol{H}_{total}(t_2)] = 0$), one can simply write down $\boldsymbol{U}(t, t_0)$ as a matrix exponential of $\boldsymbol{H}_{total}$:

$$\boldsymbol{U}(t, t_0) = e^{-\frac{i}{\hbar}\boldsymbol{H}_{total}(t-t_0)} \tag{2.3}$$

In general, $\boldsymbol{H}_{total}(t)$ need not be commute at different time points, and the expression of $\boldsymbol{U}(t, t_0)$ is thus obtained by substituting the a priori time–evolution expression of $\Psi(t)$ into time–dependent Schrödinger equation iteratively:

$$\boldsymbol{U}(t, t_0) = 1 - \frac{i}{\hbar}\int_{t_0}^{t} d\tau \boldsymbol{H}_{total}(\tau) U(\tau, t_0) \tag{2.4a}$$

$$= 1 + \left(-\frac{i}{\hbar}\right)\int_{t_0}^{t} dt' \boldsymbol{H}_{total}(t') + \left(-\frac{i}{\hbar}\right)^2 \int_{t_0}^{t} dt' \boldsymbol{H}_{total}(t') \int_{t_0}^{t'} dt'' \boldsymbol{H}_{total}(t'') + \ldots \tag{2.4b}$$

$$= exp_+ \left[-\frac{i}{\hbar}\int_{t_0}^{t} dt' \boldsymbol{H}_{total}(t')\right] \tag{2.4c}$$

where the time-ordered exponential, $exp_+ [\ldots]$, implies the total Hamiltonian at different time points do not commute. This expression is numerically exact, yet it is intractable for complicated quantum systems in which many states are involved. As will be shown later in this Chapter, the expression of $\boldsymbol{U}(t, t_0)$ can be approximated with the perturbation theory.

2.1.2 Interaction Picture

Before discussing perturbation theory, it is useful to introduce an alternative representation of quantum states and operators. In quantum mechanics, one can arbitrarily assign the time-dependence onto either wavefunctions or operators with a change of basis. Under the Schrödinger picture, the wavefunctions are solely responsible for time–dependence of the system, while in the Heisenberg picture, the operator becomes time–dependent. A third representation is an intermediate form of these two pictures. Imagine in a quantum system where the total Hamiltonian can be partitioned into two parts: a time–dependent part and a time-independent part, i.e. $\boldsymbol{H}_{total} = \boldsymbol{H}_0 + \boldsymbol{H}'(t)$, where $\boldsymbol{H}_0$ is the time-independent portion of the total Hamiltonian. Let us further define that the system wavefunction $|\Psi_I(t)\rangle$ in this representation differs from that in the Schrödinger picture in a phase factor, i.e. $|\Psi_I(t)\rangle = e^{\frac{i}{\hbar}\boldsymbol{H}_0(t-t_0)} = \boldsymbol{U}_0^\dagger(t,t_0)\,|\Psi_S(t)\rangle$, where $|\Psi_S(t)\rangle$ is the wavefunction under the Schrödinger picture and $\boldsymbol{U}_0(t,t_0)$ is the time–evolution operator of $\boldsymbol{H}_0$, and operators in this representation $\boldsymbol{A}_I(t)$ is defined as:

$$\boldsymbol{A}_I(t) = e^{\frac{i}{\hbar}\boldsymbol{H}_0(t-t_0)}\boldsymbol{A}_S(t)e^{-\frac{i}{\hbar}\boldsymbol{H}_0(t-t_0)} \tag{2.5a}$$

$$= \boldsymbol{U}_0^\dagger(t,t_0)\boldsymbol{A}_S(t)\boldsymbol{U}_0(t,t_0), \tag{2.5b}$$

where $\boldsymbol{A}_S(t)$ is an operator under the Schrödinger picture (the time–dependence here indicates the explicit time dependence irrelevant of the representation.) One can verify that these three representations are equivalent under time–dependent Schrödinger equation. This representation is called the interaction picture (or Dirac picture, named after British physicist Paul Dirac), where both operators and wavefunctions are time-dependent.

The time–evolution operator in the interaction picture is defined in a similar fashion as in the Schrödinger picture:

$$|\Psi_I(t)\rangle = \boldsymbol{U}_I(t,t_0)\,|\Psi_I(t_0)\rangle \tag{2.6}$$

where $\boldsymbol{U}_I(t,t_0) = exp_+\left[-\frac{i}{\hbar}\int_{t_0}^{t} dt' \boldsymbol{H}_I(t')\right]$; one can further deduce the relationship between time–evolution operator under different pictures: $\boldsymbol{U}(t,t_0) = \boldsymbol{U}_0(t,t_0)\boldsymbol{U}_I(t,t_0)$, which results in the following expression:

$$\boldsymbol{U}(t,t_0) = \boldsymbol{U}_0(t,t_0)\ exp_+\left[-\frac{i}{\hbar}\int_{t_0}^{t} dt' \boldsymbol{H}_I(t')\right] \tag{2.7a}$$

$$= \boldsymbol{U}_0(t,t_0) + \sum_{n=1}^{\infty}\left(-\frac{i}{\hbar}\right)^n \int_{t_0}^{t}\int_{t_0}^{t_n}\dots\int_{t_0}^{t_2} dt_1 dt_2 \dots dt_n \boldsymbol{H}_I(t_n)\boldsymbol{H}_I(t_{n-1})\dots\boldsymbol{H}_I(t_1) \tag{2.7b}$$

As will be shown in the following sections, the interaction picture will prove itself useful by providing an intuitive representation of third–order spectroscopy under the time–dependent perturbation theory.

2.1.3 Time-Dependent Perturbation Theory

In Section 2.1.1, the time-evolution operator of a quantum system is given as $\boldsymbol{U}(t,t_0)$ in terms of a power series involving time–ordered integrals of the total Hamiltonian, implying that a system wavefunction propagates under $\boldsymbol{H}_{total}(t)$. In complicated quantum systems where the degrees of freedom are large, however, propagating a large Hamiltonian matrix over time can be computationally demanding, or even intractable. A scenario in which solving the exact $\boldsymbol{U}(t,t_0)$ is unnecessary is when only part of the system Hamiltonian is known; sometimes we are only concerned with a small subsection of the entire system, regardless of the detailed time evolution of the rest of the system. In other occasions, the vast majority of the system Hamiltonian is time-independent, leaving it unnecessary to propagate the total Hamiltonian over time.

Time–dependent perturbation theory is developed by Paul Dirac to address the question of effects of a time–dependent perturbation $\boldsymbol{V}(t)$ on a time-independent (unperturbed) Hamiltonian $\boldsymbol{H}_0$, and to approximate the time dependence of quantum states and expectation

values of operators in a quantum system under the influence of $\boldsymbol{V}(t)$. By assuming the perturbation is relatively small compared to the unperturbed Hamiltonian, one can derive expressions for all kinds of time-dependent physical quantities, including those which are deemed essential to spectroscopy.

Below, a summary of time–dependent perturbation theory is given without extensive derivation. Let the total Hamiltonian be $\boldsymbol{H}_{total} = \boldsymbol{H}_0 + \boldsymbol{V}(t)$, where $\boldsymbol{V}(t)$ represents an explicit time–dependent perturbation (such as an oscillatory electric field in the electromagnetic wave), and the unperturbed stationary states and their corresponding eigenenergies of $\boldsymbol{H}_0$ be $|\phi_n\rangle$ and E_n, respectively. The collection of $\{|\phi_n\rangle\}$ (or simply, $\{|n\rangle\}$) constitutes an eigenbasis of H_0, and thus the total system wavefunction can be expressed in terms of a linear combination of this eigenbasis: $|\Psi(t)\rangle = \sum_{n=1}^{N} c_n(t) e^{-\frac{i}{\hbar}E_n t} |n\rangle$, where $c_n(t)$ is the amplitude of the total wavefunction on the basis vector $|n\rangle$ in the interaction picture. In the time-dependent perturbation theory, $c_n(t)$ can be approximated with a power series $\sum_{k=0}^{\infty} c_n^{(k)}$, with k indicating the order of perturbation.

Now let us revisit the time–evolution operator. Let $\boldsymbol{H}_I(t)$ be the perturbation in the interaction picture (i.e. $\boldsymbol{V}_I(t) = \boldsymbol{U}_0^{\dagger}(t, t_0)\boldsymbol{V}(t)\boldsymbol{U}_0(t, t_0)$). In the case where $\boldsymbol{V}_I(t)$ is presumably much smaller compared to $\boldsymbol{H}_0$, it is possible to expand $\boldsymbol{U}_I(t)$ in powers of $\boldsymbol{V}_I(t)$ and perturbation theory can be applied: $\boldsymbol{U}_I(t, t_0) = \sum_{n=0}^{\infty} \boldsymbol{U}_I^{(n)}(t, t_0)$, where the n^{th} order perturbation of the time–evolution operator is

$$\boldsymbol{U}_I^{(n)}(t, t_0) = \left(-\frac{i}{\hbar}\right)^n \int_{t_0}^{t} \int_{t_0}^{t_n} \dots \int_{t_0}^{t_2} dt_1 dt_2 ... dt_n \boldsymbol{V}_I(t_n)\boldsymbol{V}_I(t_{n-1})...\boldsymbol{V}_I(t_1), \tag{2.8}$$

and the time–ordering condition holds: $t_n \geq t_{n-1} \geq t_{n-2} \geq \ldots \geq t_1 \geq t_0$. By transforming the perturbation terms into the Schrödinger picture, the n^{th} order perturbation of the

time–evolution operator can be further simplified into the following form:

$$\begin{aligned}\boldsymbol{U}^{(n)}(t,t_0) = \left(-\frac{i}{\hbar}\right)^n \int_{t_0}^{t}\int_{t_0}^{t_n}\dots\int_{t_0}^{t_2} dt_1 dt_2 \dots dt_n \\ \boldsymbol{U}_0(t,t_n)\boldsymbol{V}(t_n)\boldsymbol{U}_0(t_n,t_{n-1})\boldsymbol{V}(t_{n-1})\dots\boldsymbol{V}(t_1)\boldsymbol{U}_0(t_1,t_0)\end{aligned} \tag{2.9}$$

where the n^{th} order perturbation of the time–evolution operator in the interaction picture can be viewed as a series of time propagations and interactions: Initially, the system is prepared at $|\Psi_S(t_0)\rangle$ and freely propagated from t_0 and t_1. At time point t_1, the system interacts with the perturbation $\boldsymbol{V}$. After the interaction, the system is again freely propagated from t_1 to t_2, until another interaction $\boldsymbol{V}$ occurs at t_2, and so on. This suggests that, for the n^{th} order perturbation, the system will interact with the perturbation n times, thus coining the name "interaction picture".

2.2 Density Matrix Formalism

In the last Section, a time evolution of a quantum system is discussed using the wavefunction approach. However, this approach has its limitation; any statistical ensemble of quantum systems cannot be described solely with a single wavefunction. An ensemble of quantum system is best described within density matrix formalism. A brief overview of density matrix formalism that circumvents this limitation will be presented in this Section.

2.2.1 Definition and Purpose of Density Matrix

In 1927 A.D., Hungarian mathematician John von Neumann published the first complete mathematical formulation of quantum mechanics; in his book, this problem circumvented this limitation by representing the whole ensemble as a density matrix. Suppose a statistical ensemble has N subsystems, each of which is described by a total wavefunction $|\Psi_i(t)\rangle$. The

density matrix that describes the ensemble is defined as follows:

$$\rho_{total}(t) = \sum_{i=1}^{N} P_i \left|\Psi_i(t)\right\rangle \left\langle\Psi_i(t)\right| \tag{2.10}$$

where P_i is the statistical probability of the subsystem i, and P_i satisfies the normalization condition: $\sum_{i=1}^{N} P_i = 1$. When $N = 1$, the total system is said to be in a pure state; whereas the ensemble is named a mixed state when $N > 1$ and all $P_i < 1$. Conventionally, the diagonal elements of a density matrix, $\rho_{nn}(t)$, are referred to as populations, while the off–diagonal elements, $\rho_{nm}(t)$, are named coherences ($n \neq m$). Together, these elements describe the full dynamics of all quantum states in the ensemble.

2.2.2 Quantum Liouville equation

Under the density matrix formalism, all quantum mechanical rules in the wavefunction approach apply to the density matrix formalism with a slightly different mathematical form. For example, the expectation value of any given operator A is $E.V.(\boldsymbol{A}) = \sum_{i=1}^{N} P_i A_i = \left\langle\Psi(t)\right| \boldsymbol{A} \left|\Psi(t)\right\rangle = Tr[\boldsymbol{A}\boldsymbol{\rho}]$, where $Tr[\ldots]$ represents the trace of a matrix. The time evolution of a density matrix is governed by Quantum Liouville–von Neumann equation, a density–matrix–formalism equivalent of the time–dependent Schrödinger equation:

$$\frac{d}{dt}\boldsymbol{\rho}(t) = -\frac{i}{\hbar}\left[\boldsymbol{H}_{total}, \boldsymbol{\rho}(t)\right] \tag{2.11}$$

2.2.3 Time-Evolution and Perturbative Treatment of a Density Matrix

Recall that under the time–dependent perturbation theory, the n^{th} order perturbation of the time–evolution operator in the interaction picture can be expressed in terms of a time–ordered exponential that specifies a series of time propagation and perturbation. The time–evolution operator for a density matrix, derived from the quantum Liouville–von

Neumann equation, takes on a similar form, albeit with a more complicated interaction scheme. In the interaction picture, the total density matrix can be expanded in terms of orders of perturbation: $\boldsymbol{\rho}_{total}(t) = \sum_{n=0}^{\infty} \boldsymbol{\rho}^{(n)}(t)$, where $\boldsymbol{\rho}^{(0)} = \boldsymbol{\rho}(t_0)$ and $\boldsymbol{\rho}^{(n)}$ is the n^{th} order perturbation of the density matrix, which involves a number of n commutators:

$$\begin{aligned}\boldsymbol{\rho}^{(n)}(t) = \left(-\frac{i}{\hbar}\right)^n \int_{t_0}^{t}\int_{t_0}^{t_n}\cdots\int_{t_0}^{t_2} dt_1 dt_2 ... dt_n \\ \left[\boldsymbol{V}_I(t_n), \left[\boldsymbol{V}_I(t_{n-1}), \ldots, \left[\boldsymbol{V}_I(t_2), [\boldsymbol{V}_I(t_1), \boldsymbol{\rho}(t_0)]\right]\right]\right]\end{aligned} \tag{2.12}$$

With a change of variable from individual time points $(t_1, t_2, \ldots, t_n)$ to time intervals between each interaction $(\tau_1 = t_2 - t_1, \tau_2 = t_3 - t_2, \ldots, \tau_{n-1} = t_n - t_{n-1}, \tau_n = t - t_n)$, and ensuring the causality of the time-ordering interactions $(t_1 \leq t_2 \leq \ldots \leq t_n)$, the n-th order density operator can be rewritten into the following form:

$$\begin{aligned}\boldsymbol{\rho}^{(n)}(t) = \left(-\frac{i}{\hbar}\right)^n \int_0^{\infty}\int_0^{\infty}\ldots\int_0^{\infty} d\tau_1 d\tau_2 ... d\tau_n \\ \left[\boldsymbol{V}_I(t-\tau_n), \left[\boldsymbol{V}_I(t-\tau_n-\tau_{n-1}), \ldots, \right.\right. \\ \left.\left.\left[\boldsymbol{V}_I(t-\tau_n-\ldots-\tau_2), [\boldsymbol{V}_I(t-\tau_n-\ldots-\tau_2-\tau_1), \boldsymbol{\rho}(t_0)]\right]\right]\right]\end{aligned} \tag{2.13}$$

As is indicated from the equation above, the pure time–ordered interactions with the perturbation $\boldsymbol{V}_I(t)$ can now interact from both the bra and the ket side of a density matrix, due to the nature of the commutator. So, for n^{th} order perturbation, there will be 2^n integrands in the expression of $\boldsymbol{\rho}^{(n)}(t)$. This perturbative expansion of the density matrix lays down the foundation of all spectroscopic formulations that will be discussed throughout this Dissertation.

2.3 Light-Matter Interaction as a Perturbation

Up till this point, the discussions of quantum dynamics are established on some generic Hamiltonian and perturbation operator. Spectroscopy is the study of quantum nature of the system of interest by utilizing one or more light–matter interactions with external electromagnetic wave and generating optical signals, which will later be detected and analyzed. In this Section, a specific form of perturbative Hamiltonian will be introduced to describe light–matter interactions, and will be used in further formulations of spectroscopy.

2.3.1 The Hamiltonian

Between 1861 and 1862 A.D., Scottish physicist James Clerk Maxwell derived the renowned Maxwell's equations of electromagnetism and proposed that light is an electromagnetic radiation. A monochromatic (i.e. single–wavelength) electromagnetic radiation is characterized by an orthogonal pair of co-propagating electric field $\vec{\boldsymbol{E}}(t)$ and magnetic field $\vec{\boldsymbol{B}}(t)$:

$$\vec{\boldsymbol{E}}(t) = \boldsymbol{E}_0 \cos\Big(\vec{\boldsymbol{k}} \cdot \vec{\boldsymbol{r}} - \omega t\Big)\hat{\boldsymbol{e}} = \frac{\boldsymbol{E}_0}{2}\left[e^{i(\vec{\boldsymbol{k}}\cdot\vec{\boldsymbol{r}}-\omega t)} + e^{-i(\vec{\boldsymbol{k}}\cdot\vec{\boldsymbol{r}}-\omega t)}\right] \tag{2.14}$$

where $\boldsymbol{E}_0$, $\vec{\boldsymbol{k}}$, $\vec{\boldsymbol{r}}$, ω, t, and $\hat{\boldsymbol{e}}$ represent the amplitude of the electric field, the wavevector of light (direction of propagation), position coordinate, the frequency of light, time coordinate, and the directional vector of the electric field, respectively. The expression of $\vec{\boldsymbol{B}}(t)$ can be obtained by the cross product between the wavevector and the electric field: $\vec{\boldsymbol{B}}(t) = \frac{1}{c_0}\vec{\boldsymbol{k}} \times \vec{\boldsymbol{E}}(t)$, where c_0 is the speed of light in vacuum.

Since any physical system can be thought of as a collection of charged particles with their distribution governed by the total wavefunction of the system, it is expected that there will be electromagnetic interactions between any physical system and light. Physically, the electrons in the system are driven by the external electromagnetic radiation, creating an oscillating electron cloud in time and space. The oscillating electron cloud itself then acts as an induced

electromagnetic wave, giving rise to optical signals. Mathematically, the interaction between light and a matter with no net charge can be written in terms of the classical Hamiltonian:

$$\boldsymbol{H}_{int}(t) = -\vec{\boldsymbol{\mu}} \cdot \vec{\boldsymbol{E}}(t) - \vec{\boldsymbol{m}} \cdot \vec{\boldsymbol{B}}(t) - \boldsymbol{Q}_{\boldsymbol{E}} \otimes \nabla \vec{\boldsymbol{E}}(t) - \boldsymbol{Q}_{\boldsymbol{B}} \otimes \nabla \vec{\boldsymbol{B}}(t) + \mathcal{O}(\vec{\boldsymbol{k}}^3) \tag{2.15}$$

where $\vec{\boldsymbol{\mu}}$ and $\vec{\boldsymbol{m}}$ are the total electric and magnetic dipole moment vector, respectively. The symbol $\otimes$ indicates the tensor product between the quadrupole moment tensor $\boldsymbol{Q}$ and the gradient of the field. Under most circumstances, the magnitude of the electric field–electric dipole interaction is at least three orders of magnitude larger than all the other interactions, and therefore the light–matter interaction Hamiltonian can be approximated as $\boldsymbol{H}_{int}(t) = -\vec{\boldsymbol{\mu}} \cdot \vec{\boldsymbol{E}}(t)$. In non–relativistic quantum mechanics, where no massive particles travel close to the speed of light, only the matter is described via Schrödinger equation; light is treated semi-classically by Maxwell's equations. Therefore, one can use this classical expression of interaction Hamiltonian in all the following formulations of spectroscopy.

In quantum mechanics, the induced electric transition dipole operator promotes transitions between two stationary states:

$$\boldsymbol{V}_{\boldsymbol{\mu}} = \sum_{i=1}^{N} \sum_{j=1}^{N} \boldsymbol{\mu}_{ij} (|i\rangle \langle j| + |j\rangle \langle i|) \tag{2.16}$$

where $\boldsymbol{\mu}_{ij}$ is the electric transition dipole moment between stationary states $|i\rangle$ and $|j\rangle$. Similar expressions for magnetic transition dipole and electric quadrupole operators can be written using the formalism. There are a group of systems with non-trivial contributions from $\boldsymbol{m}$ and $\boldsymbol{Q}$ terms, namely chiral aggregates. However, they can be probed only under particular experimental conditions, such as polarization-controlled third-order experiments [2, 3, 4, 5, 6, 7, 8, 9, 10, 11]. For most isotropic, non-magnetic quantum systems, these terms are many orders of magnitude smaller than the electric dipole $\boldsymbol{\mu}$ term. Therefore, the following discussion will only focus on the interaction between the external electric field and

the electric transition dipole of the quantum system.

2.3.2 Optical Signals From n-th Order Polarization

In classical electromagnetism, the response from the matter after interacting with light is described by the polarization density $\boldsymbol{P}(t)$, which represents the density of total electric dipole moments inside the matter (Note: in the literature, sometimes this quantity is simply called the polarization, which may create confusion with the polarization of light, which describes the plane of oscillation of light.) In a quantum system, the polarization density can be calculated as the expectation value of the electric transition dipole operator $\boldsymbol{V}_\mu$; in density matrix formalism, the polarization density can be written as the trace of the matrix product between the electric transition dipole operator and the total density matrix of the quantum system, $\boldsymbol{P}(t) = Tr[\boldsymbol{V}_\mu \boldsymbol{\rho}_{total}(t)]$. When multiple light–matter interactions are considered, the polarization density can be expanded in the same fashion as the density matrix in Section 2.2.3, resulting in the linear combination of polarization densities of different orders:

$$\boldsymbol{P}(t) = \boldsymbol{P}^{(0)} + \boldsymbol{P}^{(1)}(t) + \sum_{n=2}^{\infty} \boldsymbol{P}^{(n)}(t) \tag{2.17a}$$

$$= Tr[\boldsymbol{V}_\mu \boldsymbol{\rho}^{(0)}] + Tr[\boldsymbol{V}_\mu \boldsymbol{\rho}^{(1)}] + \sum_{n=2}^{\infty} Tr[\boldsymbol{V}_\mu \boldsymbol{\rho}^{(n)}] \tag{2.17b}$$

In the above expression, the first term describes the permanent polarization density in the system, the second term is the linear polarization, and the summation terms account for all higher–order terms. Various experimental attempts and progresses have been made to retrieve different terms of polarization density in order to gain insights into natural and artificial quantum systems. In the next Section, the details of each term will be discussed.

2.4 Response Functions

There are numerous examples where a physical system responds to external perturbation: a standing object moves upon an external force is exerted; a stream of electron starts flowing through the conductor upon connecting to a power supply which creates an electromotive force, and so on. In language of statistical physics, these phenomena can be described in the response function formalism, which conceptually suggests that there is an intrinsic property of a physical system that governs the response to a given external perturbation. Our understanding of light–matter interaction can also be conveniently formulated using this concept: each system has a response function to the electromagnetic wave, generating a time–dependent polarization density $\boldsymbol{P}(t)$ which can be detected with spectroscopic instruments. In this Section, formalism of linear and nonlinear response functions toward electromagnetic wave will be discussed. Toward the end of the Section, double–sided Feynman diagram formalism, a pictorial representation of response functions, will be introduced with the aim of simplifying the following discussions throughout this Dissertation.

2.4.1 Linear Response Theory

Recall that in Section 2.3.2, the polarization density of a physical system is defined as the total electric dipole moment within the matter. These collective dipole moments can respond to an external electromagnetic field of a given frequency ω, and the behavior of this electric response is governed by the response function $\chi(\omega)$. When non–local effects are neglected, a phenomenological expression between all these quantities can be written as:

$$\boldsymbol{P}(\omega) = \sum_{n=1}^{\infty} \chi^{(n)}(\omega)\big[\boldsymbol{E}(\omega)\big]^n \tag{2.18}$$

where n specifies the number of light–matter interactions. When only one light–matter is considered, an expression of linear response to the light is obtained: $\boldsymbol{P}^{(1)}(\omega) = \chi^{(1)}(\omega)\big[\boldsymbol{E}(\omega)\big]$,

or in time-domain representation, $\boldsymbol{P}^{(1)}(t) = R^{(1)}(t)\big[\boldsymbol{E}(t)\big]$.

Next, we want to establish a connection between the response function and the time–evolution of density matrix. For simplicity, we limit ourselves in the discussion of an isolated two–state system with the ground state $|g\rangle$ and an excited state $|e\rangle$, and assuming the system was prepared at the ground state before any light–matter interaction. Plugging in the definitions of interaction Hamiltonian and time–evolved density matrix, the linear term of polarization density $\boldsymbol{P}^{(1)}(t)$ can be written as:

$$\boldsymbol{P}^{(1)}(t) = \int_0^\infty dt_1 S^{(1)}(t_1)\boldsymbol{E}(\boldsymbol{r}, t - t_1), \tag{2.19}$$

with

$$S^{(1)}(t_1) = \left(\frac{i}{\hbar}\right)\theta(t_1)\left\langle \boldsymbol{V}(t_1)\big|\big[\boldsymbol{V}(0), \boldsymbol{\rho}(-\infty)\big]\right\rangle \tag{2.20a}$$

$$= \left(\frac{i}{\hbar}\right)\theta(t_1)\left\langle \big[\boldsymbol{V}(t_1), \boldsymbol{V}(0)\big]\big|\boldsymbol{\rho}(-\infty)\right\rangle, \tag{2.20b}$$

where $S^{(1)}(t_1)$ represents the real-valued linear response function for the quantum system of interest, and $\theta(t_1)$ is the Heaviside step function guaranteeing the causality of the response function; that is, the system response must come after the light-matter interaction. Linear response function is the basis of absorption and stimulated emission signals.

2.4.2 Third-Order Response

Third-order nonlinear response function is commonly applied in spectroscopic techniques such as pump probe and two-dimensional spectroscopy. Extending the formalism of the linear response and polarization density, the corresponding third-order term of polarization density

$\boldsymbol{P}^{(3)}(t)$ has the following expression:

$$\begin{aligned}\boldsymbol{P}^{(3)}(t) = \int_0^\infty dt_3 \int_0^\infty dt_2 \int_0^\infty dt_1 S^{(3)}(t_3, t_2, t_1) \\ \boldsymbol{E}(\boldsymbol{r}, t - t_3)\boldsymbol{E}(\boldsymbol{r}, t - t_3 - t_2)\boldsymbol{E}(\boldsymbol{r}, t - t_3 - t_2 - t_1),\end{aligned} \tag{2.21}$$

with

$$S^{(3)}(t_3, t_2, t_1) = \left(\frac{i}{\hbar}\right)^3 \theta(t_1)\theta(t_2)\theta(t_3) \left\langle \boldsymbol{V}(t_3 + t_2 + t_1) \middle| \Big[\boldsymbol{V}(t_2 + t_1), \Big[\boldsymbol{V}(t_1), \big[\boldsymbol{V}(0), \boldsymbol{\rho}(-\infty)\big]\Big]\Big] \right\rangle \tag{2.22a}$$

$$= \left(\frac{i}{\hbar}\right)^3 \theta(t_1)\theta(t_2)\theta(t_3) \left\langle \Big[\Big[\big[\boldsymbol{V}(t_3 + t_2 + t_1), \boldsymbol{V}(t_2 + t_1)\big], \boldsymbol{V}(t_1)\Big], \boldsymbol{V}(0)\Big] \middle| \boldsymbol{\rho}(-\infty) \right\rangle, \tag{2.22b}$$

where $S^{(3)}(t_3, t_2, t_1)$ is the third-order nonlinear response function of the quantum system of interest. All spectroscopic experiments seek to examine part of or the whole functional form of these response functions with an aim to provide evidences to molecular details. The 3 commutators inside Equation 2.22 for the expression of the third-order response function implies that there are a total of 8 terms in $S^{(3)}(t_3, t_2, t_1)$, including 4 distinct terms and their respective complex conjugates. In other words, we can rewrite $S^{(3)}(t_3, t_2, t_1)$ into:

$$S^{(3)}(t_3, t_2, t_1) = \left(\frac{i}{\hbar}\right)^3 \theta(t_1)\theta(t_2)\theta(t_3) \sum_{n=1}^{4} \big[R_n(t_3, t_2, t_1) - R_n^*(t_3, t_2, t_1)\big] \tag{2.23}$$

where the 4 individual pathways contributing to the overall $S^{(3)}(t_3, t_2, t_1)$ are expressed in terms of R_1 through R_4:

$$R_1(t_3, t_2, t_1) = \langle \boldsymbol{V}(t_1)\boldsymbol{V}(t_1 + t_2)\boldsymbol{V}(t_1 + t_2 + t_3)\boldsymbol{V}(0)\boldsymbol{\rho}(-\infty)\rangle \tag{2.24a}$$

$$R_2(t_3, t_2, t_1) = \langle \boldsymbol{V}(0)\boldsymbol{V}(t_1 + t_2)\boldsymbol{V}(t_1 + t_2 + t_3)\boldsymbol{V}(t_1)\boldsymbol{\rho}(-\infty)\rangle \tag{2.24b}$$

$$R_3(t_3, t_2, t_1) = \langle \boldsymbol{V}(0)\boldsymbol{V}(t_1)\boldsymbol{V}(t_1 + t_2 + t_3)\boldsymbol{V}(t_1 + t_2)\boldsymbol{\rho}(-\infty)\rangle \tag{2.24c}$$

$$R_4(t_3, t_2, t_1) = \langle \boldsymbol{V}(t_1 + t_2 + t_3)\boldsymbol{V}(t_1 + t_2)\boldsymbol{V}(t_1)\boldsymbol{V}(0)\boldsymbol{\rho}(-\infty)\rangle \tag{2.24d}$$

Due to invariance of the trace under cyclic permutations, Equation 2.24 can be recast into a form with better illustration of time-ordered interactions with external field from either the bra or the ket side:

$$R_1(t_3, t_2, t_1) = \langle \boldsymbol{V}(t_1 + t_2 + t_3)\boldsymbol{V}(0)\boldsymbol{\rho}(-\infty)\boldsymbol{V}(t_1)\boldsymbol{V}(t_1 + t_2)\rangle \tag{2.25a}$$

$$R_2(t_3, t_2, t_1) = \langle \boldsymbol{V}(t_1 + t_2 + t_3)\boldsymbol{V}(t_1)\boldsymbol{\rho}(-\infty)\boldsymbol{V}(0)\boldsymbol{V}(t_1 + t_2)\rangle \tag{2.25b}$$

$$R_3(t_3, t_2, t_1) = \langle \boldsymbol{V}(t_1 + t_2 + t_3)\boldsymbol{V}(t_1 + t_2)\boldsymbol{\rho}(-\infty)\boldsymbol{V}(0)\boldsymbol{V}(t_1)\rangle \tag{2.25c}$$

$$R_4(t_3, t_2, t_1) = \langle \boldsymbol{V}(t_1 + t_2 + t_3)\boldsymbol{V}(t_1 + t_2)\boldsymbol{V}(t_1)\boldsymbol{V}(0)\boldsymbol{\rho}(-\infty)\rangle \tag{2.25d}$$

2.4.3 Double-Sided Feynman Diagrams

The expression of the third-order response function in Equations 2.24 and 2.25 implies that there are many possible combinations of light-matter interactions, representing different photophysical processes. For example, the resulting radial frequencies from three light-matter interactions can be any combination of $\pm\omega_1 \pm \omega_2 \pm \omega_3$; similarly, the wavevector of the third-order signal can be emitted from any direction of $\pm\vec{\boldsymbol{k}}_1 \pm \vec{\boldsymbol{k}}_2 \pm \vec{\boldsymbol{k}}_3$. However, in resonant spectroscopic techniques, most of these terms become highly oscillatory and are integrated to zero when calculating the third-order polarization, $\boldsymbol{P}^{(3)}$. Thus, we can simply retain only the resonant terms in Equations 2.24 and 2.25 when considering coherent spectroscopic

experiments as those utilized in this Dissertation; this selection of resonant terms is called the rotating wave approximation (RWA)[12, 13].

Due to the often-lengthy mathematical expression of the third-order response function, it is therefore of most interest and use to express them in a more succinct and intuitive way. Double-sided Feynman diagrams are pictorial representations which carry the same information as optical response functions. They provide a convenient bridge between the theoretical expression of quantum dynamics and visualization of various nonlinear spectroscopic experiments.

An example of a double-sided Feynman diagram for one particular third-order pathway that survives RWA in a two-level system is depicted in Figure 2.1. Time propagation of the system runs from the bottom to the top of the diagram, with light-matter interactions occurring time points of $t - t_3 - t_2 - t_1$, $t - t_3 - t_2$ and $t - t_3$, indicated by arrows with corresponding wavevectors of the light field. The third-order signal is detected in the direction of $\vec{\boldsymbol{k}}_{sig}$ at time t. Initially, the system is at its equilibrium population state, $\boldsymbol{\rho(-\infty)}$, which is often the ground state. Upon each light-matter interaction, the system switches from a population state ($|g\rangle\langle g|$ or $|e\rangle\langle e|$) to a coherence state ($|e\rangle\langle g|$ or $|g\rangle\langle e|$), or vice versa. Between interactions, the system undergoes time evolution according to quantum Liouville equation [Equation 2.11]. The interaction can act from the ket side (left-hand side on the diagram) or the bra side (right-hand side on the diagram). The direction of wavevector arrows indicates whether the system undergoes an absorption or emission event upon a particular light-matter interaction; an arrow pointing toward the diagram symbolizes an absorption, whereas an arrow pointing away from the diagram symbolizes an emission.

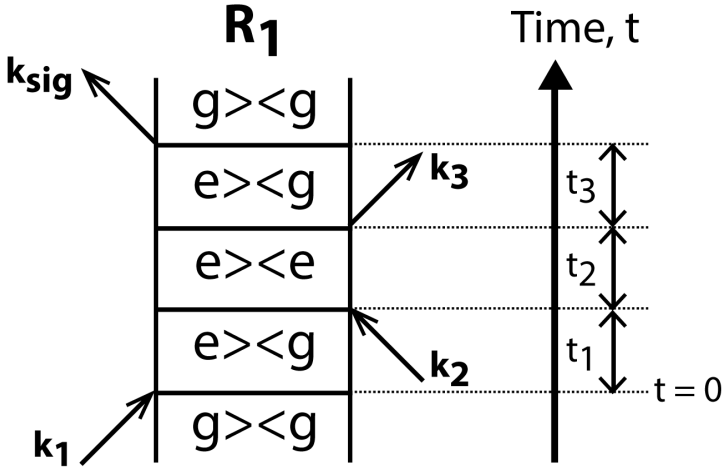

Figure 2.1: Example of a double-sided Feynman diagram for the third-order response function.

One convenience in using double-sided Feynman diagrams is the easiness to write down the mathematical expression of a specific pathway in the response function whenever it is needed. For example, the functional form of the pathway depicted in Figure 2.1 corresponds to the following equation:

$$R_1(t_1,t_2,t_3) = (-1)^2\left(\frac{i}{\hbar}\right)^3 \theta(t_1)\theta(t_2)\theta(t_3) \times \left\langle e^{+i\vec{\boldsymbol{k}}_3\cdot\vec{\boldsymbol{r}}_3 - i\omega_{eg}t_3 - \Gamma_3 t_3} \times e^{-i\vec{\boldsymbol{k}}_2\cdot\vec{\boldsymbol{r}}_2 + i\omega_{ee}t_2 - \Gamma_2 t_2} \times e^{+i\vec{\boldsymbol{k}}_1\cdot\vec{\boldsymbol{r}}_1 - i\omega_{eg}t_1 - \Gamma_1 t_1} \times \rho_{gg} \right\rangle \tag{2.26}$$

where Γ represents the lineshape function during each time evolution, and the oscillation frequency during each time duration takes up the form of $\omega_{21} = \big(E_2 - E_1\big)/\hbar$, where E_1 and E_2 are the eigenenergies of the state 1 and 2, respectively. This function has a factor of $(-1)^2$ (incidentally equal to 1), due to the fact that bra-side interaction carries a minus sign from the commutator in Equation 2.22, and that there are two interactions from the bra (right) side in the pathway shown in Figure 2.1. The wavevector of the third-order signal, $\vec{\boldsymbol{k}}_{sig}$, for

R_1 equals to the total addition of wavevectors from three interactions, $+\vec{\boldsymbol{k}}_1 - \vec{\boldsymbol{k}}_2 + \vec{\boldsymbol{k}}_3$; this direction is called the phase-matching direction.

2.5 Principles of Coherent Two-Dimensional Spectroscopy

With the advent of high–power ultrafast laser system in the late 1980s [14, 15], the amount of research in femtosecond quantum dynamics has exploded in an unprecedented way, allowing scientists to develop various nonlinear spectroscopic experiments and observe for the first time how a system evolves on the electronic excited state potential surfaces on a sub–picosecond level. The invention of high–power femtosecond laser has also led to a recognition of Nobel Prize in Physics in 2018 [16, 17, 18]. Among all nonlinear spectroscopic techniques, two–dimensional spectroscopy holds a special place in its simultaneous temporal and spectral resolving power of an optical spectrum. Since its inception and experimental realization in late 1990s in both visible [19, 20, 21, 22] and infrared [23, 24, 25, 26] regimes, two–dimensional spectroscopy has proved itself to be a novel and powerful tool of studying excited state dynamics of biological and chemical systems [Citations]. In this Section, the principles of two–dimensional spectroscopy and informational contents of a typical two–dimensional spectrum will be discussed.

2.5.1 Pulse Sequence and Response Functions

Two–dimensional spectroscopy is a third–order optical technique in which three excitation optical pulses interact with the sample, each at its distinct timing, and a resulting third–order polarization $\boldsymbol{P}^{(3)}(t)$ generated from the sample is detected by a spectrophotometer and photon detector. An illustration of the pulse sequence for two-dimensional spectroscopy is shown in Figure 2.2. The first pulse establishes a coherence between the ground and excited state, which evolves during the coherence time τ, the time duration between pulse 1 and pulse 2. After the system has freely evolved during the coherence time, the second pulse interacts

with the system to create a population on the excited state or ground state. The third pulse interacts with the system after a certain waiting time T, the time duration between pulse 2 and pulse 3, promoting the system again into a coherence, which evolves with time until the detection after the detection time, t, the time duration between pulse 3 and the detection. (Note: the literature often borrows the language from nuclear magnetic resonance and photon echo peak shift experiments, and refers to this time as the "rephasing time", as the system evolving a phase during the coherence time undergoes a reversed phase evolution during this time period. The author opts out of this usage as the system may not in fact "re-phase" during this time duration in two-dimensional spectroscopy.)

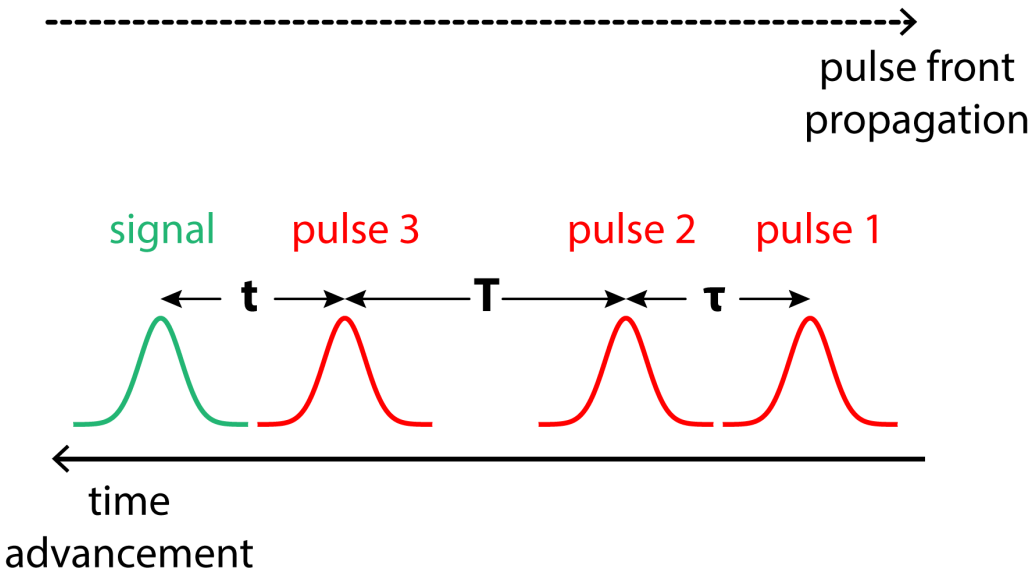

Figure 2.2: Pulse sequence of a two-dimensional spectroscopy.

The signal of an two-dimensional spectroscopy can be expressed in terms of the third-order response functions introduced in Section 2.4.2, as functions of three distinct time duration, τ, T, and t; the six representative double-sided Feynman diagrams for a hypothetical three-state system are drawn out in Figure 2.3. Depending on the dynamics occurring during

three excitations, these pathways are categorized into three types: stimulated emission (SE), ground state bleach (GSB), and excited state absorption (ESA). SE occurs where the system established on the excited state population after the first two interactions undergoes a radiative relaxation process after the third interaction, as in pathways R_1 and R_2 in Figure 2.3. GSB takes place when the ground state population is depleted, subsequently causing a decrease in the probability of an absorption process, as in pathways R_3 and R_4 in Figure 2.3. ESA happens when the excited state population establish during waiting time undergoes an absorption process, as in pathways R_5 and R_6 in Figure 2.3. In this Dissertation, all 2D data are presented in terms of changes in transmittance during the measurement; thus, SE and GSB pathways will carry positive signals, whereas ESA pathways will have negative signals in the 2D data.

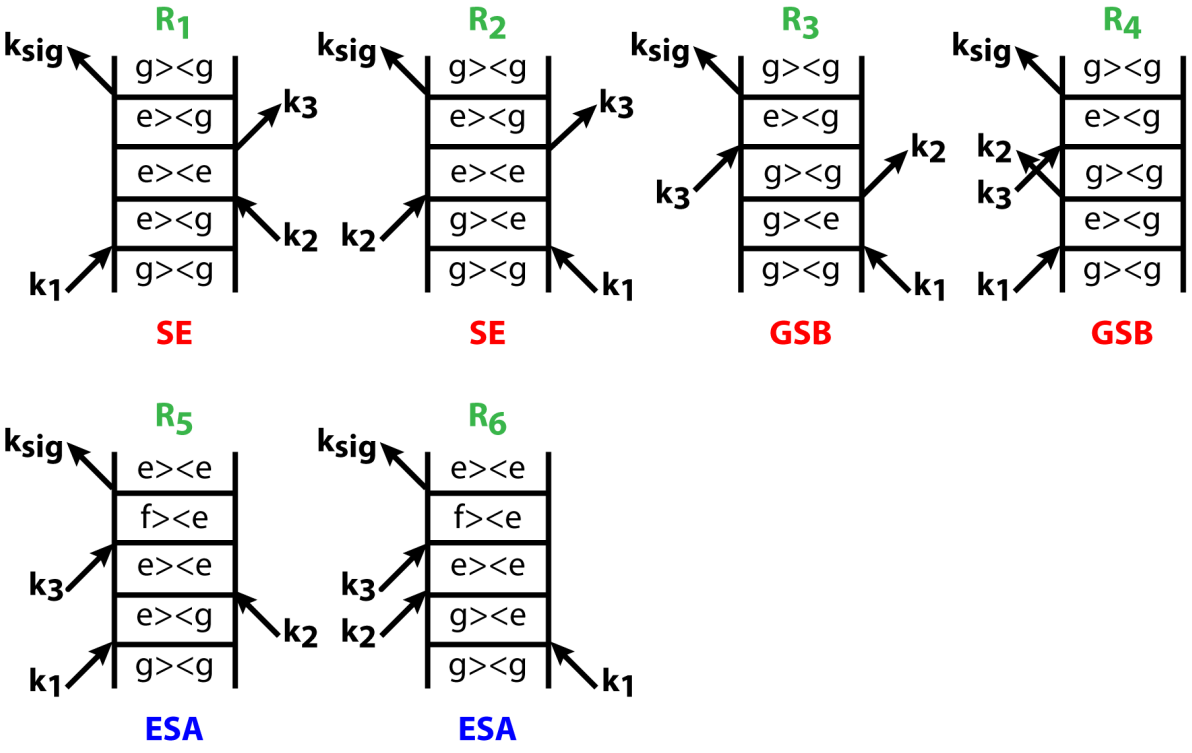

Figure 2.3: Double-sided Feynman diagrams signifying representative dynamics pathways probed in two-dimensional spectroscopy. Abbreviations- SE: stimulated emission; GSB: ground state bleach; ESA: excited state absorption.

Another way to categorize these pathways is by how the phase of the system evolves during the coherence time τ with respect to that during the detection time t. Based on their relative phase evolution, these response functions can be categorized into rephasing and nonrephasing pathways. As shown in Figure 2.3, the system acquires a phase of opposite signs during τ and t in pathways R_2, R_3 and R_6 ($e^{+i\omega_{eg}\tau}$ during τ and $e^{-i\omega_{eg}t}$ during t for R_2 and R_3; $e^{+i\omega_{eg}\tau}$ during τ and $e^{-i\omega_{fe}t}$ during t for R_6), whereas the system acquires a phase of the same signs during both time duration in pathways R_1, R_4 and R_5 ($e^{-i\omega_{eg}\tau}$ during both τ and t for R_1 and R_4; $e^{-i\omega_{eg}\tau}$ during τ and $e^{-i\omega_{fe}t}$ during t for R_5). Pathways carrying opposite signs of phase evolution, such as R_2, R_3 and R_6, are defined as rephasing pathways, while pathways carrying the same signs of phase evolution, such as R_1, R_4 and R_5, are defined as nonrephasing pathways. The results are photon echo signals and free induction decays from rephasing and nonrephasing pathways, respectively.

2.5.2 Interpreting a Coherent Two-Dimensional Spectrum

A 2D spectrum taken by two-dimensional spectroscopy is abundant in molecular information encoded in the third-order response function. The signal leading to a 2D spectrum is often presented as a double-Fourier-transform spectrum, $S_{2D}(\omega_\tau, T, \omega_t)$. Conceptually, a 2D spectrum can be considered a energy-energy correlation map, linking the excitation energy $\hbar\omega_\tau$ and the detection energy $\hbar\omega_t$ at a later waiting time T. It is distinct from some other 2D correlation spectra in a sense that, all excitation energies are excited and all detection energies are probed simultaneously, making two-dimensional spectroscopy a coherent (in-phase) technique.

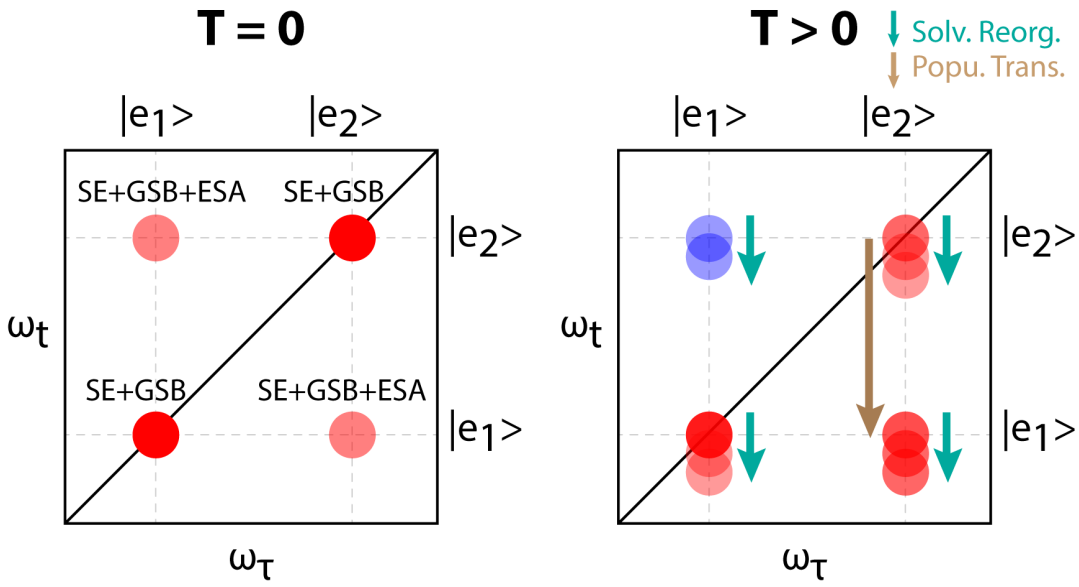

Figure 2.4: A tutorial 2D spectrum of a three-state system. Red and blue represent positive and negative values of changes in transmittance of light, respectively. At positive waiting time T $>$ 0, peak shapes start evolving due to dynamical processes such as solvent reorganization (turquoise arrows) and population transfer (light brown arrow).

A tutorial 2D spectrum of a three-state system is sketched in Figure 2.4. Each spectrum symbolizes the screenshot of dynamics of the system recorded at a given waiting time. At zero waiting time $T = 0$, the main features are diagonal peaks consisting of SE and GSB from the excited states $|e_1\rangle$ and $|e_2\rangle$. In a system where there exists couplings among excited states, negative ESA peaks can also be expected to show up at the off-diagonal cross peaks between $|e_1\rangle$ and $|e_2\rangle$. At some later waiting time, during which the system is allowed to evolve, the 2D spectrum will start to change in terms of formation of new peaks, decay in amplitude of some features, periodic oscillations in amplitudes of some peaks, changes in peak shapes, and so on. Many of the dynamical processes can be responsible for these changes, be it solvent reorganization, population transfer between states, coherence-to-coherence transfer, vibrational relaxation of a vibronic population, decay of a quantum coherence, or crossing of a conical intersection; a non-exhaustive collection of these molecular dynamical processes can

be represented by double-sided Feynman diagrams shown in Figures 2.5, 2.6, 2.7, and 2.8. This wide range of processes that can be captured by two-dimensional spectroscopy opens up new avenues in understanding excited state dynamics of molecular and materials systems.

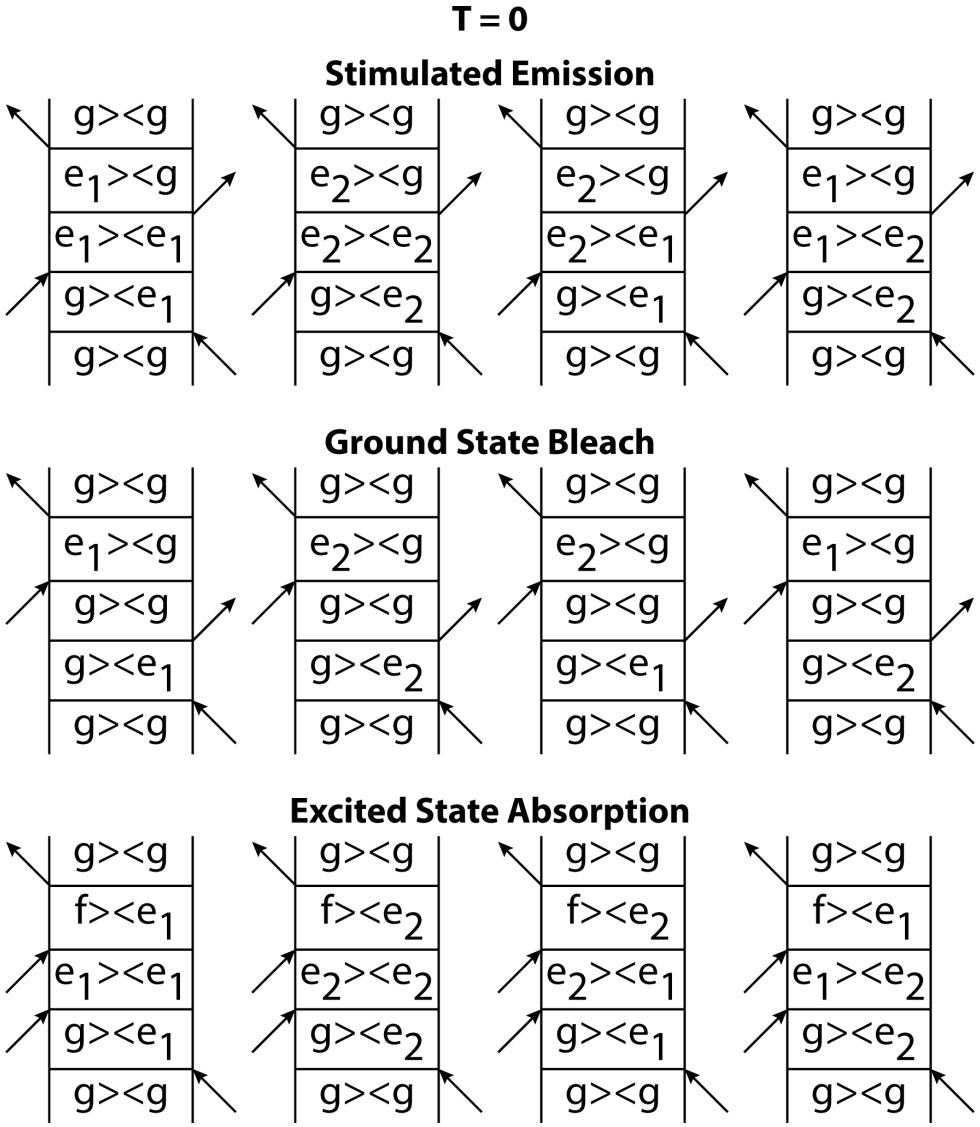

Figure 2.5: Double-sided Feynman diagrams of a three-level electronic system in a 2DES experiment at zero waiting time. Letters g, e_1, e_2 represent the electronic ground state, excited state 1, and excited state 2, respectively. Vibrational levels are ignored in this panel.

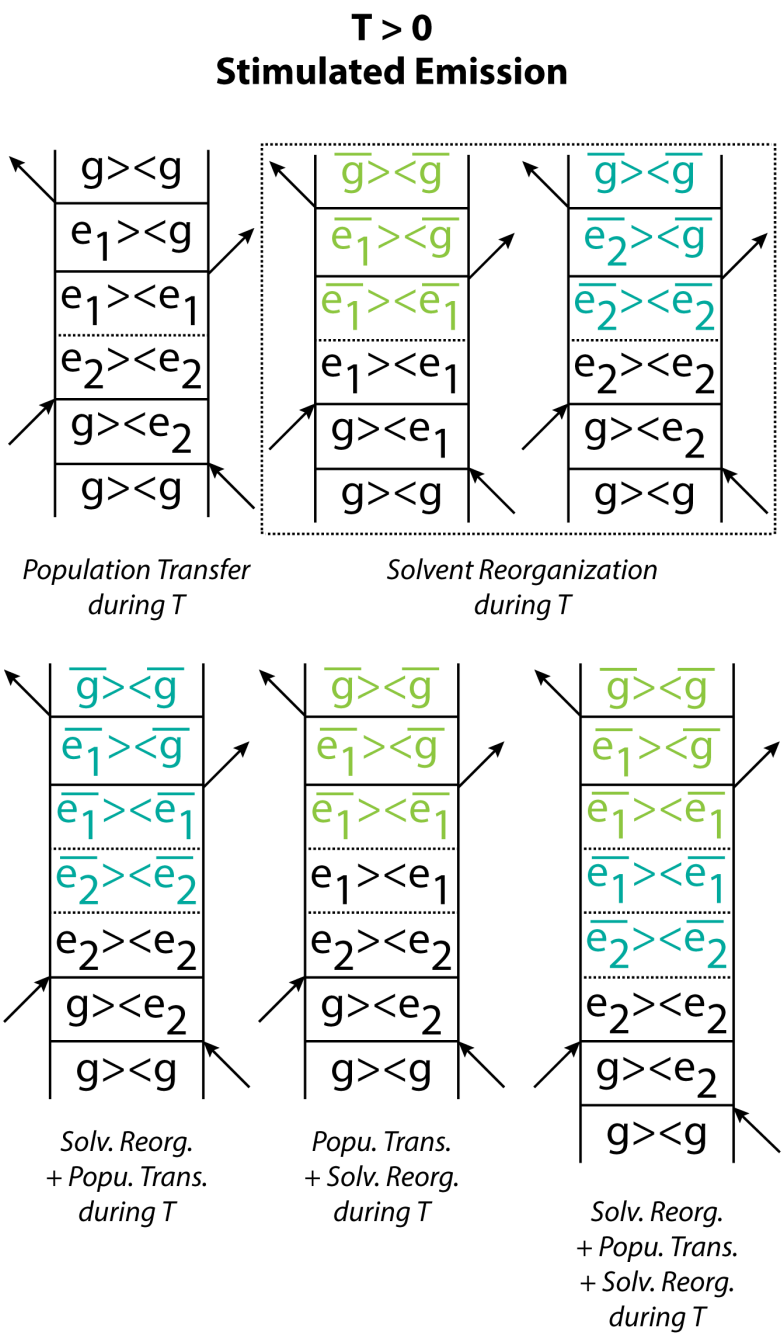

Figure 2.6: Double-sided Feynman diagrams showing stimulated emission pathways of a three-level electronic system in a 2DES experiment at positive waiting time. Letters g, e_1, e_2 represent the electronic ground state, excited state 1, and excited state 2, respectively. Vibrational levels are ignored in this panel.

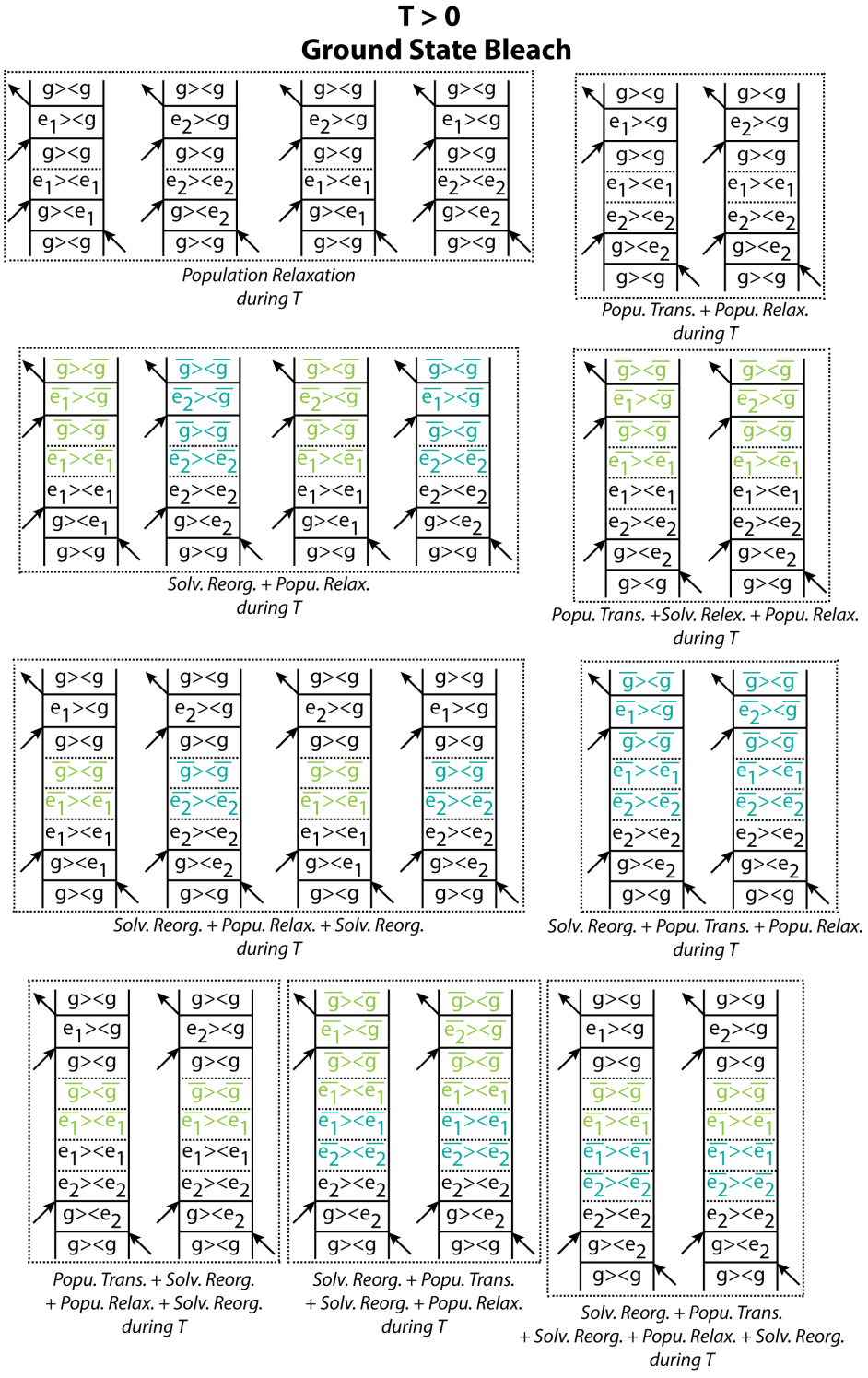

Figure 2.7: Double-sided Feynman diagrams showing ground state bleach pathways of a three-level electronic system in a 2DES experiment at positive waiting time. Letters g, e_1, e_2 represent the electronic ground state, excited state 1, and excited state 2, respectively. Vibrational levels are ignored in this panel.

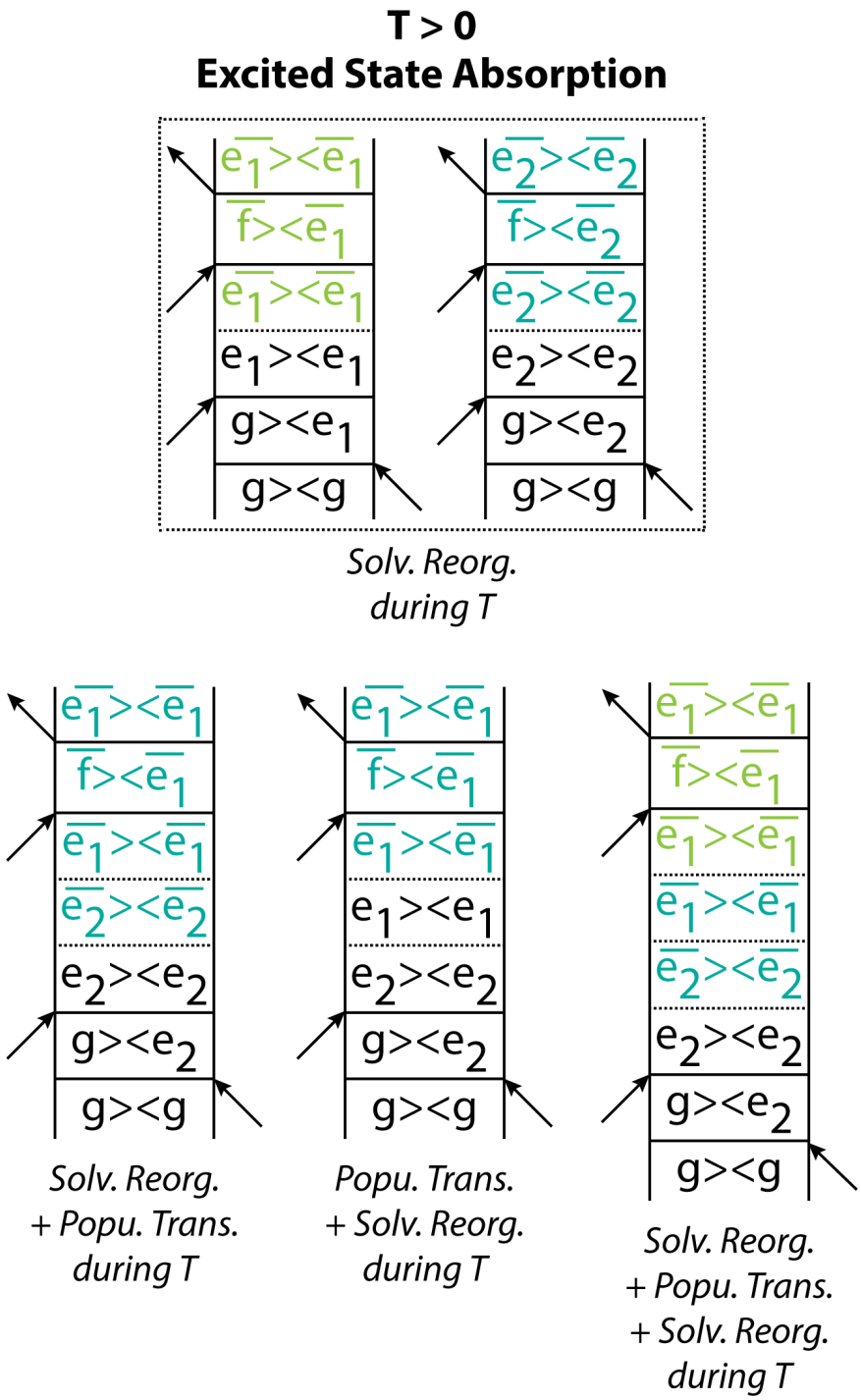

Figure 2.8: Double-sided Feynman diagrams showing excited state absorption pathways of a three-level electronic system in a 2DES experiment at positive waiting time. Letters g, e_1, e_2 represent the electronic ground state, excited state 1, and excited state 2, respectively. Vibrational levels are ignored in this panel.

REFERENCES

[1] Shaul Mukamel. *Principles of nonlinear optical spectroscopy.* Oxford University Press, New York, 1995. ISBN 978-0-19-509278-3.

[2] Minhaeng Cho. Two-dimensional circularly polarized pump-probe spectroscopy. *The Journal of Chemical Physics*, 119(14):7003, 2003.

[3] Darius Abramavicius and Shaul Mukamel. Coherent third-order spectroscopic probes of molecular chirality. *The Journal of Chemical Physics*, 122(13):134305, 2005.

[4] Darius Abramavicius and Shaul Mukamel. Chirality-induced signals in coherent multidimensional spectroscopy of excitons. *The Journal of Chemical Physics*, 124(3):034113, 2006.

[5] Darius Abramavicius, Wei Zhuang, and Shaul Mukamel. Probing molecular chirality via excitonic nonlinear response. *Journal of Physics B: Atomic, Molecular and Optical Physics*, 39(24):5051–5066, 2006.

[6] Jun-Ho Choi and Minhaeng Cho. Nonlinear optical activity measurement spectroscopy of coupled multi-chromophore systems. *Chemical Physics*, 341(1-3):57–70, 2007.

[7] Jun-Ho Choi and Minhaeng Cho. Quadrupole contribution to the third-order optical activity spectroscopy. *The Journal of Chemical Physics*, 127(2):024507, 2007.

[8] Jun-Ho Choi, Sangheon Cheon, Hochan Lee, and Minhaeng Cho. Two-dimensional nonlinear optical activity spectroscopy of coupled multi-chromophore system. *Physical Chemistry Chemical Physics*, 10(26):3839, 2008.

[9] Andrew F. Fidler, Ved P. Singh, Phillip D. Long, Peter D. Dahlberg, and Gregory S. Engel. Dynamic localization of electronic excitation in photosynthetic complexes revealed with chiral two-dimensional spectroscopy. *Nature Communications*, 5(3286):1–6, 2014.

[10] David I. H. Holdaway, Elisabetta Collini, and Alexandra Olaya-Castro. Coherence specific signal detection via chiral pump-probe spectroscopy. *The Journal of Chemical Physics*, 144(19):194112, 2016.

[11] David I. H. Holdaway, Elisabetta Collini, and Alexandra Olaya-Castro. Isolating the chiral contribution in optical two-dimensional chiral spectroscopy using linearly polarized light. *Optics Express*, 25(6):6383, 2017.

[12] F. Bloch and A. Siegert. Magnetic Resonance for Nonrotating Fields. *Physical Review*, 57(6):522–527, 1940.

[13] P. L. Knight and L. Allen. Rotating-Wave Approximation in Coherent Interactions. *Physical Review A*, 7(1):368–370, 1973.

[14] Sterling Backus, Charles G. Durfee, Margaret M. Murnane, and Henry C. Kapteyn. High power ultrafast lasers. *Review of Scientific Instruments*, 69(3):1207–1223, 1998.

[15] Colin N. Danson, Constantin Haefner, Jake Bromage, Thomas Butcher, Jean-Christophe F. Chanteloup, Enam A. Chowdhury, Almantas Galvanauskas, Leonida A. Gizzi, Joachim Hein, David I. Hillier, Nicholas W. Hopps, Yoshiaki Kato, Efim A. Khazanov, Ryosuke Kodama, Georg Korn, Ruxin Li, Yutong Li, Jens Limpert, Jingui Ma, Chang Hee Nam, David Neely, Dimitrios Papadopoulos, Rory R. Penman, Liejia Qian, Jorge J. Rocca, Andrey A. Shaykin, Craig W. Siders, Christopher Spindloe, Sándor Szatmári, Raoul M. G. M. Trines, Jianqiang Zhu, Ping Zhu, and Jonathan D. Zuegel. Petawatt and exawatt class lasers worldwide. *High Power Laser Science and Engineering*, 7:e54, 2019.

[16] The Nobel Prize in Physics 2018. URL `https://www.nobelprize.org/prizes/physics/2018/advanced-information/`.

[17] Donna Strickland and Gerard Mourou. Compression of amplified chirped optical pulses. *Optics Communications*, 56(3):219–221, 1985.

[18] D. Strickland, P. Maine, M. Bouvier, S. Williamson, G. Mourou, and U. Rochester. Picosecond pulse amplification using pulse compression techniques. In *Conference on Lasers and Electro-Optics*, page THL1, San Francisco, California, 1986. OSA. ISBN 978-0-936659-09-1.

[19] Sarah M. Gallagher, Allison W. Albrecht, John D. Hybl, Brett L. Landin, Bhavani Rajaram, and David M. Jonas. Heterodyne detection of the complete electric field of femtosecond four-wave mixing signals. *Journal of the Optical Society of America B*, 15 (8):2338–2345, 1998.

[20] John D. Hybl, Allison W. Albrecht, Sarah M. Gallagher Faeder, and David M. Jonas. Two-dimensional electronic spectroscopy. *Chemical Physics Letters*, 297(3-4):307–313, 1998.

[21] John D. Hybl, Allison Albrecht Ferro, and David M. Jonas. Two-dimensional fourier transform electronic spectroscopy. *The Journal of Chemical Physics*, 115(14):6606–6622, 2001.

[22] Tobias Brixner, Tomáš Mančal, Igor V. Stiopkin, and Graham R. Fleming. Phase-stabilized two-dimensional electronic spectroscopy. *The Journal of Chemical Physics*, 121(9):4221–4236, 2004.

[23] Peter Hamm, Manho Lim, and Robin M. Hochstrasser. Structure of the Amide I Band of Peptides Measured by Femtosecond Nonlinear-Infrared Spectroscopy. *The Journal of Physical Chemistry B*, 102(31):6123–6138, 1998.

[24] Peter Hamm, Manho Lim, William F. DeGrado, and Robin M. Hochstrasser. Stimulated

Photon Echoes from Amide I Vibrations. *The Journal of Physical Chemistry A*, 103(49): 10049–10053, 1999.

[25] P. Hamm, M. Lim, W. F. DeGrado, and R. M. Hochstrasser. The two-dimensional IR nonlinear spectroscopy of a cyclic penta-peptide in relation to its three-dimensional structure. *Proceedings of the National Academy of Sciences*, 96(5):2036–2041, 1999.

[26] M. C. Asplund, M. T. Zanni, and R. M. Hochstrasser. Two-dimensional infrared spectroscopy of peptides by phase-controlled femtosecond vibrational photon echoes. *Proceedings of the National Academy of Sciences*, 97(15):8219–8224, 2000.

CHAPTER 3

INSTRUMENTATIONS ON THIRD–ORDER SPECTROSCOPY

Linear spectroscopy techniques such as absorption and fluorescence are commonly used as first-degree characterization of chemical systems; they can reveal steady-state information such as energy levels, oscillator strengths and solvent reorganization energies within molecular systems. However, such techniques are unable to pick up any dynamic events occurring on the excited state potential energy surfaces. One must therefore resort to higher-order spectroscopic techniques that can retrieve time-domain information on the molecular excited states. From a parity argument, even-order spectroscopic techniques are insensitive to isotropic samples and are thus deemed unsuitable to be applied in this Dissertation. As a result, the simplest experimental techniques capable of probing an isotropic system, such as a solution containing photosynthetic antenna complexes, are third-order spectroscopy. In this Chapter, the concepts and the experimental setups of two specific third-order techniques used in this Dissertation, namely pump-probe spectroscopy and two-dimensional electronic spectroscopy, will be introduced.

3.1 Generation of a Femtosecond Pulse

To study sub-picosecond excited-state dynamics inside light-harvesting complexes with third-order spectroscopy, one will need ultrashort optical pulses to successfully capture all relevant energy relaxation and transfer events. An ultrashort optical pulse has two key aspects: a broad optical spectrum and a femtosecond-range temporal duration. Our experimental setup first utilizes chirped pulse amplification with a Ti-sapphire laser system to generate a relative narrow-band near-IR pulse centered around 800 nm. The pulse is subsequently passed through an argon gas-filled steel tube, with quartz windows on both openings, to generate a supercontinuum spectrum spanning from 400 nm to 900 nm. This supercontinuum

generation involves higher-order nonlinear processes, including self-phase modulation and Kerr lens effect, and is highly sensitive with respect to the peak power and stability of the incoming pulse, the dispersive temporal broadening of the incoming pulse, and the pressure of the argon gas, the alignment within the steel tube, just to name a few.

3.2 Optical Heterodyne Detection

In time-domain optical spectroscopic experiments of biological systems, one often suffers from multiple issues at hand: low signal counts, large background noise, and timing uncertainties between excitation pulses and the nonlinear signal. Another hurdle is the preservation of phase information despite fast modulation of optical frequency light disabling the direct detection of the optical field; photodetectors for the visible light are energy detectors, recording only the intensities of incoming light. Fortunately, these problems can be suppressed by using the technique of optical heterodyne detection [1]. Borrowed from the radio-wave communities, the concept of optical heterodyne detection has been applied to various nonlinear experiments in the optical regime since the 1990s [2, 3, 4, 5, 6, 7]. is that the signal of interest is mixed with a separate wave called the local oscillator (LO), before detecting with an energy (intensity) detector.

A mathematical expression for a spectroscopic signal under the optical heterodyne detection scheme S_{OHD} with an energy detector can be written as followed:

$$S_{OHD} = \left|\boldsymbol{E}_{sig} + \boldsymbol{E}_{LO}\right|^2 \tag{3.1a}$$

$$= \left|\boldsymbol{E}_{sig}\right|^2 + \left|\boldsymbol{E}_{LO}\right|^2 + 2 \cdot \mathrm{Re}\{\boldsymbol{E}_{sig}\boldsymbol{E}_{LO}\} \tag{3.1b}$$

where $\boldsymbol{E}_{sig}$, $\boldsymbol{E}_{LO}$ are complex-valued electric fields of the signal and the LO, respectively.

Optical heterodyne detection increases the signal-to-noise ratio (SNR) of an experiment by amplifying the small nonlinear signal with a much more intense LO, raising the signal above

the large background signals and low-frequency noises. Optical heterodyne detection also preserve the phase information by recording the heterodyned signal as a spectral interferogram between the signal and the LO.

There is still a cautionary detail worth mentioning regarding optical heterodyne detection. Since this technique uses an extra LO to facilitate the signal detection, the intensity and phase stability of the LO are crucial in ensuring a high-SNR experiment. The LO with fluctuating intensity and phase will unavoidably introduce random noise and sometimes shifted signals in the acquired spectral data [8]. Numerous advances have been made to overcome this issue, particularly using balanced heterodyne detection [9] or reference detection [10]. These improvements involve more details descriptions and are therefore beyond the scope of this Dissertation.

3.3 Pump-Probe Spectroscopy

Pump-probe spectroscopy, alternatively called transient absorption spectroscopy, is a third-order spectroscopic technique in which a pump pulse establishes the population on either the excited state or the ground state potential energy surface, followed by a probe pulse after the system is let evolve for a time delay T. Pump-probe spectroscopy has been widely implemented in probing femtosecond population dynamics of molecular systems due to its straightforwardness of experimental setup and data acquisition. The pulse diagram of a typical pump-probe experiment is illustrated in Figure 3.1. Despite the presence of only two laser beams, pump-probe spectroscopy indeed involves three light-matter interactions; the third-order signal travels along the phase-matching direction, which is the direction of the probe pulse: $\vec{\boldsymbol{k}}_{signal} = -\vec{\boldsymbol{k}}_{pump} + \vec{\boldsymbol{k}}_{pump} + \vec{\boldsymbol{k}}_{probe} = \vec{\boldsymbol{k}}_{probe}$. The probe pulse also acts as LO, facilitating the self-heterodyne detection of the pump-probe signal. In a typical pump-probe experiment, a narrow-band pump selectively excites the system into an electronic excited state, and a broadband probe pulse capable of covering the entire absorption spectrum

of interest is used. In the contrary, all pump-probe experiments in this Dissertation were conducted with broadband pump and probe pulses, whose temporal and spectral profiles are identical to those used in the 2DES experiments, so as to match the pump-probe results with the 2DES data.

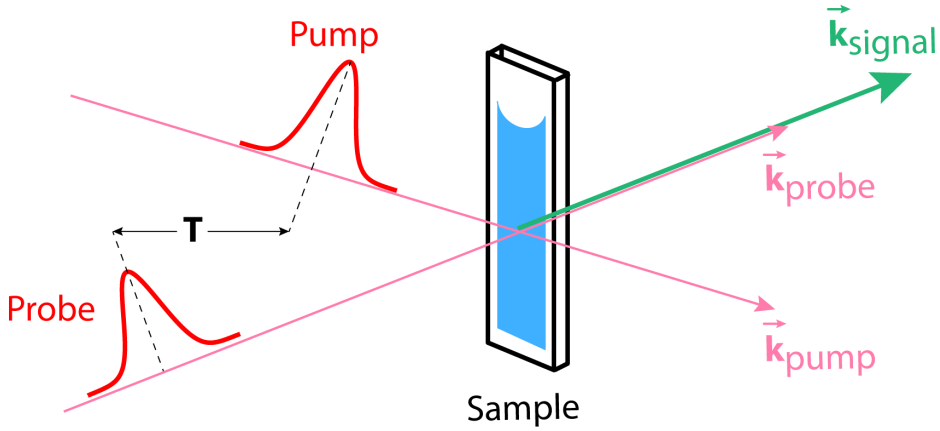

Figure 3.1: Pulse diagram of a pump-probe spectroscopy. The time delay between the pump pulse and the probe pulse is denoted T. The resulting pump-probe signal is generated along the direction of $\vec{k}_{signal}$

The theoretical expression of a pump-probe signal can be derived using the similar formalism described in Chapter 2 and references therein. For a broadband experiment, the resulting pump-probe signal $S_{pp}(\omega_{probe}, T)$ is a function of pump-probe time delay T and the probe frequency ω_{probe} [11]:

$$S_{pp}(\omega_{probe}, T) = \mathrm{Re}\left\{ \int_0^\infty dt_3 e^{i\omega_{probe} t_3} \Big[R_2(t_3, T, 0) + R_3(t_3, T, 0) \Big] \right\} \tag{3.2}$$

The experimental setup of pump-probe spectroscopy used in this Dissertation is shown in Figure 3.2. The compressed supercontinuum pulse is split into the pump and the probe pulses by a beamsplitter, where the pump pulse is sent through a retroreflector on a computer-controlled translational stage, which sets the waiting time delay T between the pump and the probe pulse. A controllable chopper blade is put along the beam path of the pump

pulse, enabling the acquisition of probe-only reference signals. The probe pulse is attenuated properly to around 0.1% of the pump power. Both the pump and the probe pulses are then focused onto the sample cell, where the third-order pump-probe signal is generated along the traveling direction of the probe pulse. The pump pulse after the sample cell is blocked by a spatial filter to minimize the pump scatters in the final pump-probe data, whereas the pump-probe signal from the sample is self-heterodyned with the probe pulse, spectrally resolved with a spectrometer, and recorded by a square-law photodetector.

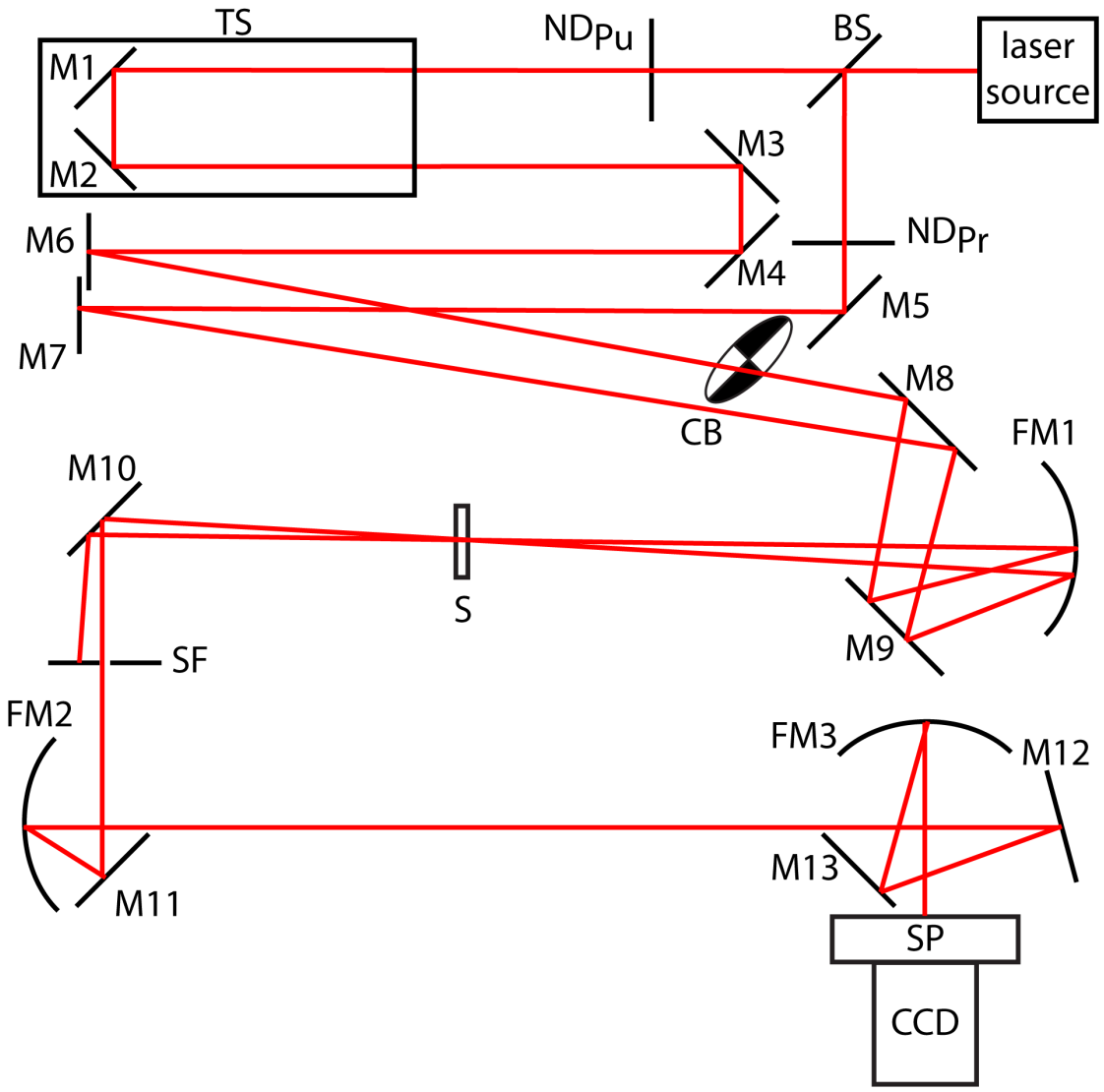

Figure 3.2: The schematic of the pump-probe experimental setup used in this Dissertation. Red lines indicate the beam paths of both pump and probe beams starting from the super-continuum ultrashort pulse and ending at the CCD camera detector. Abbreviations used in the schematic correspond to the following parts: M1-M13: flat mirrors; FM1-FM3: concave spherical mirrors; BS: beamsplitter; ND$_{Pu}$, ND$_{Pr}$: neutral density filters for the pump and the probe beam, respectively; TS: computer-controlled translational stage; CB: chopper blade; S: sample cell; SF: spatial filter for the pump beam; SP: spectrometer; CCD: CCD detector.

3.4 Two-Dimensional Electronic Spectroscopy (2DES)

In this Dissertation, two-dimensional electronic spectroscopy (2DES) is utilized as the core experimental method. The physical origin of 2DES signals is already described in Chapter 2, and this Section will be devoted to actual experimental setup and consideration of 2DES practice.

3.4.1 Experimental Setup

The pulse diagram of a conventional 2DES experiment is sketched out in Figure 3.3. Pulses 1, 2, and 3, each propagating in the direction of its wavevector ($\vec{k}_1$, $\vec{k}_2$, and $\vec{k}_3$, respectively), interact with the sample at different time, generating a third-order signal in the phase-matching direction $\vec{k}_{signal}$. An attenuated fourth pulse, arriving at the sample prior to all three excitation pulses and acting as the LO, is sent in the same direction as that of the third-order signal. Attenuation of the LO is achieved by taking the Fresnel reflection from a quartz crystal. The timing of the LO in 2DES experiments is set up such that the contamination of the third-order signal from unwanted pump probe artifacts of the LO is minimized [12]. The accuracy of relative timings down to fractions of a femtosecond is ensured by computer-controlled mechanical stages during a 2DES experiment, and is assessed by spectral interferometry [1, 7, 13].

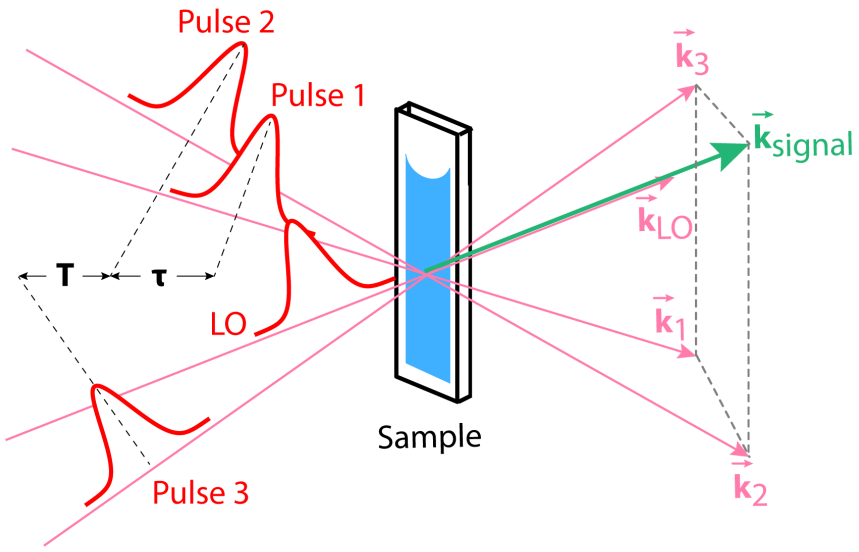

Figure 3.3: Pulse diagram of a 2DES experiment. The time delay between pulses 1 and 2 is denoted τ, and the time delay between pulses 2 and 3, T. The resulting 2DES signal is generated along the phase-matching direction of $\vec{k}_{signal} = -\vec{k}_1 + \vec{k}_2 + \vec{k}_3$. The local oscillator (LO) serves as heterodyne detection of the 2DES signal, and its wavevector $\vec{k}_{LO}$ is set up to be in the same direction as $\vec{k}_{signal}$.

3.4.2 Gradient-Assisted Photon Echo Spectroscopy

In this Dissertation, 2DES experiments were carried out using a variant developed recently within our group, called gradient-assisted photon echo spectroscopy (GRAPES) [14, 15]. GRAPES can be thought of as an optical analogue of magnetic resonance imaging, utilizing the spatial gradient of light-matter interaction. In GRAPES, all pulses are focused by a cylindrical mirror onto a vertical line the sample cell with respect to the lab frame. A geometric tilt of the wavevector is introduced in pulse 1 relative to pulses 2 and 3 by a separate silver mirror for pulse 1, while no pulse-front tilts are introduced deliberately at any point of the setup. This generates a spatially-dependent time delay between pulses 1 and 2 (the coherence time τ). The tilt angle of pulse 1 with respect to pulse 2 is set such that the coherence time gradient across the sample is faster than the Nyquist sampling frequency at the pulse center wavelength. The tilt angle of the LO with respect to pulse 3 can be

set to mirror that between pulses 1 and 2, ensuring the co-propagation of the LO and the third-order signal in the phase-matching direction; in this scenario, relative timings between the LO and the third-order signal, $t_{3,LO}$, remain theoretically the same along the vertical axis onto which all pulses are focused at the sample. In some cases, however, the direction of propagation of the LO can be adjusted to be slightly off the phase-matching direction, creating a quasi-rotating frame scenario [16]. This scenario shifts some non-resonant scatters away from the zero-frequency region in the Fourier domain of $t_{3,LO}$, and can be advantageous in dealing with highly scattering samples such as biological light harvesting complexes and live cells [17].

3.4.3 Phasing: Projection-Slice Theorem

After obtaining the Fourier-transformed 2DES data from processing raw camera images, the final step is to determine the absolute phase of the data at each pixel. Heterodyne detection allows the retrieval of phase information of the complex-valued 2DES signal; however, this phase carries the timing uncertainties between pulses 1 and 2, and between pulses 3 and local oscillator. This phase stability problem is prominent in 2DES due to the shorter optical period of the laser pulses used in the experiment and, if not treated well, will obscure the actual spectral features and interfere with unambiguous peak assignments. Uncertainties in timing can arise from various issues such as mechanical stability, existence of dispersive materials in the beam paths, fluctuations in environmental temperature that cause time-dependent expansion and contraction of optical parts. Excellent engineering control is therefore required for a phase-stable 2DES measurement.

Most of the time, phase errors still need to be corrected via data post-processing even under engineering control. This process is referred to as phasing in the literature [cite reference]. Phasing a 2DES dataset relies on the projection-slice theorem that links data in two Fourier conjugate domains. For a two-dimension data $s(x, y)$, the projection-slice

theorem states that the projection of $s(x, y)$ onto x-axis is equivalent to a slice of data in its Fourier domain $S(k_x, k_y)$ at the Fourier axis k_x. Putting it into a mathematical equation, the projection-slice theorem in two-dimensional space becomes:

$$\int_{-\infty}^{\infty} s(x, y)dy = \mathcal{F}_y\Big[S(k_x, k_y = 0)\Big] \tag{3.3}$$

The correctly-phased 2DES data can be retrieved with aid of a separately acquired pump-probe data through the projection-slice theorem [12]. To make this connection, one can take the projection of a 2DES data at any given waiting time T along the detection frequency axis ω_t. This projection can be shown to be equivalent to a pump-probe spectrum taken at the same waiting time T. In other words,

$$\int_{-\infty}^{\infty} S_{2D}(\omega_\tau, T, \omega_t)d\omega_\tau = \mathcal{F}_{\omega_\tau}\Big[S_{2D}(\tau = 0, T, \omega_t)\Big] \tag{3.4a}$$

$$= S_{pump-probe}(T, \omega_t) \tag{3.4b}$$

A separately acquired pump-probe data can thus be used in phasing the 2DES data. In a typical phasing procedure, a non-linear phase function Φ_{2D} with fitting coefficients is assumed to be the functional form of the true phase. The functional form of Φ_{2D} used throughout this Dissertation has the following expression:

$$\Phi_{2D}(\omega_\tau, \omega_t) = A\left\{e^{i\left[\phi_0+(\omega_\tau-\omega_{ctr})\phi_{\tau,1}+(\omega_\tau-\omega_{ctr})^2\phi_{\tau,2}+(\omega_t-\omega_{ctr})\phi_{t,1}+(\omega_t-\omega_{ctr})^2\phi_{t,2}\right]}\right\} \tag{3.5}$$

where ω_{ctr} is the center frequency of the laser pulse, and coefficients $A, \phi_0, \phi_{\tau,1}, \phi_{\tau,2}, \phi_{t,1}$, and $\phi_{t,2}$ are determined by minimizing the following cost function $J_{phasing}(T)$, representing

the error between the projection of the phased 2DES and the slice of the pump-probe data:

$$J_{phasing}(T) = \sum_{\omega_t} \left[S_{pump-probe}(T, \omega_t) - \sum_{\omega_\tau} S_{2D}(\omega_\tau, T, \omega_t) \Phi_{2D}(\omega_\tau, \omega_t) \right]^2 \tag{3.6}$$

The above expression of the cost function for phasing can be evaluated at a particular waiting time T, but also can be applied to a global phasing procedure, in which 2DES data from all waiting time are used as input data of the optimization procedure. This global phasing strategy yields a higher confidence toward the accuracy of the final phased 2DES data, provided that no outrageous phase instability exists in the duration of data acquisition [18].

In the past decade, 2DES techniques have been developed to overcome or even circumvent the need for phasing, such as phase-cycling scheme for 2DES in the pump-probe geometry [cite references from Zanni, Ogilvie]. Nonetheless, the phase-matching scheme was implemented in the 2DES setup in this Dissertation to suppressed unwanted background scatters effectively.

REFERENCES

[1] L. Lepetit, G. Chériaux, and M. Joffre. Linear techniques of phase measurement by femtosecond spectral interferometry for applications in spectroscopy. *Journal of the Optical Society of America B*, 12(12):2467–2474, 1995.

[2] Wim P. de Boeij, Maxim S. Pshenichnikov, and Douwe A. Wiersma. Phase-locked heterodyne-detected stimulated photon echo. A unique tool to study solute-solvent interactions. *Chemical Physics Letters*, 238(1-3):1–8, 1995.

[3] Yong Joon Chang, Peijun Cong, and John D. Simon. Optical heterodyne detection of impulsive stimulated Raman scattering in liquids. *The Journal of Physical Chemistry*, 99(20):7857–7859, 1995.

[4] J.-P. Likforman, M. Joffre, and V. Thierry-Mieg. Measurement of photon echoes by use of femtosecond Fourier-transform spectral interferometry. *Optics Letters*, 22(14): 1104–1106, 1997.

[5] Shigeki Matsuo and Tahei Tahara. Phase-stabilized optical heterodyne detection of impulsive stimulated Raman scattering. *Chemical Physics Letters*, 264(6):636–642, 1997.

[6] Michel F. Emde, Wim P. de Boeij, Maxim S. Pshenichnikov, and Douwe A. Wiersma. Spectral interferometry as an alternative to time-domain heterodyning. *Optics Letters*, 22(17):1338–1340, 1997.

[7] Sarah M. Gallagher, Allison W. Albrecht, John D. Hybl, Brett L. Landin, Bhavani Rajaram, and David M. Jonas. Heterodyne detection of the complete electric field of femtosecond four-wave mixing signals. *Journal of the Optical Society of America B*, 15 (8):2338–2345, 1998.

[8] Yuan Feng, Ilya Vinogradov, and Nien-Hui Ge. General noise suppression scheme with reference detection in heterodyne nonlinear spectroscopy. *Optics Express*, 25(21):26262, 2017.

[9] G. L. Abbas, V. W. S. Chan, and T. K. Yee. Local-oscillator excess-noise suppression for homodyne and heterodyne detection. *Optics Letters*, 8(8):419, 1983.

[10] A. L. Dobryakov, S. A. Kovalenko, A. Weigel, J. L. Pérez-Lustres, J. Lange, A. Müller, and N. P. Ernsting. Femtosecond pump/supercontinuum-probe spectroscopy: Optimized setup and signal analysis for single-shot spectral referencing. *Review of Scientific Instruments*, 81(11):113106, 2010.

[11] Shaul Mukamel. *Principles of nonlinear optical spectroscopy*. Oxford University Press, New York, 1995. ISBN 978-0-19-509278-3.

[12] Tobias Brixner, Tomáš Mančal, Igor V. Stiopkin, and Graham R. Fleming. Phase-stabilized two-dimensional electronic spectroscopy. *The Journal of Chemical Physics*, 121(9):4221–4236, 2004.

[13] Christophe Dorrer, Nadia Belabas, Jean-Pierre Likforman, and Manuel Joffre. Spectral resolution and sampling issues in Fourier-transform spectral interferometry. *Journal of the Optical Society of America B*, 17(10):1795, 2000.

[14] Elad Harel, Andrew F. Fidler, and Gregory S. Engel. Real-time mapping of electronic structure with single-shot two-dimensional electronic spectroscopy. *Proceedings of the National Academy of Sciences*, 107(38):16444–16447, 2010.

[15] Elad Harel, Andrew F. Fidler, and Gregory S. Engel. Single-Shot Gradient-Assisted Photon Echo Electronic Spectroscopy. *The Journal of Physical Chemistry A*, 115(16): 3787–3796, 2011.

[16] Patrick L. Kramer, Chiara H. Giammanco, Amr Tamimi, David J. Hoffman, Kathleen P. Sokolowsky, and Michael D. Fayer. Quasi-rotating frame: accurate line shape determination with increased efficiency in noncollinear 2D optical spectroscopy. *Journal of the Optical Society of America B*, 33(6):1143, 2016.

[17] Sara Hess Sohail. *Photosynthetic Design Principles for Ultrafast Energy Transfer Processes*. PhD thesis, The University of Chicago, 2020.

[18] Lawson T. Lloyd, Ryan E. Wood, Marco A. Allodi, Siddhartha Sohoni, Jacob S. Higgins, John P. Otto, and Gregory S. Engel. Leveraging scatter in two-dimensional spectroscopy: passive phase drift correction enables a global phasing protocol. *Optics Express*, 28(22): 32869, 2020.

CHAPTER 4

EVIDENCE OF HIGHER-LYING EXCITED STATES IN LIGHT-HARVESTING COMPLEX 1 FROM PURPLE BACTERIUM *RHODOBACTER SPHAEROIDES*

4.1 Functional Purposes of the Core Antenna Complex in Photosynthetic Light Harvesting

Photosynthetic organisms have developed a nearly universal strategy in light harvesting, by which they spatially separate the absorption of solar energy and the use of that energy to generate separated charges [1]. Rapid energy transfer from the site of absorption to the site of charge separation is crucial for efficient solar harvesting. In photosynthetic organisms, the absorption and charge separation sites can be separated by nearly one hundred nanometers, yet transfer occurs on the order of tens of picoseconds and with near unity quantum efficiency in low light [2, 3]. To accomplish this feat, they employ specialized pigment-proteins known as antenna complexes to absorb solar energy. Antenna complexes are packed with strongly coupled chromophores. This strong coupling leads to delocalized states with strong transition dipoles and a complex electronic structure that is essential for energy transfer. In this manuscript, we employ two-dimensional electronic spectroscopy (2DES) to observe the electronic structure and dynamics of light harvesting complex 1 (LH1) from *Rhodobacter sphaeroides* (*R. sphaeroides*) embedded in its native photosynthetic membrane.

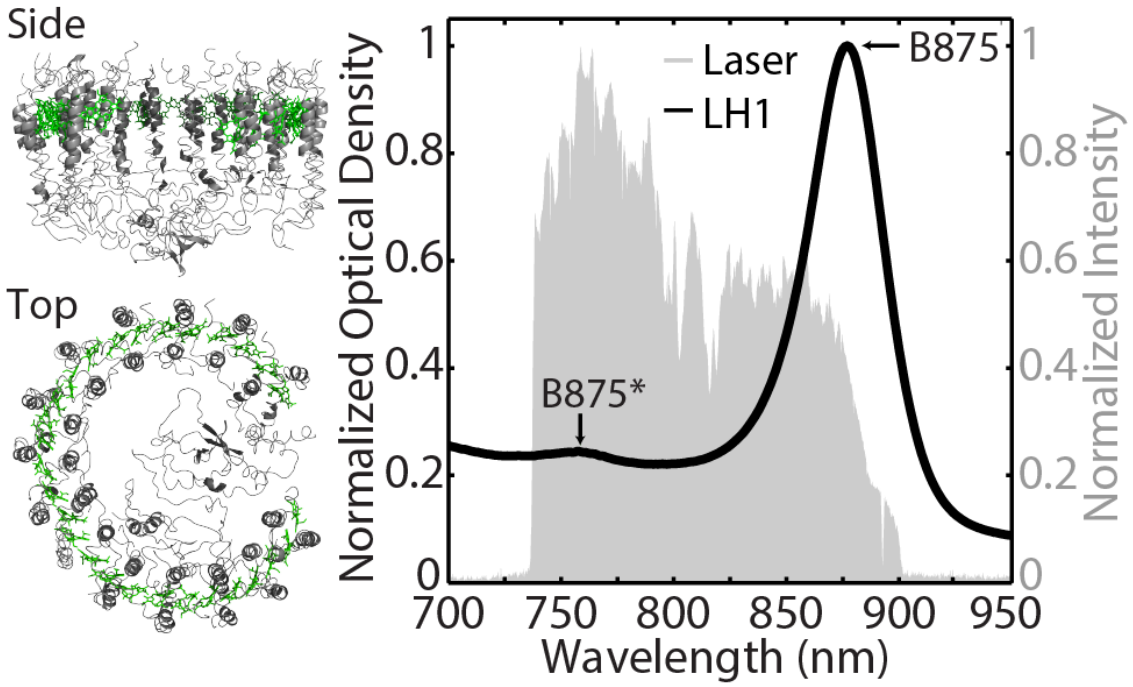

Figure 4.1: Left: 8 Å-resolution structure of a monomer of LH1 complex in *R. sphaeroides* reconstructed from the RC-LH1 dimeric crystal structure found in PDB ID: 4V9G [4]. The protein backbone (shown in gray) holds 28 BChl a (shown in green) tightly in space. Right: Absorption spectrum of LH1-only membranes is shown in black. The two visible features near 765 nm and 875 nm correspond to B875* and B875, respectively. The normalized laser excitation spectrum used for the 2DES experiments is shown in shaded gray. Reprinted (adapted) with permission from J. Phys. Chem. A 2016, 120, 24, 4124–4130. Copyright (2016) American Chemical Society.

R. sphaeroides is a purple bacterium known for its near unity quantum efficiency[3] and highly symmetric antenna complexes. *R. sphaeroides* has two types of antenna complexes: a peripheral complex, light harvesting complex 2 (LH2) and a core complex, light harvesting complex 1, that surrounds the reaction center (RC). An 8-Å resolution structure of an RC-LH1-PufX dimer was obtained from a combination of X-ray crystallography and cryo-electron microscopy [5, 6]. This structure reveals an S-shaped array of chromophores that intertwines around two RCs. The bacteriochlorophyll (BChl) within the LH1 complex absorb maximally at 875 nm, and are often designated as B875; they share many characteristics with the B850 ring of BChl in LH2. The RC-LH1-PufX complex exists in *R. sphaeroides* as both a monomer and a dimer, but the dimer is the dominant structure in vivo. Each monomer in the dimer contains 28 BChl a molecules bound in alternating α- and β-polypeptides (Figure 4.1) [5]. The electronic coupling between BChl a in LH1 is well approximated by dipolar coupling except in the case of nearest neighbors where the Mg-Mg distance is on the order of 10 Å [5]. The coupling strength of nearest neighbors is estimated to be a few hundred wavenumbers [7, 8]. This strong coupling leads to the delocalization of excitations across BChl a and the existence of higher-lying excited states. A special pair of BChl a embedded in each RC absorbs at 870 nm and accepts excitations from LH1 [9, 10]. The LH1 complex used in this manuscript was obtained from a mutant of *R. sphaeroides* that lacked LH2, PufX, and the RC. In the absence of PufX and the RC, the predominant structure of the membrane-embedded LH1 is likely a closed, but empty ring [11, 12]. High-resolution AFM topographs of membrane-embedded LH1-only complexes showed that they are 9.9 $\pm$ 0.7 nm in diameter, smaller than the 11.2 $\pm$ 0.6 nm measured for monomeric RC-LH1 core complexes with 16 $\alpha_1\beta_1\text{BChl}_2$ LH1 subunits [13]. Accordingly, the LH1-only complex was assigned to be a ring of 15 $\alpha_1\beta_1\text{BChl}_2$ subunits [12].

A closed ring, unlike an open ring, has an additional circular symmetry that leads to a series of pairwise degenerate electronic states. The manifold of states in a closed ring of LH1

adopts a labeling scheme to reflect these degeneracies. The lowest and highest energy states are the only non-degenerate states and, in the case of an LH1, are composed of 15 $\alpha_1\beta_1$BChl$_2$ subunits; these states are labeled k = 0 and k = 15. All other states are pairwise degenerate and are labeled k = $\pm 1 \ldots \pm 14$. In a perfectly symmetric monomeric ring, the transition dipole for most excited states becomes vanishingly small, so the only states with finite transition dipole strength are k = ± 1 and k = ± 14, with k = ± 1 being the dominant transition dipole. However, in nature, this perfect circular symmetry is never realized due to disorder. In the dimeric RC-LH1-PufX complex, the "S" shape breaks the circular symmetry and therefore the degeneracies. Observation of the higher-lying excited states and their lifetime in the photosynthetic membrane can inform on the nearest-neighbor coupling strengths, site energies and coupling to the bath, thus providing great insight into the electronic structure of LH1 in vivo.

Previous ultrafast spectroscopy studies have been performed on detergent isolated preparations of LH1. Fluorescence anisotropy data suggest the energy transfer between BChl a molecules occurs on 110 fs and 400 fs timescales [14]. Three-photon echo peak shift, pump-probe, and transient grating experiments resolved four dominant vibrational modes and two decay lifetimes [4, 15]. Pump-dump-probe and pump-probe experiments have characterized the exciton equilibration between the low-energy states as taking place on a 100 fs timescale [16, 17]. To date, none of these ultrafast studies have analyzed simultaneously the higher-lying excited states and their coupling to the strongly allowed k = ± 1 states. In this paper, we present a 2DES waiting time series of monomeric LH1-only complexes embedded in the photosynthetic membrane from *R. sphaeroides*. We find evidence of higher-lying excited states and resolve waiting time dynamics. We use this information to refine the site energies and nearest-neighbor couplings within the B875 band of chromophores and find good agreement between calculated and experimentally observed energy transfer rates.

4.2 Investigating Electronic Structures of LH1 Complex from *Rhodobacter sphaeroides*

4.2.1 Preparation of LH1-Only Membranes

A mutant containing only LH1 complexes, designated L3 (Δpuc1BA ΔpufLMX), was created by genomic deletion of puc1BA and pufLMX genes using the methodology described in Mothersole et al [18]. The cells were cultured semi-aerobically in the dark at 30 °C. LH1-only membranes were obtained by disrupting the cells using a French press at 14,000 PSI. A slow spin was performed (12,000 RPM JA 30.STI for 20 minutes) to remove large cellular debris. The supernatant was diluted to an optical density of 0.3 at 875 nm in a 200-μm path length quartz cell (Starna Cells Inc.), which was used for analysis.

4.2.2 Two-Dimensional Electronic Spectroscopy

Two-dimensional electronic spectroscopy correlates excitation energies (λ_τ) and stimulated emission/ground state bleach/excited state absorption energies (λ_t) as a function of an ultrafast time delay. Spectrally and temporally resolved signals acquired from this spectroscopic technique are beneficial for determining the electronic structure of systems with dense absorption spectra, such as those of antenna complexes [19]. The theory and experimental design are described elsewhere [20, 21, 22, 23, 24]; here, the working principle and information content of a 2DES spectrum is summarized. 2DES is a third-order optical technique involving three ultrafast laser pulses interacting with a sample. The third-order polarization, created by the three light-matter interactions, generates a photon echo signal in a phase-matched direction. The signal is heterodyned with a fourth pulse known as the local oscillator and is spectrally resolved in a spectrometer, and the heterodyned signal is collected on a camera. A 2DES spectrum is a frequency-frequency correlation map, acquiring extra spectral resolution by Fourier transforming across the coherence time (τ, time delay between

pulses 1 and 2) axis. 2DES spectra are collected as a function of the waiting time delay (T, time delay between pulses 2 and 3). 2DES has advantages of both spectral and temporal resolution, correlating energy transfer between excited states with different energies while obtaining lifetimes of excited states.

2DES spectra in this study were acquired using the GRadient-Assisted Photon Echo Spectroscopy (GRAPES) technique [25, 26, 27, 28]. A Ti:Sapphire regenerative amplifier (Coherent Inc.) was used to generate a 30-fs FWHM pulse centered at 800 nm with a 5-kHz repetition rate and a power of 2 W. The pulse was focused through argon gas (4 psi) and then again through air to obtain a 140 nm broadband pulse. An SLM-based pulse shaper (Biophotonics Solutions) compressed the pulse to 15 fs and shaped the spectrum producing the excitation spectrum shown in Figure 1, which was sufficiently broad to excite both the low energy and high energy states simultaneously. The power for pulses 1-3 was attenuated to 33 μJ/cm^2 (1.37 $\times 10^{14}$ photons/cm^2). Pulse 4 was attenuated an additional 2 orders of magnitude. The coherence times were sampled from 0 to 200 fs in 0.9 fs steps using the gradient-assisted method. The echo signal was spectrally resolved and heterodyne detected on a high-speed CMOS camera (Phantom Miro M310) triggered at $1/100^{th}$ the repetition rate of the regenerative amplifier. The spectral phase was determined using separately acquired pump-probe spectra, see Figure 4.2 [29]. To extract timescales of waiting time dynamics, each waiting time trace in the phased data was fit to a model function with a bi-exponential decay plus an offset to recover both early-time dynamics and vibrational relaxations. The residuals from curve fitting at each point in the 2DES map were Fourier transformed to obtain information on vibrational frequencies associated with waiting time dynamics.

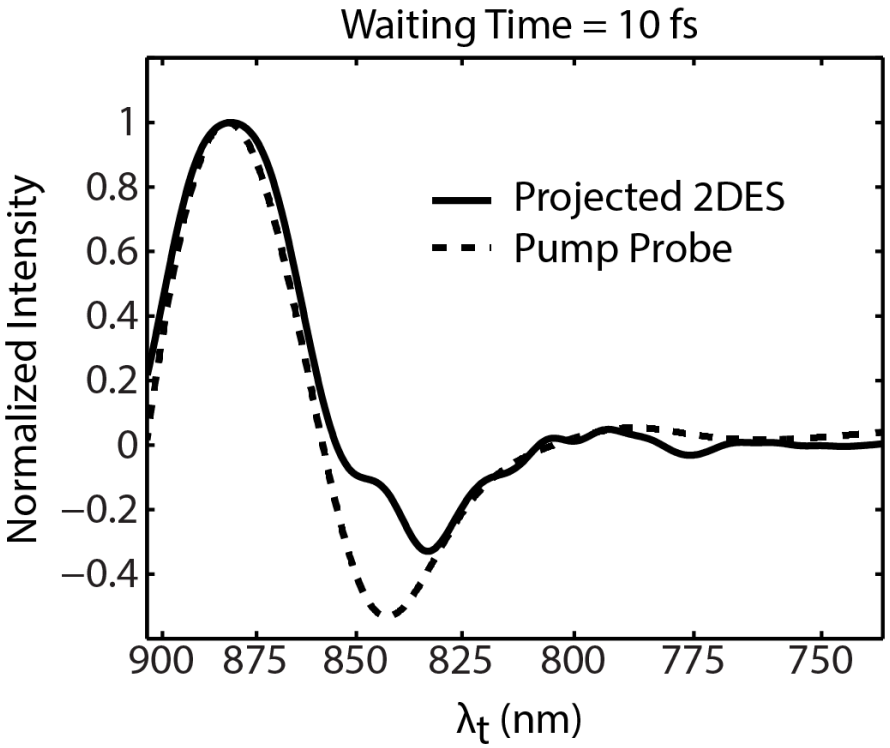

Figure 4.2: Projection of the real rephasing 2DES signal across the λ_τ axis compared to the pump probe spectra at a waiting time of 10 fs. Reprinted (adapted) with permission from J. Phys. Chem. A 2016, 120, 24, 4124–4130. Copyright (2016) American Chemical Society.

4.2.3 Effective Hamiltonian of LH1

Model Hamiltonians were constructed to reproduce the experimental results and revise physical parameters such as nearest neighbor coupling, site energies, and spectral density. Our sample contains a mixture of structures containing 14, 15, and 16 $\alpha_1\beta_1$BChl$_2$ subunits in both open and closed ring configurations. However, prior AFM studies indicate that the most prevalent structure of LH1 in the absence of PufX and the RC is a closed ring of 15 $\alpha_1\beta_1$BChl$_2$ subunits [11, 12]. Therefore, we constructed three separate effective Hamiltonians to account for the ill-defined structure of monomeric LH1 in the absence of PufX and the RC. The first Hamiltonian, $H^{(15)}_{closed}$, describes a closed ring of 15 subunits. Because no crystal structures exist with this geometry, a model was constructed with 30 equally spaced BChl a in the XY plane arranged in a ring with a radius of 5 nm. The Q_y dipole orientations were alternated between pointing at 203° and 21° in the XY plane. The orientation of the dipoles was taken from the average over the first 20 chromophores in the dimeric crystal structure starting from one end of the S-shaped band [5]. The site energies were made to alternate between 12 150 cm^{-1} (823 nm) and 12 450 cm-$^{-1}$ (803 nm) and the nearest neighbor coupling was approximated as 435 cm^{-1}. These values were comparable to previous studies and reproduced features in the absorption spectra [7]. The coupling for all other chromophores was calculated assuming purely dipolar interaction. A dipole strength of 8.3 Debye was adopted for all BChl a following the calculations in Sener et al [7]. The second Hamiltonian, $H^{(14)}_{open}$, was calculated in the same manner except the distances and orientations of chromophores were taken directly from one half of the LH1 in the dimeric RC-LH1-PufX crystal structure shown in Figure 1 which consists of a nearly-closed ring of 14 $\alpha_1\beta_1$BChl$_2$ LH1 subunits.[9] The third Hamiltonian, $H^{(16)}_{closed}$, was constructed in the same manner using the monomeric RC-LH1 structure from a similar organism, *Thermochromatium tepidum* [30]. This 3.0 Å-resolution structure has a closed ring of 16 $\alpha_1\beta_1$BChl$_2$ subunits that is slightly elliptical. The ellipticity breaks some of the degeneracies that arise from a closed ring.

The eigenstate energies and dipole strengths for $H_{open}^{(14)}$, $H_{closed}^{(15)}$, and $H_{closed}^{(16)}$ are listed in Table 4.1, 4.2, and 4.3, respectively, and stick spectra for all the Hamiltonians can be seen in Figure 4.3 along with the linear absorption spectrum of LH1-only membranes after the removal of Mie scatter. A comparison of the stick spectra to a 77 Kelvin absorption spectrum is made in Figures 4.4 and 4.5. All three Hamiltonians give rise to a strongly allowed band of excitonic states at low energy around 875 nm. This feature is the well-known B875 absorption band of LH1. In the cases of $H_{closed}^{(15)}$, and $H_{closed}^{(16)}$, the transition dipole strength is carried almost exclusively by the $k_{\pm 1}$ states that have transition energies of 11 443 (874)/11 401 (877) cm^{-1} (nm). $H_{open}^{(14)}$ provides a similar electronic structure, with the majority of the oscillator strength being carried by the three lowest energy states, E_{1-3}, with transition energies of between 11 396 (877) and 11 445 (874) cm^{-1} (nm). All three Hamiltonians also produce weak higher-lying excited states with transition energies at approximately 13 195 cm^{-1} (760 nm). These higher-lying excited states, in analogy to the higher-lying B850* states in LH2, will be referred to as B875*. The absorption spectrum is mirrored in the excitation fluorescence spectrum (Figure 4.6), indicating electronic coupling between the B875* states and the B875 states. Without further analysis, it would be difficult to separate this absorption feature from free BChl a in the sample, which absorbs at 770 nm and overlaps B875*, or from vibrationally excited B875 states. Both free BChl a as well as vibrationally excited states would likely relax to the B875 states before fluorescing. Therefore, the assignment of this feature is not conclusive based on linear absorption or fluorescence spectra alone and we therefore employ to 2DES and Redfield theory for an unambiguous assignment.

Table 4.1: Eigenvalues and their transition dipole strengths for the effective Hamiltonian $H^{(14)}_{open}$. $H^{(14)}_{open}$ was produced by taking an LH1 monomer from the RC-LH1-PufX dimer crystal structure, which has 14 $\alpha_1\beta_1$ $BChl_2$ subunits. The states primarily responsible for B875 and B875$*$ are shown in bold. The dipole strengths of individual BChl a were assumed to be 8.3 Debye. Reprinted (adapted) with permission from J. Phys. Chem. A 2016, 120, 24, 4124–4130. Copyright (2016) American Chemical Society.

Eigenstate, k	Eigenvalues E_k in cm^{-1} (nm)	Transition Dipole Strength (Debye)
1	**11396 (877)**	**17.5**
2	**11416 (876)**	**30.5**
3	**11445 (874)**	**20.3**
4	11485 (870)	3.6
5	11534 (867)	10.0
6	11590 (863)	1.3
7	11654 (868)	5.5
8	11725 (853)	1.7
9	11801 (847)	5.2
10	11878 (842)	0.5
11	11959 (836)	3.1
12	12038 (831)	0.4
13	12109 (826)	1.9
14	12157 (823)	1.5
15	12472 (802)	1.7
16	12519 (799)	0.7
17	12588 (794)	2.0
18	12663 (790)	1.9
19	12739 (785)	2.7
20	12813 (780)	2.2
21	12882 (776)	1.0
22	12946 (772)	0.7
23	13003 (769)	1.7
24	13053 (766)	2.0
25	13094 (764)	1.6
26	13127 (762)	2.2
27	13151 (760)	2.1
28	**13164 (760)**	**6.5**

Table 4.2: Eigenvalues and their transition dipole strengths for the effective Hamiltonian $H^{(15)}_{closed}$. $H^{(15)}_{closed}$ was produced from an ideal closed ring structure with 15 $\alpha_1\beta_1$ $BChl_2$ subunits. The states primarily responsible for B875 and B875$*$ are shown in bold. The dipole strengths of individual BChl a were assumed to be 8.3 Debye. Reprinted (adapted) with permission from J. Phys. Chem. A 2016, 120, 24, 4124–4130. Copyright (2016) American Chemical Society.

Eigenstate, k	Eigenvalues E_k in cm^{-1} (nm)	Transition Dipole Strength (Debye)
0	**11377 (879)**	**0**
±1	**11443 (874)**	**32.0**
±2	11495 (870)	0
±3	11580 (864)	0
±4	11696 (855)	0
±5	11835 (845)	0
±6	11987 (834)	0
±7	12120 (825)	0
±8	12470 (802)	0
±9	12604 (793)	0
±10	12758 (784)	0
±11	12901 (775)	0
±12	13022 (768)	0
±13	13112 (763)	0
±14	**13168 (759)**	**2.9**
15	13188 (758)	0

Table 4.3: Eigenvalues and their transition dipole strengths for the effective Hamiltonian $H^{(16)}_{closed}$. $H^{(16)}_{closed}$ was produced from the monomeric crystal structure of LH1-RC from *Thermochromatium tepidum*, which has 16 $\alpha_1\beta_1$ $BChl_2$ subunits. The states primarily responsible for B875 and B875$*$ are shown in bold. The dipole strengths of individual BChl a were assumed to be 8.3 Debye. Reprinted (adapted) with permission from J. Phys. Chem. A 2016, 120, 24, 4124–4130. Copyright (2016) American Chemical Society.

Eigenstate, k	Eigenvalues E_k in cm^{-1} (nm)	Transition Dipole Strength (Debye)
0	**11377 (879)**	**2.1**
±1	**11401 (877)**	**32.8**
±2	11464 (872)	0.8
±3	11558 (865)	1.3
±4	11675 (856)	0.6
±5	11811 (847)	0.5
±6	11957 (836)	0.5
±7	12097 (827)	0.4
−8	12172 (822)	0.3
+8	12473 (802)	0.5
±9	12546 (797)	0.3
±10	12677 (789)	0.4
±11	12811 (780)	0.4
±12	12930 (772)	0.3
±13	13029 (768)	0.4
±14	13102 (763)	0.5
±15	13148 (761)	3.1
16	**13163 (760)**	**8.7**

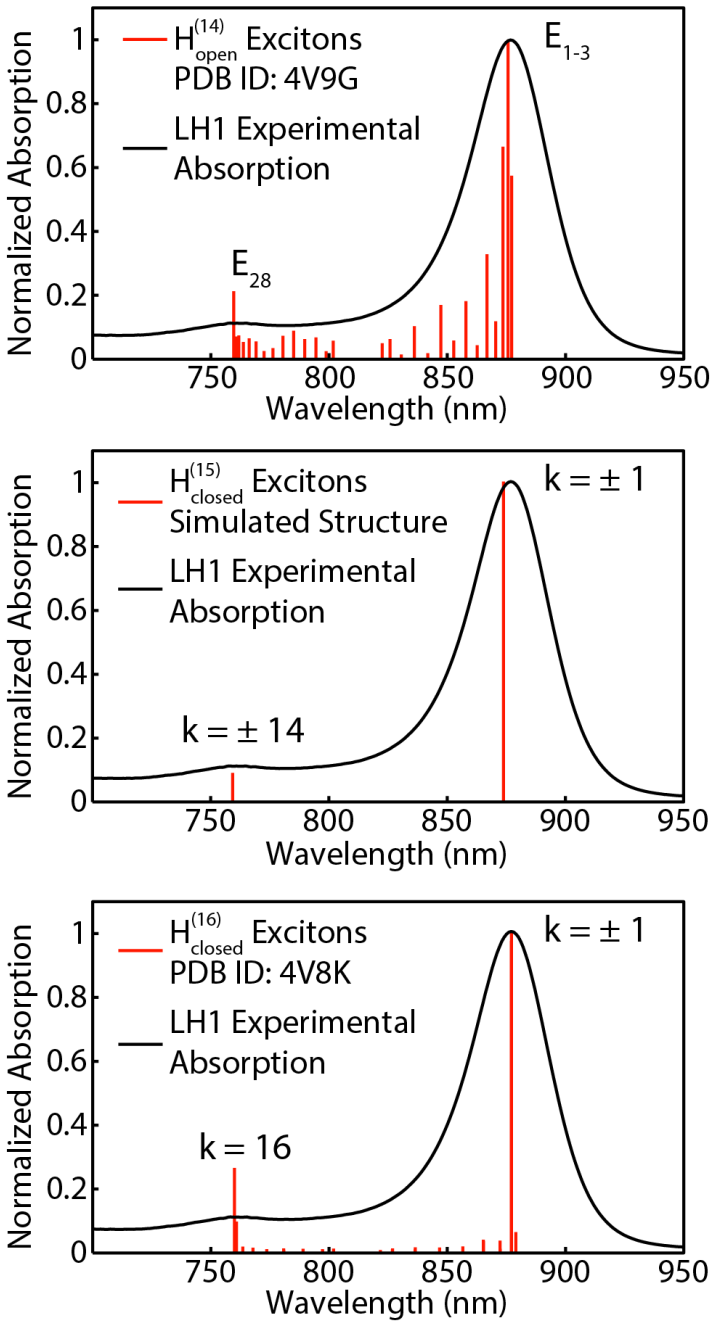

Figure 4.3: Stick spectra from $H^{(14)}_{open}$, $H^{(15)}_{closed}$, and $H^{(16)}_{closed}$ are overlaid with the absorption spectra of LH1-only membranes after the removal of Mie scatter. The stick spectra are in good agreement with the absorption spectra, recapitulating the strong B875 states and the weak B875* states. Reprinted (adapted) with permission from J. Phys. Chem. A 2016, 120, 24, 4124–4130. Copyright (2016) American Chemical Society.

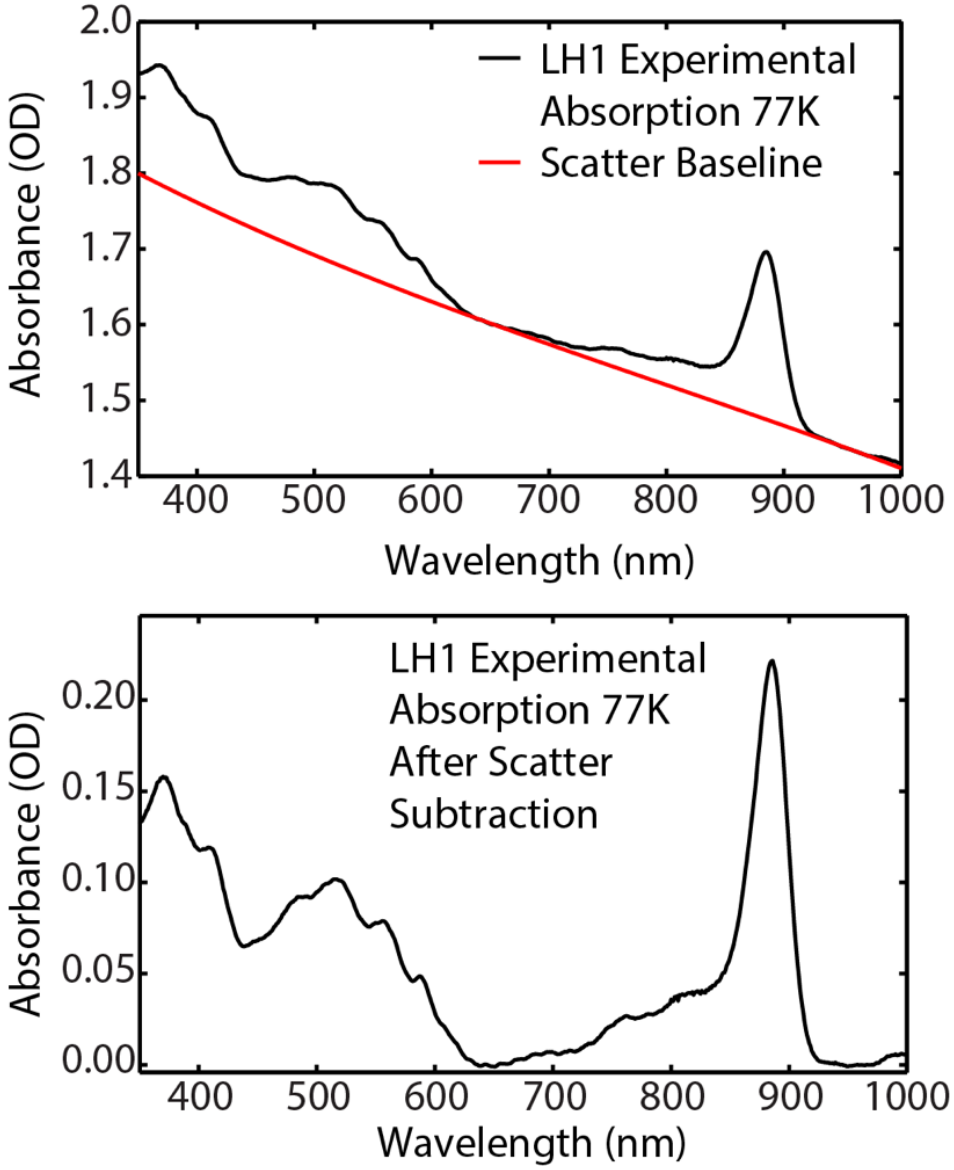

Figure 4.4: (top) Absorption spectrum of LH1-only membranes at 77 K is shown in black. The red trace shows a cubic polynomial fit used to subtract the contributions for scattering. (bottom) Absorption spectrum of LH1-only membranes at 77 K after the scatter subtraction operation. Reprinted (adapted) with permission from J. Phys. Chem. A 2016, 120, 24, 4124–4130. Copyright (2016) American Chemical Society.

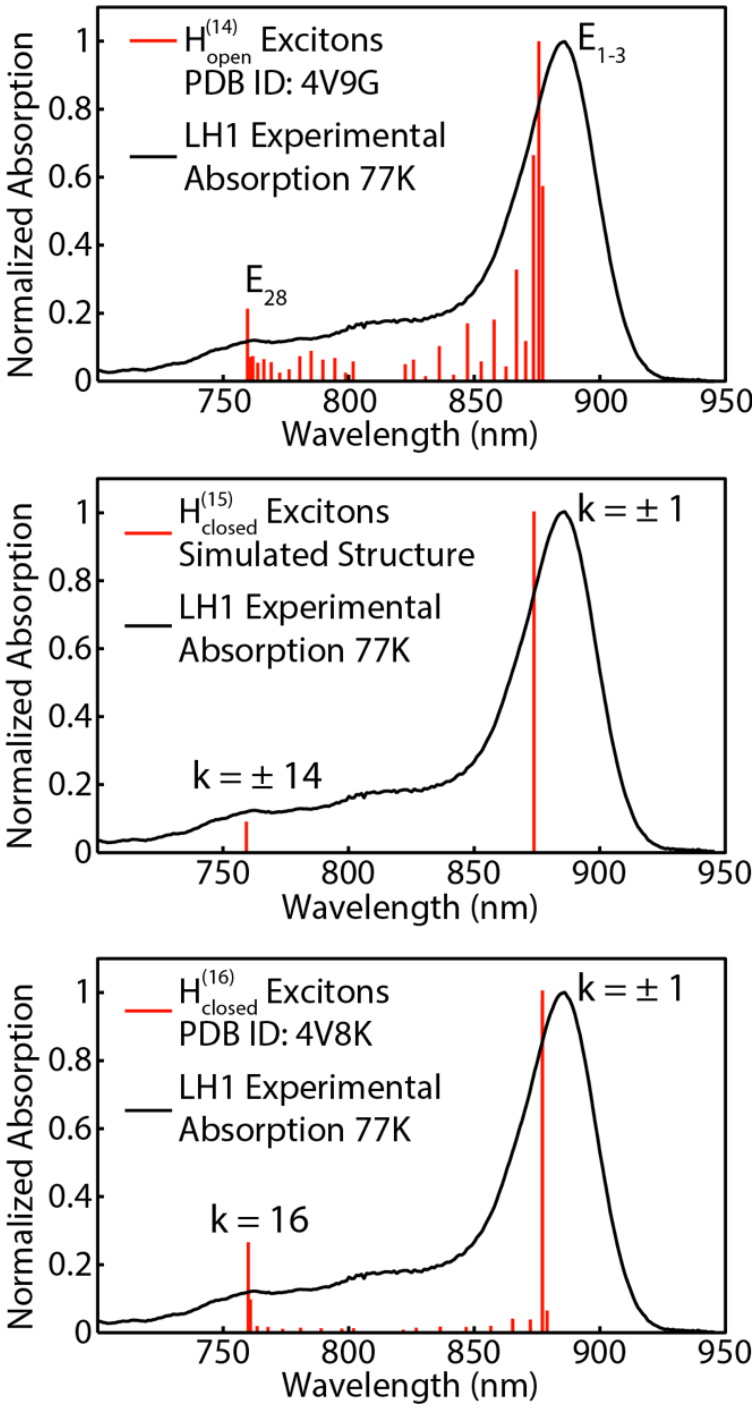

Figure 4.5: Stick spectra from $H^{(14)}_{open}$, $H^{(15)}_{closed}$, and $H^{(16)}_{closed}$ are overlaid with the absorption spectra of LH1-only membranes at 77 K after the removal of scatter. The stick spectra are in better agreement with the absorption spectra taken at room temperature, but significant structure at higher energies than the strong B875 feature can be seen in the 77 K structure. Reprinted (adapted) with permission from J. Phys. Chem. A 2016, 120, 24, 4124–4130. Copyright (2016) American Chemical Society.

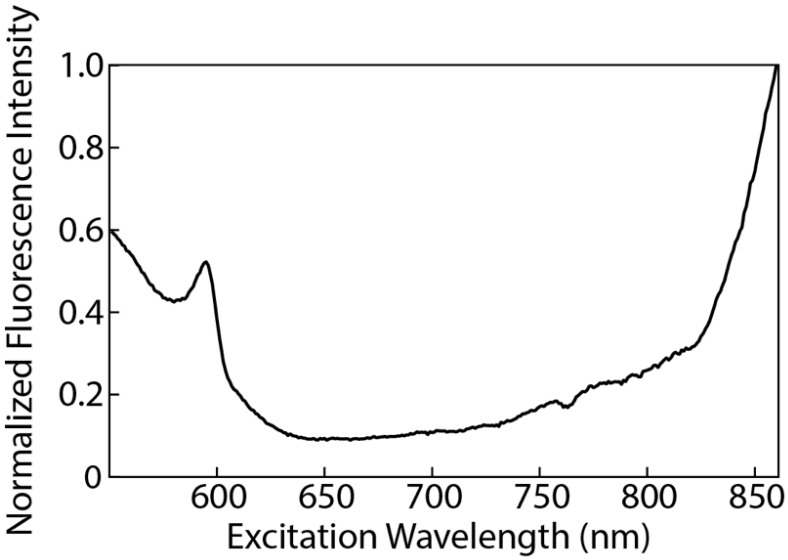

Figure 4.6: Fluorescence excitation spectrum of LH1-only membranes. Fluorescence intensity was monitored at 890 nm. The clear fluorescence signal from excitation at 750-800 nm shows energy transfer from B875* to B875. Reprinted (adapted) with permission from J. Phys. Chem. A 2016, 120, 24, 4124–4130. Copyright (2016) American Chemical Society.

4.2.4 Fitting of Waiting Time Dynamics

Waiting time traces were fit to a model bi-exponential function of the form:

$$A(T) = a_1 e^{-\frac{T}{\tau_1}} + a_2 e^{-\frac{T}{\tau_2}} + a_3 \tag{4.1}$$

where $A(T)$ is the phased real amplitude of the 2DES signal at waiting time T, and $a_1, a_2, a_3, \tau_1, \tau_2$ are fitted parameters obtained by using a trust-region-reflective algorithm contained within MATLAB's lsqcurvefit function. The separation of τ_1 and τ_2 by more than an order of magnitude allowed for the growth and decay lifetimes of the waiting time features to be assigned simply as τ_1 and τ_2. The power spectrum of the residuals to this fit were then used for the vibrational mode analysis in Figures 4.13 and 4.15.

4.3 2DES Revealing Hidden Higher-Lying Excitonic States and Ultrafast Dynamics within LH1 Complex

The real portion of the phased rephasing 2DES spectra of LH1-only membranes at early waiting times, shown in Figure 4.7, reveal more features than the linear absorption spectrum. The strongest feature in the phased 2DES spectra appears as the near-diagonal peak at λ_τ = 870 nm, λ_t = 880 nm. The offset from the diagonal is likely due to overlapping excited state absorption and stimulated emission. The absolute-valued spectra for the same waiting times are shown in Figure 4.8 and show a peak centered at λ_τ = 875 nm, λ_t = 875 nm. A regression of the phased data to a bi-exponential function yields two time constants of τ_1 = 55 $\pm$ 2 fs and τ_2 = 1130 $\pm$ 26 fs (Figure 4.9). Similar dynamics have been reported previously in LH1 and in the B850 ring from LH2 and have been attributed to vibrational relaxation, protein reorganization and spectral diffusion [4].

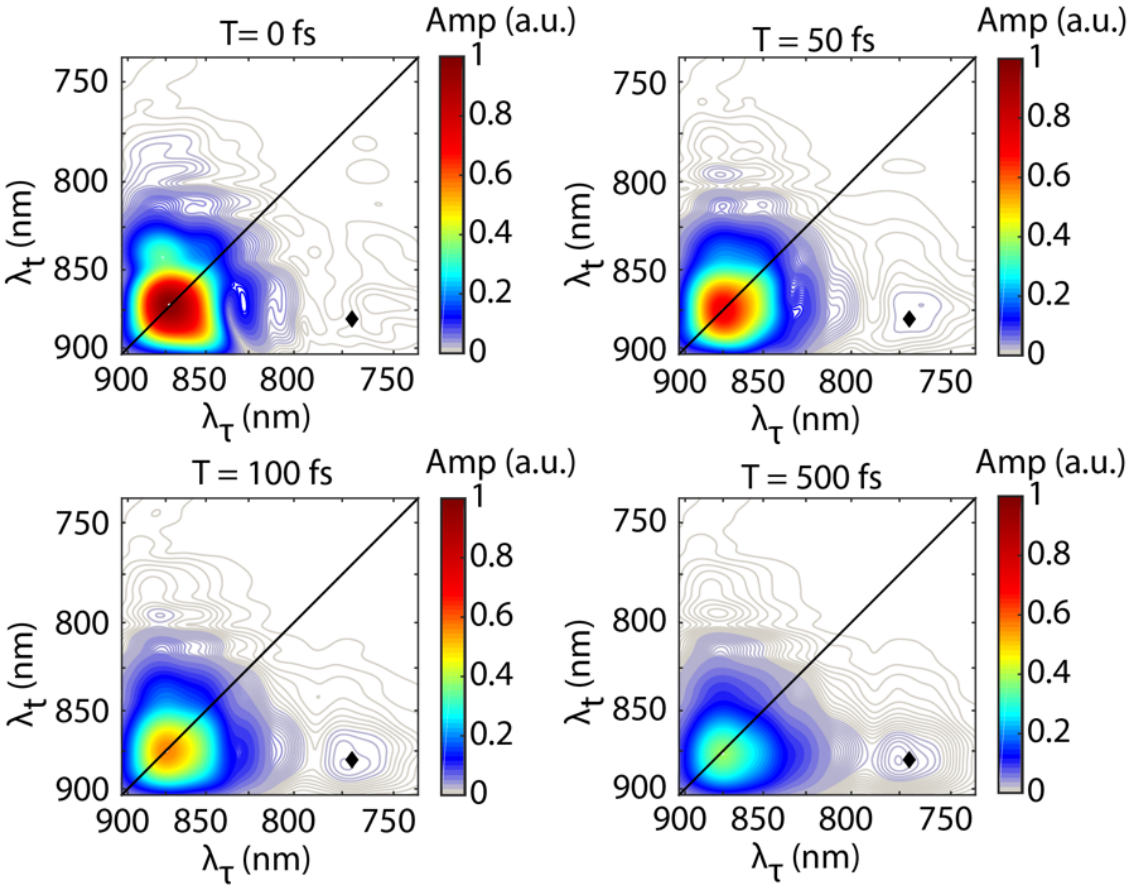

Figure 4.7: Absolute-valued rephasing 2DES spectra of LH1-only membranes. The strong signal on the diagonal corresponds to the B875 states. The cross peak centered on the black diamond is indicative of B875* to B875 energy transfer. Reprinted (adapted) with permission from J. Phys. Chem. A 2016, 120, 24, 4124–4130. Copyright (2016) American Chemical Society.

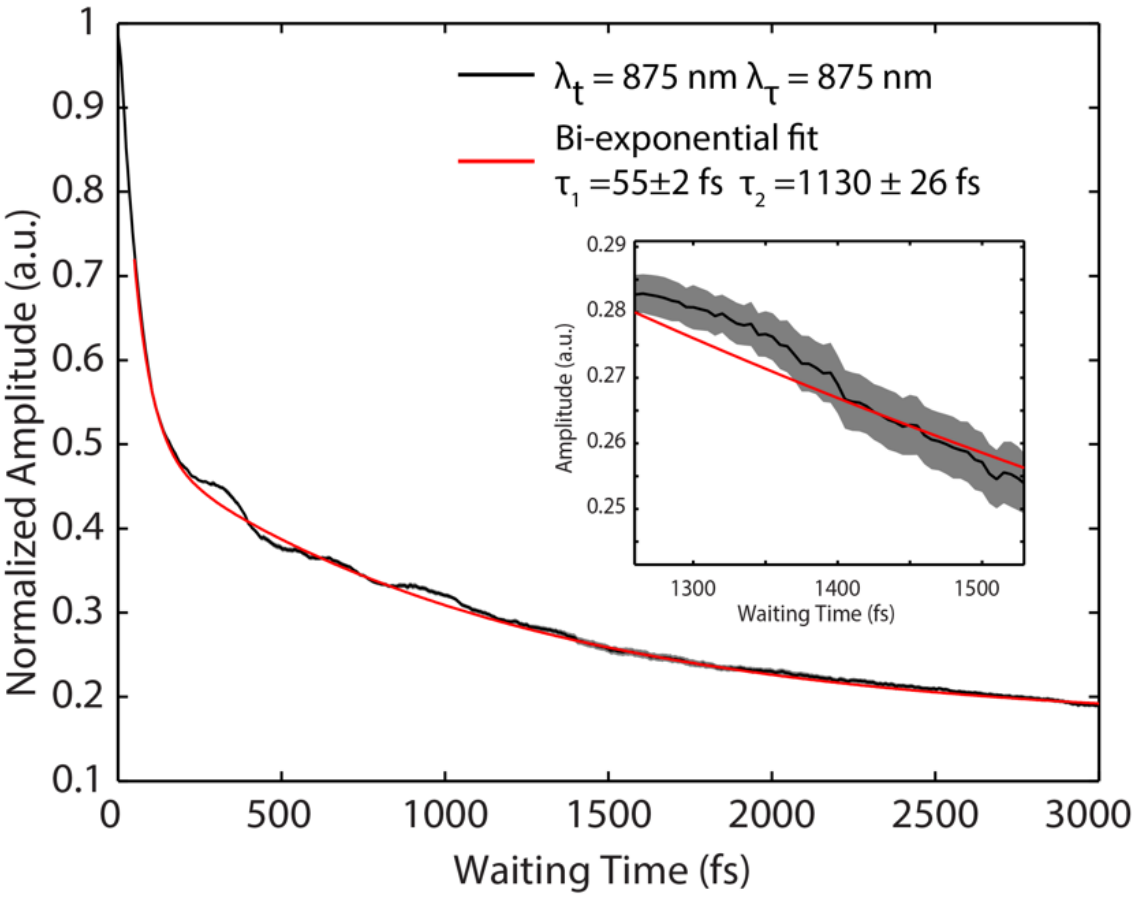

Figure 4.8: The averaged waiting time trace from the main diagonal of LH1-only membranes at $\lambda_\tau = \lambda_t = 875$ nm in absolute-valued signal intensity (shown in black). The black trace is the average of 10 replicates completed in rapid succession over the course of 2 hours. Dynamics are recovered by fitting to a bi-exponential and are similar to previous results. The width of the gray shading is the standard error (1σ) representing our uncertainty in the mean. Reprinted (adapted) with permission from J. Phys. Chem. A 2016, 120, 24, 4124–4130. Copyright (2016) American Chemical Society.

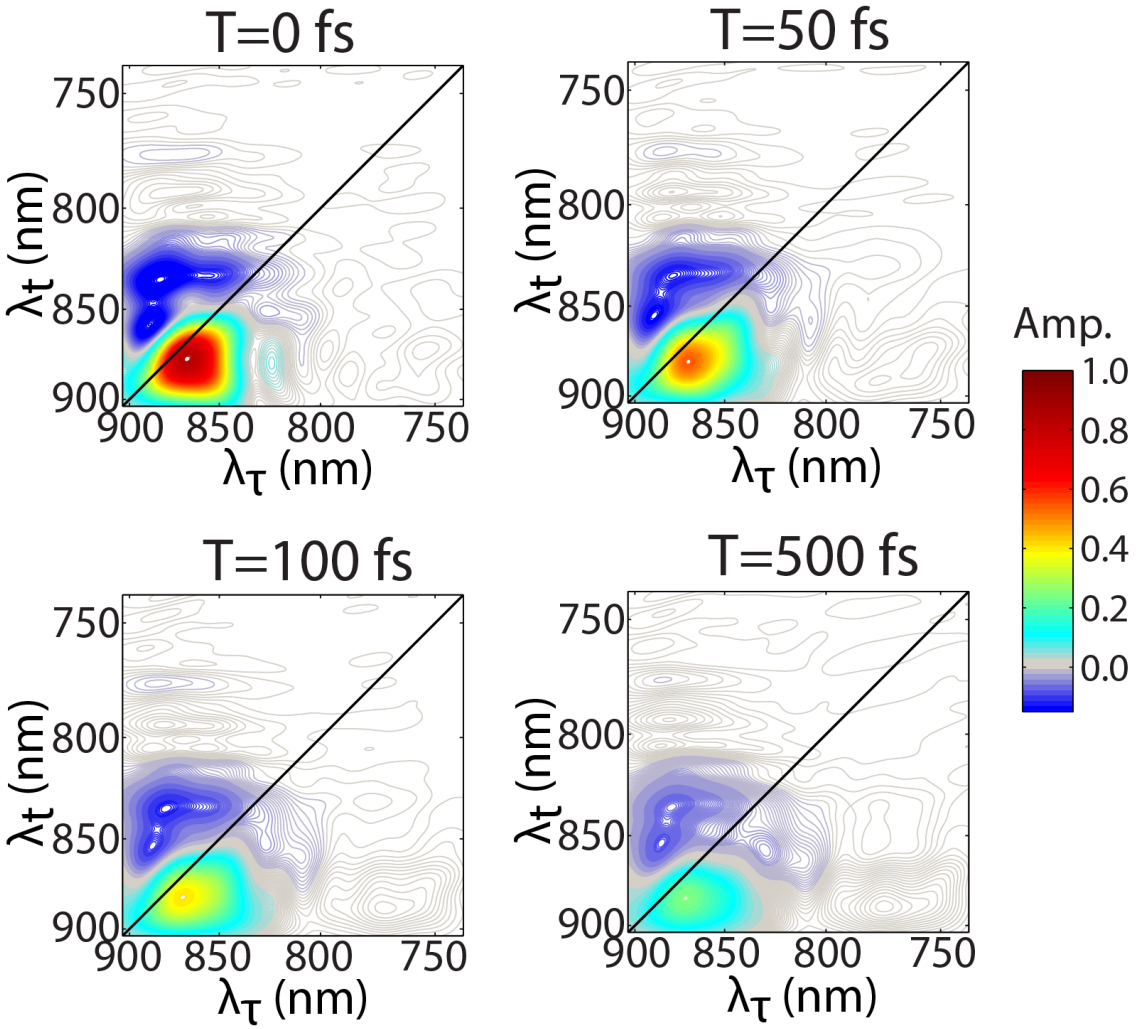

Figure 4.9: Representative phased rephasing 2DES spectra of LH1-only membranes at waiting times of $T = 0$ fs, $T = 50$ fs, $T = 100$ fs and $T = 500$ fs. All spectra are normalized to the signal maximum across all waiting times. Reprinted (adapted) with permission from J. Phys. Chem. A 2016, 120, 24, 4124–4130. Copyright (2016) American Chemical Society.

A diagonal peak near $\lambda_\tau = \lambda_t = 770$ nm corresponding to B875* is not visible due to its low intensity relative to the B875 diagonal peak. In third-order experiments, the signal intensity scales with the fourth power of transition dipoles, whereas a signal in first-order experiments, such as that in a linear absorption spectrum, scales with the square of transition dipoles. Based on the linear absorption spectrum, we expect the relative strength of the B875* diagonal peak to be $(0.05)^2$, or 0.25%, of the intensity at the B875 diagonal peak, which is too weak to be observed. The signal intensity of a cross peak in a 2DES spectrum is the result of two interactions with each of the corresponding diagonal features. Based on the linear absorption spectrum, the intensity at $\lambda_\tau = 770$ nm and $\lambda_t = 880$ nm would be 5% of the B875 diagonal feature if energy transferred from B875* to B875. The cross peak observed between $\lambda_\tau = 770$ nm and $\lambda_t = 880$ nm has a maximum of 0.023 in the normalized spectra (Figure 4.10 and Figure 4.11).

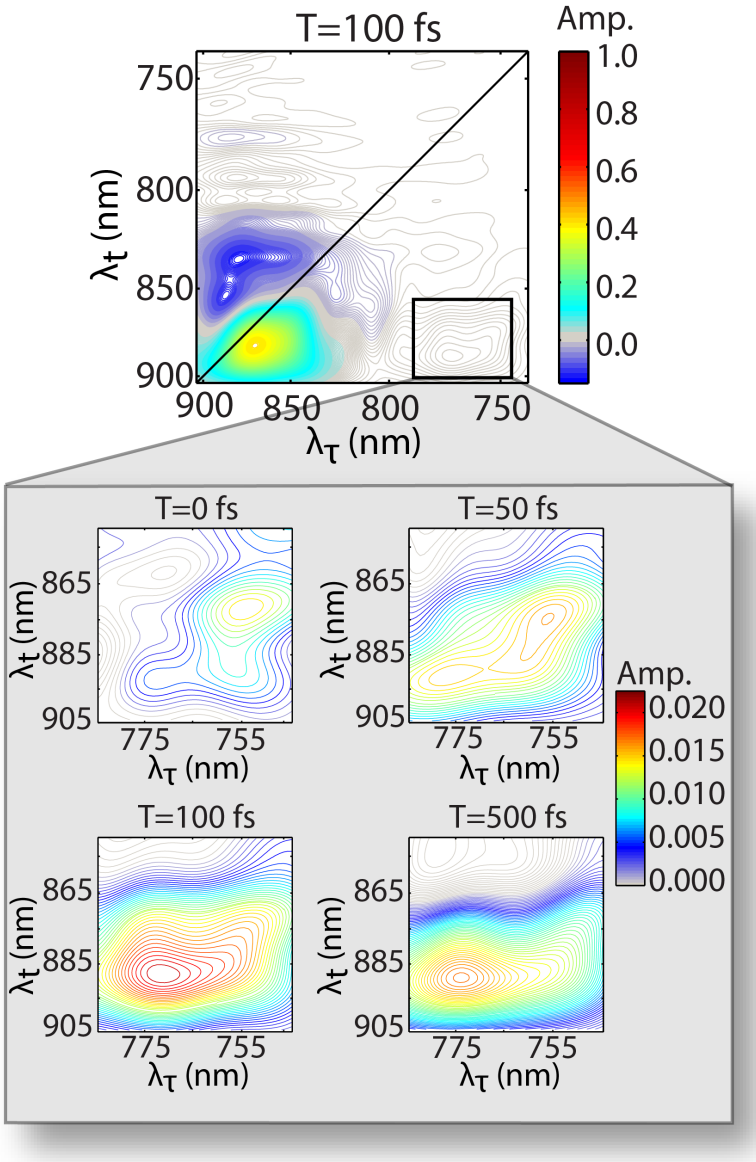

Figure 4.10: Phased rephasing 2DES spectra of the cross peak between B875* and B875 (region enclosed by the red rectangle in the 2DES spectrum above) in LH1-only membranes showing stimulated emission around $\lambda_\tau = 770$ nm and $\lambda_t = 880$ nm at waiting times of $T = 0$ fs, $T = 50$ fs, $T = 100$ fs and $T = 500$ fs, respectively. All spectra are normalized to the signal maximum across all waiting times. Reprinted (adapted) with permission from J. Phys. Chem. A 2016, 120, 24, 4124–4130. Copyright (2016) American Chemical Society.

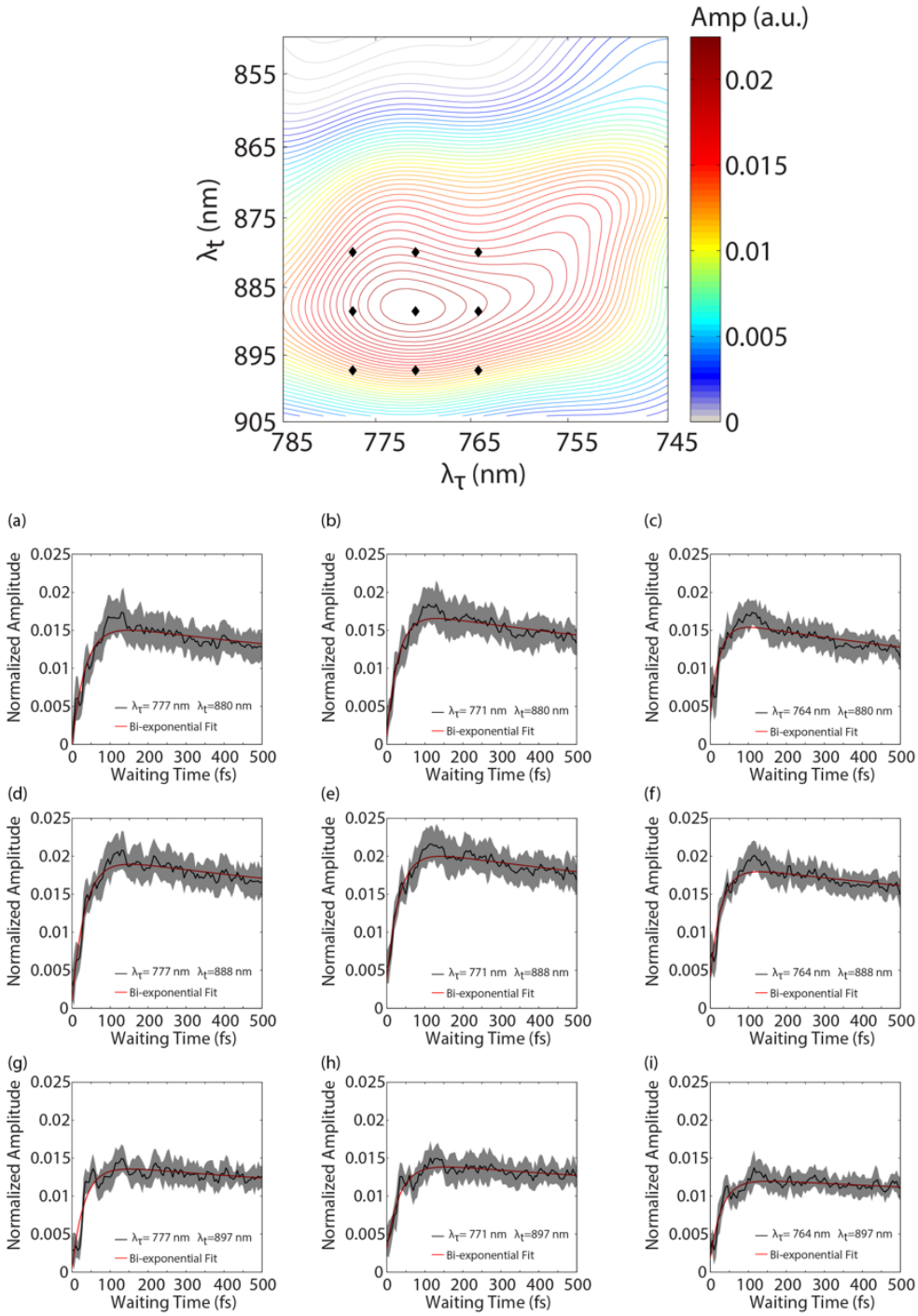

Figure 4.11: Waiting time traces from throughout the B875*-B875 cross peak shown in the zoomed-in phased 2DES spectrum (real part) at the top. Plots are reproduced in the same order as the black diamonds on the 2DES spectrum. The width of the gray shading is the standard error (1σ) representing our uncertainty in the mean. Red traces show a regression of the data to a model bi-exponential function. Reprinted (adapted) with permission from J. Phys. Chem. A 2016, 120, 24, 4124–4130. Copyright (2016) American Chemical Society.

The position and amplitude of the cross peak indicate that the states observed in the linear absorption spectrum around 770 nm are transferring excitations to B875. Nevertheless, the existence of coupling and transfer could be due to vibrationally excited B875 states or free BChl a that are loosely coupled to the B875 states, rather than transfer from higher-lying B875* states. These possibilities can be excluded by analysis of the waiting time dynamics. The cross peak between B875* and B875 grows in rapidly at early waiting times. A representative waiting time trace at $\lambda_\tau = 770$ nm and $\lambda_t = 880$ nm is shown in Figure 4.12. We observe that the waiting time trace reaches its maximum within 100 fs. When a bi-exponential function is fit to the data, the trace gives a fast rise of 31 $\pm$ 3 fs and a slow decay of 1280 $\pm$ 100 fs. Analysis of the complete cross peak region can be seen in Figure 4.12b. The rapid timescale for the growth of this cross peak excludes any possibility of energy transfer from free BChl a to the B875 states, because any energy transfer between free BChl a and LH1 would occur on a picosecond timescale due to weak coupling.

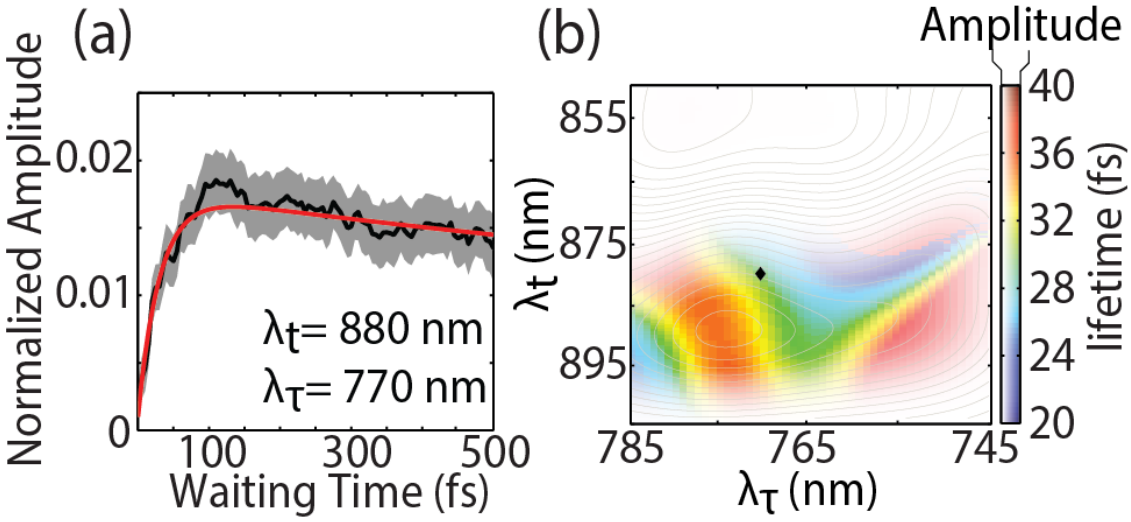

Figure 4.12: Representative waiting time trace and lifetime map at the B875*-B875 cross peak of LH1-only membranes show rapid energy transfer within 40 fs. (a) The black curve is the average waiting time trace of LH1-only membranes at $\lambda_\tau = 770$ nm and $\lambda_t = 880$ nm (indicated by black diamond in the spectrum to the right) of 10 scans acquired in rapid succession over the course of 2 hours. The width of the gray shading is the standard error (1σ) representing our uncertainty in the mean. The red trace is a regression of the data to a model bi-exponential function. (b) Lifetime map for the rapid component of the bi-exponential around $\lambda_\tau = 770$ nm and $\lambda_t = 880$ nm. The saturation level of the map is weighted by both the signal strengths at $T = 500$ fs for each pixel. The contour curves represent the phased 2DES spectrum at waiting time of 100 fs. Reprinted (adapted) with permission from J. Phys. Chem. A 2016, 120, 24, 4124–4130. Copyright (2016) American Chemical Society.

Fourier analysis in the waiting time domain is further utilized to elucidate the origin of the cross peaks. In 2DES, vibrational states give clear oscillations in the waiting time domain that result from vibrational coherences [31, 32, 33]. A vibrational coherence is a superposition between two vibrational states within the same electronic excited state. In phased 2DES spectra, we observe excited state absorption features in the upper off-diagonal region of the map (Figure 4.9). From the waiting time trace, we see clear oscillations from this region that persist for more than 2 ps (Figure 4.13a), which is on the appropriate timescale for vibrational coherences at room temperature. Fourier transforming the residual from exponential fitting yields four distinct vibrational modes at 96, 288, 558, and 728 cm^{-1} (Figure 4.13b). These vibrational modes are also observed in the Raman spectrum of LH1 and free BChl a [15, 34, 35, 36]. When the cross peak between B875* and B875 is analyzed, no clear oscillations indicative of vibrational coherences can be resolved (Figure 4.13c and d). Thus, we attribute the cross peak on the lower off-diagonal region to be energy transfer from higher-lying B875* states to lower-lying B875 states.

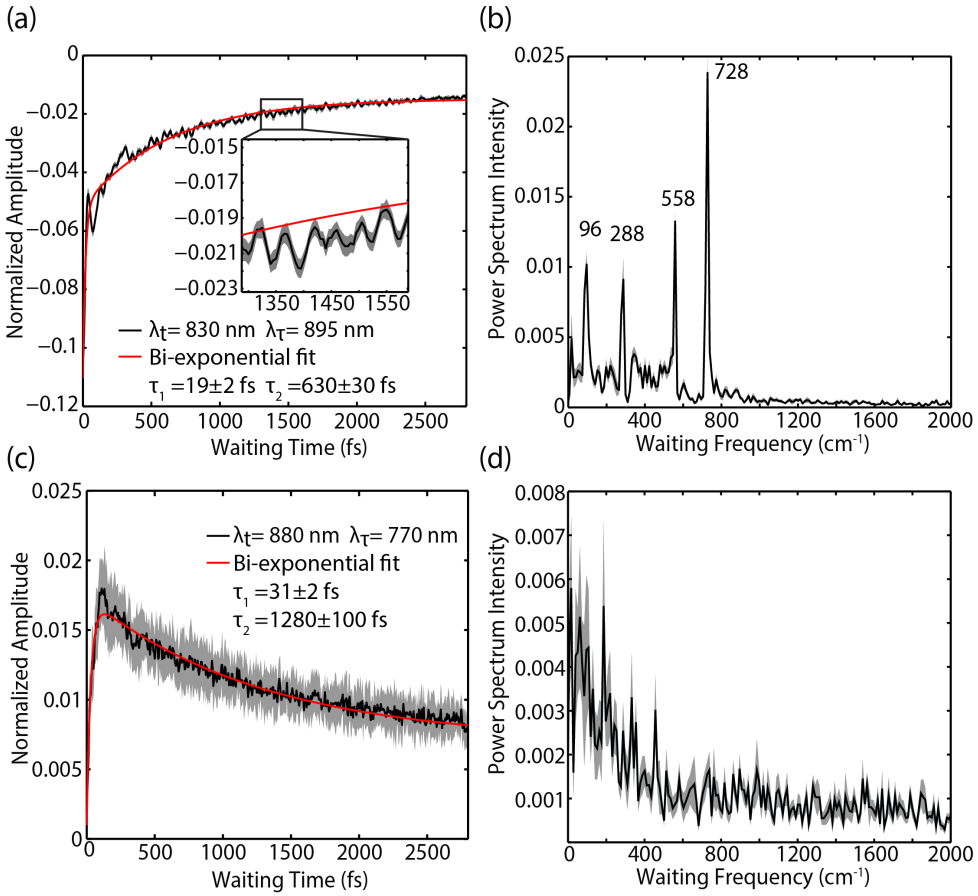

Figure 4.13: Waiting time traces from two locations in the 2DES spectra and their conjugate waiting time frequency traces show no clear vibrations at the cross peak between B875* and B875. All black traces in the figures represent an average of 10 scans. The width of the gray shading is the standard error (1σ) representing our uncertainty in the mean. (a) Waiting time trace of LH1-only membranes at $\lambda_\tau = 895$ nm and $\lambda_t = 830$ nm showing oscillations due to vibrational coherences at this location. (b) Average power spectrum of the residuals from fitting the same waiting time trace in (a) for each of the 10 scans (resolution is 11 cm^{-1}). These peaks are known vibrational modes of BChl a [34]. (c) Waiting time trace from the B875*-B875 lower cross peak at $\lambda_\tau = 770$ nm and $\lambda_t = 880$ nm. (d) Average power spectrum of the residuals from fitting the same waiting time trace in (c) for each of the 10 scans. Reprinted (adapted) with permission from J. Phys. Chem. A 2016, 120, 24, 4124–4130. Copyright (2016) American Chemical Society.

Redfield theory was further used to validate the rapid energy transfer rates observed from B875* to B875. The sub-100 fs transfer rate is similar to results obtained in LH2 from B850* to B850 [37]. The rapid energy transfer is largely due to the co-localization of the excitations on the same ring of chromophores. Figure 4.14 shows the transition dipole weight for the B875 and B875* states for the three Hamiltonians. In addition to spatially overlapping states, the rapid rate of energy transfer is also due to high-energy bath modes, some of which can be seen in the vibrational coherences in Figures 4.12 and 4.15. In order to properly weight these high-energy bath modes, we used a log-normal spectral density given by

$$J(\omega) = \frac{S}{\sigma\omega\sqrt{2\pi}} \exp\left\{ -\frac{\left[\ln\left(\frac{\omega}{\omega_c}\right)\right]}{2\sigma^2} \right\} \tag{4.2}$$

with a high cutoff frequency, ω_c, of 1000 cm^{-1} [38]. The Huang-Rhys factor, S, was 0.5 and the standard deviation, σ, was 0.8 cm^{-1}. Using this spectral density, the population transfer time was calculated following the procedure outlined by M. Reppert [39]. The lifetime for $H^{(15)}_{closed}$, calculated as the transfer time from $\text{k}_{\pm 14}$ to k_0 and $\text{k}_{\pm 1}$, was found to be 51 fs. Similarly, the lifetime for $H^{(16)}_{closed}$, calculated as the transfer time from k_{16} to k_0 and $\text{k}_{\pm 1}$, was found to be 54 fs. Lastly, the lifetime for $H^{(14)}_{open}$, calculated as the transfer time from E_{28} to E_{1-3}, was found to be 42 fs. All values are within a factor of two of the observed energy transfer lifetimes of 30-40 fs.

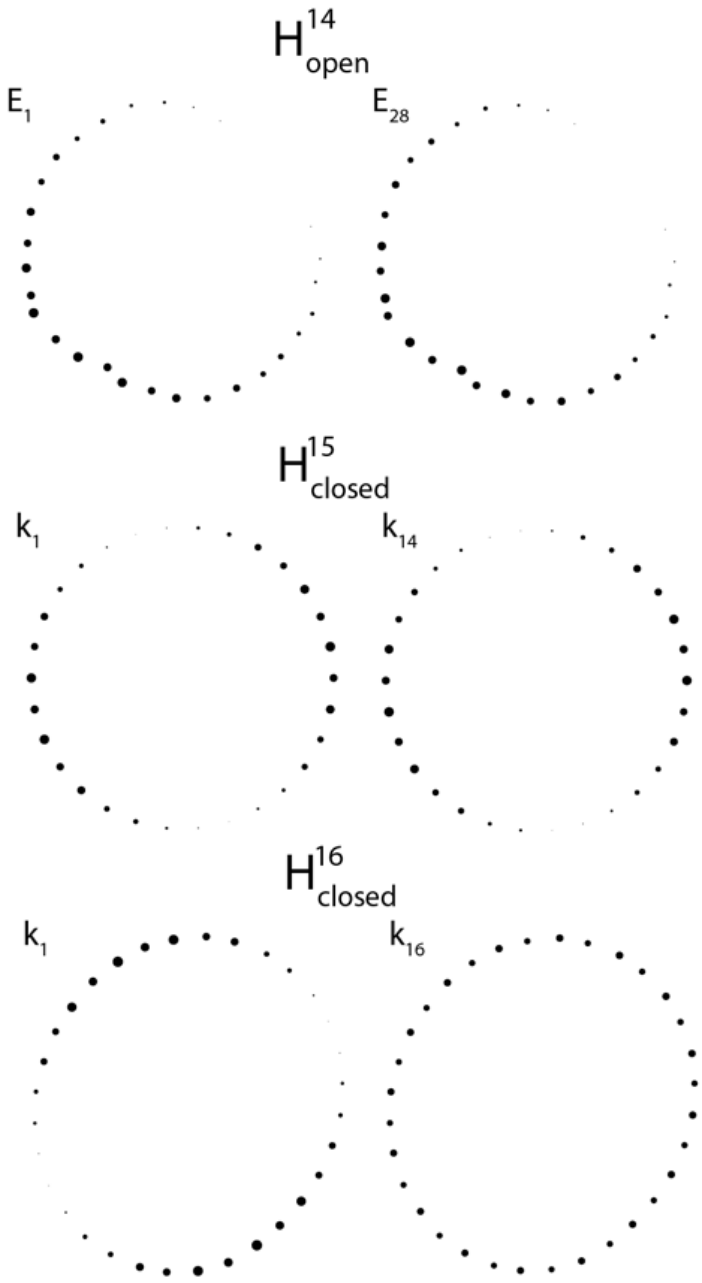

Figure 4.14: The chromophore transition dipole strengths for B875 and B875* are displayed for each Hamiltonian. The diameter of the dots scale linearly with the dipole strength. There is a large overlap between B875 and B875*, which leads to the rapid rates of observed energy transfer. Reprinted (adapted) with permission from J. Phys. Chem. A 2016, 120, 24, 4124–4130. Copyright (2016) American Chemical Society.

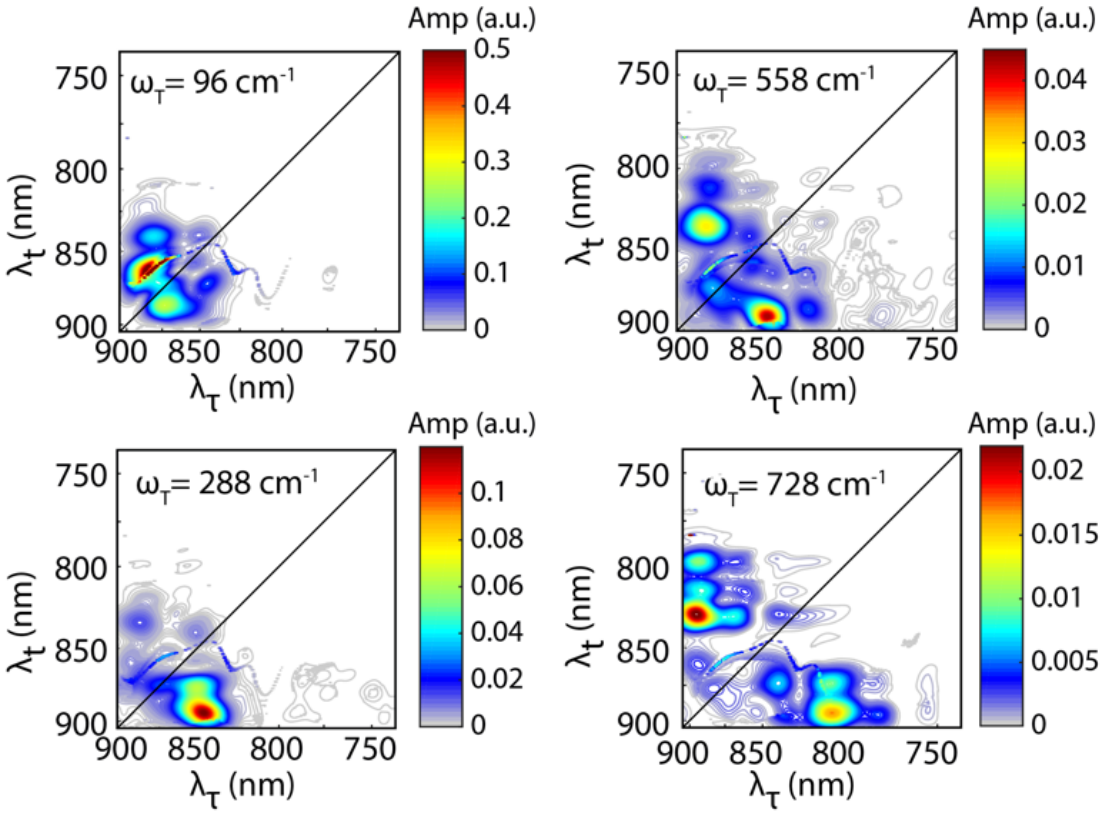

Figure 4.15: Waiting frequency amplitude maps of LH1 membranes. These maps were obtained by fitting a bi-exponential function to each (λ_τ, λ_t) waiting time trace in the average 2DES cube of data and taking the power spectrum of the residuals. The resulting power spectra were normalized to the maximum of the frequency-frequency-frequency cube and select waiting time frequencies are displayed above. Each is a well-known vibrational mode of BChl a. Near nodes in the 2D spectra where signal is small, our fitting algorithm fails to converge leading to artifacts in the Fourier spectrum of the residuals along the nodes. Reprinted (adapted) with permission from J. Phys. Chem. A 2016, 120, 24, 4124–4130. Copyright (2016) American Chemical Society.

4.4 Ultrafast Interstate Relaxation as an Extra Mechanistic Information on Light Harvesting within Purple Bacteria

The rapid growth of the cross peak and lack of vibrational coherences in the waiting time frequency domain firmly assigns the B875* states as electronic in origin. Their rapid transfer to B875 mirrors the dynamics found in the B850* and B850 states of LH2 and is in agreement with the effective Hamiltonians and Redfield theory calculations of population transfer rates. The role of B875* remains uncertain. The energy of B875* and its proximity to the RC and LH2 raises the possibility of it being an intermediate state as energy is transferred from the peripheral antenna to the RC, though this is unlikely. Due to the short lifetime of B875*, direct transfer to the RC would not compete with relaxation to the B875 ring despite the strong spectral overlap of the H and B peaks of the RC with the B875* states. Also, the distance between B800 and B875 makes energy transfer from B800 to B875* an unlikely pathway. While other mechanisms such as super-transfer or moderation of energy transfer based the state of the reaction center are conceivable, the presence of the B875* states is likely an informative byproduct of the strong coupling between chromophores in the B875 ring, which is essential for biological function.

REFERENCES

[1] Robert E. Blankenship. *Molecular Mechanisms of Photosynthesis*. Wiley/Blackwell, Chichester, West Sussex, second edition edition, 2014. ISBN 978-1-4051-8976-7 978-1-4051-8975-0.

[2] Herbert van Amerongen, Leonas Valkunas, and Rienk van Grondelle. *Photosynthetic Excitons*. World Scientific, Singapore, 2000. ISBN 978-981-02-3280-1.

[3] Colin A. Wraight and Roderick K. Clayton. The absolute quantum efficiency of bacteriochlorophyll photooxidation in reaction centres of Rhodopseudomonas spheroides. *Biochimica et Biophysica Acta (BBA) - Bioenergetics*, 333(2):246–260, 1974.

[4] Ralph Jimenez, Frank van Mourik, Jae Young Yu, and Graham R. Fleming. Three-Pulse Photon Echo Measurements on LH1 and LH2 Complexes of *Rhodobacter sphaeroides* : A Nonlinear Spectroscopic Probe of Energy Transfer. *The Journal of Physical Chemistry B*, 101(37):7350–7359, 1997.

[5] Pu Qian, Miroslav Z. Papiz, Philip J. Jackson, Amanda A. Brindley, Irene W. Ng, John D. Olsen, Mark J. Dickman, Per A. Bullough, and C. Neil Hunter. Three-Dimensional Structure of the *Rhodobacter sphaeroides* RC-LH1-PufX Complex: Dimerization and Quinone Channels Promoted by PufX. *Biochemistry*, 52(43):7575–7585, 2013.

[6] Pu Qian, Per A. Bullough, and C. Neil Hunter. Three-dimensional Reconstruction of a Membrane-bending Complex: *THE RC-LH1-PufX CORE DIMER OF RHODOBACTER SPHAEROIDES*. *Journal of Biological Chemistry*, 283(20):14002–14011, 2008.

[7] Melih Şener, Jen Hsin, Leonardo G. Trabuco, Elizabeth Villa, Pu Qian, C. Neil Hunter, and Klaus Schulten. Structural model and excitonic properties of the dimeric RC-LH1-PufX complex from Rhodobacter sphaeroides. *Chemical Physics*, 357(1-3):188–197, 2009.

[8] Ana Damjanović, Thorsten Ritz, and Klaus Schulten. Excitation energy trapping by the reaction center of Rhodobacter Sphaeroides. *International Journal of Quantum Chemistry*, 77(1):139–151, 2000.

[9] Kees J. Visscher, Hans Bergström, Villy Sundström, C. Neil Hunter, and Rienk van Grondelle. Temperature dependence of energy transfer from the long wavelength antenna BChl-896 to the reaction center in Rhodospirillum rubrum, Rhodobacter sphaeroides (w.t. and M21 mutant) from 77 to 177K, studied by picosecond absorption spectroscopy. *Photosynthesis Research*, 22(3):211–217, 1989.

[10] Lucas M. P. Beekman, Frank van Mourik, Michael R. Jones, H. Matthieu Visser, C. Neil Hunter, and Rienk van Grondelle. Trapping Kinetics in Mutants of the Photosynthetic Purple Bacterium Rhodobacter sphaeroides: Influence of the Charge Separation Rate and Consequences for the Rate-Limiting Step in the Light-Harvesting Process. *Biochemistry*, 33(11):3143–3147, 1994.

[11] Svetlana Bahatyrova, Raoul N. Frese, Kees O. van der Werf, Cees Otto, C. Neil Hunter, and John D. Olsen. Flexibility and Size Heterogeneity of the LH1 Light Harvesting Complex Revealed by Atomic Force Microscopy: FUNCTIONAL SIGNIFICANCE FOR BACTERIAL PHOTOSYNTHESIS. *Journal of Biological Chemistry*, 279(20): 21327–21333, 2004.

[12] John D. Olsen, Peter G. Adams, Philip J. Jackson, Mark J. Dickman, Pu Qian, and C. Neil Hunter. Aberrant Assembly Complexes of the Reaction Center Light-harvesting 1 PufX (RC-LH1-PufX) Core Complex of *Rhodobacter sphaeroides* Imaged by Atomic Force Microscopy. *Journal of Biological Chemistry*, 289(43):29927–29936, 2014.

[13] Stuart J. Jamieson, Peiyi Wang, Pu Qian, John Y. Kirkland, Matthew J. Conroy, C. Neil Hunter, and Per A. Bullough. Projection structure of the photosynthetic reaction centre-

antenna complex of Rhodospirillum rubrum at 8.5 A resolution. *The EMBO Journal*, 21 (15):3927–3935, 2002.

[14] Stephen E. Bradforth, Ralph Jimenez, Frank van Mourik, Rienk van Grondelle, and Graham R. Fleming. Excitation Transfer in the Core Light-Harvesting Complex (LH-1) of Rhodobacter sphaeroides: An Ultrafast Fluorescence Depolarization and Annihilation Study. *The Journal of Physical Chemistry*, 99(43):16179–16191, 1995.

[15] Mirianas Chachisvilis, Tonu Pullerits, Michael R. Jones, C. Neil Hunter, and Villy Sundström. Vibrational dynamics in the light-harvesting complexes of the photosynthetic bacterium Rhodobacter sphaeroides. *Chemical Physics Letters*, 224(3-4):345–354, 1994.

[16] Thomas A. Cohen-Stuart, Mikas Vengris, Vladimir I. Novoderezhkin, Richard J. Cogdell, C. Neil Hunter, and Rienk van Grondelle. Direct Visualization of Exciton Reequilibration in the LH1 and LH2 Complexes of Rhodobacter sphaeroides by Multipulse Spectroscopy. *Biophysical Journal*, 100(9):2226–2233, 2011.

[17] Tonu Pullerits, Mirianas Chachisvilis, Michael R. Jones, C. Neil Hunter, and Villy Sundström. Exciton dynamics in the light-harvesting complexes of Rhodobacter sphaeroides. *Chemical Physics Letters*, 224(3-4):355–365, 1994.

[18] David J. Mothersole, Philip J. Jackson, Cvetelin Vasilev, Jaimey D. Tucker, Amanda A. Brindley, Mark J. Dickman, and C. Neil Hunter. PucC and LhaA direct efficient assembly of the light-harvesting complexes in *Rhodobacter sphaeroides*: Photosystem assembly in *Rba. sphaeroides*. *Molecular Microbiology*, 99(2):307–327, 2016.

[19] Tobias Brixner, Jens Stenger, Harsha M. Vaswani, Minhaeng Cho, Robert E. Blankenship, and Graham R. Fleming. Two-dimensional spectroscopy of electronic couplings in photosynthesis. *Nature*, 434(7033):625–628, 2005.

[20] John D. Hybl, Allison Albrecht Ferro, and David M. Jonas. Two-dimensional Fourier transform electronic spectroscopy. *The Journal of Chemical Physics*, 115(14):6606–6622, 2001.

[21] John D. Hybl, Allison W. Albrecht, Sarah M. Gallagher Faeder, and David M. Jonas. Two-dimensional electronic spectroscopy. *Chemical Physics Letters*, 297(3-4):307–313, 1998.

[22] Shaul Mukamel. *Principles of Nonlinear Optical Spectroscopy*. Number 6 in Oxford series in optical and imaging sciences. Oxford University Press, New York, NY, 1999. ISBN 978-0-19-513291-5.

[23] Peter Hamm and Martin T. Zanni. *Concepts and Methods of 2D Infrared Spectroscopy*. Cambridge University Press, Cambridge, UK; New York, NY, 2011. ISBN 978-1-107-00005-6.

[24] Tobias Brixner, Tomáš Mančal, Igor V. Stiopkin, and Graham R. Fleming. Phase-stabilized two-dimensional electronic spectroscopy. *The Journal of Chemical Physics*, 121(9):4221–4236, 2004.

[25] Elad Harel, Andrew F. Fidler, and Gregory S. Engel. Real-time mapping of electronic structure with single-shot two-dimensional electronic spectroscopy. *Proceedings of the National Academy of Sciences*, 107(38):16444–16447, 2010.

[26] Elad Harel, Phillip D. Long, and Gregory S. Engel. Single-shot ultrabroadband two-dimensional electronic spectroscopy of the light-harvesting complex LH2. *Optics Letters*, 36(9):1665–1667, 2011.

[27] Elad Harel, Andrew F. Fidler, and Gregory S. Engel. Single-Shot Gradient-Assisted Photon Echo Electronic Spectroscopy. *The Journal of Physical Chemistry A*, 115(16): 3787–3796, 2011.

[28] Peter D. Dahlberg, Andrew F. Fidler, Justin R. Caram, Phillip D. Long, and Gregory S. Engel. Energy Transfer Observed in Live Cells Using Two-Dimensional Electronic Spectroscopy. *The Journal of Physical Chemistry Letters*, 4(21):3636–3640, 2013.

[29] Ved P. Singh, Andrew F. Fidler, Brian S. Rolczynski, and Gregory S. Engel. Independent phasing of rephasing and non-rephasing 2D electronic spectra. *The Journal of Chemical Physics*, 139(8):084201, 2013.

[30] Satomi Niwa, Long-Jiang Yu, Kazuki Takeda, Yu Hirano, Tomoaki Kawakami, Zheng-Yu Wang-Otomo, and Kunio Miki. Structure of the LH1-RC complex from Thermochromatium tepidum at 3.0 å. *Nature*, 508(7495):228–232, 2014.

[31] Kelly A. Fransted and Gregory S. Engel. Probing vibrational dynamics of PM650 with two-dimensional electronic spectroscopy. *Chemical Physics*, 403:59–67, 2012.

[32] Kelly A. Fransted, Justin R. Caram, Dugan Hayes, and Gregory S. Engel. Two-dimensional electronic spectroscopy of bacteriochlorophyll *a* in solution: Elucidating the coherence dynamics of the Fenna-Matthews-Olson complex using its chromophore as a control. *The Journal of Chemical Physics*, 137(12):125101, 2012.

[33] Vytautas Butkus, Donatas Zigmantas, Leonas Valkunas, and Darius Abramavicius. Vibrational vs. electronic coherences in 2D spectrum of molecular systems. *Chemical Physics Letters*, 545:40–43, 2012.

[34] Robert J. Donohoe, Harry A. Frank, and David F. Bocian. Resonance Raman Spectra And Normal Mode Descriptions of a Bacteriochlorophyll a Model Complex. *Photochemistry and Photobiology*, 48(4):531–537, 1988.

[35] Nerine J. Cherepy, Andrew P. Shreve, Laura J. Moore, Steven G. Boxer, and Richard A. Mathies. Temperature Dependence of the Q $_{\mathrm{y}}$ Resonance Raman Spectra of Bacteri-

ochlorophylls, the Primary Electron Donor, and Bacteriopheophytins in the Bacterial Photosynthetic Reaction Center. *Biochemistry*, 36(28):8559–8566, 1997.

[36] Andrew P. Shreve, Nerine J. Cherepy, Stefan Franzen, Steven G. Boxer, and Richard A. Mathies. Rapid-flow resonance Raman spectroscopy of bacterial photosynthetic reaction centers. *Proceedings of the National Academy of Sciences*, 88(24):11207–11211, 1991.

[37] Vladimir Novoderezhkin, Markus Wendling, and Rienk van Grondelle. Intra- and Interband Transfers in the B800-B850 Antenna of *Rhodospirillum m olischianum* : Redfield Theory Modeling of Polarized Pump-Probe Kinetics. *The Journal of Physical Chemistry B*, 107(41):11534–11548, 2003.

[38] Adam Kell, Ximao Feng, Mike Reppert, and Ryszard Jankowiak. On the Shape of the Phonon Spectral Density in Photosynthetic Complexes. *The Journal of Physical Chemistry B*, 117(24):7317–7323, 2013.

[39] Mike Reppert. Modeling of Resonant Hole-Burning Spectra in Excitonically Coupled Systems: The Effects of Energy-Transfer Broadening. *The Journal of Physical Chemistry Letters*, 2(21):2716–2721, 2011. ISSN 1948-7185.

CHAPTER 5

VIBRONIC COHERENCES IN THE CORE LIGHT HARVESTING COMPLEX LH1 FROM PURPLE BACTERIUM *RHODOBACTER SPHAEROIDES*

5.1 Vibronic Coherences inside Photosynthetic Light Harvesting Complexes

Photosynthetic organisms capture sunlight and convert solar energy into chemical energy through their light harvesting machinery optimized by natural evolution. Research on photosynthetic light harvesting has gathered a growing interest among the scientific community due to advances in theoretical and experimental methods over the past few decades enabling scientists to probe the structural and electronic processes at shorter time scales and smaller length scales. Light harvesting machinery in purple bacteria has been under extensive studying on its photosynthetic mechanisms since the structural characterizations were made available [1, 2, 3, 4, 5, 6]. Closely packed bacteriochlorophyll (BChl) molecules held noncovalently by the membrane protein scaffold creates an aggregate-like local arrangement of chromophores and a resulting excitonic manifold, whose energy levels are modulated by the local electronic and vibrational interactions. LH1 complex is the core antenna complex in purple bacteria, enclosing the reaction center (RC) responsible for the process of charge separation and subsequent chemical reactions. Structural characterizations of LH1 complexes in several purple bacteria species have shown variations in both the composition and arrangement of BChl molecules [4, 6, 7, 8, 9, 10, 11, 12]; the number of BChl within one LH1 complex can range from 14 to 32, and the arrangement of BChl can be either circular or S-shaped, depending on the particular species. Nevertheless, BChl molecules in LH1 complexes from purple bacteria are held in a J-aggregate-like fashion, producing a red-shifted absorption and

finely spaced electronic energy levels in LH1 complexes. Although it is widely conceived that these electronic states serve as direct energy channels bridging LH1 complex and RC, details on how the energy transfer efficiency and rate are modulated inside LH1 complexes are still much ambiguous.

One question of particular interest hinges upon how much local environment around chromophores affects the overall light harvesting speed and efficiency. It is generally acknowledged that the structure of a light harvesting protein can act as a modulator to the energy levels of the entire multi-chromophore light harvesting unit. Both amino acid residues on the protein scaffold and solvent molecules form non-covalent interactions with chromophores, leading to instantaneous disorders of exciton energies. Degrees to which these instantaneous disorders extend manifest themselves in the spectral linewidths of the experimental absorption and fluorescence spectra. The alteration of excitonic energy levels in the multi-chromophoric system by local environment can also occur via local vibrations on amino acid residues or chromophores themselves. This phenomenon, often coined as vibronic coupling, accounts for the interaction between electronic and vibrational degrees of freedom in a quantum system. Local environment around chromophores also contributes to energy transfer processes in a light harvesting protein by providing a dissipation pathway for excess excitation energy during energy transfer from higher energy states to lower energy states, as described by Redfield theory [13, 14]. All the above reasons suggest that one may obtain abundant insights on natural light harvesting through examining the effect of local interactions between chromophores and their surrounding environment.

Quantum coherence is a sensitive probe to interactions between quantum states and has been proposed to play a role in photosynthetic energy transfer from early experimental efforts on the Fenna-Matthews-Olsen (FMO) complex in green sulfur bacteria [15, 16]. Many research articles debating on the nature and functions of quantum coherences in biology have since been published [17, 18, 19]. Vibronic coherence, a mixed electronic-

vibrational type of coherences established among the electronic excited states with strongly coupled vibrations, are suggested to exist in a variety of biological [20, 21] and synthetic [22, 23, 24, 25, 26, 27, 28, 29] systems. Vibrational coherence, on the other hand, involves no electronic states and reflects a vibrational wavepacket propagating on either the ground or the excited electronic states. Two-dimensional electronic spectroscopy (2DES) has been proven to be a quintessential tool to answer the questions regarding physical origins of coherences. Due to its ability to separate the experimental spectra into different quantum pathways, 2DES has been repeatedly applied to analyzed coherences from small molecules, such as chlorophylls [30, 31, 32, 33] and bacteriochlorophylls [34, 35, 36, 37], to larger photosynthetic complexes, such as the FMO complex in green sulfur bacteria [15, 16, 38], the PC645 complex from cryptophyte algae [39, 40], light harvesting complexes and reaction center in purple bacteria [41, 42, 43, 44, 45, 46], and the photosystem II reaction center in plants [47, 48]. Some recent studies on vibrational coherences in molecular systems extract extra information by analyzing both the rephasing and nonrephasing 2DES signals to determine the electronic states on which the observed vibrational coherences are established [39, 40, 49, 50]. Whether vibronic couplings and vibrational wavepackets play significant roles in photosynthetic light harvesting remains to be investigated, yet given the large electronic and nuclear degrees of freedom in natural light harvesting complexes, it is conceivable that we can obtain useful pieces of knowledge on the design principles of natural photosynthesis through the lens of quantum coherence.

In this Chapter, we aim to provide an insight on the origins of coherences observed in the core light harvesting complex, the LH1 complex, from purple bacteria *Rhodobacter sphaeroides*. We conduct a 2DES experiment on LH1-only membranes from the L3 mutant (Δpuc1BA ΔpufLMX, expressing only LH1 complexes as sole light harvesting proteins) to simultaneously acquire and analyze signals from both the rephasing and nonrephasing pathways. We observe distinct vibrational and vibronic coherences in both B875 and higher-lying B875* excitonic

states by a combination of Fourier analysis and predictions from theoretical modeling.

5.2 Resolving Coherences within LH1 Complex from *Rhodobacter sphaeroides*

5.2.1 Sample Preparation of LH1-Only Membranes

The procedure of preparing the LH1-only membranes from *Rhodobacter sphaeroides* was followed by Dahlberg et al. [51] and briefly stated here. The L3 mutant of *Rhodobacter sphaeroides* containing only LH1 as the sole light harvesting complex and void of the reaction center was graciously provided by Prof. C. Neil Hunter at University of Sheffield. Cells of *Rhodobacter sphaeroides* were grown in a semi-aerobic incubator at 30°C before being disrupted with a French press at 14,000 psi, after which the large cell debris was removed by centrifugation. The resulting supernatant containing the LH1-only membranes was diluted to the desire O.D. of 0.3 at 875 nm in a 200-μm path for spectroscopy.

5.2.2 Two-Dimensional Electronic Spectroscopy on LH1-Only Membranes

Spectroscopic data on LH1-only membranes were acquired by a home-built 2DES spectrometer in GRAPE configuration [52, 53] with recent modification in post-processing and fine sampling that allowed simultaneous retrieval of both rephasing and nonrephasing portions of 2D spectra [28, 54]. Descriptions of working principles of 2DES [55, 56, 57, 58] and the spectroscopic setup of GRAPE spectrometer [51, 59] have been detailed in previous works, and only the concise summary is provided in this manuscript.

For our 2DES experiment setup, illustrated in Figure 5.11 in the Appendices section, an 800-nm, 30-fs laser pulse with a 5 kHz repetition rate was focused once through argon gas (4 psi) and again through the atmosphere to generate a near-infrared spectrum. The pulse was compressed to 15 fs with an SLM-based pulse shaper, split into four beams with

a beamsplitter and wedged optics in the GRAPE setup, focused onto a vertical line with a cylindrical lens at the sample position. The third-ordered signal from the sample was heterodyned with an attenuated local oscillator, spectrally resolved with a spectrometer, and detected by a high-speed CMOS camera. The delay time between pulses 2 and 3 (waiting time, T) was scanned by a computer-controlled mechanical stage from -200 fs to 3 ps with a 1-fs step. Rather than scanned with another mechanical stage, the time delay between pulses 1 and 2 (coherence time, τ) was mapped along the vertical direction and scanned in a single camera shot. The effective coherence time axis was determined to be -200 fs to $+200$ fs with a 0.9-fs step via interferometry with a referencing local oscillator pulse. Each camera image collected 2DES signals from 100 independent laser shots. The 2DES data were taken in 10 replicates.

5.2.3 Data Analysis

Raw data from a stack of camera images was processed into a full 2DES 3-D data matrix. Nonrephasing portions ($\tau < 0$ pixels) of the data were interpolated post-experimentally [28, 54]; the interpolated nonrephasing data was then processed in the same way as the raw rephasing data: filtered in the waiting time with a low-pass filter, divided by the amplitude of the local oscillator, filtered in the detection time domain with a Tukey window, filtered in the coherence time domain with a sigmoidal window, and transformed into the Fourier domain of the coherence time axis. The frequency-dependent spectral phases of the complex-valued rephasing and nonrephasing data were retrieved by fitting to a separately acquired set of pump-probe spectra of LH1 membranes [58]. All data were processed using MATLAB installed on a desktop computer with 32 GB RAM and a 4-core CPU.

In order to further distinguish the origins of waiting time coherences seen in the LH1 membranes, we resorted to the Fourier spectral analysis on both rephasing and nonrephasing 2DES signals of LH1 membranes. In this analysis, the complex-valued signal in the waiting

time domain was first de-trended using the fitting results from the global kinetics analysis [60] (See more details in the Appendices), after which a Fourier transform was performed on each residual at all excitation/detection wavelength pairs to obtain spectral amplitudes of oscillations in the waiting frequency (ω_T) domain. This analysis would provide information on vibrational and/or vibronic coherence features in the LH1 membranes during the waiting time. Furthermore, depending on the locations on the 2DES map where these coherences appeared, we could assign the origins of coherences to either ground or excited state coherences due to their distinct features in rephasing and nonrephasing pathways. The Nyquist sampling frequency was determined to be 11.5 cm^{-1} by the total waiting time range used in the global kinetics analysis.

5.3 2DES Revealing Distinct Origins of Coherences on Different LH1 Exciton States

Representative real-valued 2DES spectra of LH1-only membranes from *Rhodobacter sphaeroides* at 20 fs and 200 fs were plotted in Figure 5.1. All rephasing, nonrephasing, and purely absorptive (sum of rephasing and nonrephasing) spectra consisted of two major features: a positive stimulated emission (SE)/ground state bleach (GSB) feature centered around the detection wavelength of 880 nm corresponding to the B875 peak in the absorption spectrum of LH1 complex, and a negative excited state absorption (ESA) feature around the detection wavelengths between 800 nm and 860 nm. The positive SE feature also exhibited a sub-200 fs, downhill relaxation at the excitation wavelength of 860 nm, which was better visualized in the rephasing [Figure 5.1(a), 5.1(b)] and absorptive [Figure 5.1(e), 5.1(f)] 2DES spectra. By 200 fs, most amplitudes of the SE feature arising from a broad manifold of excitonic states between the 760 nm and 860 nm region had relaxed to the lowest excitonic state centered around 880 nm. The ESA feature around the excitation wavelength of 830 nm in the nonrephasing 2DES spectra [Figure 5.1(c), 5.1(d)], as well as the ESA feature

around the detection wavelength of 830 nm in the absorptive 2DES spectra [Figure 5.1(e), 5.1(f)] both suggested the existence of higher-lying excited states in the LH1 complex. These characteristics in 2DES spectra were qualitatively comparable to those seen in the 2DES spectra of LH1-only live cells from the L3 mutant [59, 61]. Although most excitonic states of the LH1 complex were close in energy, a few could be resolved in the rephasing 2DES map at the waiting time of 200 fs [Figure 5.1(b)]. Zooming in on the broad SE feature in the lower off-diagonal region, there were four major peaks at the excitation wavelengths of 875 nm, 860 nm, 830 nm, and 810 nm, which would be designated as B875, B860, B830, and B810 state, respectively, in the following discussion.

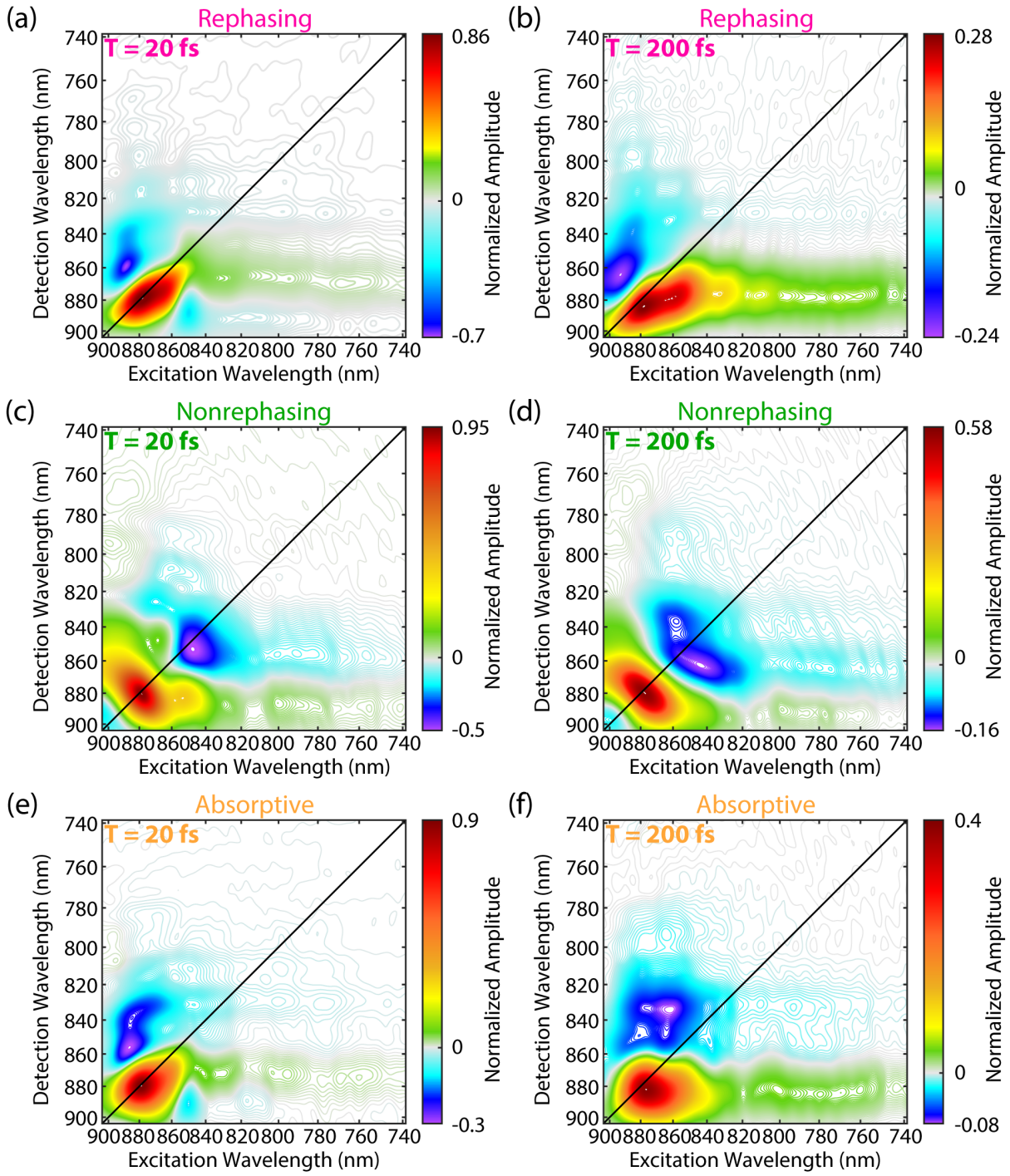

Figure 5.1: Real part of the experimental 2DES spectra of LH1-only membranes in R. sphaeroides at selected waiting time frames of (a, c, e) T = 20 fs and (b, d, f) T = 200 fs. The results were separated into the (a, b) rephasing, (c, d) nonrephasing, and (e, f) purely absorptive spectra (the sum of both rephasing and nonrephasing signals.) Each spectrum was plotted with 500 contour lines and normalized to its respective maximum amplitude across all wavelengths and waiting time.

Upon selecting a pair of excitation and detection wavelengths on the 2DES amplitude map, a waiting time trace representing the state-correlated population dynamics could be drawn by plotting the corresponding amplitude in each waiting time frame. Selected waiting time traces of rephasing and nonrephasing 2DES signals were plotted in Figure 5.2. In the rephasing 2DES signals, both the real and imaginary part carry visible oscillations [Figure 5.2 (a), (b)] that mostly diminished after 200 fs. Both the trace of the SE/GSB feature at $P1_R$ near the B860/B875 cross peak and the trace of the ESA feature at $N2_R$ near the B875/B830 cross peak showed a slightly underdamped oscillation that lasts around 1 ps. In the nonrephasing 2DES signals, there existed overdamped but observable oscillations in the lower-energy (B875 and B860) regions of the 2DES amplitude map between 840 nm and 890 nm, seen in the B860 diagonal peak ($N1_{NR}$) as well as in the B860/B840 ($N2_{NR}$), B860/B875 ($P1_{NR}$) cross peaks [Figure 5.2(c), (d)], whereas in the higher-energy (B830 and B810) regions of the nonrephasing 2DES signals between 800 and 830 nm, oscillations on the B830 ($N3_{NR}$) and B810 ($N4_{NR}$) diagonal peaks were partially overshadowed by the errors on the mean values of 10 experimental replicates [Figure 5.2(e), (f)].

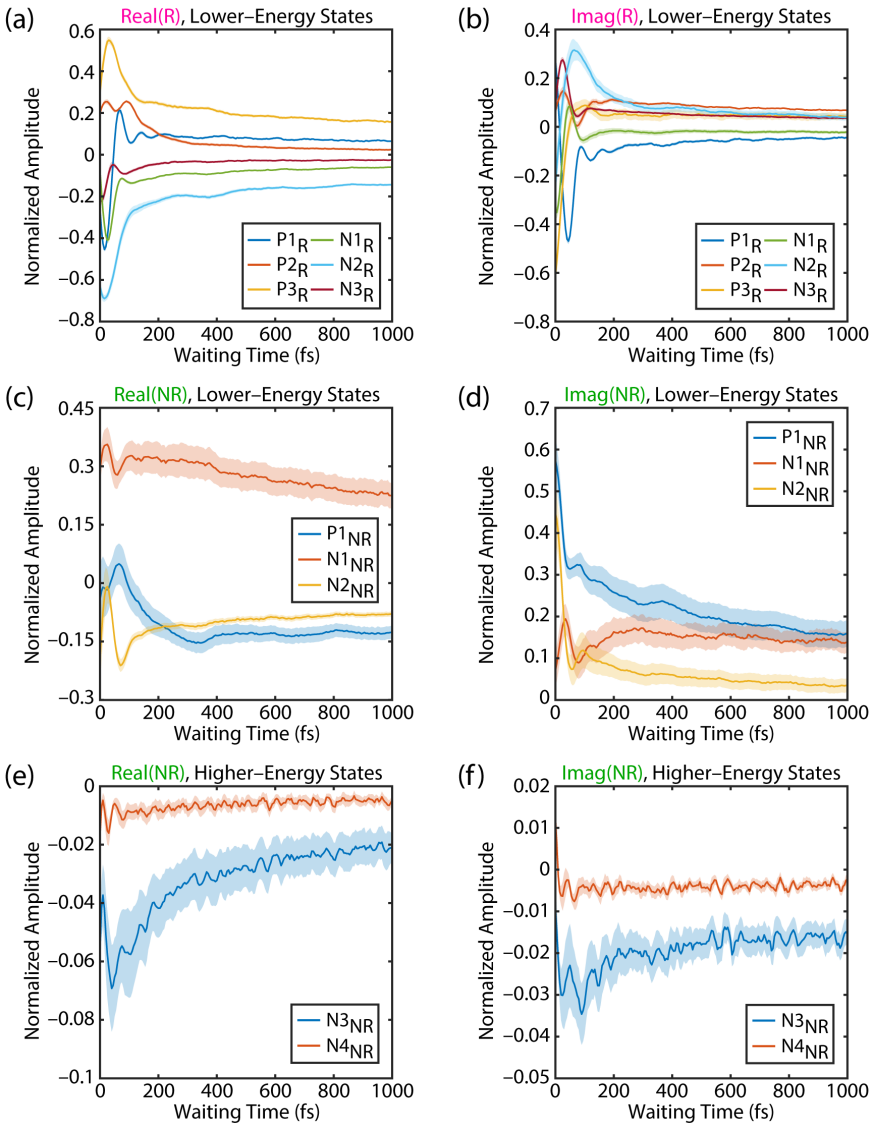

Figure 5.2: 2DES waiting time traces of LH1-only membranes at selected wavelengths on the 2DES map showing oscillations, indicating coherences resulting from simultaneous excitations of multiple excited states. The top row shows time traces from the (a) real part and (b) imaginary part of rephasing 2DES signals; the center row showed time traces from the (c) real part and (d) imaginary part of nonrephasing 2DES signals within lower-energy region between 840 nm and 890 nm; the bottom row showed time traces from the (e) real part and (f) imaginary part of nonrephasing 2DES signals within higher-energy region between 800 nm and 830 nm. Selected wavelengths (λ_{ex}, λ_{det}) were labeled as: $P1_R$ (850, 890) nm, $P2_R$ (850, 860) nm, $P3_R$ (880, 890) nm, $N1_R$ (860, 840) nm, $N2_R$ (890, 840) nm, $N3_R$ (890, 860) nm, $P1_{NR}$ (860, 890) nm, $N1_{NR}$ (860, 860) nm, $N2_{NR}$ (860, 840) nm, $N3_{NR}$ (830, 830) nm, and $N4_{NR}$ (820, 810) nm. Each waiting time trace was normalized to the maximum absolute value of the corresponding 2DES signal, and was overlaid with the standard error on the mean (shaded area) from 10 replicates at each time point.

To further analyze the patterns of oscillations seen in the waiting time traces in Figure 5.2, coherence beating maps of LH1-only membranes were generated after de-trending the traces with exponential decaying kinetics and performing Fourier transform to the residuals at each frequency point on the 2DES spectra. Due to the complex-valued nature of 2DES signals, beating maps resulting from Fourier transform in positive and negative frequencies had complementary yet distinct features. The sign convention used in this work was defined such that a density matrix element of $|e_1\rangle \langle e_2|$ evolving during the waiting time T would have a positive oscillation frequency when the state $|e_1\rangle$ is higher in energy than the state $|e_2\rangle$.

Beating maps at the ± 563 cm^{-1}, ± 735 cm^{-1} from both rephasing and nonrephasing 2DES signals of LH1-only membranes were plotted in Figure 5.3 and 5.4. In the coherence beating maps from rephasing 2DES signals, the lower-excitation energy region of the broad SE/GSB feature near the B860/B875 cross peak exhibited negative beating at both frequencies in the rephasing signals [Figure 5.3(a) and 5.4(a)], while the upper diagonal region of the ESA feature around the B875/B830 cross peak had intense positive beatings at both frequencies [Figure 5.3(b) and 5.4(b)]. In the nonrephasing beating maps, the SE/GSB feature around the B875 diagonal peak showed negative beatings at both frequencies [Figure 5.3(c) and 5.4(c)].

Upon closer examination, however, some unusual patterns could be seen in the coherence beating maps at the beating frequency of $+563$ cm^{-1} and $+735$ cm^{-1} from the nonrephasing 2DES signals [Figure 5.3 (d) and 5.4 (d)]. In the higher-energy (B830 and B810 states) region on the nonrephasing 2DES map between 800 nm and 830 nm, where the ESA feature had only less than 3% of the maximum amplitude, beating modes at $+563$ cm^{-1} and $+735$ cm^{-1} consistently showed up in all of the replicate experiments. These frequencies matched with peak locations observed in the resonance Raman spectrum of BChl with accuracy given our spectral resolution [62, 63].

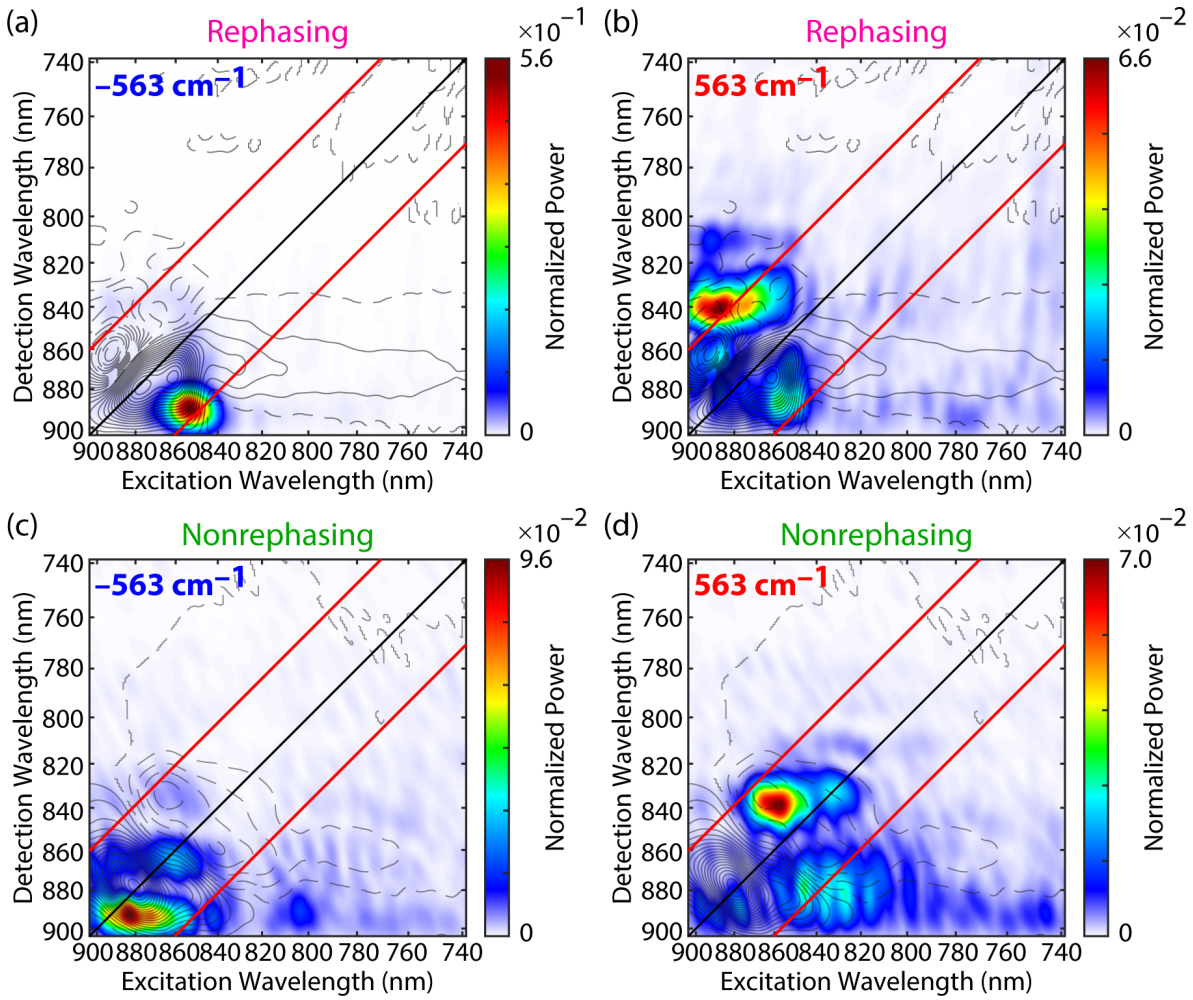

Figure 5.3: Coherence beating maps of LH1-only membranes showing the Fourier transform spectra of residuals from global analysis. Four beating maps are plotted from (a) Rephasing part at the beating frequency $\omega_T = -563$ cm^{-1}; (b) rephasing part at $\omega_T = +563$ cm^{-1}; (c) nonrephasing part at $\omega_T = -563$ cm^{-1}, and (d) nonrephasing part at $\omega_T = +563$ cm^{-1}, respectively. Each beating map is plotted with 500 color-filled contours, on which the corresponding 2DES signal is overlaid as 25 contours. Solid contours indicate positive 2DES signals, whereas dotted contours indicate negative 2DES signals. Red diagonals are drawn to guide the eye for the beating frequency offset from the electronic states.

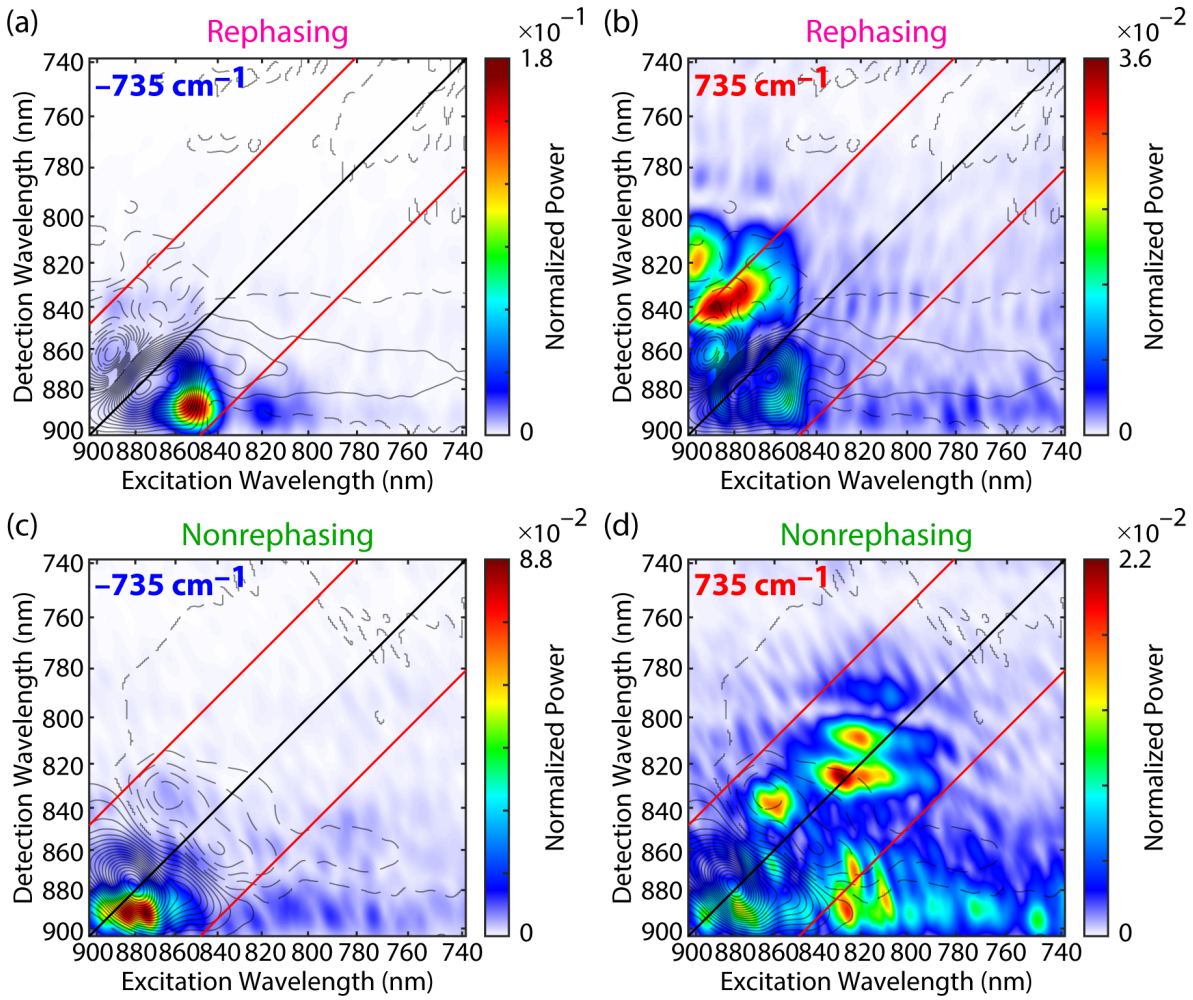

Figure 5.4: Coherence beating maps of LH1-only membranes showing the Fourier transform spectra of residuals from global analysis. Four beating maps are plotted from (a) Rephasing part at the beating frequency $\omega_T = -735$ cm^{-1}; (b) rephasing part at $\omega_T = +735$ cm^{-1}; (c) nonrephasing part at $\omega_T = -735$ cm^{-1}, and (d) nonrephasing part at $\omega_T = +735$ cm^{-1}, respectively. Each beating map is plotted with 500 color-filled contours, on which the corresponding 2DES signal is overlaid as 25 contours. Solid contours indicate positive 2DES signals, whereas dotted contours indicate negative 2DES signals. Red diagonals are drawn to guide the eye for the beating frequency offset from the electronic states.

Beating maps at lower frequencies show

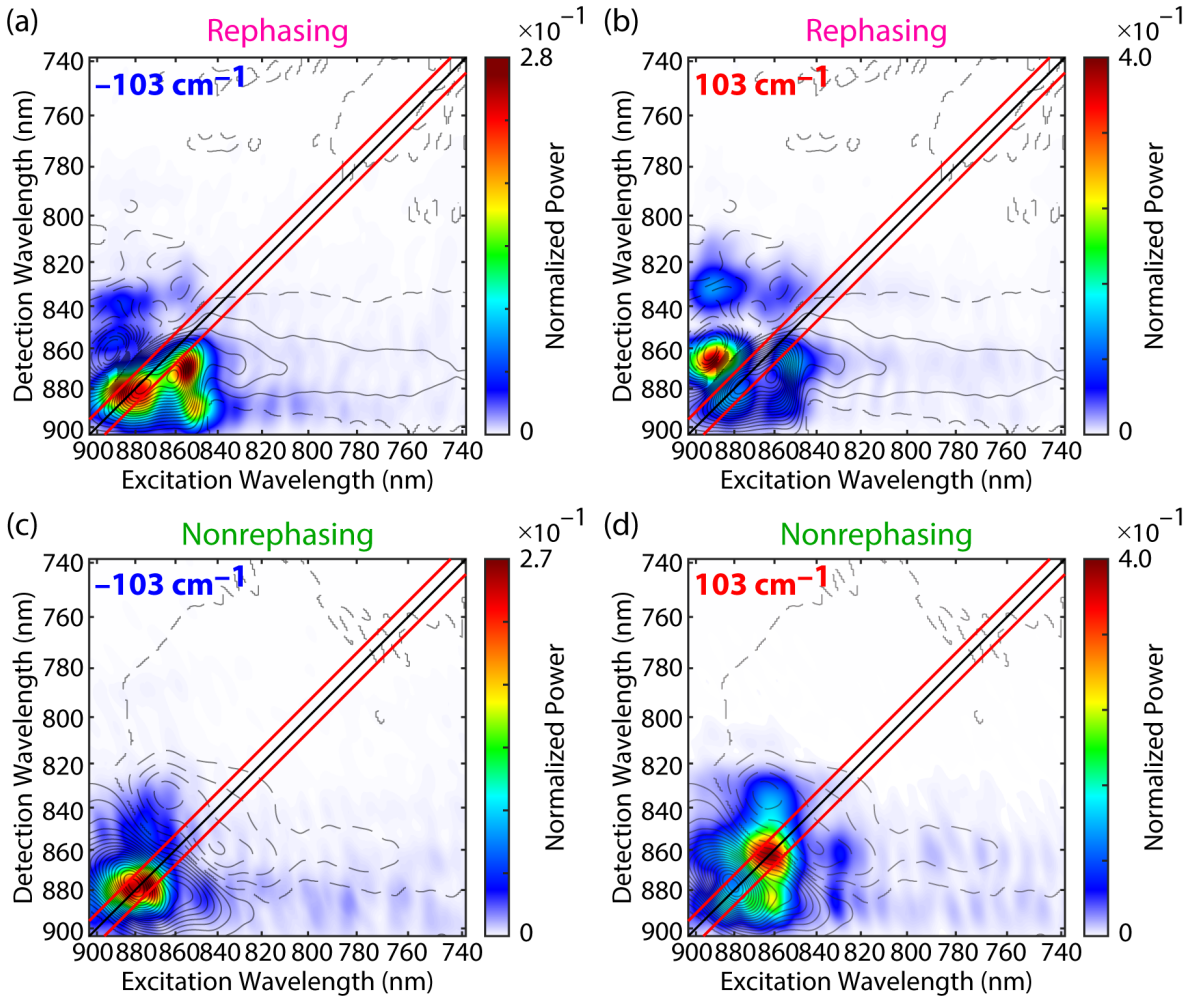

Figure 5.5: Coherence beating maps of LH1-only membranes showing the Fourier transform spectra of residuals from global analysis. Four beating maps are plotted from (a) Rephasing part at the beating frequency $\omega_T = -103$ cm^{-1}; (b) rephasing part at $\omega_T = +103$ cm^{-1}; (c) nonrephasing part at $\omega_T = -103$ cm^{-1}, and (d) nonrephasing part at $\omega_T = +103$ cm^{-1}, respectively. Each beating map is plotted with 500 color-filled contours, on which the corresponding 2DES signal is overlaid as 25 contours. Solid contours indicate positive 2DES signals, whereas dotted contours indicate negative 2DES signals. Red diagonals are drawn to guide the eye for the beating frequency offset from the electronic states.

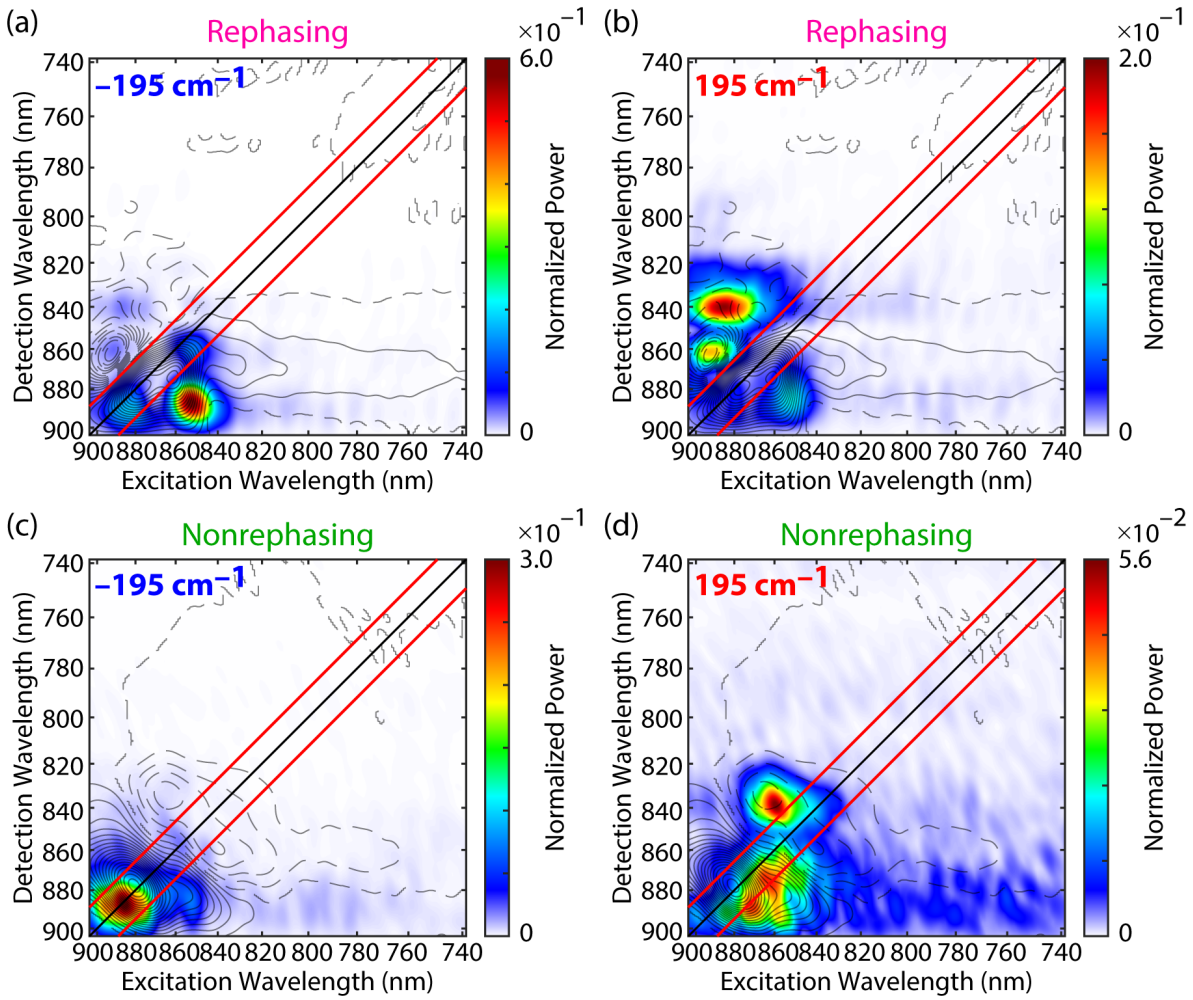

Figure 5.6: Coherence beating maps of LH1-only membranes showing the Fourier transform spectra of residuals from global analysis. Four beating maps are plotted from (a) Rephasing part at the beating frequency $\omega_T = -195$ cm^{-1}; (b) rephasing part at $\omega_T = +195$ cm^{-1}; (c) nonrephasing part at $\omega_T = -195$ cm^{-1}, and (d) nonrephasing part at $\omega_T = +195$ cm^{-1}, respectively. Each beating map is plotted with 500 color-filled contours, on which the corresponding 2DES signal is overlaid as 25 contours. Solid contours indicate positive 2DES signals, whereas dotted contours indicate negative 2DES signals. Red diagonals are drawn to guide the eye for the beating frequency offset from the electronic states.

Coupling between excitonic states and vibrational modes in the LH1 complex can be visualized by the integrated power spectra in Figure 5.7. The power spectra of coherence beating maps were summed over all detection wavelengths; the resulting power spectra were plotted against excitation wavelength axis and beating frequency axis. The integrated power spectra in Figure 5.7 thus highlighted the coherences that were active upon excitation at a certain wavelength. This analysis was recently used to examine the dependency of vibrational coupling on specific electronic bands in LH2 and FMO complexes [64]. From the nonrephasing integrated power spectrum [Figure 5.7(a)], coupling to lowest beating frequencies ($<$100 cm^{-1}) appeared to be ubiquitous across all accessible excitonic states, among which the strongest coupling intensity lay in the main absorption band at 875 nm.

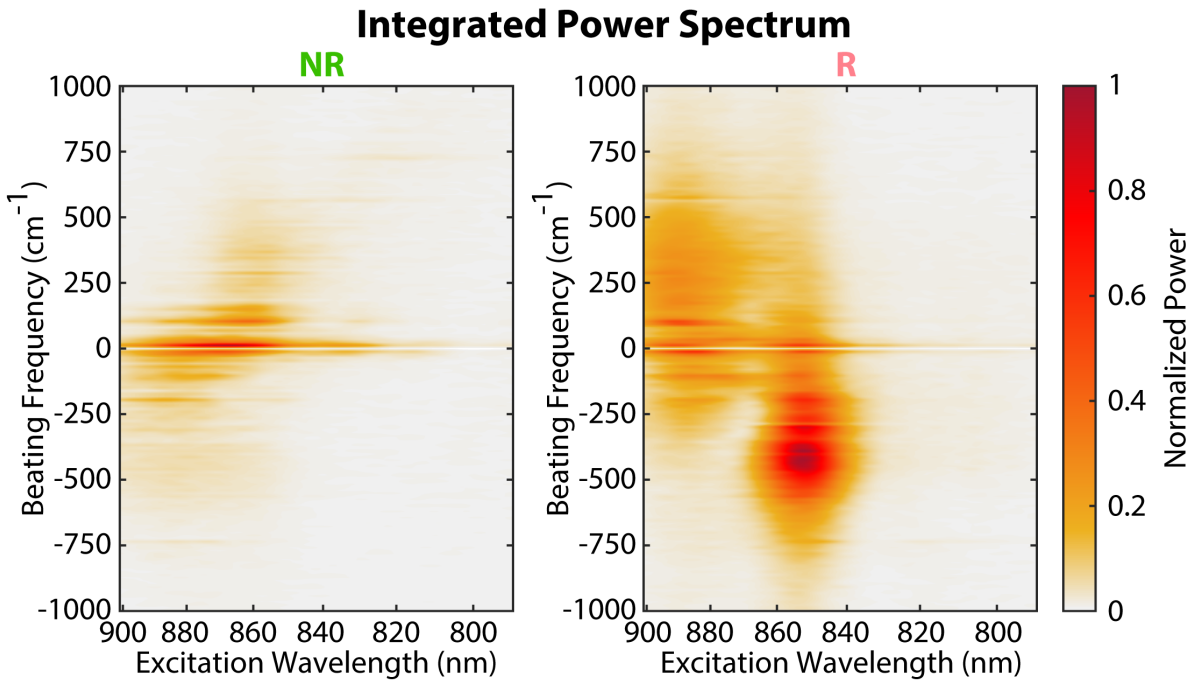

Figure 5.7: Integrated power spectra of beating maps over all detection wavelengths of (a) nonrephasing and (b) rephasing 2DES beating maps of LH1-only membranes. Two bands of vibrations observed in the rephasing power spectrum indicated that different pools of local vibrations were coupled to individual excited state in the LH1 exciton manifold.

There are a number of explanations that may account for these observations: (1) BChl vibrational wave packets on the ground electronic state; (2) BChl vibrational wave packets on the excited electronic states; (3) mixed vibronic coherences arising from the mixing of electronic and vibrational characters among excited-state potential energy surfaces; (4) two or more vibrational modes activated simultaneously among coupled excited states. Vibrational coherences observed in 2DES are identified using predictions from the displaced harmonic oscillator (DHO) model [65]. The DHO model depicts a quantum system as a collection of harmonic potentials representing an electronic ground state and multiple excited states, each having a displaced nuclear coordinate with respect to the ground state potential energy surface. This model has been commonly used to describe couplings between electronic degrees of freedom and nuclear coordinates. In the following analysis, we assume a simple three-state system with one vibrational mode. Double-sided Feynman diagrams of major pathways contributing to the rephasing and nonrephasing 2DES signals according to the DHO model were drawn in Figure 5.8 [39, 40, 65].

From the high-frequency coherence beating maps of rephasing 2DES signals at ± 563 cm^{-1} and ± 735 cm^{-1}[Figure 5.3(a), 5.3(b), 5.4(a), and 5.4(b)], we see that the upper off-diagonal features in positive frequencies along with the lower off-diagonal features in negative frequencies resemble those found in DHO model [Figure 5.9(a)]. Given the fact that these beating frequencies are also consistent with the vibrational modes seen in the Q_y-excited resonance Raman spectrum of BChl a films [63], our observations of these high-frequency beatings in the rephasing 2DES signals could be vibrational coherences established on the bright B875 excitonic state of the LH1 complex. From the predictions of double-sided Feynman diagrams, we know that vibrational coherences with positive beating frequencies arising from GSB features (stars and triangles in Figure 5.8, 5.9 and 5.10) at the upper off-diagonal region appear only when the initial equilibrium state of the system has no vibrational quanta. Given the fact that the experiment was conducted at ambient temperature, with the thermal energy

around 200 cm^{-1}, we can safely assume that the vibrational modes of neither 563 cm^{-1} nor 735 cm^{-1} on the ground electronic state potential energy surface can be significantly occupied. Thus, any upper off-diagonal coherences carrying positive beating frequencies observed in the rephasing 2DES must be of excited state origins, confirming our suggestion that +563 cm^{-1} and +735 cm^{-1} coherences exist on the bright B875 excitonic state.

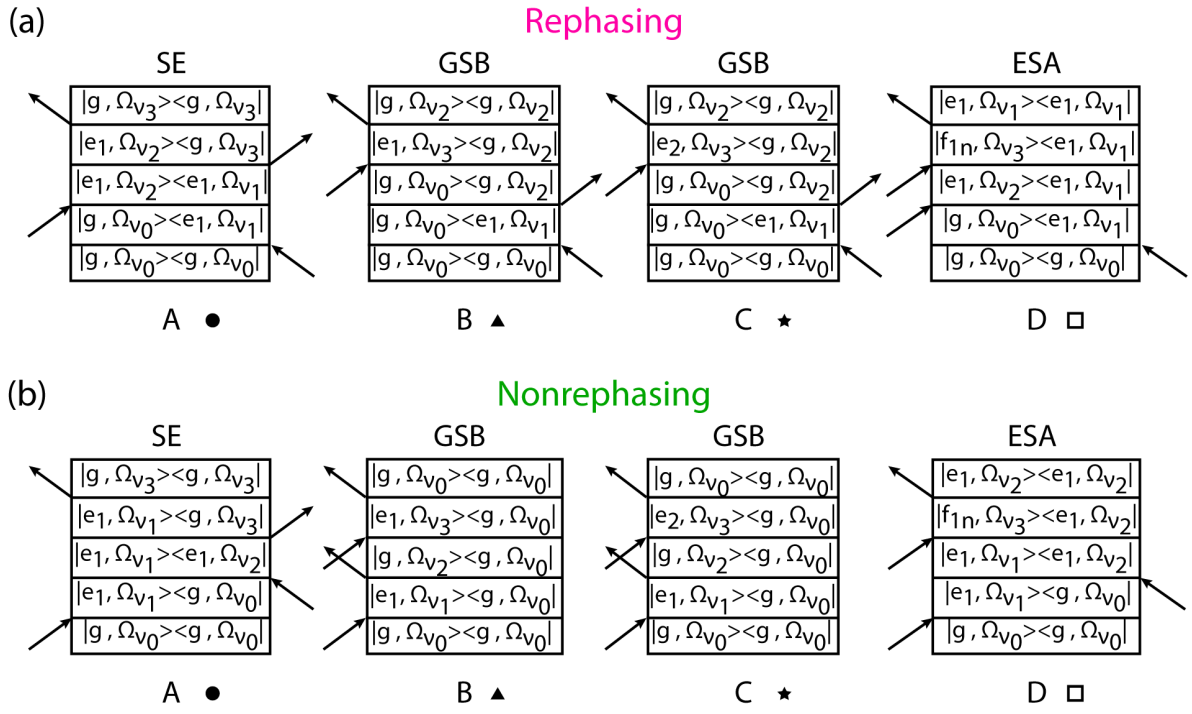

Figure 5.8: Double-sided Feynman diagrams showing dynamic pathways contributing to the (a) rephasing and (b) nonrephasing 2DES signal from a three-state system coupled to a vibrational mode. Time evolves from the bottom to the top of each diagram. Arrows indicate light-matter interactions in the third-ordered nonlinear signals. Abbreviations used in the figure are: SE for stimulated emission, GSB for ground-state bleach, and ESA for excited-state absorption.

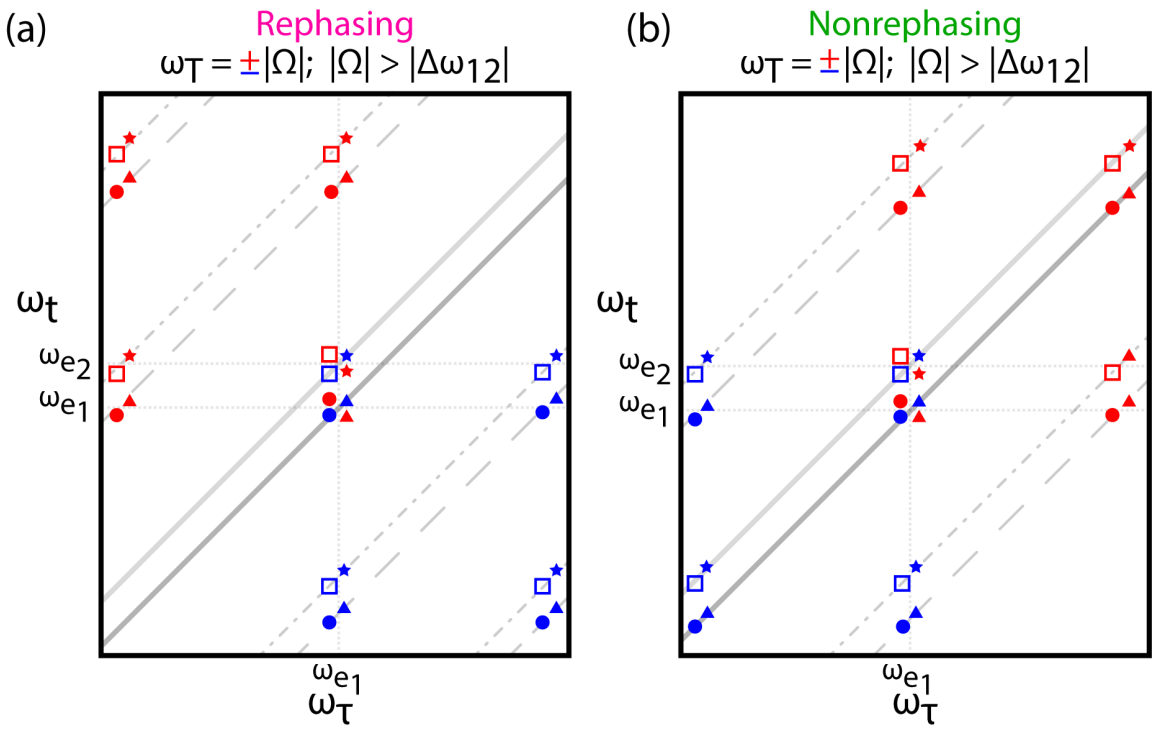

Figure 5.9: Model beating maps of (a) rephasing and (b) nonrephasing 2DES signals from an electronic system coupled to a high frequency vibrational mode at $\omega_T = +\Omega$ (red) and $\omega_T = -\Omega$ (blue), respectively. Symbols indicating coherences from distinct Feynman pathways are denoted in Figure 5.8. Bold diagonals indicate the electronic energies, whereas the thin diagonals are drawn with offsets equal to the difference in energy between two electronic states. Dashed diagonals indicate the vibrational frequency offsets from the electronic state (bold gray), while dashed-dotted diagonals indicate the vibrational frequency offsets from the electronic energy gap diagonals (thin gray).

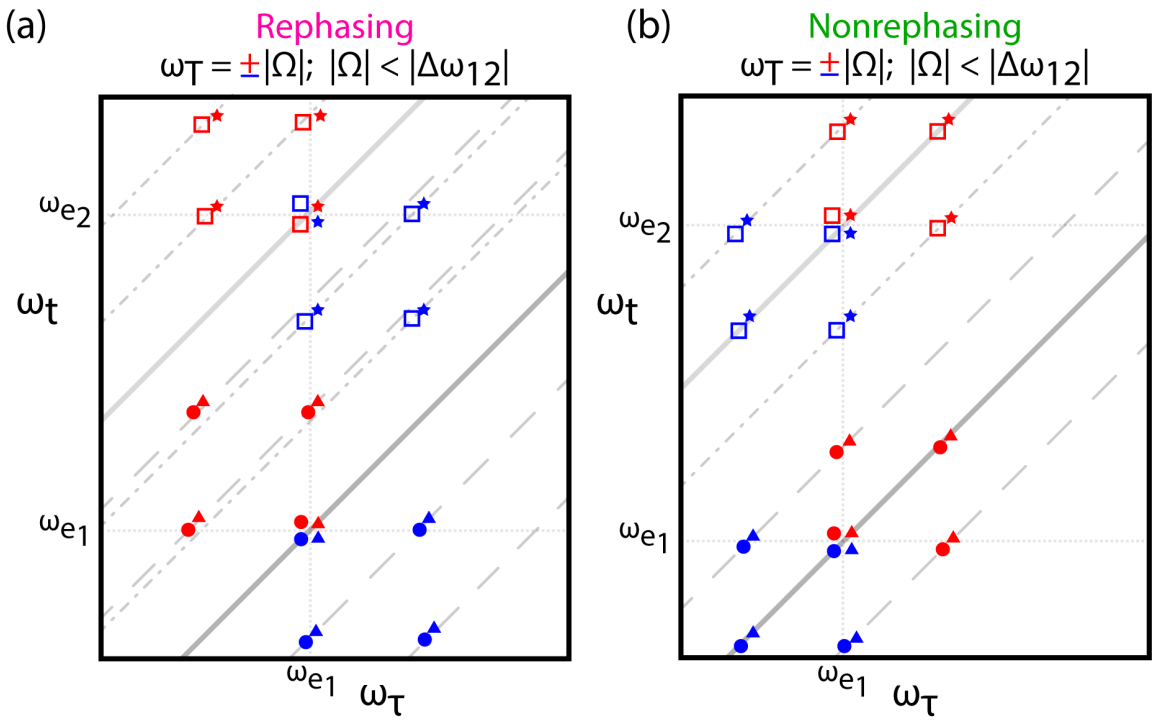

Figure 5.10: Model beating maps of (a) rephasing and (b) nonrephasing 2DES signals from an electronic system coupled to a low frequency vibrational mode at $\omega_T = +\Omega$ (red) and $\omega_T = -\Omega$ (blue), respectively. Symbols indicating coherences from distinct Feynman pathways are denoted in Figure 5.8. Bold diagonals indicate the electronic energies, whereas the thin diagonals are drawn with offsets equal to the difference in energy between two electronic states. Dashed diagonals indicate the vibrational frequency offsets from the electronic state (bold gray), while dashed-dotted diagonals indicate the vibrational frequency offsets from the electronic energy gap diagonals (thin gray).

It is worth noting that the separations between individual peaks in the higher-energy region (B810 and B830 states) in both +563 cm^{-1} and +735 cm^{-1} coherence beating maps were smaller than the respective observed beating frequencies, ruling out the possibility that these beatings were due to pure vibrational coherences on either the ground state or the excited states; a pure vibrational coherence would have appeared at an offset from the diagonal as predicted in Figure 5.9 and 5.10. We therefore hypothesize that the observed beatings patterns at +563 cm^{-1} and +735 cm^{-1} on the two higher-lying LH1 excitonic states, B810 and B830, were of vibronic origins.

From the double-sided Feynman diagrammatic analysis in Figure 5.8, it was predicted that coherences from ground state vibrations will show up at the diagonal locations as GSB features on the 2DES coherence beating maps in positive (negative) frequencies from nonrephasing (rephasing) 2DES signals. In the beating maps of ±103, ±195, and ±345 cm^{-1} from our results [Figure 5.5, 5.6, and 5.13 (a), (d)], beating amplitudes at the diagonal peak of (860, 860) nm could be seen, suggesting these vibrations exist on the ground state potential energy surface of the LH1 complex. Ground state coherences were thought to have impacts on energy transfer efficiencies by modulating the energy levels of energy-donor and energy-acceptor states and therefore establishing resonant conditions that are ideal for energy transfer processes [66].

One intriguing fact from the high-frequency coherence beating map of rephasing 2DES signals is that, no beating intensity at B810/B830 states was resolved in the +735 cm^{-1} map from rephasing 2DES signals [Figure 5.4 (b)], contrary to the ones seen in the nonrephasing counterpart [Figure 5.4 (d)]. Predictions from Figure 5.8(a) and 5.9(a) indicated that a high-frequency vibrational coherence on the excited state contributing to an ESA pathway would show up on the upper off-diagonal part of the rephasing 2D coherence beating map [red squares in Figure 5.9(a)]. Lack of resolvable excited-state vibration coherences in the rephasing 2D coherence beating maps thus further increased our confidence in the vibronic

origins of coherences on B810/B830 higher-lying excitonic states seen in the nonrephasing 2D beating maps.

From the -103 cm^{-1} and -195 cm^{-1} of rephasing 2D coherence beating maps [Figure 5.5(a) and 5.6(a)], coherences on the B875 exciton state of LH1 complexes had decaying intensities as the detection wavelength decreases. This effect could presumably arise from, but not limited to, two factors: (1) relative Franck-Condon factors of B8750-to-B830 and B875-to-B860 transitions, or (2) strengths of Huang-Rhys factors of the B875-to-B860 transition with vibrational degrees of freedom. From the Feynman diagram analysis in Figure 5.8(a), the strength of an ESA pathway, thus the strength of the excited-state vibrational coherence observed through this pathway, depended on electronic transitions $\langle g, \Omega_{\nu_0}| \rightarrow \langle e_1, \Omega_{\nu_1}|$ and $|e_1, \Omega_{\nu_2}\rangle \rightarrow |f_{1n}, \Omega_{\nu_3}\rangle$. Therefore, a difference in Franck-Condon factors between different $|e_1\rangle \rightarrow |f_{1n}\rangle$ transitions would produce a distribution of beating intensities seen in our beating map. On the other hand, if there were significant couplings between the B875-to-B860 transition and low-frequency vibrations at 103 cm^{-1} and 195 cm^{-1}, relative intensities of ESA signals and their associated vibrational coherences would be determined by the relative Huang-Rhys factors from corresponding vibrational modes.

Multiple beating frequencies resolved in this work have been identified in isolated BChl and the peripheral antenna complex LH2 in purple bacteria. In one work on BChl [34], several beating frequencies of 80, 160, 200, 280, 340, 400 cm^{-1} were resolved in rephasing 2DES and assigned to mutually-coupling modes responsible for wave packets on both the ground state and the excited state potential energy surfaces. In another work on BChl [35], beating frequencies of 572 and 741 cm^{-1} in the rephasing 2DES were shown in agreement with the DHO model and thus concluded to be of vibrational origins; low frequencies of 202 and 349 cm^{-1}, however, were shown to deviate from the DHO model. A separate work focusing on exciting both Q_y (0-0) and Q_y (0-1) vibronic transitions in BChl [36] assigned a beating frequency of 745 cm^{-1} with a 500-fs dephasing time to the vibrational coherence on the Q_y

excited state, based on the beating coherence maps from both rephasing and nonrephasing 2DES signals. In a recent work, the vibrational mode of 728 cm^{-1} was reported to have strong vibronic coupling to the Q_y transition in BChl [37].

The resolved coherences in the LH1 membranes from *R. sphaeroides* in this work have been seen in some other purple bacterial species. In one work on the BChl dimer-containing B820 subunit of the LH1 complex from another purple bacteria *R. rubrum G9* [67], beating frequencies of 345, 416, 546, and 735 cm^{-1} were observed in the rephasing 2DES at the main diagonal peak at (820, 820) nm, as well as at the off-diagonal peaks at (830, 810) nm and (810, 830) nm; these beating frequencies were assigned to vibronic coherences after assuming the disorder in site energies of two BChl molecules in the B820 subunit, though a later study [68] suggested that the observed coherences were not unique in B820 subunit but were Franck-Condon active vibrational modes of the BChl monomer. In another 2DES work, coherences at 110 and 190 cm^{-1} were resolved in the LH1 complex from *Thermochromatium tepidum* [43]. Earlier studies on the LH2 complex in *R. sphaeroides* [41, 42] found the existence of coherence around 750 cm^{-1}, the frequency close to the energy gap between two major electronic states in the LH2 complex, B800 and B850; this observed coherence was considered a vibrational mode that could assist the energy transport between B800 and B850 [69, 70]. A recent study on the LH2 complex [64] further suggests that B800 and B850 states were coupled to distinct pools of vibrational modes.

The ultimate question here is whether our observed beating patterns in LH1 membranes from *R. sphaeroides* were purely vibrational coherences originated from ground-state BChl molecules, on the LH1 excitonic states, or vibronic coherences due to strong coupling of certain excitonic states to nuclear motions. The DHO model with one vibrational mode used in this work partially explained the observed coherences. Discrepancies between the DHO model and our coherence analysis, especially the coherences on B810/B830 states in nonrephasing beating maps, could result from the fact that these coherences were of vibronic

origins, or that there were multiple vibrational modes coupled to the electronic transitions to higher-lying excited states, or that multiple coherent pathways were opened through multi-vibrational-mode couplings [71].

5.4 Vibronic Coherences in LH1 Complex as Evolutionary Knobs for Light Harvesting within Purple Bacteria

In summary, we have conducted a detailed study on coherences observed in LH1-only membranes from Rhodobacter sphaeroides with simultaneous Fourier analysis on the rephasing and nonrephasing 2DES experiments. We have extracted cell membranes from a mutant expressing only the LH1 complex as its sole light harvesting protein. We have simultaneously analyzed rephasing and nonrephasing 2DES data and generated coherence beating maps that contain abundant information on detailed electronic structures of LH1-only membranes. Vibrational coherences on the B875 exciton state and vibronic coherences on B810/B830 higher-lying excitonic states are assigned. These assignments are nevertheless subject to challenges, given the complexity of overall electronic structures of LH1 complexes. Future research efforts, such as conducting 2DES experiments across other mutants, under different excitation laser spectra [72], or incorporating more sophisticated theoretical models like a DHO model with multiple vibrational modes, are expected to provide a more comprehensive understanding on the energy landscape of the excited states in bacterial light harvesting. Lastly, we conjecture that the existence of a dense, broad manifold of excitonic states within the LH1 complex, combined with the observed vibronic couplings and vibrational network in this research work, may facilitate the overall light harvesting process by creating vastly accessible channels through which excitation energy flows.

5.5 Supplementary Details

5.5.1 Linear Absorption Spectra from UV-Vis Measurement and Frenkel Exciton Model

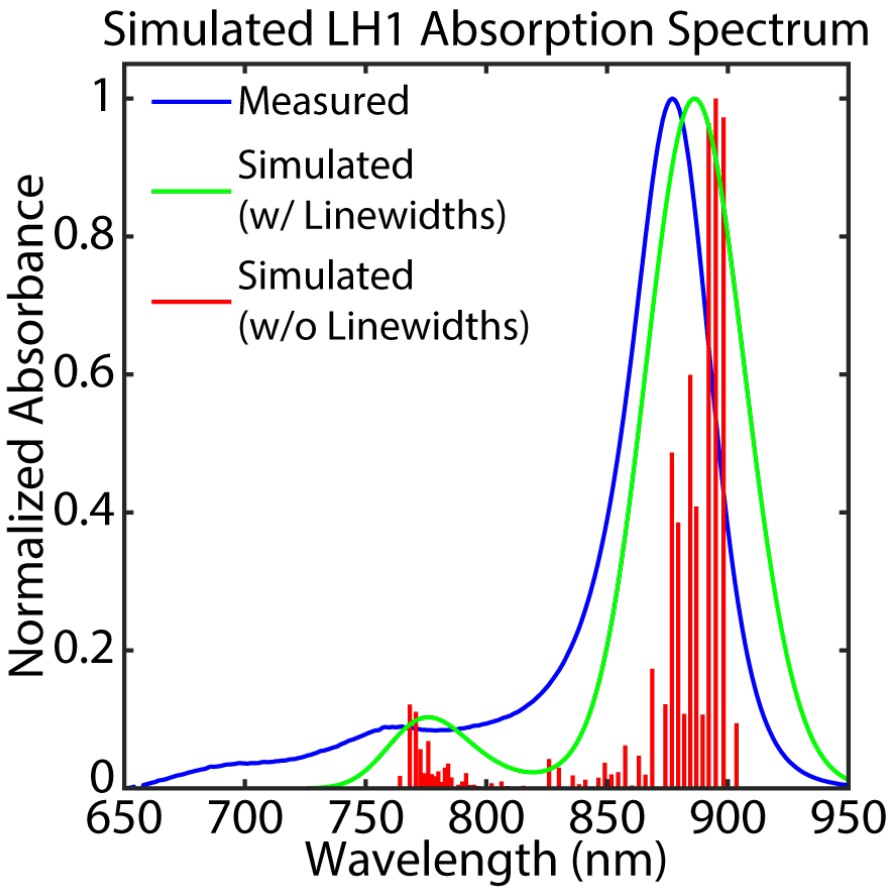

Figure 5.11: Linear absorption spectra of LH1-only membranes from the UV-Vis measurement (blue curve) and from simulation results of the Frenkel exciton model without (red sticks) and with (green curve) homogeneous linewidths.

5.5.2 Details on the Frenkel Exciton Modeling of LH1 Complex

Excitonic states of LH1 were simulated to aid the analysis of our 2DES results. A Frenkel exciton model was used, including the Q_y, Q_x, Soret (B_y, and B_x) bands of bacteriochlorophyll a (BChl) molecules as well as the first four S_0-S_2 vibronic transitions of carotenoid (Car) molecules, to simulate the excitonic states of LH1; the dipole moments, transition energies, and the orientations of transition dipoles of these site transitions are selected and empirically fitted to match the experimental linear absorption spectrum at room temperature [73, 74]. Rather than adopting a ring-shaped arrangement of 32 BChl molecules as that in our previous study, we chose an S-shaped arrangement of 56 BChl molecules identified in the electron microscope images of LH1 complexes [6]. As a second major change from our previous model, dipolar couplings between BChl (Q and Soret bands) and Car (S_0-S_2 bands) molecules were included based on the evidence that these couplings resulted in the non-conservative Q_y CD signal [74]. Due to the limited resolution from the EM images, 28 Car molecules were inserted into the LH1 complex by using their relative positions and orientations with respect to the β-BChl molecules in the crystal structure of LH2 complex of *Rhodopseudomonas acidophila* as a proxy [2].

To account for local fluctuations of the protein environment, we used the established LH1 model Hamiltonian and added site disorders *a posteriori* as Gaussian distributions around the site transition energies. The site inhomogeneous disorders were set at 230 cm^{-1}, 316 cm^{-1}, 502 cm^{-1}, 476 cm^{-1}, and 339 cm^{-1} for BChl (Q_y, Q_x, B_y, B_x) and Car (S_0-S_2) bands, respectively. A total of 3,000 Hamiltonians was realized to reflect the nature of inhomogeneous ensemble of LH1 complexes in the condensed phase.

Table 5.1: Calculated result of the 56 lowest excitonic state (BChl Q_y band) energies (in both wavenumber and wavelength) and their corresponding oscillator strengths of an S-shaped LH1 complex from *R. sphaeroides*. No site inhomogeneous disorders were included.

Eigenstate k	Eigenenergy E_k in nm (cm^{-1})	Norm. Osc. Strength	Eigenstate k	Eigenenergy E_k in nm (cm^{-1})	Norm. Osc. Strength
1	877.1 (11401)	0.27	29	806.8 (12395)	0.0034
2	876.44 (11410)	0.032	30	806.1 (12405)	0.0016
3	**875.4 (11423)**	**1**	31	805.5 (12414)	0.0014
4	874.2 (11440)	0.0054	32	804.9 (12423)	1.2×10^{-4}
5	873.24 (11452)	0.77	33	804.0 (12438)	0.0028
6	871.7 (11472)	0.054	34	803.1 (12452)	6.6×10^{-4}
7	869.7 (11499)	0.012	35	802.0 (12469)	8.8×10^{-4}
8	868.4 (11515)	7.9×10^{-4}	36	800.8 (12488)	0.0021
9	866.6 (11539)	0.051	37	799.8 (12503)	0.0016
10	864.3 (11570)	0.0080	38	798.5 (12523)	0.0028
11	862.2 (11598)	0.017	39	797.2 (12543)	0.0023
12	860.9 (11615)	0.0016	40	796.4 (12557)	0.0037
13	858.5 (11649)	0.0089	41	795.3 (12573)	1.0×10^{-4}
14	856.0 (11682)	3.9×10^{-4}	42	794.2 (12591)	0.0020
15	853.9 (11711)	0.0093	43	793.3 (12606)	0.0011
16	852.2 (11735)	1.8×10^{-4}	44	792.5 (12619)	0.0020
17	849.8 (11767)	0.0093	45	791.8 (12630)	0.0011
18	847.2 (11803)	4.7×10^{-4}	46	790.8 (12645)	0.0025
19	845.6 (11826)	0.0021	47	790.1 (12657)	0.0018
20	843.7 (11852)	4.6×10^{-5}	48	789.5 (12666)	0.0025
21	841.4 (11885)	0.0012	49	789.0 (12674)	0.0014
22	839.5 (11911)	0.0020	50	788.5 (12683)	0.0074
23	838.0 (11934)	0.0017	51	788.1 (12688)	0.0048
24	836.4 (11955)	2.4×10^{-5}	52	787.8 (12694)	0.081
25	835.0 (11976)	1.7×10^{-4}	53	787.4 (12700)	0.0018
26	834.0 (11991)	1.5×10^{-4}	54	787.2 (12703)	0.085
27	833.2 (12001)	7.0×10^{-4}	55	787.2 (12704)	0.032
28	832.8 (12007)	3.5×10^{-4}	56	787.0 (12706)	0.023

Table 5.2: Calculated result of the 56 lowest excitonic state (BChl Q_y band) energies (in both wavenumber and wavelength) and their corresponding oscillator strengths of an S-shaped LH1 complex from *R. sphaeroides*. Site inhomogeneous disorders of BChl Q_y, Q_x, B_y, B_x transitions were included. The result was generated from an ensemble of 3000 LH1 complexes.

Eigenstate k	Eigenenergy E_k in nm (cm^{-1})	Norm. Osc. Strength	Eigenstate k	Eigenenergy E_k in nm (cm^{-1})	Norm. Osc. Strength
1	903.6 (11067)	0.095	29	815.3 (12266)	0.0039
2	898.3 (11132)	0.97	30	811.3 (12326)	0.0022
3	**894.96 (11174)**	**1**	31	808.6 (12367)	0.0036
4	892.1 (11209)	0.96	32	806.2 (12403)	0.010
5	889.5 (11242)	0.11	33	804.1 (12436)	7.8×10^{-4}
6	887.0 (11274)	0.41	34	802.2 (12466)	0.0073
7	884.5 (11306)	0.60	35	800.2 (12496)	0.0013
8	882.0 (11338)	0.11	36	798.4 (12525)	0.0032
9	879.4 (11371)	0.39	37	796.6 (12553)	0.0035
10	876.8 (11405)	0.49	38	794.9 (12580)	0.0054
11	874.1 (11440)	0.12	39	793.2 (12607)	0.0049
12	871.5 (11475)	1.3×10^{-4}	40	791.6 (12633)	0.022
13	868.7 (11512)	0.17	41	790.1 (12657)	0.010
14	865.9 (11549)	0.020	42	788.5 (12682)	0.0053
15	863.1 (11586)	0.048	43	787.0 (12707)	0.0031
16	860.3 (11624)	0.0041	44	785.6 (12730)	0.016
17	857.5 (11662)	0.062	45	784.2 (12752)	0.036
18	854.6 (11701)	0.024	46	782.8 (12775)	0.030
19	851.8 (11740)	0.020	47	781.4 (12797)	0.0091
20	849.1 (11777)	0.037	48	780.1 (12819)	0.025
21	846.4 (11815)	0.016	49	778.7 (12841)	0.018
22	843.7 (11853)	0.0024	50	777.3 (12864)	0.021
23	841.0 (11891)	0.013	51	775.9 (12888)	0.069
24	838.4 (11928)	0.0061	52	774.4 (12913)	0.022
25	835.8 (11965)	0.019	53	772.7 (12941)	0.057
26	833.0 (12005)	0.0025	54	770.8 (12973)	0.11
27	830.0 (12048)	0.030	55	768.3 (13016)	0.12
28	826.0 (12106)	0.043	56	764.2 (13085)	0.018

To facilitate the interpretation of the observed beating results, we first resorted to the Frenkel exciton model of a single LH1 complex, i.e. with no static or dynamic disorder induced due to the fluctuation of the protein environment. As seen from the simulated LH1 Hamiltonian results from Table 5.1, the strongest peak was located at 875.4 nm (11 423 cm^{-1}), closer to the position of the commonly known B875 absorption peak in the LH1 complex from *Rhodobacter sphaeroides*.

Upon closer scrutiny, there were two main discrepancies between the simulated excitonic states and the experimental 2DES results of LH1 complexes in our no-disorder Frenkel exciton model: the energy mismatch between the lowest-energy state in the simulation and the broad stimulated emission feature in the 2DES, as well as a red shift of the upper BChl Q_y band. First, the state with the lowest energy was located at 877.1 nm (11 401 cm^{-1}), compared to 880 nm (11 364cm^{-1}) for the observed stimulated emission features of LH1 complexes in the 2DES. Second, the peak positions of the highest-energy state associated with BChl Q_y transitions were mismatched between the simulated and the measured absorption spectrum.

Two possible assumptions exist to explain these observed discrepancies. The first assumption is that, the absence of static disorders in the model has led to an overestimation of the homogeneous linewidth of BChl Q_y band during the Hamiltonian fitting process. In other words, spectral broadening of the absorption peak at 875 nm seen in the measured UV-Visible spectrum was largely due to both homogeneous broadening and the excitonic energy splitting within the lower-energy BChl Q_y band. To compensate for this discrepancy, we generated a separate simulated absorption spectrum averaged over 3,000 LH1 complexes with normally distributed site inhomogeneous disorders (Figure 5.11 and Table 5.2). A major improvement from including static disorders in the Frenkel exciton model can be seen by the red-shifting of lower-energy BChl Q_y band, in agreement with the observation of the B896 band, the lowest excitonic state assigned to the LH1 complex, in spectral hole-burning experiments [75].

The second assumption is that the lack of excitonic/vibronic couplings in the model LH1 Hamiltonian has diminished the energy splitting between the lower- and higher-energy BChl Q_y bands in the LH1 complexes. From a two-level system, we know that the energy splitting between the lower- and the higher-energy eigenstates after mixing will increase as the coupling between two levels increases. Following a similar logic, we can argue that the energy splitting between lower- and higher-energy BChl Q_y bands can be increased by introducing more couplings among all possible site transitions on BChl molecules in the LH1 complex, thus pushing the lower-energy BChl Q_y band toward the longer-wavelength side of the spectrum.

5.5.3 Summary on Two-Dimensional Electronic Spectroscopy (2DES)

2DES is a third-order technique that involves three ultrafast laser pulses, each delayed by a time interval, interacting with a sample in a time-sequential fashion. After the first pulse interacts with the sample, the system is promoted to a coherence between the ground and electronic excited state and starts evolving a time-dependent phase related to the energy gap between ground and the electronic excited state until the second pulse arrives at the sample after a time delay (coherence time, τ). The system is let to evolve for another time delay (waiting time, T), during which excited-state dynamics of the sample can be probed, before the third pulses interacts with the sample. Afterwards, the system is put to another coherence between two electronic states. The 2DES signal emerges from the sample as a function of the time elapsed after the interaction with the third pulse (detection time, t; it was also referred to as the "rephasing time" in early 2DES works) and is detected at a specific phase-matching direction. Spectral data from a 2DES experiment elucidates excited-state dynamics by correlating the excitation and detection energy at different delay time.

Depending on the relative phase evolution during coherence time and detection time, 2DES signals can be categorized into two types. A rephasing 2DES signal occurs when

the phase evolves with opposite signs between the two time delays, which means the phase acquired by the system during these delays is subtractive. A rephasing signal becomes the largest when the phase evolution during the detection time fully cancels out that during the coherence time. For a nonrephasing signal, on the other hand, the phase evolves with the same signs during the two time delays; that is, the phase acquired by the system is accumulative rather than subtractive. The strength of a nonrephasing signal, therefore, follows the behavior of a free-induction decay: it peaks right when the third pulse interacts with the sample and exponentially decays to an asymptotic zero.

5.5.4 *Experimental Setup of Gradient-Assisted Photon Echo Spectroscopy (GRAPES)*

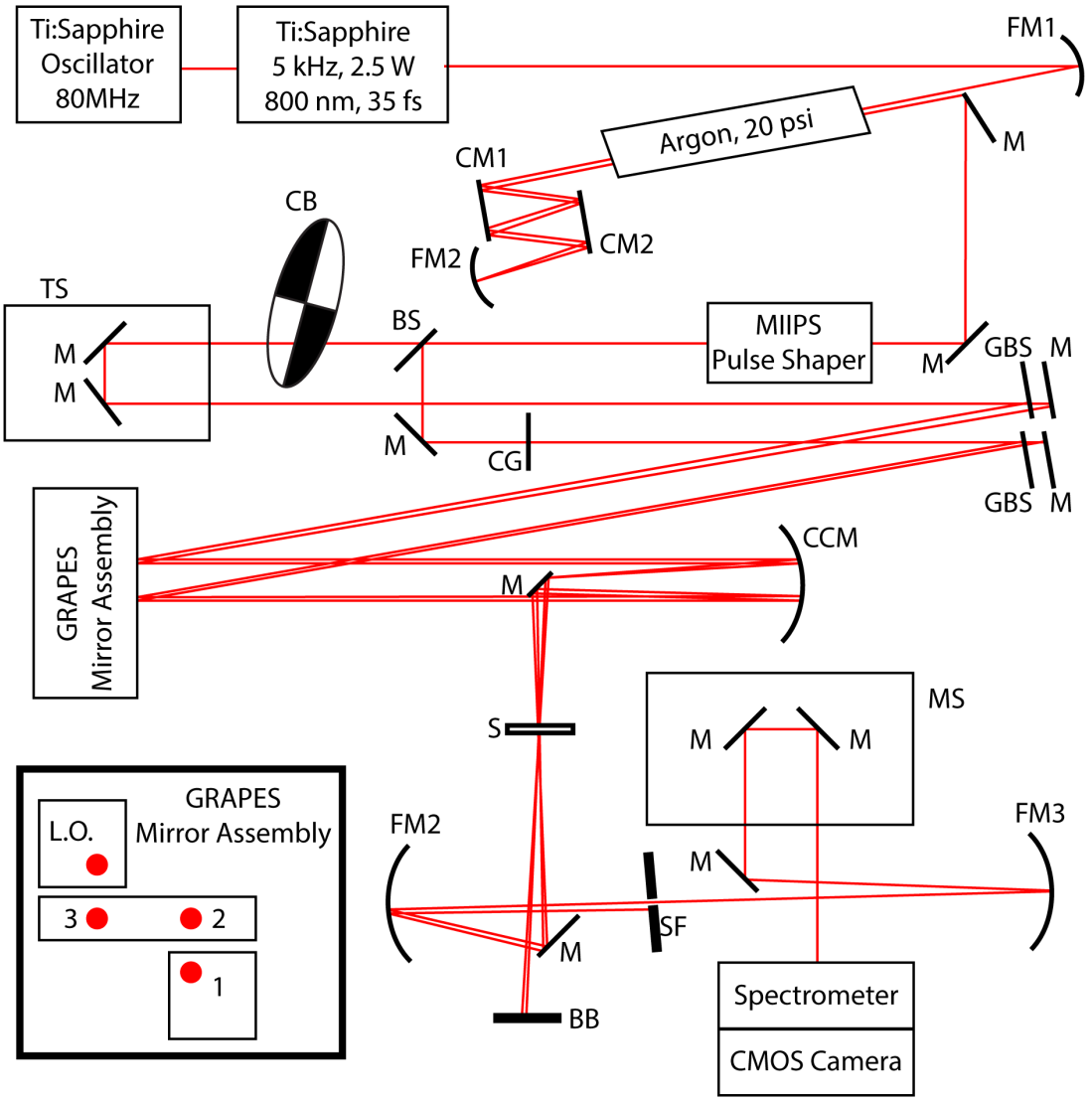

Figure 5.12: Schematic of GRAPES experimental setup. Red lines indicate the beam paths from the Ti:sapphire regenerative amplifier laser source to the CMOS camera detector. Abbreviations used in the schematic correspond to the following parts: M: flat mirrors; FM1, FM2, FM3: concave spherical mirrors; CM1, CM2: chirped mirrors; BS: 50/50 beamsplitter; GBS: 60/40 beamsplitter for GRAPES; CG: 1-mm compensating glass; TS: computer-controlled translational stage; CB: chopper blade; CCM: cylindrical concave mirror; MS: mechanical stage mount; S: sample cell; BB: beam block for beams 1 and 2; SF: spatial filter for beam 3. The setup for GRAPES mirror assembly is drawn as an inset [53].

5.5.5 Procedure for Fitting Exponential Dynamics in the Waiting Time Domain

The 2DES data from our experiment was a function of three variables: excitation wavelength (λ_τ), detection wavelength (λ_t), and waiting time (T). For each (λ_τ, λ_t) pair, we assumed the kinetics in T-domain to be in the form of a multi-exponential decays:

$$S_{2D}(T, \lambda_\tau, \lambda_t) = \sum_{n=1}^{K} A_n(\lambda_\tau, \lambda_t) e^{-b_n(\lambda_\tau, \lambda_t)T} \tag{5.1}$$

To extract the oscillating frequencies of waiting time traces, we chose the number of exponentials to be 3 (i.e., K=3), and added a coefficient A_4 (λ_τ, λ_t) to account for the spontaneous decay lifetime of the excited states that exceeded beyond our experimental time frame. Each time trace in the whole (λ_τ, λ_t) range was fitted independently to the multi-exponential model to obtain a set of decay constants, (b_1, b_2, b_3), followed by averaging each decay constant over the (λ_τ, λ_t) regions where main signals appeared in the 2DES data. The averaged decay constants, ($\bar{b}_1$, $\bar{b}_2$, $\bar{b}_3$), were then set for all time traces in the second multi-exponential fitting process to obtain the (λ_τ, λ_t)-dependent amplitude maps, A_1 (λ_τ, λ_t), A_2 (λ_τ, λ_t), A_3 (λ_τ, λ_t), and A_4 (λ_τ, λ_t). The experimental data was de-trended using the tri-exponential model with fitted parameters, and the resulting residuals were transformed into the frequency domain (ω_T) by Fast Fourier Transform (FFT) algorithm.

5.5.6 *Additional 2DES Coherence Beating Maps of LH1-Only Membranes*

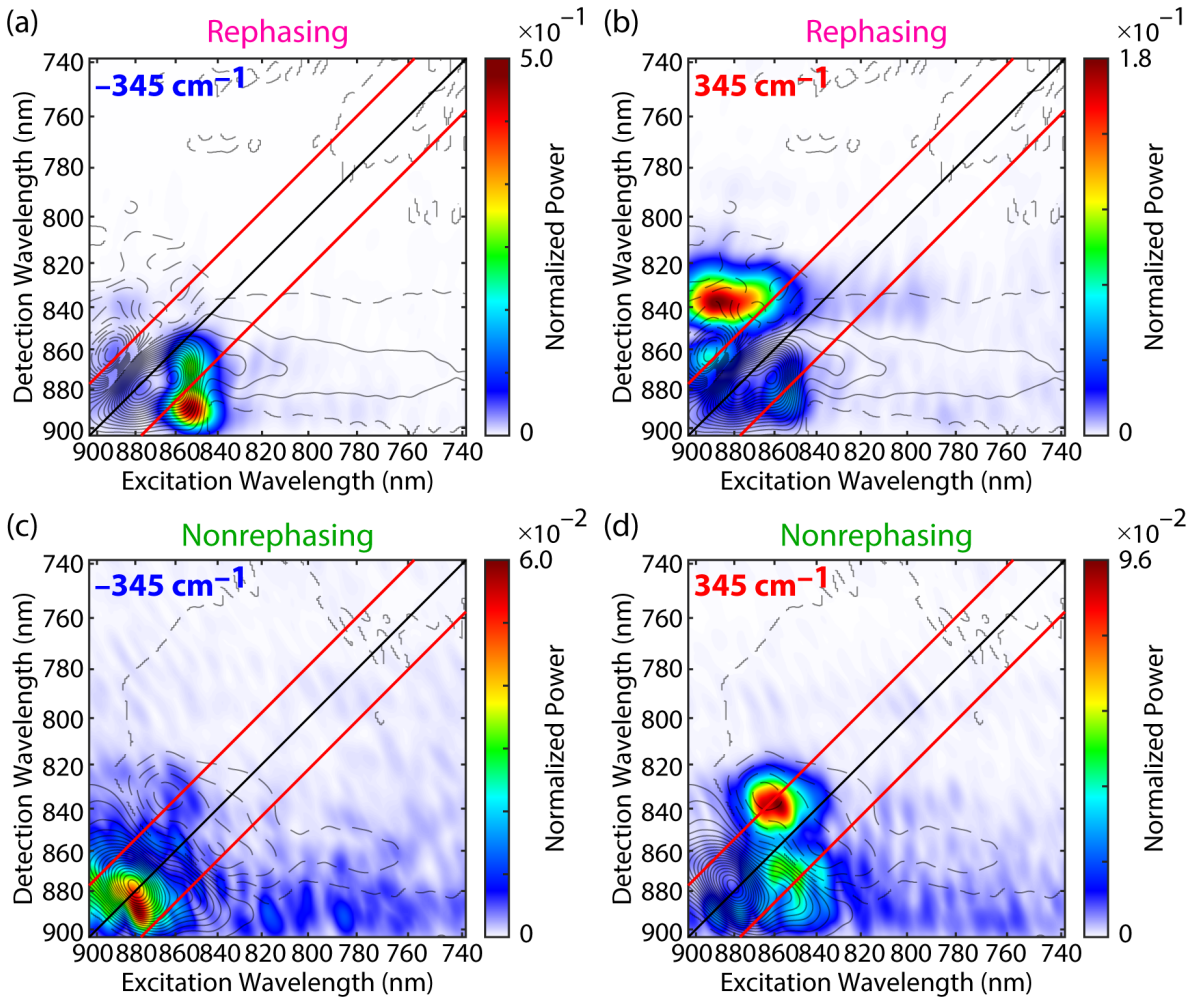

Figure 5.13: Coherence beating maps of LH1-only membranes showing the Fourier transform spectra of residuals from global analysis. Four beating maps are plotted from (a) Rephasing part at the beating frequency $\omega_T = -345$ cm^{-1}; (b) rephasing part at $\omega_T = +345$ cm^{-1}; (c) nonrephasing part at $\omega_T = -345$ cm^{-1}, and (d) nonrephasing part at $\omega_T = +345$ cm^{-1}, respectively. Each beating map is plotted with 500 color-filled contours, on which the corresponding 2DES signal is overlaid as 25 contours. Solid contours indicate positive 2DES signals, whereas dotted contours indicate negative 2DES signals. Red diagonals are drawn to guide the eye for the beating frequency offset from the electronic states.

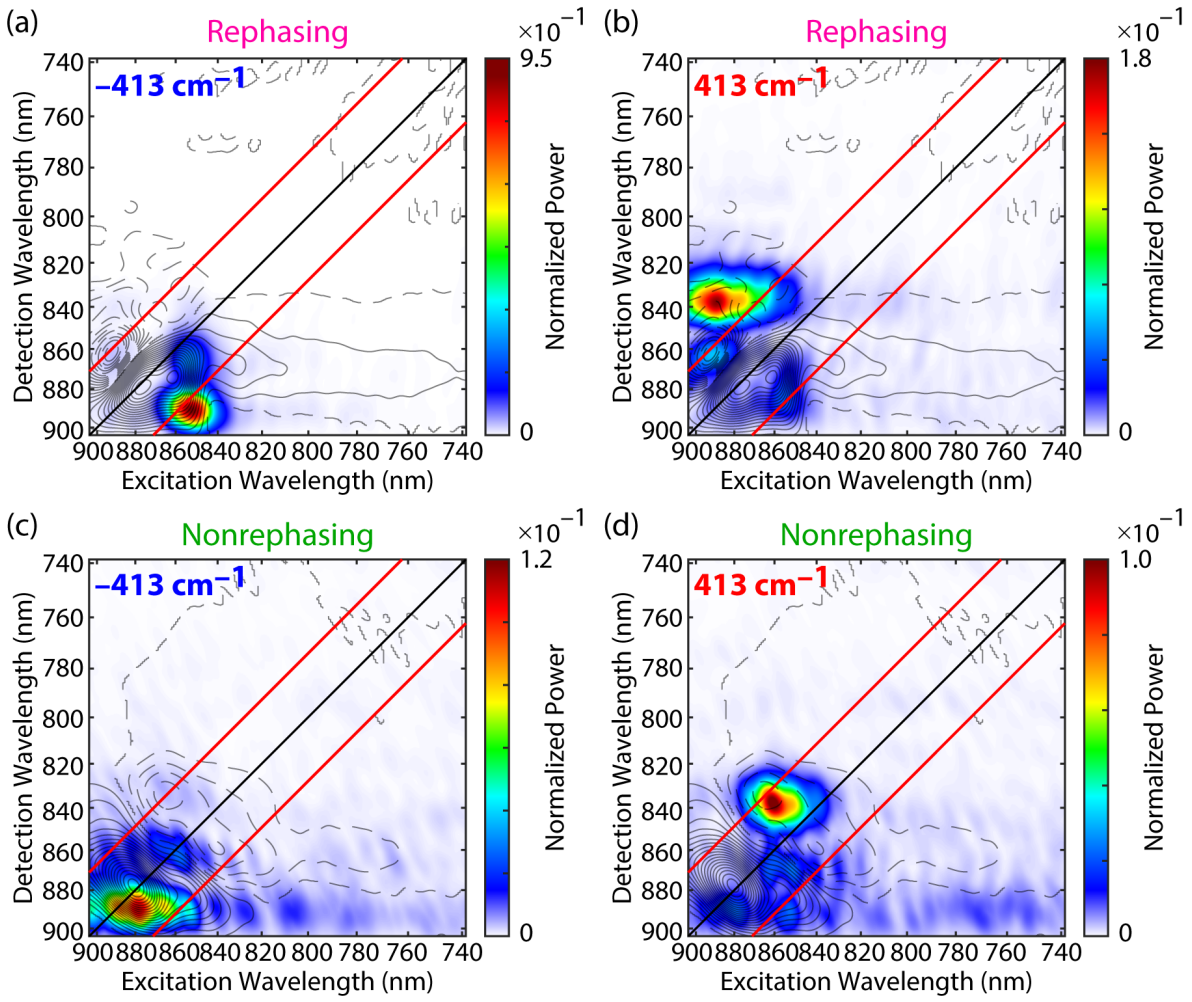

Figure 5.14: Coherence beating maps of LH1-only membranes showing the Fourier transform spectra of residuals from global analysis. Four beating maps are plotted from (a) Rephasing part at the beating frequency $\omega_T = -413$ cm^{-1}; (b) rephasing part at $\omega_T = +413$ cm^{-1}; (c) nonrephasing part at $\omega_T = -413$ cm^{-1}, and (d) nonrephasing part at $\omega_T = +413$ cm^{-1}, respectively. Each beating map is plotted with 500 color-filled contours, on which the corresponding 2DES signal is overlaid as 25 contours. Solid contours indicate positive 2DES signals, whereas dotted contours indicate negative 2DES signals. Red diagonals are drawn to guide the eye for the beating frequency offset from the electronic states.

5.5.7 *Integrated Power Spectra of Coherence Beating Maps Over All Excitation Wavelengths*

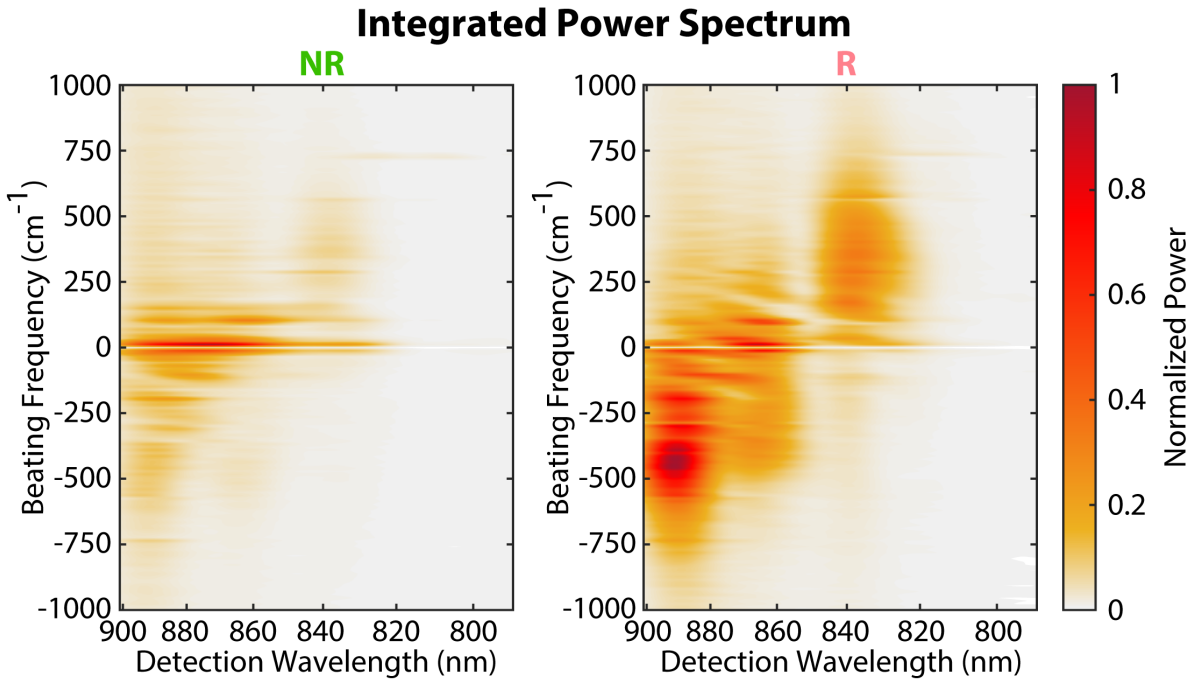

Figure 5.15: Integrated power spectra of coherence beating maps over all excitation wavelengths of (a) nonrephasing and (b) rephasing 2DES beating maps of LH1-only membranes.

REFERENCES

[1] Juergen Koepke, Xiche Hu, Cornelia Muenke, Klaus Schulten, and Hartmut Michel. The crystal structure of the light-harvesting complex II (B800-850) from *Rhodospirillum molischianum*. *Structure*, 4(5):581–597, 1996.

[2] S. M. Prince, M. Z. Papiz, A. A. Freer, G. McDermott, A. M. Hawthornthwaite-Lawless, R. J. Cogdell, and N. W. Isaacs. Apoprotein structure in the LH2 complex from Rhodopseudomonas acidophila strain 10050: modular assembly and protein pigment interactions. *Journal of Molecular Biology*, 268(2):412–423, 1997.

[3] Miroslav Z. Papiz, Steve M. Prince, Tina Howard, Richard J. Cogdell, and Neil W. Isaacs. The Structure and Thermal Motion of the B800-850 LH2 Complex from Rps.acidophila at 2.0Å Resolution and 100K: New Structural Features and Functionally Relevant Motions. *Journal of Molecular Biology*, 326(5):1523–1538, 2003.

[4] Aleksander W. Roszak, Tina D. Howard, June Southall, Alastair T. Gardiner, Christopher J. Law, Neil W. Isaacs, and Richard J. Cogdell. Crystal Structure of the RC-LH1 Core Complex from Rhodopseudomonas palustris. *Science*, 302(5652):1969–1972, 2003.

[5] Vadim Cherezov, Jeffrey Clogston, Miroslav Z. Papiz, and Martin Caffrey. Room to Move: Crystallizing Membrane Proteins in Swollen Lipidic Mesophases. *Journal of Molecular Biology*, 357(5):1605–1618, 2006.

[6] Pu Qian, Miroslav Z. Papiz, Philip J. Jackson, Amanda A. Brindley, Irene W. Ng, John D. Olsen, Mark J. Dickman, Per A. Bullough, and C. Neil Hunter. Three-Dimensional Structure of the *Rhodobacter sphaeroides* RC-LH1-PufX Complex: Dimerization and Quinone Channels Promoted by PufX. *Biochemistry*, 52(43):7575–7585, 2013.

[7] Satomi Niwa, Long-Jiang Yu, Kazuki Takeda, Yu Hirano, Tomoaki Kawakami, Zheng-Yu

Wang-Otomo, and Kunio Miki. Structure of the LH1–RC complex from Thermochromatium tepidum at 3.0 å. *Nature*, 508(7495):228–232, 2014.

[8] Long-Jiang Yu, Michihiro Suga, Zheng-Yu Wang-Otomo, and Jian-Ren Shen. Structure of photosynthetic LH1-RC supercomplex at 1.9 å resolution. *Nature*, 556(7700):209–213, 2018.

[9] Pu Qian, C. Alistair Siebert, Peiyi Wang, Daniel P. Canniffe, and C. Neil Hunter. Cryo-EM structure of the Blastochloris viridis LH1-RC complex at 2.9 å. *Nature*, 556 (7700):203–208, 2018.

[10] Kazutoshi Tani, Ryo Kanno, Yuki Makino, Malgorzata Hall, Mizuki Takenouchi, Michie Imanishi, Long-Jiang Yu, Jörg Overmann, Michael T. Madigan, Yukihiro Kimura, Akira Mizoguchi, Bruno M. Humbel, and Zheng-Yu Wang-Otomo. Cryo-EM structure of a Ca^{2+}-bound photosynthetic LH1-RC complex containing multiple $\alpha\beta$-polypeptides. *Nature Communications*, 11(1):4955, 2020.

[11] David J. K. Swainsbury, Pu Qian, Philip J. Jackson, Kaitlyn M. Faries, Dariusz M. Niedzwiedzki, Elizabeth C. Martin, David A. Farmer, Lorna A. Malone, Rebecca F. Thompson, Neil A. Ranson, Daniel P. Canniffe, Mark J. Dickman, Dewey Holten, Christine Kirmaier, Andrew Hitchcock, and C. Neil Hunter. Structures of *Rhodopseudomonas palustris* RC-LH1 complexes with open or closed quinone channels. *Science Advances*, 7 (3):eabe2631, 2021.

[12] Tomoaki Kawakami, Long-Jiang Yu, Tai Liang, Koudai Okazaki, Michael T. Madigan, Yukihiro Kimura, and Zheng-Yu Wang-Otomo. Crystal structure of a photosynthetic LH1-RC in complex with its electron donor HiPIP. *Nature Communications*, 12(1):1104, 2021.

[13] A. G. Redfield. On the theory of relaxation processes. *IBM Journal of Research and Development*, 1(1):19–31, 1957.

[14] A.G. Redfield. The Theory of Relaxation Processes. In *Advances in Magnetic and Optical Resonance*, volume 1, pages 1–32. Elsevier, 1965.

[15] Gregory S. Engel, Tessa R. Calhoun, Elizabeth L. Read, Tae-Kyu Ahn, Tomáš Mančal, Yuan-Chung Cheng, Robert E. Blankenship, and Graham R. Fleming. Evidence for wavelike energy transfer through quantum coherence in photosynthetic systems. *Nature*, 446(7137):782–786, 2007.

[16] G. Panitchayangkoon, D. Hayes, K. A. Fransted, J. R. Caram, E. Harel, J. Wen, R. E. Blankenship, and G. S. Engel. Long-lived quantum coherence in photosynthetic complexes at physiological temperature. *Proceedings of the National Academy of Sciences*, 107(29): 12766–12770, 2010.

[17] Gregory D. Scholes, Graham R. Fleming, Lin X. Chen, Alán Aspuru-Guzik, Andreas Buchleitner, David F. Coker, Gregory S. Engel, Rienk van Grondelle, Akihito Ishizaki, David M. Jonas, Jeff S. Lundeen, James K. McCusker, Shaul Mukamel, Jennifer P. Ogilvie, Alexandra Olaya-Castro, Mark A. Ratner, Frank C. Spano, K. Birgitta Whaley, and Xiaoyang Zhu. Using coherence to enhance function in chemical and biophysical systems. *Nature*, 543(7647):647–656, 2017.

[18] Elisabet Romero, Javier Prior, Alex W. Chin, Sarah E. Morgan, Vladimir I. Novoderezhkin, Martin B. Plenio, and Rienk van Grondelle. Quantum coherent dynamics in photosynthetic charge separation revealed by wavelet analysis. *Scientific Reports*, 7 (2890):1–7, 2017.

[19] Lili Wang, Marco A. Allodi, and Gregory S. Engel. Quantum coherences reveal excited-state dynamics in biophysical systems. *Nature Reviews Chemistry*, 3(8):477–490, 2019.

[20] V. P. Singh, M. Westberg, C. Wang, P. D. Dahlberg, T. Gellen, A. T. Gardiner, R. J. Cogdell, and G. S. Engel. Towards quantification of vibronic coupling in photosynthetic antenna complexes. *The Journal of Chemical Physics*, 142(21):212446, 2015.

[21] Jacob S. Higgins, Lawson T. Lloyd, Sara H. Sohail, Marco A. Allodi, John P. Otto, Rafael G. Saer, Ryan E. Wood, Sara C. Massey, Po-Chieh Ting, Robert E. Blankenship, and Gregory S. Engel. Photosynthesis tunes quantum-mechanical mixing of electronic and vibrational states to steer exciton energy transfer. *Proceedings of the National Academy of Sciences*, 118(11):e2018240118, 2021.

[22] James Lim, David Paleček, Felipe Caycedo-Soler, Craig N. Lincoln, Javier Prior, Hans von Berlepsch, Susana F. Huelga, Martin B. Plenio, Donatas Zigmantas, and Jürgen Hauer. Vibronic origin of long-lived coherence in an artificial molecular light harvester. *Nature Communications*, 6(7755):1–7, 2015.

[23] Lili Wang, Graham B. Griffin, Alice Zhang, Feng Zhai, Nicholas E. Williams, Richard F. Jordan, and Gregory S. Engel. Controlling quantum-beating signals in 2D electronic spectra by packing synthetic heterodimers on single-walled carbon nanotubes. *Nature Chemistry*, 9(3):219–225, 2017.

[24] Adrian F. Morrison and John M. Herbert. Evidence for Singlet Fission Driven by Vibronic Coherence in Crystalline Tetracene. *The Journal of Physical Chemistry Letters*, 8(7):1442–1448, 2017.

[25] Wei Zhao, Zhengyuan Qin, Chunfeng Zhang, Guodong Wang, Xingcan Dai, and Min Xiao. Coherent exciton-phonon coupling in perovskite semiconductor nanocrystals studied by two-dimensional electronic spectroscopy. *Applied Physics Letters*, 115(24):243101, 2019.

[26] Andrea Volpato, Mirco Zerbetto, Luca Bolzonello, Elena Meneghin, Barbara Fresch, Tiziana Benelli, Loris Giorgini, and Elisabetta Collini. Effect of Different Conformational

Distributions on the Ultrafast Coherence Dynamics in Porphyrin-Based Polymers. *The Journal of Physical Chemistry C*, 123(16):10212–10224, 2019.

[27] Jonathan D. Schultz, Adam F. Coleman, Aritra Mandal, Jae Yoon Shin, Mark A. Ratner, Ryan M. Young, and Michael R. Wasielewski. Steric Interactions Impact Vibronic and Vibrational Coherences in Perylenediimide Cyclophanes. *The Journal of Physical Chemistry Letters*, 10(23):7498–7504, 2019.

[28] Sara H. Sohail, John P. Otto, Paul D. Cunningham, Young C. Kim, Ryan E. Wood, Marco A. Allodi, Jacob S. Higgins, Joseph S. Melinger, and Gregory S. Engel. DNA scaffold supports long-lived vibronic coherence in an indodicarbocyanine (Cy5) dimer. *Chemical Science*, 11(32):8546–8557, 2020.

[29] Jonathan D. Schultz, Jae Yoon Shin, Michelle Chen, James P. O'Connor, Ryan M. Young, Mark A. Ratner, and Michael R. Wasielewski. Influence of Vibronic Coupling on Ultrafast Singlet Fission in a Linear Terrylenediimide Dimer. *Journal of the American Chemical Society*, 143(4):2049–2058, 2021.

[30] Roberta Moca, Stephen R. Meech, and Ismael A. Heisler. Two-Dimensional Electronic Spectroscopy of Chlorophyll a: Solvent Dependent Spectral Evolution. *The Journal of Physical Chemistry B*, 119(27):8623–8630, 2015.

[31] Elena Meneghin, Cristina Leonardo, Andrea Volpato, Luca Bolzonello, and Elisabetta Collini. Mechanistic insight into internal conversion process within Q-bands of chlorophyll a. *Scientific Reports*, 7(11389):1–7, 2017.

[32] Elisa Fresch and Elisabetta Collini. Relaxation Dynamics of Chlorophyll b in the Sub-ps Ultrafast Timescale Measured by 2D Electronic Spectroscopy. *International Journal of Molecular Sciences*, 21(8):2836, 2020.

[33] Eglė Bukartė, Anja Haufe, David Paleček, Claudia Büchel, and Donatas Zigmantas. Revealing vibronic coupling in chlorophyll c1 by polarization-controlled 2D electronic spectroscopy. *Chemical Physics*, 530:110643, 2020.

[34] Shuai Yue. Coupling of multi-vibrational modes in bacteriochlorophyll a in solution observed with 2D electronic spectroscopy. *Chemical Physics Letters*, 683:591–597, 2017.

[35] Veronica R. Policht, Andrew Niedringhaus, and Jennifer P. Ogilvie. Characterization of Vibrational Coherence in Monomeric Bacteriochlorophyll a by Two-Dimensional Electronic Spectroscopy. *The Journal of Physical Chemistry Letters*, 9(22):6631–6637, 2018.

[36] Elena Meneghin, Danilo Pedron, and Elisabetta Collini. Characterization of the coherent dynamics of bacteriochlorophyll a in solution. *Chemical Physics*, 519:85–91, 2019.

[37] JunWoo Kim, Jonggu Jeon, Tai Hyun Yoon, and Minhaeng Cho. Two-dimensional electronic spectroscopy of bacteriochlorophyll a with synchronized dual mode-locked lasers. *Nature Communications*, 11(6029):1–10, 2020.

[38] Shawn Irgen-Gioro, Karthik Gururangan, Rafael G. Saer, Robert E. Blankenship, and Elad Harel. Electronic coherence lifetimes of the Fenna–Matthews–Olson complex and light harvesting complex II. *Chemical Science*, 10(45):10503–10509, 2019.

[39] Daniel B. Turner, Krystyna E. Wilk, Paul M. G. Curmi, and Gregory D. Scholes. Comparison of Electronic and Vibrational Coherence Measured by Two-Dimensional Electronic Spectroscopy. *The Journal of Physical Chemistry Letters*, 2(15):1904–1911, 2011.

[40] Daniel B. Turner, Rayomond Dinshaw, Kyung-Koo Lee, Michael S. Belsley, Krystyna E. Wilk, Paul M. G. Curmi, and Gregory D. Scholes. Quantitative investigations of quantum

coherence for a light-harvesting protein at conditions simulating photosynthesis. *Physical Chemistry Chemical Physics*, (14):4857–4874, 2012.

[41] Elad Harel and Gregory S. Engel. Quantum coherence spectroscopy reveals complex dynamics in bacterial light-harvesting complex 2 (LH2). *Proceedings of the National Academy of Sciences*, 109(3):706–711, 2012.

[42] Andrew F. Fidler, Ved P. Singh, Phillip D. Long, Peter D. Dahlberg, and Gregory S. Engel. Time Scales of Coherent Dynamics in the Light-Harvesting Complex 2 (LH2) of *Rhodobacter sphaeroides*. *The Journal of Physical Chemistry Letters*, 4(9):1404–1409, 2013.

[43] Fei Ma, Long-Jiang Yu, Ruud Hendrikx, Zheng-Yu Wang-Otomo, and Rienk van Grondelle. Excitonic and Vibrational Coherence in the Excitation Relaxation Process of Two LH1 Complexes as Revealed by Two-Dimensional Electronic Spectroscopy. *The Journal of Physical Chemistry Letters*, 8(12):2751–2756, 2017.

[44] David Paleček, Petra Edlund, Sebastian Westenhoff, and Donatas Zigmantas. Quantum coherence as a witness of vibronically hot energy transfer in bacterial reaction center. *Science Advances*, 3(9):e1603141, 2017.

[45] Fei Ma, Elisabet Romero, Michael R. Jones, Vladimir I. Novoderezhkin, and Rienk van Grondelle. Vibronic Coherence in the Charge Separation Process of the *Rhodobacter sphaeroides* Reaction Center. *The Journal of Physical Chemistry Letters*, 9(8):1827–1832, 2018.

[46] Fei Ma, Elisabet Romero, Michael R. Jones, Vladimir I. Novoderezhkin, and Rienk van Grondelle. Both electronic and vibrational coherences are involved in primary electron transfer in bacterial reaction center. *Nature Communications*, 10(933):1–9, 2019.

[47] Franklin D. Fuller, Jie Pan, Andrius Gelzinis, Vytautas Butkus, S. Seckin Senlik, Daniel E. Wilcox, Charles F. Yocum, Leonas Valkunas, Darius Abramavicius, and Jennifer P. Ogilvie. Vibronic coherence in oxygenic photosynthesis. *Nature Chemistry*, 6 (8):706–711, 2014.

[48] Elisabet Romero, Ramunas Augulis, Vladimir I. Novoderezhkin, Marco Ferretti, Jos Thieme, Donatas Zigmantas, and Rienk van Grondelle. Quantum coherence in photosynthesis for efficient solar-energy conversion. *Nature Physics*, 10(9):676–682, 2014.

[49] Justin R. Caram, Andrew F. Fidler, and Gregory S. Engel. Excited and ground state vibrational dynamics revealed by two-dimensional electronic spectroscopy. *The Journal of Chemical Physics*, 137(2):024507, 2012.

[50] Yin Song, Christoph Hellmann, Natalie Stingelin, and Gregory D. Scholes. The separation of vibrational coherence from ground- and excited-electronic states in P3HT film. *The Journal of Chemical Physics*, 142(21):212410, 2015.

[51] Peter D. Dahlberg, Po-Chieh Ting, Sara C. Massey, Elizabeth C. Martin, C. Neil Hunter, and Gregory S. Engel. Electronic Structure and Dynamics of Higher-Lying Excited States in Light Harvesting Complex 1 from *Rhodobacter sphaeroides*. *The Journal of Physical Chemistry A*, 120(24):4124–4130, 2016.

[52] Elad Harel, Andrew F. Fidler, and Gregory S. Engel. Real-time mapping of electronic structure with single-shot two-dimensional electronic spectroscopy. *Proceedings of the National Academy of Sciences*, 107(38):16444–16447, 2010.

[53] Elad Harel, Andrew F. Fidler, and Gregory S. Engel. Single-Shot Gradient-Assisted Photon Echo Electronic Spectroscopy. *The Journal of Physical Chemistry A*, 115(16): 3787–3796, 2011.

[54] Sara C. Massey, Po-Chieh Ting, Shu-Hao Yeh, Peter D. Dahlberg, Sara H. Sohail, Marco A. Allodi, Elizabeth C. Martin, Sabre Kais, Christopher Neil Hunter, and Gregory S. Engel. Orientational Dynamics of Transition Dipoles and Exciton Relaxation in LH2 from Ultrafast Two-Dimensional Anisotropy. *The Journal of Physical Chemistry Letters*, 10(2):270–277, 2019.

[55] Sarah M. Gallagher, Allison W. Albrecht, John D. Hybl, Brett L. Landin, Bhavani Rajaram, and David M. Jonas. Heterodyne detection of the complete electric field of femtosecond four-wave mixing signals. *Journal of the Optical Society of America B*, 15 (8):2338–2345, 1998.

[56] John D. Hybl, Allison W. Albrecht, Sarah M. Gallagher Faeder, and David M. Jonas. Two-dimensional electronic spectroscopy. *Chemical Physics Letters*, 297(3-4):307–313, 1998.

[57] John D. Hybl, Allison Albrecht Ferro, and David M. Jonas. Two-dimensional fourier transform electronic spectroscopy. *The Journal of Chemical Physics*, 115(14):6606–6622, 2001.

[58] Tobias Brixner, Tomáš Mančal, Igor V. Stiopkin, and Graham R. Fleming. Phase-stabilized two-dimensional electronic spectroscopy. *The Journal of Chemical Physics*, 121(9):4221–4236, 2004.

[59] Peter D. Dahlberg, Po-Chieh Ting, Sara C. Massey, Marco A. Allodi, Elizabeth C. Martin, C. Neil Hunter, and Gregory S. Engel. Mapping the ultrafast flow of harvested solar energy in living photosynthetic cells. *Nature Communications*, 8(988):1–7, 2017.

[60] Andrea Volpato, Luca Bolzonello, Elena Meneghin, and Elisabetta Collini. Global analysis of coherence and population dynamics in 2D electronic spectroscopy. *Optics Express*, 24(21):24773, 2016.

[61] Sara H. Sohail, Peter D. Dahlberg, Marco A. Allodi, Sara C. Massey, Po-Chieh Ting, Elizabeth C. Martin, C. Neil Hunter, and Gregory S. Engel. Communication: Broad manifold of excitonic states in light-harvesting complex 1 promotes efficient unidirectional energy transfer *in vivo*. *The Journal of Chemical Physics*, 147(13):131101, 2017.

[62] A. Matitoli, D. G. Sockalingum, Bruno Robert, and Marc Lutz. Application of near-IR Fourier transform resonance Raman spectroscopy to the study of photosynthetic proteins. *Spectrochimica Acta Part A: Molecular Spectroscopy*, 49A(5-6):785–799, 1993.

[63] James R. Diers and David F. Bocian. Qy-Excitation Resonance Raman Spectra of Bacteriochlorophyll Observed under Fluorescence-Free Conditions. Implications for Cofactor Structure in Photosynthetic Proteins. *Journal of the American Chemical Society*, 117(24):6629–6630, 1995.

[64] Shawn Irgen-Gioro, Karthik Gururangan, Austin P. Spencer, and Elad Harel. Non-Uniform Excited State Electronic-Vibrational Coupling of Pigment–Protein Complexes. *The Journal of Physical Chemistry Letters*, 11(24):10388–10395, 2020.

[65] Shaul Mukamel. *Principles of nonlinear optical spectroscopy*. Number 6 in Oxford series in optical and imaging sciences. Oxford University Press, New York, 1995. ISBN 978-0-19-509278-3.

[66] Joachim Seibt and Tomáš Mančal. Ultrafast energy transfer with competing channels: Non-equilibrium Förster and Modified Redfield theories. *The Journal of Chemical Physics*, 146(17):174109, 2017.

[67] Marco Ferretti, Vladimir I. Novoderezhkin, Elisabet Romero, Ramunas Augulis, Anjali Pandit, Donatas Zigmantas, and Rienk van Grondelle. The nature of coherences in the B820 bacteriochlorophyll dimer revealed by two-dimensional electronic spectroscopy. *Physical Chemistry Chemical Physics*, 16(21):9930–9939, 2014.

[68] Shawn Irgen-Gioro, Austin P. Spencer, William O. Hutson, and Elad Harel. Coherences of Bacteriochlorophyll a Uncovered Using 3D-Electronic Spectroscopy. *The Journal of Physical Chemistry Letters*, 9(20):6077–6081, 2018.

[69] Jordan M. Womick and Andrew M. Moran. Vibronic Enhancement of Exciton Sizes and Energy Transport in Photosynthetic Complexes. *The Journal of Physical Chemistry B*, 115(6):1347–1356, 2011.

[70] Shu-Hao Yeh, Ross D. Hoehn, Marco A. Allodi, Gregory S. Engel, and Sabre Kais. Elucidation of near-resonance vibronic coherence lifetimes by nonadiabatic electronic-vibrational state character mixing. *Proceedings of the National Academy of Sciences*, 116(37):18263–18268, 2019.

[71] Ruidan Zhu, Jiading Zou, Zhuan Wang, Hailong Chen, and Yuxiang Weng. Electronic State-Resolved Multimode-Coupled Vibrational Wavepackets in Oxazine 720 by Two-Dimensional Electronic Spectroscopy. *The Journal of Physical Chemistry A*, 124(45): 9333–9342, November 2020.

[72] Franco V. de A. Camargo, Lena Grimmelsmann, Harry L. Anderson, Stephen R. Meech, and Ismael A. Heisler. Resolving Vibrational from Electronic Coherences in Two-Dimensional Electronic Spectroscopy: The Role of the Laser Spectrum. *Physical Review Letters*, 118(3):033001, 2017.

[73] Sofia Georgakopoulou, Gert van der Zwan, John D. Olsen, C. Neil Hunter, Robert A. Niederman, and Rienk van Grondelle. Investigation of the Effects of Different Carotenoids on the Absorption and CD Signals of Light Harvesting 1 Complexes. *The Journal of Physical Chemistry B*, 110(7):3354–3361, 2006.

[74] Sofia Georgakopoulou, Rienk van Grondelle, and Gert van der Zwan. Explaining the Visible and Near-Infrared Circular Dichroism Spectra of Light-Harvesting 1 Complexes

from Purple Bacteria: A Modeling Study. *The Journal of Physical Chemistry B*, 110(7): 3344–3353, 2006.

[75] N. R. S. Reddy, R. Picorel, and G. J. Small. B896 and B870 components of the Rhodobacter sphaeroides antenna: a hole burning study. *The Journal of Physical Chemistry*, 96(15):6458–6464, 1992.

CHAPTER 6

INTER-EXCITONIC COUPLING AND RELAXATION DYNAMICS IN PHYCOBILISOMES FROM CYANOBACTERIUM *SYNECHOCOCCUS ELONGATUS* PCC 7942 EXAMINED BY TWO-DIMENSIONAL ELECTRONIC SPECTROSCOPY

6.1 Challenges of Studying Excited-State Dynamics in Phycobilisomes

Photosynthesis is an intricate cascade of biochemical processes that convert solar energy into chemical energy with which organisms provide their various cellular activities. Most photosynthetic processes, including those occurring in plants, algae and cyanobacteria, produce oxygen as their byproducts, and serve as one of the most influential results of the evolutions leading to the current oxygen-rich atmospheric composition. In oxygenic photosynthesis, the organisms develop a collection of molecular machinery to convert photons from sunlight to proton gradients across organelle membranes, inducing water splitting and the subsequent oxygen formation. The sunlight is first absorbed by the light-harvesting complexes, the pigment-protein complexes with distinct photophysical properties specific to each photosynthetic organism.

Cyanobacteria are one of the first group of photosynthetic prokaryotes that evolved during the early stage of Earth. First appearing around 3.5 billion years ago on Earth, cyanobacteria are now found dwelling in a wide range of aquatic terrains. The light harvesting apparatus of cyanobacteria sits on their thylakoid membranes, which are predominantly phospholipid bilayers. The light harvesting complexes in cyanobacteria are categorized into two types, depending on their functions and absorption maxima: phycobilisomes (PBS) and

photosystems (PS). Photosystems contain chlorophylls as their main chromophores and the reaction center at their center. Photosystems bind chlorophylls tightly together to allow excitation energy to transfer to the reaction center and initiate electron transfer reactions in light–dependent reactions of photosynthesis; the energy transferred within photosystems are often around 680 nm or 700 nm. Phycobilisomes, on the other hand, absorb in a higher–energy region of the solar spectrum between 550 and 670 nm, not covered by chlorophyll absorption spectrum, with the aid of chromophores called phycobilins, a family of tetrapyrrole compounds that are covalently bound to the phycobiliproteins (PBP), comprising the structural basis of phycobilisomes.

The hemidiscoidal structure of PBS on cyanobacterial and algal thylakoid membranes has been observed via transmission electron microscopy [1, 2]. A PBS complex generally consist of two major components: the core that sits on top of the thylakoid membranes and are often connected to the PS; the rods of PBS extend from the core with four to six PBP hexamers. PBS structures vary across all cyanobacterial and algal species in their number and protein composition of rods and cores [3, 4, 5]: *Synechocystis* PCC 6803, for example, has a tri-cylindrical core structure; whereas in *Synechococcus elongatus*, the core is made of only two cylinders of PBP complexes [6], as seen in the cartoon illustration in Figure 6.1. Rods of the PBS supercomplex are responsible for absorbing lights between 550 and 650 nm, complementing the absorption spectrum of chlorophylls. The absorbed energy then flows through the rods and is concentrated at the terminal emitter of the rods, where the energy transfer between rods and cores take place. The cores of the PBS supercomplex ultimately pass down the excitation energy to the photosystem II (PSII) or photosystem I (PSI) embedded in the thylakoid membrane.

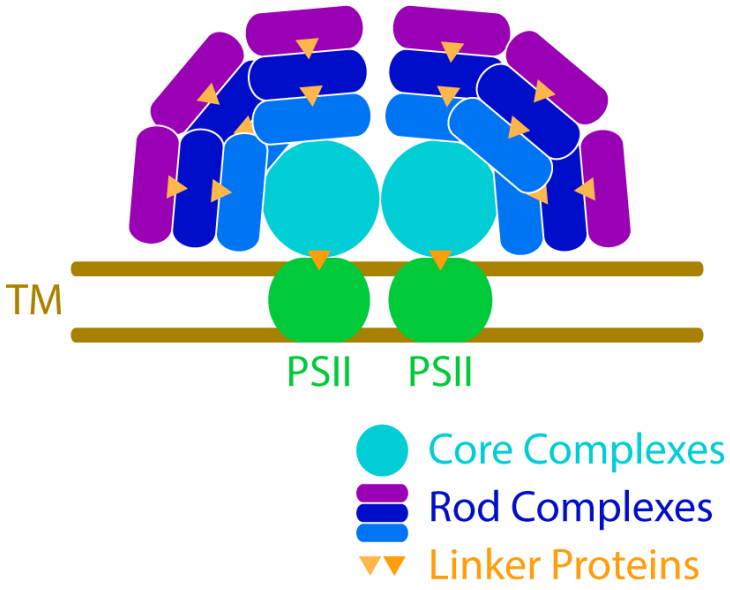

Figure 6.1: Illustration of the phycobilisome supercomplex showing its generic assembly. TM: thylakoid membrane; PSII: Photosystem II.

It is intriguing to ponder how energy transfer processes between PBS supercomplexes and PSII/PSI are facilitated or regulated in the nature, and numerous studies have been attempting to answer this question. Nonetheless, conducting time-resolved spectroscopic measurements on PBS has its own obstacles. One important challenge arises from the structural fragility of isolated PBS *in vitro*. In live cyanobacteria, PBS supercomplexes are not embedded within but anchored onto the thylakoid membrane with anchoring proteins; more linker proteins are responsible for holding rods and cores together. Typical isolation processes often break the linkages established by linker proteins, making isolated PBS susceptible to spontaneous disassembly. Even with a good isolation protocol, isolated PBS supercomplexes have short shelf-lives and can limit the actual time frame, thus the ability to average out random noises from optical scatters, in time-resolved spectroscopic experiments that usually takes up several

hours of lab time.

In this Chapter, we present, to the best of our knowledge, the first 2DES results of isolated PBS from the wild-type cyanobacterium *Synechococcus elongatus* PCC 7942 under ambient temperature. We compare spectroscopic data from the original and revised isolation protocols, and have shown that the revised protocol improves the purity of isolation by effectively removing the chlorophylls from the ruptured cell solutions without significantly increasing the complexity or time of the isolation process. We leverage the single-shot capability of GRAPE spectroscopy to realize rapid averaging of 2D electronic spectra on isolated PBS in real-time. We also discuss findings and some speculation from the 2DES results of isolated PBS regarding its ultrafast dynamics.

6.2 Probing Inter-Complex Couplings and Energy Transfer within PBS

6.2.1 Cell Culture and Isolation of PBS

Cell cultures of cyanobacterium *Synechococcus elongatus* PCC 7942 were grown phototrophically in a pasteurized BG-11 medium. PBS supercomplexes were isolated following a modified procedure from the literature [7]. Cell cultures were pelleted down by centrifugation at 3,200 g (Eppendorf 5810R with A-4-81 Rotor) for 15 minutes, washed twice with a 0.8 M phosphate buffer (pH 7.5) containing 1 mM EDTA, 1 mM phenylmethylsulfonyl fluoride, 1 mM hexanoic acid, 1 mM benzamidine and 50 μg/mL DNase. The cells were then ruptured with 1-mm glass beads by vortexing on a homogenizer (BeadBug, Benchmark Scientific). Broken cells were immediately incubated with Triton X-100 (2% v/v) for 30 minutes, after which the solution was centrifuged at 20,000 g (IEC Micromax RF with IEC 851 Rotor) for 20 minutes to remove the cell debris. The supernatant was loaded onto a sucrose gradient solution containing steps of 1.5 M, 0.75 M, 0.5 M, and 0.25 M sucrose. The sucrose gradient

was then centrifuged at 100,000 g (Beckman) for 5 hours. Isolated PBS were collected from the deep-blue portions of the gradient between 0.75 M and 1.5 M layers, and concentrated with centrifugal filter units (MilliporeSigma Amicon, 10,000 Da) to the desired O.D. of 0.3 in a 500-μm optical path. The purity and structural integrity of isolated PBS were examined by both UV-Vis absorption and steady-state fluorescence spectra. All chemicals were purchased from Sigma-Aldrich.

6.2.2 Steady-State Absorption and Fluorescence Spectroscopy

All measurements were performed under ambient temperature. The absorption spectrum of PBS was recorded by a photodioarray single beam spectrophotometer (Agilent 8453), in which a 1.0-mm quartz cuvette filled with PBS solutions was used. The fluorescence spectra were measured using a spectrofluorometer (Fluorolog-3, Horiba) with a CCD array detector (Synapse). Samples were prepared to have the O.D. between 0.01 and 0.03 in a 1.0-cm quartz cuvette for fluorescence measurements. Fluorescence emission spectra of isolated PBS were collected at the excitation wavelength between 550 nm and 700 nm with a 2-nm step size. The range of detection wavelength was set to be between 560 nm and 860 nm with 0.25-nm spectral resolution.

6.2.3 Two-Dimensional Electronic Spectroscopy

Details of 2DES have been documented extensively in the literature [8, 9, 10, 11], and are provided here in brief for completion. The schematic of the 2DES experimental setup for this study is drawn in Figure 6.2. The 2DES results of cyanobacterial phycobilisomes presented here were obtained via GRadient-Assisted Photon Echo Spectroscopy (GRAPES) [12, 13], a variation of 2DES that spatially encodes the time delay between the first two pulses, coherence time τ, by focusing all excitation pulses to a vertical line onto the sample, such that different vertical portions of the sample illuminated by excitation pulses experience

difference coherence time delay.

The ultrafast laser pulse was generated from a 5-kHz Ti:sapphire regenerative amplifier (Coherent Legend Elite USP), seeded with a 80-MHz Ti:sapphire laser (Coherent Micra), resulting in a 35-fs pulse centered at 806 nm with a full width at half maximum of 30 nm. The pulse was then focused into a pipe filled with argon gas (argon pressure = 18 psi) and broadened spectrally, bounced off of a pair of chirped mirrors (-60 fs^{-2} at 800 nm) four times, passed through the argon-filled pipe again and collimated. The intense residual power of the fundamental spectrum was filtered with hot mirrors with a cutoff wavelength at 700 nm. The spectrally broadened pulse was compressed to 25 fs with a spatial light modulator through multiphoton intrapulse interference phase scan algorithm [14]. The compressed pulse was then split into two via a 50/50 beamsplitter, with one of them passing through a motor-controlled translational stage (Soloist) to generate the waiting time delay, T. Two pulses were further split into four pulses used in the 2DES experiment via a home-built beamsplitter assembly containing a customized 60/40 beamsplitter and a silver mirror for each beam path. The 60/40 beamsplitter had an anti-reflective-coating front surface and a partially reflective back surface to allow for total compensation of the amount of dispersion materials each pulse was passed through. Four pulses were focused via a cylindrical silver mirror onto a vertical line at the sample. The attenuated local oscillator pulse, arriving around 2 ps ahead of the other pulses and traveling at the same phase-matching direction as the photon echo signal, was then passed through a spatial filter, spectrally dispersed inside the spectrophotometer, and detected by a CMOS camera (Andor Zyla 5.5).

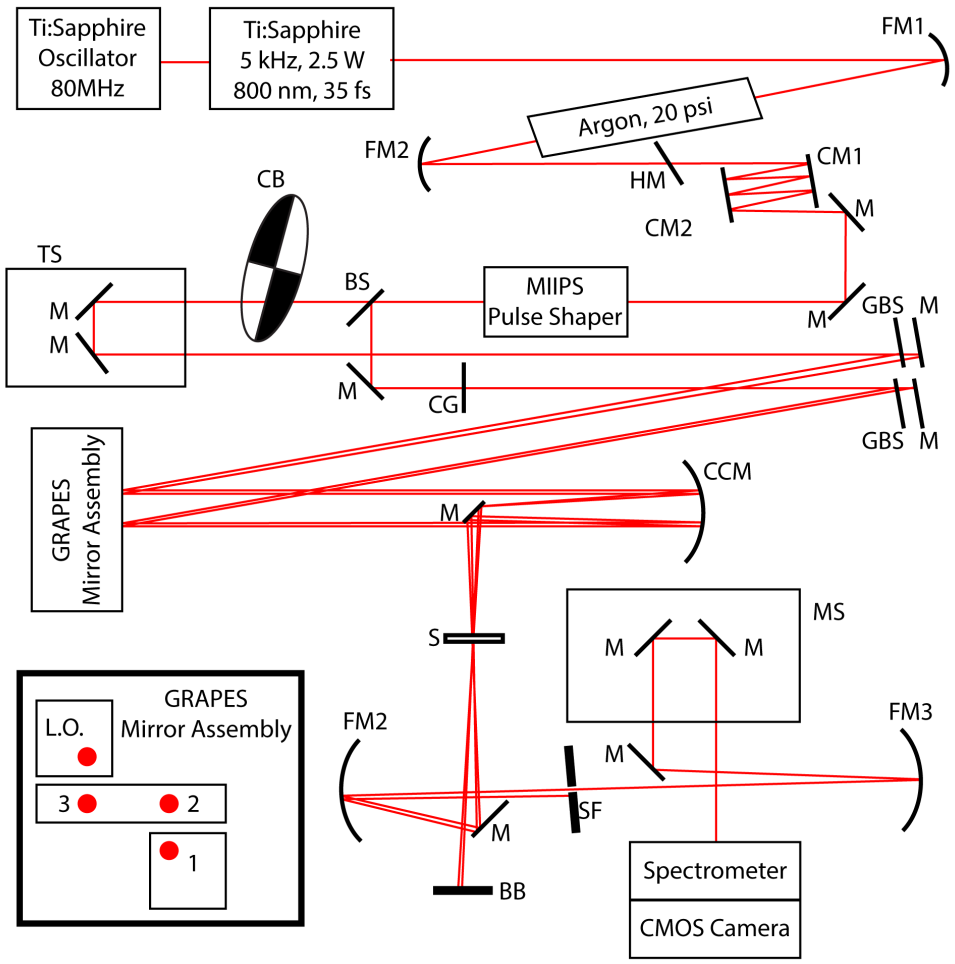

Figure 6.2: Schematic of GRAPES experimental setup adopted in this work. Red lines indicate the beam paths from the Ti:sapphire regenerative amplifier laser source to the CMOS camera detector. Abbreviations used in the schematic correspond to the following parts: M: flat mirrors; FM1, FM2, FM3: concave spherical mirrors; HM: 45° hot mirror at 700 nm; CM1, CM2: chirped mirrors; BS: 50/50 beamsplitter; GBS: 60/40 beamsplitter for GRAPES; CG: 1-mm compensating glass; TS: computer-controlled translational stage; CB: chopper blade; CCM: cylindrical concave mirror; MS: mechanical stage mount; S: sample cell; BB: beam block for beams 1 and 2; SF: spatial filter for beam 3. The setup for GRAPES mirror assembly is drawn as an inset [13].

6.2.4 Signal Processing and Analysis

The coherence time range was set to be from −350 fs to 350 fs over 1,080 camera pixels, ensuring an above-Nyquist sampling frequency for both rephasing and nonrephasing signal collection [15]. Each camera image was collected at a frequency of 8 Hz, equivalent to an average of 625 laser shots. The waiting time stage is scanned from −500 fs to 2 ps with a step size of 5 fs. A raw camera image contains the interference between the signal and the local oscillator, as well as that between the local oscillator and unwanted pump scatters. A Welch (parabolic) window was employed in Fourier domain of the waiting time to filter high-frequency scatters [16]. A 40-pixel Hann window was applied in the detection time (t) domain to isolate the heterodyned third-order signal. A Fourier transform in both coherence time and detection time domain yielded a purely absorptive 2D spectrum at a single waiting time. The absolute phase of the complex 2DES signal was assigned by fitting the processed signal to a separately acquired pump-probe spectrum of the same waiting time range; this procedure has been shown to be theoretically exact by projection-slice theorem [11]. All data processing was performed by MATLAB on a 32-GB RAM desktop computer.

6.3 2DES Results of Isolated PBS

Representative 2DES amplitude maps of isolated PBS from *Synechococcus elongatus* PCC 7942 at selected waiting time frames of 20 fs, 50 fs, 100 fs, and 2 ps were plotted in Figure 6.3. The 2DES signals are dominated by the broad stimulated emission (SE) feature around detection wavelength $\lambda_{det} = 650$ nm. There was a minor excited-state absorption (ESA) feature to the higher excitation energy side of the 2DES maps at all waiting times, accounting for around 5% of the total signal magnitudes. At first glance, there appeared to be no apparent change in overall lineshapes of both SE and ESA features, and there was little decay in amplitude for the SE feature within the first 2 ps of excitation.

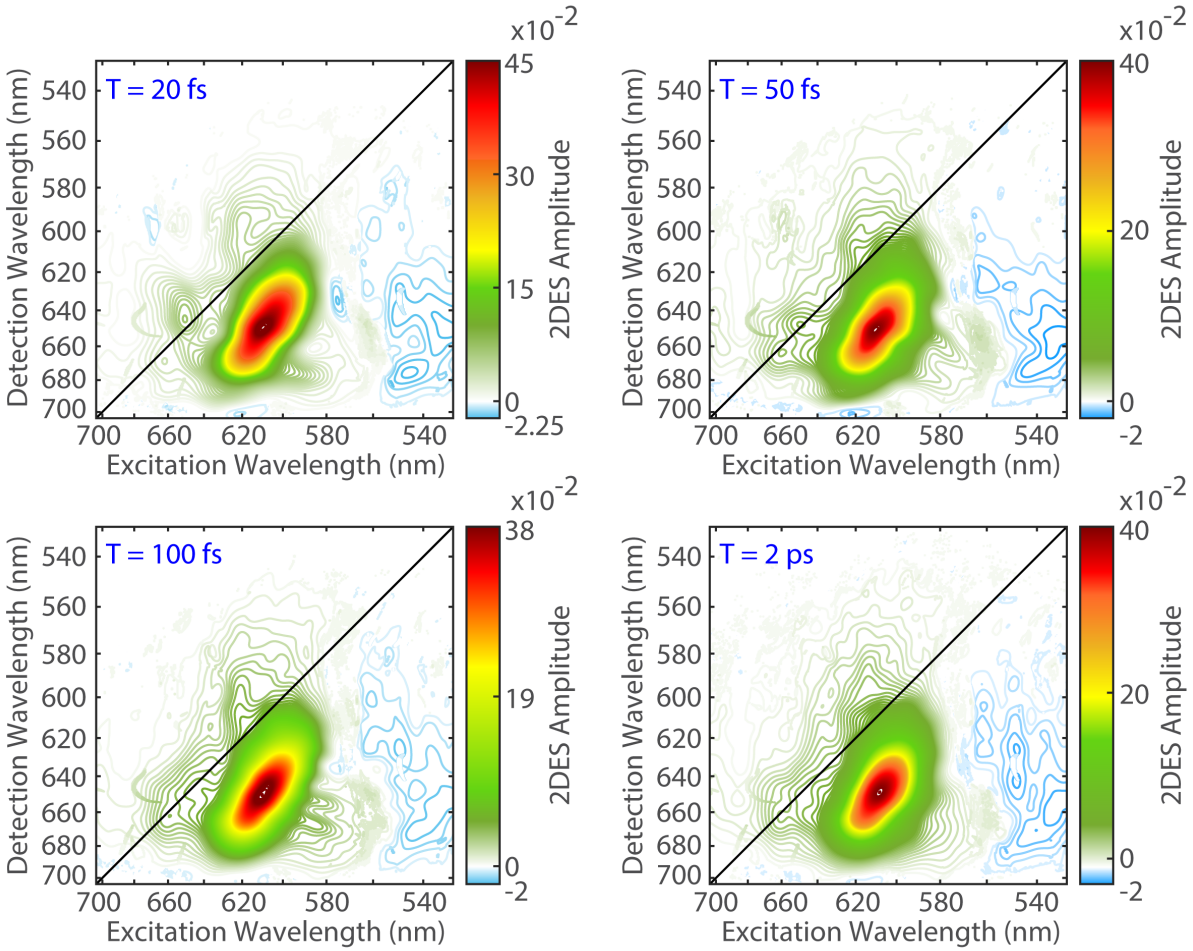

Figure 6.3: Representative 2DES amplitude maps of isolated PBS from *Synechococcus elongatus* PCC 7942 at early waiting time frames of 20 fs, 50 fs, 100 fs, and 2 ps. All spectra were averaged over 3 replicates and normalized to the global maximal magnitude of the acquired 2DES data.

To examine the early-time dynamics in isolated PBS, several waiting time traces were plotted at selected wavelength pairs on the 2DES amplitude map [Figure 6.4]. We could follow the flow of excitation energy by taking a closer look on several states: the rod absorber state at 623 nm, the rod emitter state at 650 nm, and the core emitter state at 680 nm. One apparent observation from Figure 6.4 was that, amplitudes of traces from 623/623 nm (blue) and 623/650 nm (red) seemed to be complementary, with a fast sub-30 fs kinetic process followed by a much slower process; the fast process might be attributed to energy transfer/re-equilibrium processes taking place within the rod, whereas the slow process might reflect the radiative lifetime of excited states on the rod.

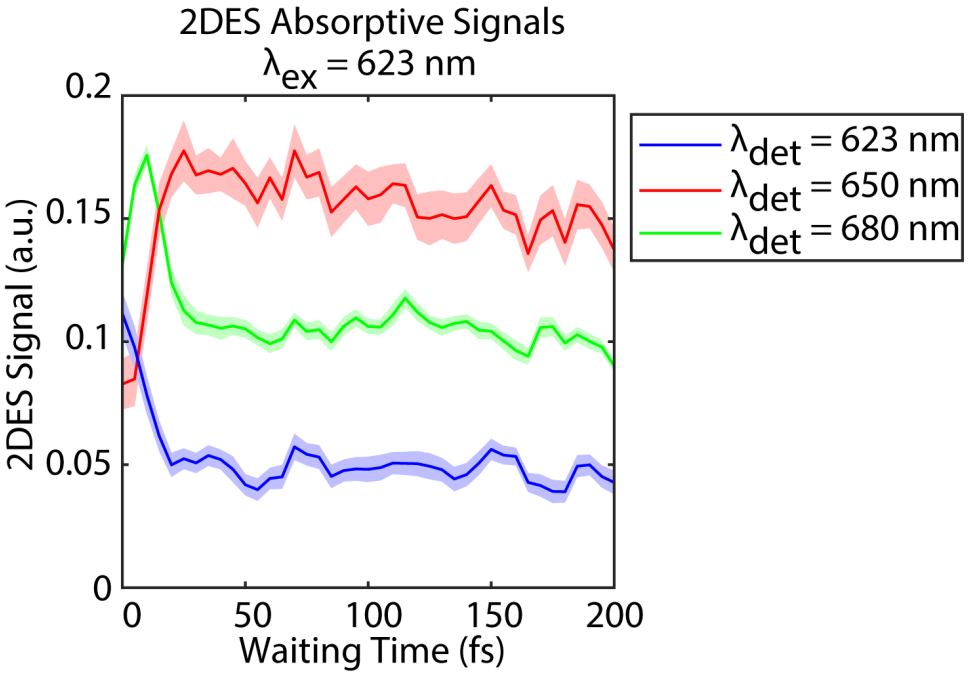

Figure 6.4: Selected waiting time traces from absorptive 2DES signals of isolated PBS. The shaded areas overlaid on each trace indicated the standard on the mean of 3 replicates. Traces were plotted from the excitation/detection wavelength pairs of 623/623 nm (blue), 623/650 (red), and 623/680 nm (green).

We also performed a Fourier analysis on selected waiting time traces to see if there is any sign of periodic oscillation, a signature of couplings between electronic states or vibronic states. We subtracted the traces in Figure 6.4 from a bi-exponential fit, and performed Fourier transform on the residuals, and plotted the normalized power spectra of each residual in Figure 6.5. The strongest beating signals came from the trace at 623/650 nm (red) with many resolved beatings. Another observation was that, some cross peaks in the 2D spectrum share the same subsets of beating frequencies. For example, beatings at -72 cm^{-1}, $+200$ cm^{-1}, $+258$ cm^{-1}, $+300$ cm^{-1} and $+944$ cm^{-1} were present in both 623/650 nm (red) and 623/680 nm (green) cross peaks; beatings at -29 cm^{-1} and -500 cm^{-1} could be seen in both 623/623 nm (blue) diagonal peak and 623/650 nm (red) cross peak. One particular beating frequency, $+128$ cm^{-1}, was shared among three peaks.

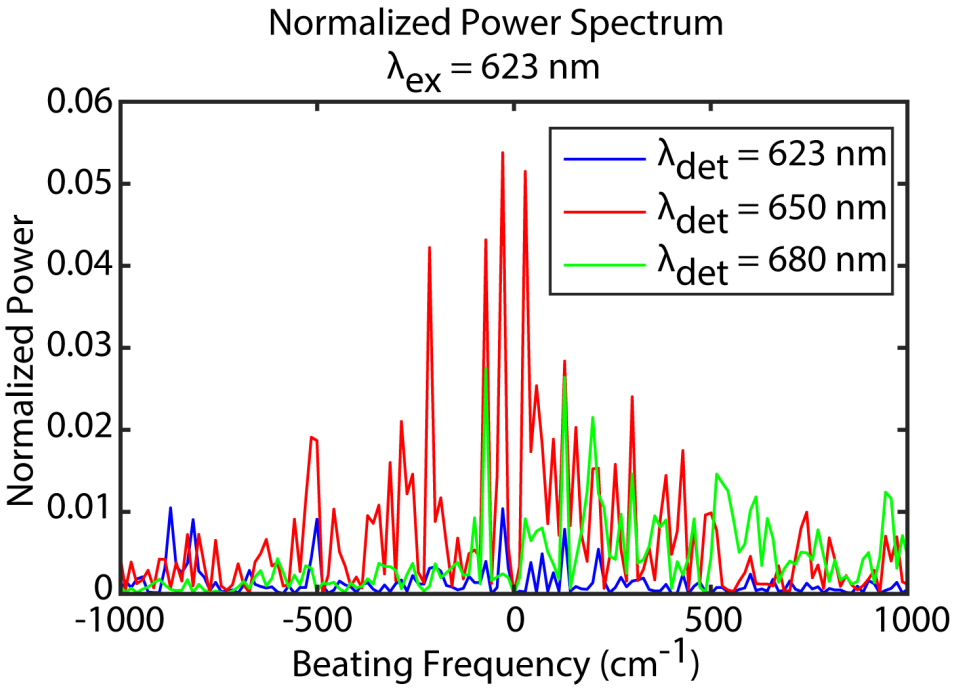

Figure 6.5: Normalized beating power spectra from residuals of selected waiting time traces plotted in Figure 6.4. at the excitation/detection wavelength pairs of 623/623 nm (blue), 623/650 (red), and 623/680 nm (green).

6.4 Supplementary Experimental Details

6.4.1 Detailed Experimental Protocol for Isolating Intact PBS from Synechococcus elongatus Cell Cultures

This protocol describes a normal two-day preparation of isolated phycobilisomes samples for spectroscopic measurements. All procedures are to be conducted at ambient temperature unless specified otherwise. The phosphate buffer used in this protocol includes 1 M potassium phosphate, 1 mM EDTA, 1 mM hexanoid acid (caproic acid), 1 mM phenylmethylsulfonyl fluoride (PMSF), 1 mM benzamidine, and 50 μg/mL Deoxyribonuclease I (DNase). Pellet down the cell cultures at 4,000 r.p.m. (Sorvell centrifuge) for 30 minutes. Discard the supernatant and transfer the cell pellet to a 50 mL falcon tube, followed by washing with 5 mL phosphate buffer twice to remove brownish white impurities. Centrifuge at 4,000 r.p.m. (Eppendorf) for 10 min, decant out the supernatant, and resuspend the cell pellet in minimal amount of phosphate buffer. From this point forward, all procedures are required to be conducted in dark or minimal light condition due to the fragility of phycobilisomes when devoid of attachment to intact thylakoid membranes. Load the suspended cell pellet solution into 2.0 mL tubes already containing 1.0-mm silica beads (Benchmark Scientific) while maintaining a 1:1 volume ratio between the cell solution and beads. Vortex the cell solution in bead beating tubes in a homogenizer (Benchmark Scientific) for 1 min and immediately chill the tubes on ice for 1 min. Repeat the vortexing one more time to complete the cell rupturing process. Add Triton X-100 into the tubes to a 2% volume ratio (usually around 20-25 μL) and incubate for 30 min to extract water-soluble phycobilisomes from other cell debris. Centrifuge the incubated solution at 20,000 g (IEC Micromax RF) for 20 min to separate phycobilisomes supernatant from cell debris. Carefully pipette out blue supernatant and avoid collecting green impurities. Wash the cell debris with 300 μL phosphate buffer 3-5 times and repeat the centrifugation step once to extract more phycobilisomes into the

blue supernatant. Combine all blue supernatant parts and carefully load it onto a sucrose step gradient containing layers of 1.5, 0.75, 0.5, and 0.25 M sucrose (volume ratio = 3:5:3:3) in 1 M phosphate buffer, and centrifuge overnight at 100,000 g (Beckman) at 23°C. Collect the major blue band at the bottom of the sucrose gradient (between 0.75 and 1.5 M sucrose layers), and concentrate with centrifugal filter units (MilliporeSigma Amicon, 10,000 Da) to desired O.D. for UV-Vis, fluorescence, and 2DES measurements.

6.4.2 Spectroscopic Characterization of Isolated PBS

The UV-visible absorption spectrum of PBS isolated from *Synechococcus elongatus* PCC 7942 with the aforementioned isolation protocol is plotted in Figure 6.7, along with the laser spectrum used in the 2DES experiment. There are three general features in the absorption spectrum of PBS: the major peak at 621 nm representing large absorption cross sections of phycocyanobilins (PCB) inside C-phycocyanins (C-PC) in the rod assembly, a red shoulder around 650 nm arising from allophycocyanins (APC) in the core assembly, and a blue shoulder around 580 nm, presumably also from PCB chromophores in the C-PC complex in the rod assembly. Since C-PC is the only type PBP in the PBS from *Synechococcus elongatus* PCC 7942, and given the fact that the absorption of isolated PC peaks at 620 nm, the origin of the 580 nm shoulder is very likely a result of either some H-type aggregation between chromophores among C-PCs on the rod assembly. The X-ray crystal structure of C-PC from *Synechococcus elongatus* PCC 7942 shows that there are three PCB chromophores covalently bound to one C-PC: one at the α-84 cysteine residue on the α subunit, one at the β-84 cysteine residue on the β subunit, and one at the β-155 cysteine residue on the β subunit [17]. The α-84 PCB and β-84 PCB are much closer in distance and more likely to have red-shifted excitonic features in the absorption spectrum, whereas the β-155 PCB will behave more like a stand-alone chromophore. We thus attribute the 580 nm shoulder seen in our absorption spectrum to the absorption from β-155 PCB, and the major peak at 621 nm to

the absorption from the α-84 PCB/β-84 PCB dimer structure.

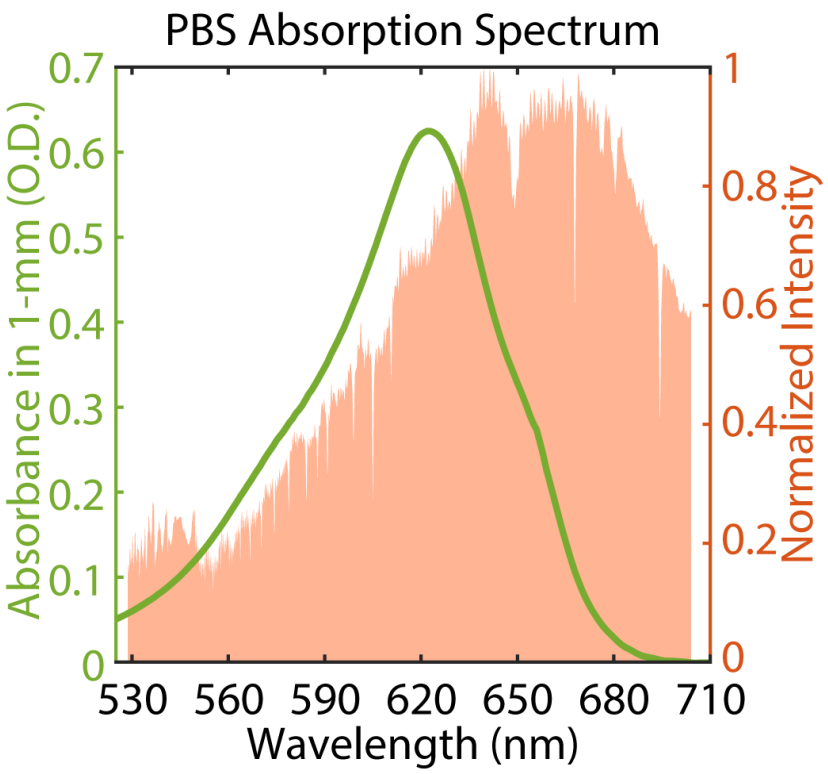

Figure 6.6: Measured UV-visible absorption spectrum of isolated PBS in 0.8 M phosphate buffer (green curve) and the laser spectrum used in the 2DES experiment (orange shaded area).

We also conduct a preliminary assessment on structural integrity of isolated PBS with steady-state fluorescence measurement, plotted in Figure 6.8. The idea is that, for an intact PBS, an excitation at the blue edge of the rod absorption spectrum will excite the rod assembly, which passes down the energy to the core assembly in a series of excitation energy transfer processes, and the spontaneous emission of the core assembly can be detected as a fluorescence signal peaked at 680 nm. For degraded PBS samples, however, the absence of energy transfer from the rod to core assembly means that only the emission around or below 650 nm, corresponding to the red edge of the rod emission, will occur after exciting at the rod absorption peak. From our fluorescence spectrum in Figure 6.8, we see that an

excitation at 620 nm indeed result in an emission at 680 nm, confirming that our isolation protocol yields structurally intact PBS supercomplexes.

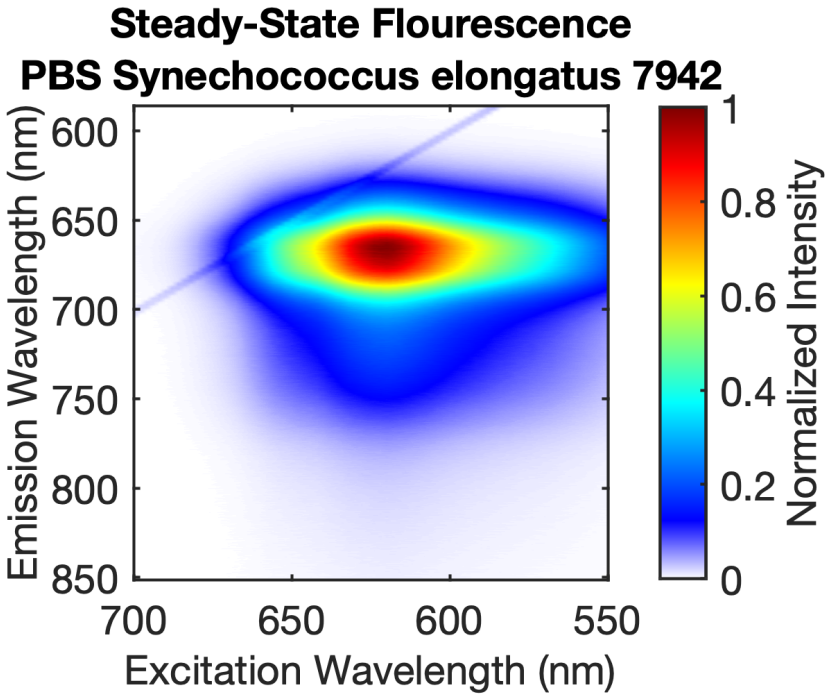

Figure 6.7: Steady-state fluorescence spectrum of isolated PBS in 0.8 M phosphate buffer. The scan step of the excitation wavelength is 2 nm. The spectral resolution of the emission wavelength is 0.25 nm.

REFERENCES

[1] Ana A. Arteni, Ghada Ajlani, and Egbert J. Boekema. Structural organisation of phycobilisomes from Synechocystis sp. strain PCC6803 and their interaction with the membrane. *Biochimica et Biophysica Acta (BBA) - Bioenergetics*, 1787(4):272–279, 2009.

[2] Leifu Chang, Xianwei Liu, Yanbing Li, Cui-Cui Liu, Fan Yang, Jindong Zhao, and Sen-Fang Sui. Structural organization of an intact phycobilisome and its association with photosystem II. *Cell Research*, 25(6):726–737, 2015.

[3] A. N. Glazer. Phycobilisomes: Structure and Dynamics. *Annual Review of Microbiology*, 36(1):173–198, 1982.

[4] Niraj Kumar Singh, Ravi Raghav Sonani, Rajesh Prasad Rastogi, and Datta Madamwar. The phycobilisomes: an early requisite for efficient photosynthesis in cyanobacteria. *EXCLI Journal*, 14:268–289, 2015.

[5] Noam Adir, Shira Bar-Zvi, and Dvir Harris. The amazing phycobilisome. *Biochimica et Biophysica Acta (BBA) - Bioenergetics*, 1861(4):148047, 2020.

[6] G. Yamanaka, A. N. Glazer, and R. C. Williams. Molecular architecture of a light-harvesting antenna. Comparison of wild type and mutant Synechococcus 6301 phycobilisomes. *The Journal of Biological Chemistry*, 255(22):11104–11110, 1980.

[7] Michal Gwizdala, Adjélé Wilson, and Diana Kirilovsky. In Vitro Reconstitution of the Cyanobacterial Photoprotective Mechanism Mediated by the Orange Carotenoid Protein in *Synechocystis* PCC 6803. *Plant Cell*, 23(7):2631–2643, 2011.

[8] Sarah M. Gallagher, Allison W. Albrecht, John D. Hybl, Brett L. Landin, Bhavani Rajaram, and David M. Jonas. Heterodyne detection of the complete electric field of

femtosecond four-wave mixing signals. *Journal of the Optical Society of America B*, 15 (8):2338–2345, 1998.

[9] John D. Hybl, Allison W. Albrecht, Sarah M. Gallagher Faeder, and David M. Jonas. Two-dimensional electronic spectroscopy. *Chemical Physics Letters*, 297(3-4):307–313, 1998.

[10] John D. Hybl, Allison Albrecht Ferro, and David M. Jonas. Two-dimensional fourier transform electronic spectroscopy. *The Journal of Chemical Physics*, 115(14):6606–6622, 2001.

[11] Tobias Brixner, Tomáš Mančal, Igor V. Stiopkin, and Graham R. Fleming. Phase-stabilized two-dimensional electronic spectroscopy. *The Journal of Chemical Physics*, 121(9):4221–4236, 2004.

[12] Elad Harel, Andrew F. Fidler, and Gregory S. Engel. Real-time mapping of electronic structure with single-shot two-dimensional electronic spectroscopy. *Proceedings of the National Academy of Sciences*, 107(38):16444–16447, 2010.

[13] Elad Harel, Andrew F. Fidler, and Gregory S. Engel. Single-Shot Gradient-Assisted Photon Echo Electronic Spectroscopy. *The Journal of Physical Chemistry A*, 115(16): 3787–3796, 2011.

[14] Vadim V. Lozovoy, Igor Pastirk, and Marcos Dantus. Multiphoton intrapulse interference IV Ultrashort laser pulse spectral phase characterization and compensation. *Optics Letters*, 29(7):775, 2004.

[15] Sara H. Sohail, Peter D. Dahlberg, Marco A. Allodi, Sara C. Massey, Po-Chieh Ting, Elizabeth C. Martin, C. Neil Hunter, and Gregory S. Engel. Communication: Broad manifold of excitonic states in light-harvesting complex 1 promotes efficient unidirectional energy transfer *in vivo*. *The Journal of Chemical Physics*, 147(13):131101, 2017.

[16] Peter D. Dahlberg, Andrew F. Fidler, Justin R. Caram, Phillip D. Long, and Gregory S. Engel. Energy Transfer Observed in Live Cells Using Two-Dimensional Electronic Spectroscopy. *The Journal of Physical Chemistry Letters*, 4(21):3636–3640, 2013.

[17] Ailie Marx and Noam Adir. Allophycocyanin and phycocyanin crystal structures reveal facets of phycobilisome assembly. *Biochimica et Biophysica Acta (BBA) - Bioenergetics*, 1827(3):311–318, 2013.

CHAPTER 7

FUTURE DIRECTIONS

The projects presented in this Dissertation cover spectroscopic studies on two light-harvesting complexes in two organisms, opening up promising outlook for future research endeavors on photosynthetic light harvesting. In addition, throughout the research process, several improvements on the instrument are believed to provide more unobscured interpretations on our 2DES data from GRAPE spectrometer. This chapter aims to address some working hypotheses to issues on, but not limited to, broader topics on photosynthetic studies as well as revisions on the GRAPE instrument.

7.1 Advanced 2DES Studies on Purple Bacteria

In Chapters 4 and 5 of this Dissertation, 2DES studies on LH1-only membranes from the purple bacterium *Rhodobacter sphaeroides* were conducted at ambient temperature of 20°C. Reasons for the choice of experimental temperature include both an appropriate reflection of *in vivo* environment for purple bacteria and convenience in conducting our studies in GRAPE spectrometer at the time of the experiments.

Though some valuable information of the LH1 complex was able to be extracted by ambient temperature 2DES, the existence of multiple low-frequency vibrational modes in bacteriochlorophyll molecules and protein backbones means that thermal energy would have non-trivial effects in the resulting electronic spectra. In addition, small energy spacings between different excitonic states in the LH1 complex leads to broad absorption and emission features observed in our 2DES experiments, further confounding the vibrational components in the 2DES spectra. In order to decipher the contributions of vibrational modes to the overall electronic structures of the LH1 complex, more efforts need to be made to disentangle the thermal effect on the experimental spectra.

7.1.1 Cryogenic 2DES on LH1 membranes

One solution to address this concern will be to conduct the 2DES experiment under cryogenic temperatures. It is worth re-examining the excited-state dynamics of the LH1 complex at lower temperatures for a few purposes. First, low temperature essentially "freezes" nuclear motions and isolate the electronic behaviors. Second, due to reduced nuclear motions at low temperature, spectral diffusion and lineshape broadening on 2DES spectra is minimized, yielding spectra with higher spectral resolution and revealing the inhomogeneous nature of an ensemble of the LH1 complex. Dominant excited states that contribute to ultrafast relaxation and coherences observed in this Dissertation are hence expected to be better identified.

7.1.2 Polarization-Controlled 2DES on LH1 membranes

Another experiment worthy of considering will be polarization-controlled 2DES experiments. Under normal circumstances, 2DES experiments are conducted without altering the polarization of laser pulses, sometimes referred to as "all-parallel" 2DES due to the fact that all laser pulses in the 2DES pulse sequence remain parallel with respect to one another. All-parallel 2DES is a rather straightforward experimental approach; however, some important pathways contributing to the overall 2DES signals can be buried underneath dominant features on 2DES spectra. Pathways including electronic coherences and/or significant changes in direction of transition dipoles during the waiting time often fall into this category. Another family of third-order pathways not easily accessible in all-parallel 2DES experiments are wavevector-dependent pathways such as chirality-sensitive signals [1, 2, 3, 4]. These pathways carry smaller or, in the case of chiral pathways, no signal magnitudes in all-parallel 2DES often because of larger diminishing effects of orientational averaging on signals from the ensemble. Some polarization sequences are designed to isolate cross-peak dynamics or coherence-specific pathways [5, 6, 7, 8, 9, 10, 11, 12, 13, 14, 15, 16, 17, 18], which can provide complementary information on vibronic couplings. The potential of polarization-controlled 2DES remains

high, and the increasing ability to precisely control the polarization of individual pulses and minimizing the phase drift posed by the overall instrument setup will be keys to success in future polarization-controlled 2DES experiments.

7.1.3 Photoprotective Mechanisms in LH1-RC membranes

Due to the inhibiting nature of singlet oxygen molecules to the light harvesting process in purple bacteria, the organism has developed strategies to handle such oxidative stress. Aside from complementary light harvesting in the blue-to-green region of the spectrum, carotenoids such as spheroidene, spheroidenone, rhodopin glucoside and spirilloxanthin [19] are intercalated in both LH1 and LH2 complexes through non-covalent interactions, providing extra structural support and protecting light harvesting antenna from photo-oxidative damages by converting the single oxygen into a less-toxic triplet form [20, 21, 22, 23, 24]. Studies have suggested that carotenoids are promoted to its S_2 singlet excited state, followed by a fast relaxation to its optically-dark S_1 singlet excited state. When purple bacteria are exposed to excessive light, both S_2 and S_1 states are involved in quenching excess energy from the triplet excited state of bacteriochlorophyll a (BChl a) molecules in LH2 complexes through triplet-triplet excitation energy transfer. A recent study conducted on the ring-shaped LH1 complex enclosing one reaction center (RC) from *Rhodospirillum rubrum* estimates that over 60% of excess energy from triplet BChl a to carotenoids [24], compared to 100% BChl a-to-carotenoid energy transfer observed in the LH2 complex from *Rhodobacter sphaeroides* [25]. Enclosing two RCs and forming an S-shaped conformation, the native LH1-RC complex inside *Rhodobacter sphaeroides* has potentially different nonphotochemical quenching channels than those observed in *Rhodospirillum rubrum*. Future broadband 2DES studies on mutants carrying LH1-RC-only membranes from *Rhodobacter sphaeroides* would perhaps shed light to how carotenoids participate in photoprotective mechanisms within its LH1-RC complex.

7.2 Future Topics on Cyanobacteria

In Chapter 6 of this Dissertation, 2DES studies were conducted on the antenna supercomplex, phycobilisomes (PBS), from the cyanobacterium *Synechococcus elongatus* 7942. Preliminary results from PBS have shown promising outlook on the capability of tackling larger cyanobacterial antenna systems with our instrument. One such system may be the intact thylakoid membranes containing all protein complexes: PBS, photosystem I (PSI), and photosystem II (PSII). Another system worthy of future investigation includes the association of orange carotenoid protein (OCP) and PBS, namely PBS-OCP complex. Questions regarding these two systems inside cyanobacteria will be proposed in the following subsections.

7.2.1 Non-Photochemical Quenching

Cyanobacteria, like many other photosynthetic organisms, needs to deal with excessive exposure to sunlight during most of the day. To date, there are a number of photoprotective mechanisms observed within cyanobacteria [26]. The way in which organisms dissipate the excess energy from sunlight is through nonphotochemical quenching (NPQ). Bound to the PBS in some cyanobacteria such as *Synechocystis* sp. PCC 6803, OCP is a photoactive protein binding a single keto-carotenoid molecule [27]. OCP is thought to be responsible for some photoprotective functions in cyanobacteria through dissipating excess energy taken up by the PBS under some high-light growth conditions [28, 29], although the detailed mechanism through which OCP is involved in cyanobacterial NPQ is still under investigation. Specifically, questions one may ask are: what processes occur through excited states inside OCP, whether there exists any vibronic interaction between OCP and PBS, and to what degrees OCP preserves the overall light harvesting efficiency inside cyanobacteria. Answering these questions may open new routes to understanding the evolution of photo-regulation and unveiling new design principles of light harvesting.

7.2.2 State Transitions

State transitions are a acclimation mechanism of cyanobacteria under a low-light growth stress, in which the excitation energy absorbed by cyanobacteria is redistributed between PSI and PSII [30, 31]. State transitions allow both photosystems in cyanobacteria to reach optimal efficiency by ensuring no photosystems are exposing to excess energy or experiencing a deficiency in excitation energy. It has been suggested that the mobility of PBS across both photosystems may be a necessity for state transitions [32]. PBS may facilitate state transitions through migrating from PSI to PSII or vice versa, or through reorienting itself to redirect the excitation energy to the photosystem in greater energy deficiency under certain light conditions. Although recent spectroscopic studies have shed more light on deciphering the molecular mechanism of state transitions [33, 34, 35, 36, 37], the question on what exact role PBS plays is still yet to be determined. Future research on mechanisms of association between PBS and different photosystems under different external conditions may be able to answer such question.

7.2.3 Electrostatic Effects on Light Harvesting

A recent study has examined the effect of cationic antiseptics molecules on the energy transfer efficiency in purple bacteria [38]. It has been hypothesized that cationic antiseptics bind to the hydrophilic ends of the cytoplasmic membranes and alter the zeta potential of the chromatophores, which in return disrupts the overall energy transfer mechanism. This hypothesis is chemically straightforward, yet it is intriguing to observe such effects. Subjecting photosynthetic membranes to a different electrostatic environment can be also considered adding an intrinsic local electric field, thus inducing Stark effect. This disruption of the zeta potential across the membrane may be another design principle of ultrafast dynamics on light harvesting complexes, which are membrane-bound pigment-protein complexes; an ultrafast dynamics has been recently resolved in bacterial reaction center through 2DES [39].

These experimental findings lead us to wonder whether this Stark effect can be observed in cyanobacteria as well.

7.2.4 Other Acclimation Strategies to Extreme Growth Conditions

Photosynthetic organisms are at times growing under various extreme factors, such as inadequate light intensities, high environmental temperature, low CO_2 concentration, deficiency in metal cofactors necessary for biochemical processes inside organisms. For example, cyanobacteria growing under iron deficiency synthesize a Chl a-binding protein IsiA, which has been suggested to act as an alternative non-photochemical quencher through the cysteine-mediated regulation of excitation energy transfer [40, 41]. By drawing parallels to the recent studies on redox-dependent energy transfer in FMO from green sulfur bacteria [42, 43, 44], we can hypothesize that the energy transfer dynamics within photosystems from cyanobacteria grown under iron deficiency may have some similar mechanisms for tuning the energy transfer efficiency. Each of these factors may cause an organism to mutate and evolve into a more competitive mutant that better acclimates to its extreme growth habitat. Whether and how these mutations impact the efficiency of photosynthetic light harvesting, thus overall photosynthetic activity, becomes an interesting question, as it may provide valuable insights on Nature's evolutionary strategies in optimizing photosynthesis and design principles of light harvesting.

7.3 Areas of Improvement for GRAPE Spectrometer

Scientific discoveries and technological advances often happen concurrently: new technology allows the discovery of previously unseen phenomena, and with newly available data comes more challenges that may require a different research tool. Our GRadient-Assisted Photon Echo (GRAPE) spectrometer were developed to speed up the data acquisition of 2DES; the development of GRAPE has proven to be very useful in dealing with biological

systems, often generating non-resonant scatters during optical experiments and overwhelming the actual spectroscopic signals that carry molecular information. Throughout the process of completing research projects in this Dissertation, however, the author believes there are a few areas where GRAPE spectrometer has left something to be desired. In the following subsections, these areas of inconvenience will be addressed, and hopefully will serve as future references for whomever wishes to work on complicated biological systems using the GRAPE spectrometer.

7.3.1 Global Phasing Strategy

GRAPE spectrometer, like conventional 2DES spectrometers, utilizes three independent laser pulses and one weaker-powered pulse as a local oscillator (LO) in a displaced BOX-CARS geometry to generate the third-order signal from the sample. Therefore, there exists uncertainties in the relative arrival time of pulses 1 & 2 and that of pulse 3 & LO. In all 2DES setups with non-collinear beam geometry (GRAPE spectrometer included), these timing uncertainties, or phase uncertainties, are corrected using separately-acquired pump-probe spectra through projection-slice theorem. The quality of minimizing phase uncertainties of 2DES spectra using this method requires extreme phase stability in the lab environment, as well as high-quality pump-probe spectra. Recently in our research group, one phasing strategy leveraging scatters in the acquired 2DES data has been successfully implemented on the all-reflective point-by-point 2DES spectrometer, eliminating long-term phase drift due to phase instability caused by lab conditions and subsequently enabling a global phasing protocol [45]. With a few modification in the data acquisition LabView software, the author believes that this phasing strategy can be implemented on the 2DES data acquired with the GRAPE spectrometer and that the overall data reliability will see a significant boost.

7.3.2 Increasing Signal-To-Noise Ratios

One crucial disadvantage inevitably resulting from the leverage of single-shot coherence-time scanning in GRAPE spectrometer is the decreased light fluence compared to point-by-point scanning 2DES techniques. Focusing the excitation laser pulses onto a vertical line instead of a diffraction-limited point cause the fluence of pulses in GRAPE spectrometer by about, in our case, a hundred times lower. This drawback can severely inhibit our ability to collect 2DES data on low-O.D. samples, as often are the cases where high-O.D. samples are prohibitively hard to obtain within a reasonable time frame for a single doctoral degree (e.g. challenges on organic/materials synthesis, extremely slow growth of cell cultures, low efficiency on protein isolation, aggregation/precipitation of samples under high concentration in solution, thin-film samples with small extinction coefficients.)

There are two areas of improvement to this drawback: increasing pulse powers and decreasing scattering noises. To increase pulse powers for GRAPE spectrometer, we would need to diminish possible losses of pulse energy due to imperfect reflectance of reflection optics, increase the power conversion efficiency of spatial light modulators inside MIIPS pulse shaper, enhance the generation efficiency of white light supercontinuum, or improve the laser power from the regenerative amplifier. To lower scattering noises for GRAPE spectrometer, we could consider strategies such as deploying intelligent scatter-removal beam-chopping schemes, correcting signals with a second reference camera, shortening signal acquisition time with compressed sensing techniques. None of these technical improvements is small feat, yet if implemented successfully, these improvements will with no doubt boost the capability of GRAPE spectrometer tremendously.

REFERENCES

[1] Darius Abramavicius and Shaul Mukamel. Coherent third-order spectroscopic probes of molecular chirality. *The Journal of Chemical Physics*, 122(13):134305, 2005.

[2] Darius Abramavicius and Shaul Mukamel. Chirality-induced signals in coherent multidimensional spectroscopy of excitons. *The Journal of Chemical Physics*, 124(3):034113, 2006.

[3] Darius Abramavicius, Wei Zhuang, and Shaul Mukamel. Probing molecular chirality via excitonic nonlinear response. *Journal of Physics B: Atomic, Molecular and Optical Physics*, 39(24):5051–5066, 2006.

[4] Andrew F. Fidler, Ved P. Singh, Phillip D. Long, Peter D. Dahlberg, and Gregory S. Engel. Dynamic localization of electronic excitation in photosynthetic complexes revealed with chiral two-dimensional spectroscopy. *Nature Communications*, 5(3286):1–6, 2014.

[5] Peter Hamm and Martin T. Zanni. *Concepts and Methods of 2D Infrared Spectroscopy*. Cambridge University Press, Cambridge, UK; New York, NY, 2011.

[6] Elizabeth L. Read, Gregory S. Engel, Tessa R. Calhoun, Tomáš Mančal, Tae Kyu Ahn, Robert E. Blankenship, and Graham R. Fleming. Cross-peak-specific two-dimensional electronic spectroscopy. *Proceedings of the National Academy of Sciences*, 104(36): 14203–14208, 2007.

[7] Elizabeth L. Read, Gabriela S. Schlau-Cohen, Gregory S. Engel, Jianzhong Wen, Robert E. Blankenship, and Graham R. Fleming. Visualization of Excitonic Structure in the Fenna-Matthews-Olson Photosynthetic Complex by Polarization-Dependent Two-Dimensional Electronic Spectroscopy. *Biophysical Journal*, 95(2):847–856, 2008.

[8] Naomi S. Ginsberg, Jeffrey A. Davis, Matteo Ballottari, Yuan-Chung Cheng, Roberto Bassi, and Graham R. Fleming. Solving structure in the CP29 light harvesting complex

with polarization-phased 2D electronic spectroscopy. *Proceedings of the National Academy of Sciences*, 108(10):3848–3853, 2011.

[9] Andrew F. Fidler, Ved P. Singh, Phillip D. Long, Peter D. Dahlberg, and Gregory S. Engel. Time Scales of Coherent Dynamics in the Light-Harvesting Complex 2 (LH2) of *Rhodobacter sphaeroides*. *The Journal of Physical Chemistry Letters*, 4(9):1404–1409, 2013.

[10] Andrew F. Fidler, Ved P. Singh, Phillip D. Long, Peter D. Dahlberg, and Gregory S. Engel. Probing energy transfer events in the light harvesting complex 2 (LH2) of *Rhodobacter sphaeroides* with two-dimensional spectroscopy. *The Journal of Chemical Physics*, 139(15):155101, 2013.

[11] V. P. Singh, M. Westberg, C. Wang, P. D. Dahlberg, T. Gellen, A. T. Gardiner, R. J. Cogdell, and G. S. Engel. Towards quantification of vibronic coupling in photosynthetic antenna complexes. *The Journal of Chemical Physics*, 142(21):212446, June 2015.

[12] James Lim, David Paleček, Felipe Caycedo-Soler, Craig N. Lincoln, Javier Prior, Hans von Berlepsch, Susana F. Huelga, Martin B. Plenio, Donatas Zigmantas, and Jürgen Hauer. Vibronic origin of long-lived coherence in an artificial molecular light harvester. *Nature Communications*, 6(7755):1–7, 2015.

[13] Randy D. Mehlenbacher, Thomas J. McDonough, Nicholas M. Kearns, Matthew J. Shea, Yongho Joo, Padma Gopalan, Michael S. Arnold, and Martin T. Zanni. Polarization-Controlled Two-Dimensional White-Light Spectroscopy of Semiconducting Carbon Nanotube Thin Films. *The Journal of Physical Chemistry C*, 120(30):17069–17080, 2016.

[14] Erling Thyrhaug, Karel Žídek, Jakub Dostál, David Bína, and Donatas Zigmantas. Exciton Structure and Energy Transfer in the Fenna-Matthews-Olson Complex. *The Journal of Physical Chemistry Letters*, 7(9):1653–1660, 2016.

[15] David Paleček, Petra Edlund, Sebastian Westenhoff, and Donatas Zigmantas. Quantum coherence as a witness of vibronically hot energy transfer in bacterial reaction center. *Science Advances*, 3(9):e1603141, 2017.

[16] Erling Thyrhaug, Roel Tempelaar, Marcelo J. P. Alcocer, Karel Žídek, David Bína, Jasper Knoester, Thomas L. C. Jansen, and Donatas Zigmantas. Identification and characterization of diverse coherences in the Fenna-Matthews-Olson complex. *Nature Chemistry*, 10(7):780–786, 2018.

[17] Eglė Bukartė, Anja Haufe, David Paleček, Claudia Büchel, and Donatas Zigmantas. Revealing vibronic coupling in chlorophyll c1 by polarization-controlled 2D electronic spectroscopy. *Chemical Physics*, 530:110643, 2020.

[18] Andy S. Sardjan, Floris P. Westerman, Jennifer P. Ogilvie, and Thomas L. C. Jansen. Observation of Ultrafast Coherence Transfer and Degenerate States with Polarization-Controlled Two-Dimensional Electronic Spectroscopy. *The Journal of Physical Chemistry B*, 124(42):9420–9427, 2020.

[19] C. Neil Hunter and Fevzi Daldal, editors. *The purple phototrophic bacteria*. Number 28 in Advances in photosynthesis and respiration. Springer, Dordrecht, 2009.

[20] Tomáš Polívka and Villy Sundström. Ultrafast Dynamics of Carotenoid Excited States-From Solution to Natural and Artificial Systems. *Chemical Reviews*, 104(4):2021–2072, 2004.

[21] Tomáš Polívka and Villy Sundström. Dark excited states of carotenoids Consensus and controversy. *Chemical Physics Letters*, 477(1-3):1–11, 2009.

[22] Dariusz M. Niedzwiedzki, Preston L. Dilbeck, Qun Tang, Elizabeth C. Martin, David F. Bocian, C. Neil Hunter, and Dewey Holten. New insights into the photochemistry

of carotenoid spheroidenone in light-harvesting complex 2 from the purple bacterium *Rhodobacter* sphaeroides. *Photosynthetic Research*, 131(3):291–304, 2017.

[23] Hideki Hashimoto, Chiasa Uragami, Nao Yukihira, Alastair T. Gardiner, and Richard J. Cogdell. Understanding/unravelling carotenoid excited singlet states. *Journal of The Royal Society Interface*, 15(141):20180026, 2018.

[24] Chiasa Uragami, Hiroki Sato, Nao Yukihira, Masazumi Fujiwara, Daisuke Kosumi, Alastair T. Gardiner, Richard J. Cogdell, and Hideki Hashimoto. Photoprotective mechanisms in the core LH1 antenna pigment-protein complex from the purple photosynthetic bacterium, *Rhodospirillum* rubrum. *Journal of Photochemistry and Photobiology A: Chemistry*, 400:112628, 2020.

[25] Daisuke Kosumi, Tomoko Horibe, Mitsuru Sugisaki, Richard J. Cogdell, and Hideki Hashimoto. Photoprotection Mechanism of Light-Harvesting Antenna Complex from Purple Bacteria. *The Journal of Physical Chemistry B*, 120(5):951–956, 2016.

[26] N. N. Sluchanko, Y. B. Slonimskiy, and E. G. Maksimov. Features of protein-protein interactions in the cyanobacterial photoprotection mechanism. *Biochemistry Moscow*, 82 (13):1592–1614, 2017.

[27] Diana Kirilovsky and Cheryl A. Kerfeld. The Orange Carotenoid Protein: a blue-green light photoactive protein. *Photochemical & Photobiological Sciences*, 12(7):1135–1143, 2013.

[28] Adjélé Wilson, Ghada Ajlani, Jean-Marc Verbavatz, Imre Vass, Cheryl A. Kerfeld, and Diana Kirilovsky. A Soluble Carotenoid Protein Involved in Phycobilisome-Related Energy Dissipation in Cyanobacteria. *The Plant Cell*, 18(4):992–1007, 2006.

[29] Marina G. Rakhimberdieva, Irina V. Elanskaya, Wim F. J. Vermaas, and Navassard V. Karapetyan. Carotenoid-triggered energy dissipation in phycobilisomes of *Synechocystis*

sp. PCC 6803 diverts excitation away from reaction centers of both photosystems. *Biochimica et Biophysica Acta (BBA) - Bioenergetics*, 1797(2):241–249, 2010.

[30] Sarah Joshua and Conrad W. Mullineaux. Phycobilisome Diffusion Is Required for Light-State Transitions in Cyanobacteria. *Plant Physiology*, 135(4):2112–2119, 2004.

[31] Jun Minagawa. State transitions-The molecular remodeling of photosynthetic supercomplexes that controls energy flow in the chloroplast. *Biochimica et Biophysica Acta (BBA) - Bioenergetics*, 1807(8):897–905, 2011.

[32] Conrad W. Mullineaux. State transitions: an example of acclimation to low-light stress. *Journal of Experimental Botany*, 56(411):389–393, 2004.

[33] XiuLing Xu, Rui Zhang, Jie Xie, and JingQuan Zhao. New mechanism revealed for light-state transition in cyanobacterium Arthrospira platensis according to 77-K fluorescence kinetics. *Chinese Science Bulletin*, 57(11):1261–1265, 2012.

[34] Volha Chukhutsina, Luca Bersanini, Eva-Mari Aro, and Herbert van Amerongen. Cyanobacterial Light-Harvesting Phycobilisomes Uncouple From Photosystem I During Dark-To-Light Transitions. *Scientific Reports*, 5(14193):1–10, 2015.

[35] Y. V. Bolychevtseva, F. I. Kuzminov, I. V. Elanskaya, M. Y. Gorbunov, and N. V. Karapetyan. Photosystem activity and state transitions of the photosynthetic apparatus in cyanobacterium *Synechocystis* PCC 6803 mutants with different redox state of the plastoquinone pool. *Biochemistry Moscow*, 80(1):50–60, 2015.

[36] Reza Ranjbar Choubeh, Emilie Wientjes, Paul C. Struik, Diana Kirilovsky, and Herbert van Amerongen. State transitions in the cyanobacterium *Synechococcus elongatus* 7942 involve reversible quenching of the photosystem II core. *Biochimica et Biophysica Acta (BBA) - Bioenergetics*, 1859(10):1059–1066, 2018.

[37] Ahmad Farhan Bhatti, Diana Kirilovsky, Herbert van Amerongen, and Emilie Wientjes. State transitions and photosystems spatially resolved in individual cells of the cyanobacterium *Synechococcus elongatus*. *Plant Physiology*, page kiab063, 2021.

[38] Marina G. Strakhovskaya, Eugene P. Lukashev, Boris N. Korvatovskiy, Ekaterina G. Kholina, Nuranija Kh. Seifullina, Peter P. Knox, and Vladimir Z. Paschenko. The effect of some antiseptic drugs on the energy transfer in chromatophore photosynthetic membranes of purple non-sulfur bacteria *Rhodobacter sphaeroides*. *Photosynthesis Research*, 147: 197–209, 2021.

[39] Fei Ma, Elisabet Romero, Michael R. Jones, Vladimir I. Novoderezhkin, Long-Jiang Yu, and Rienk van Grondelle. Dynamic stark effect in two-dimensional spectroscopy revealing modulation of ultrafast charge separation in bacterial reaction centers by an inherent electric field. *The Journal of Physical Chemistry Letters*, 12:5526–5533, 2021.

[40] Hui-Yuan S. Chen, Michelle Liberton, Himadri B. Pakrasi, and Dariusz M. Niedzwiedzki. Reevaluating the mechanism of excitation energy regulation in iron-starved cyanobacteria. *Biochimica et Biophysica Acta (BBA) - Bioenergetics*, 1858(3):249–258, 2017.

[41] Hui-Yuan S. Chen, A. Bandyopadhyay, and Himadri B. Pakrasi. Function, regulation and distribution of IsiA, a membrane-bound chlorophyll a-antenna protein in cyanobacteria. *Photosynthetica*, 56(1):322–333, 2018.

[42] Gregory S. Orf, Rafael G. Saer, Dariusz M. Niedzwiedzki, Hao Zhang, Chelsea L. McIntosh, Jason W. Schultz, Liviu M. Mirica, and Robert E. Blankenship. Evidence for a cysteine-mediated mechanism of excitation energy regulation in a photosynthetic antenna complex. *Proceedings of the National Academy of Sciences*, 113(31):E4486–E4493, 2016.

[43] Marco A. Allodi, John P. Otto, Sara H. Sohail, Rafael G. Saer, Ryan E. Wood, Brian S.

Rolczynski, Sara C. Massey, Po-Chieh Ting, Robert E. Blankenship, and Gregory S. Engel. Redox Conditions Affect Ultrafast Exciton Transport in Photosynthetic Pigment-Protein Complexes. *The Journal of Physical Chemistry Letters*, 9(1):89–95, 2018.

[44] Jacob S. Higgins, Lawson T. Lloyd, Sara H. Sohail, Marco A. Allodi, John P. Otto, Rafael G. Saer, Ryan E. Wood, Sara C. Massey, Po-Chieh Ting, Robert E. Blankenship, and Gregory S. Engel. Photosynthesis tunes quantum-mechanical mixing of electronic and vibrational states to steer exciton energy transfer. *Proceedings of the National Academy of Sciences*, 118(11):e2018240118, 2021.

[45] Lawson T. Lloyd, Ryan E. Wood, Marco A. Allodi, Siddhartha Sohoni, Jacob S. Higgins, John P. Otto, and Gregory S. Engel. Leveraging scatter in two-dimensional spectroscopy: passive phase drift correction enables a global phasing protocol. *Optics Express*, 28(22): 32869, 2020.

CHAPTER 8

CONCLUSION

Throughout the history of our planet Earth, the Nature has never ceased to impress us with its continuing effort on optimizing the survivability of living organisms through generations of evolution. Photosynthetic organisms have also benefited from natural evolution by establishing robust machinery and structural network for solar light harvesting processes.

In Chapter 1, I gave an broad overview of topics pertaining to this Dissertation. I provided my motivation for researching on light harvesting through the lens of dealing with global climate change and developing alternative energy sources. Then, I introduced the principles of light harvesting. Finally, I provided two examples in biology on the schemes and components of light harvesting in photosynthetic bacteria; one on purple bacteria and the other on cyanobacteria, which constitutes the bulk of my Dissertation projects.

In Chapter 2, I reviewed the theoretical basis of the technical methods employed in this Dissertation. I described the basics of quantum mechanics, the density matrix notation, time-evolution of density matrix, mathematical and pictorial representations of optical response functions, and principles of coherent two-dimensional spectroscopy.

In Chapter 3, I introduced the experimental techniques in this Dissertation. Specifically, I gave a brief overview on the working principles of pump-probe spectroscopy and two-dimensional electronic spectroscopy (2DES), as well as means to obtain the final data from start to finish, including generating a broadband ultrashort laser pulse, applying heterodyne detection scheme to record the spectral phase of 2DES signals, and retrieving the absolute spectral phase by a phasing procedure.

In Chapter 4, I presented the first 2DES experimental results on the photosynthetic membrane embedding only the core antenna complex, the LH1 complex, from the L3 mutant (Δpuc1BA ΔpufLMX) of purple bacterium *Rhodobacter sphaeroides*, a mutant that produces the LH1 complex as its sole light harvesting protein. I have resolved a weak spectroscopic

feature resulting from an ultrafast inter-state population relaxation from the higher-lying excitonic state, B875* to the bright excitonic state, B875. I have characterized the lifetime of this ultrafast relaxation to be sub-40 fs.

In Chapter 5, I presented a complete characterization on the coherences observed in the 2DES experiment on the LH1 complex-only membranes from *Rhodobacter sphaeroides*. I have performed Fourier analysis on both rephasing and nonrephasing part of the 2DES signals of LH1-only membranes. I have attributed some observed high-frequency coherences to vibronic couplings among higher-lying B875* states, and also characterized low-frequency vibrational coherences on the bright B875 state.

In Chapter 6, I presented the first 2DES experimental results on the light harvesting supercomplex, the phycobilisomes (PBS), from cyanobacterium *Synechococcus elongatus* PCC 7942. I have developed an improved, easy-to-implement isolation protocol to prepare isolated PBS with structure integrity. I have also utilized the scatter-removal and bulk-averaging advantages of GRAPE spectrometer to acquire 2DES results on fast-degrading isolated PBS samples.

In Chapter 7, I provided some future directions for projects seeking to further explore the design principles of photosynthetic light harvesting. I raised some challenges and opportunities in studying photobiology in purple bacteria and cyanobacteria. I also made some suggestions on areas in which the 2D spectrometer utilized in this Dissertation, GRAPE spectrometer, could be improved.

Scientific research has no ending, as every day our understanding of this Universe continues to grow and get challenged. This Chapter concludes my small steps in contributing knowledge to the world of photosynthetic light harvesting. I hope the results presented in this Dissertation will, just as the ones I have based my doctoral research upon, be a part of foundation to future aspiring scientists.